

AREVA NP GmbH

Forschungszentrum Karlsruhe in der Helmholtz-Gemeinschaft

Fluidic diode for critical two-phase flows

Zur Erlangung des akademischen Grades eines

Doktors der Ingenieurwissenschaften

der Fakultät für Maschinenbau
Karlsruher Institut für Technologie (KIT)

genehmigte

Dissertation

von

Dipl.-Ing. Julien Xavier Pierre Dumond

aus Versailles

Hauptreferent: Prof. Dr.-Ing. Andreas Class

Korreferent: Prof. Dr.-Ing. Bettina Frohnappel

Eingereicht: am 19. Oktober 2012

Mündliche Prüfung: am 14. Dezember 2012

Acknowledgment

Foremost, I would like to thank my advisor Prof. Andreas Class for supporting me during these three past years. He has been actively interested in my work and has always been available to advise me. His support and guidance made this thesis work possible. I have to thank Stefan Leyer, from AREVA NP GmbH, and Prof. Thomas Schulenberg, head of the Institut für Kern- und Energietechnik (IKET), for providing me the opportunity to complete my PhD thesis at the Karlsruhe Institute of Technology (Campus North) in the framework of the AREVA Nuclear Professional School. Thereby, I acknowledge the funding sources provided by AREVA NP GmbH. I also want to thank Stefan Leyer and Bettina Frohnappfel for being members of my PhD committee.

For the design and validation of the POR design, I have to thank the members of the departments PEER4-G, PEPA3-G, PESB-G, PTBD-G, PTCTC-G and NTCTA-G of AREVA NP GmbH for the pleasant collaboration. In particular, I want to thank Fabian Maisberger who was in charge of performing the validation tests at the AREVA Technical Center in Karlstein and Álvaro PÉREZ-SALADO for providing me a convenient routine to calculate two-phase critical mass flux.

The numerical analysis of cavitation in this dissertation would not have been possible without Franco Magagnato and his code SPARC. I am very grateful for his scientific advice and knowledge, and many insightful discussions. I also thank Prof. Martin Gabi for giving me the opportunity to use SPARC in his department Fachgebiet Strömungsmaschinen (FSM) at the Karlsruhe Institute of Technology (Campus South).

I am also grateful to the members of both departments IKET and FSM. My time at the Karlsruhe Institute of Technology was made enjoyable in large part thanks to them. I have not only appreciated their technical support but also their delightful discussions especially during the coffee-breaks. Among them, I would like to thank my reading committee members: Jana Fetzner, Christian Glück, Benjamin Jastrow, Michael Ranft, Markus Stokmaier, Tobias Szabó and Mathias Viellieber for their time and interest. I do not forget to thank Stefan Holst among my reading committee members. I also thank Balazs Pritz for his time and good advice.

Lastly and most of all, I would like to thank my family for all their love and encouragement. Their faithful support during this Ph. D. is so appreciated. Thank you.

Julien Xavier Pierre Dumond
Karlsruhe
October 2012

Abstract

The goal of the present thesis is to develop an innovative fluidic diode for the boiling water reactor KERENA of AREVA. This component, called the passive outflow reducer, must limit the loss of coolant in one flow direction, the backward direction, after the break of a large pipe connected to the reactor pressure vessel. In the opposite flow direction, the forward direction, the pressure loss in this component must be minimized not to jeopardize emergency core cooling. Finally, the passive outflow reducer must be compact and perform without moving part.

Vortex diodes are developed to achieve high ratios between the backward and forward flow resistances. For this purpose, they produce a strong swirl in the backward direction. After the postulated break of this large pipe, the coolant is moderately subcooled or saturated. Under these conditions, the efficiency of the vortex diodes is adversely affected because the swirl they produce is degraded by two-phase effects.

Therefore, the innovative passive outflow reducer design developed in the framework of this Ph. D. does not rely on swirl. It consists of profiled channels composed of two Venturi nozzles. The loss of coolant is reduced by enforcing energy dissipation and vaporization with the first nozzle and efficient choking of the two-phase mixture in the second nozzle where low sound speed and density are encountered.

A compact and robust component is achieved by parallel arrangement of multiple identical double Venturi-nozzle channels. For the KERENA reactor, 37 channels are proposed. This yields a cluster with 250mm diameter and 900mm length which conveniently fits into the heavy duty reactor pressure vessel nozzle assuring no failure of the passive outflow reducer.

A three-dimensional cavitation code is developed to describe the flow behavior of this innovative fluidic diode in the backward and forward directions under cavitating conditions. The stochastic-field method developed by Valiño is adapted to cavitating flows to combine the advantages of Euler and Euler-Lagrange formulations. With this stochastic-field cavitation model, the various shapes of the bubble size spectrum are captured and the stochastic processes are treated in a fully Euler manner, and thus without excessive computational demand and complex algorithms.

Large eddy simulations of the proposed passive outflow reducer design demonstrate the capability of the new modeling approach.

Kurzfassung

Fluidische Diode für kritische Zwei-Phasen-Gemische

Ziel der vorliegenden Arbeit ist es, eine innovative passive fluidische Diode ohne bewegliche Teile für den Siedewasserreaktor KERENA von AREVA zu entwickeln. Diese Komponente, der sogenannte passive Rückflussbegrenzer, limitiert den Kühlmittelverlust in rückwärtiger Strömungsrichtung nach dem postuliertem Bruch einer an dem Reaktordruckbehälter angeschlossen großen Leitung. In der entgegengesetzten Strömungsrichtung, der Vorwärtsrichtung, muss der Druckverlust in dieser Komponente minimiert werden, um die Notkühlung des Reaktorkerns nicht zu mindern.

Um ein hohes Verhältnis zwischen Vorwärts- und Rückwärtsströmungswiderstand zu erreichen, werden Wirbeldioden entwickelt. Diese Dioden erzeugen einen starken Drall, der den Rückwärtsströmungswiderstand erhöht. Nach dem postulierten Bruch der großen Leitung im KERENA Reaktor ist das Kühlmittel moderat unterkühlt oder gesättigt. Unter diesen Bedingungen verschlechtert sich die Effizienz der Wirbeldiode, da der Drall durch zweiphasige Effekte vermindert wird.

Daher ist ein innovativer Rückflussbegrenzer im Rahmen dieser Doktorarbeit entwickelt worden, der nicht auf Drall beruht. Der innovative Rückflussbegrenzer ist eine parallele Anordnung von profilierten Strömungskanälen, bestehend aus je zwei aufeinanderfolgenden Venturi-Düsen. Der Verlust von Kühlmittel wird durch Energiedissipation und Verdampfung in der ersten Düse und effiziente Sperrung des Zwei-Phasen-Gemisches in der zweiten Düse, wo geringe Schallgeschwindigkeit und Dichte auftreten, erzielt.

Die parallele Anordnung mehrerer identischer Strömungskanäle ermöglicht eine kompakte und robuste Bauweise. Für die KERENA Reaktor werden 37 Kanäle vorgeschlagen. Daraus ergibt sich ein Block mit 250mm Durchmesser und 900mm Länge, der in dem robusten Reaktordruckbehälteranschluss passt und sicherstellt, dass der Rückflussbegrenzer nicht ausfallen kann.

Ein dreidimensionales Kavitationsmodell wurde entwickelt, um das Strömungsverhalten dieser innovativen fluidischen Diode in der vorwärts und rückwärts Richtungen unter kavitierenden Bedingungen zu beschreiben. Die stochastische Feldmethode von Valiño wurde für Kavitation erweitert, um die Vorteile von Euler und Euler-Lagrange Formulierungen zu kombinieren. Mit diesem Stochastischenfelderkavitationsmodell, sind die verschiedenen Formen des Blasengrößespektrums erfasst und die stochastischen Prozesse werden vollständig in einem Eulerschen Rahmen, und somit ohne übermäßige Rechenleistung und komplexe Algorithmen, behandelt.

Large-Eddy Simulationen der vorgeschlagenen passiven Rückflussbegrenzer demonstrieren die Leistungsfähigkeit des neuen Modellierungsansatzes.

Table of content

1	INTRODUCTION	3
1.1	BACKGROUND	3
1.2	SCOPE OF THE PRESENT STUDY	8
1.3	OUTLINE OF THE PRESENT STUDY	11
2	PHYSICS	13
2.1	SINGLE PHASE FLOWS	13
2.2	TWO PHASE FLOWS	22
3	CAVITATION	29
3.1	GOVERNING EQUATIONS	29
3.2	CHARACTERISTICS OF CAVITATING FLOWS	37
4	NUMERICAL MODELING	43
4.1	NUMERIC	43
4.2	MODELING OF SINGLE-PHASE FLOWS	53
4.3	MODELING OF TWO-PHASE FLOWS	60
4.4	MODELING OF CRITICAL TWO-PHASE MASS FLUX	71
4.5	MODELING OF POLYDISPERSE FLOWS	73
4.6	MODELING OF CAVITATION	78
5	PROBABILITY DENSITY FUNCTION APPROACH	83
5.1	STOCHASTIC PROCESSES	83
5.2	STOCHASTIC EQUATIONS	86
5.3	MODELING WITH STOCHASTIC PROCESSES	89
5.4	PDF TRANSPORT EQUATIONS	91
5.5	LAGRANGE APPROACH FOR PDF EQUATIONS	95
6	DEVELOPMENT OF THE PASSIVE OUTFLOW REDUCER	97
6.1	INTRODUCTION	97
6.2	BACKWARD DIRECTION	97
6.3	FORWARD DIRECTION	100
6.4	SIZE REDUCTION	103
7	PERFORMANCE TESTS	105
7.1	INTRODUCTION	105
7.2	BACKWARD DIRECTION	105
7.3	FORWARD DIRECTION	109
7.4	PERFORMANCE FACTOR	115
7.5	CONCLUSION	116
8	STOCHASTIC-FIELD CAVITATION MODEL	117
8.1	INTRODUCTION	117
8.2	OBJECTIVE OF THE MODEL	119
8.3	DERIVATION OF THE MODEL	120
8.4	SOLVER SPARC	124
8.5	GOVERNING EQUATIONS	124
8.6	VALIDATION CASES	135
9	POR ANALYSIS	149
9.1	BACKWARD DIRECTION	149
9.2	FORWARD DIRECTION	161
9.3	CONCLUSION	168
10	CONCLUSION	169
	NOMENCLATURE	170

BIBLIOGRAPHY	182
APPENDIX A: FORCES ACTING ON BUBBLES DISPERSED IN A LIQUID PHASE.	197
APPENDIX B: DEFINITION AND PROPERTIES OF STOCHASTIC PROCESS.....	199

1 Introduction

1.1 Background

The accident of Fukushima in 2011 has strengthened the discussion about safety in nuclear power stations. Following an earthquake, reactor shut down was automatically actuated and emergency generators started to control electronics and coolant systems. Due to a tsunami, reactor's power grid connection was broken and the room containing the emergency generators was flooded. As a result, those generators ceased working and the pumps could not circulate coolant water in the core. The core started to overheat. External assistance was hindered by flooding and earthquake damage. In spite of the existing safety system, radioactive release was not avoided. Actually this accident demonstrates that the technology of the 40 years old Fukushima nuclear power station was outdated and that active safety system alone cannot assure safety requirements.

1.1.1 KERENA reactor

Increased safety and reduced costs are achieved in the boiling water reactor (BWR) KERENA with a smart combination of active and passive safety systems. The passive safety systems use physical phenomena such as gravity and natural energy exchange to perform their designated safety functions without electrical power or active actuation by instrumentation and control (I&C) systems. This combination of active and passive systems is able to provide a protection of the core without operator intervention for three days. Furthermore, it reduces the costs and complexities in comparison to today's active safety systems.

The KERENA BWR of AREVA is a mid-capacity generation 3+ BWR. Its net electrical output is 1250 MWe by design. Mid capacity power stations represent a good compromise between reduced operating and capital costs and electrical network stability. The main components and operating mode of the KERENA BWR are illustrated schematically in Figure 1-1. Saturated steam is produced in KERENA reactor core (1). It is routed through the high-pressure turbine (3) and the moisture separator/reheater (4) to the low pressure turbine (3). Due to the expansion of the steam, the turbines rotate and drive the generator (10). The steam leaving the low-pressure turbine condenses in the main condensers (5). The condensate returns to the reactor by condensate (6) and feedwater pumps (8) via a condensate cleanup system and a feedwater heating train (7).

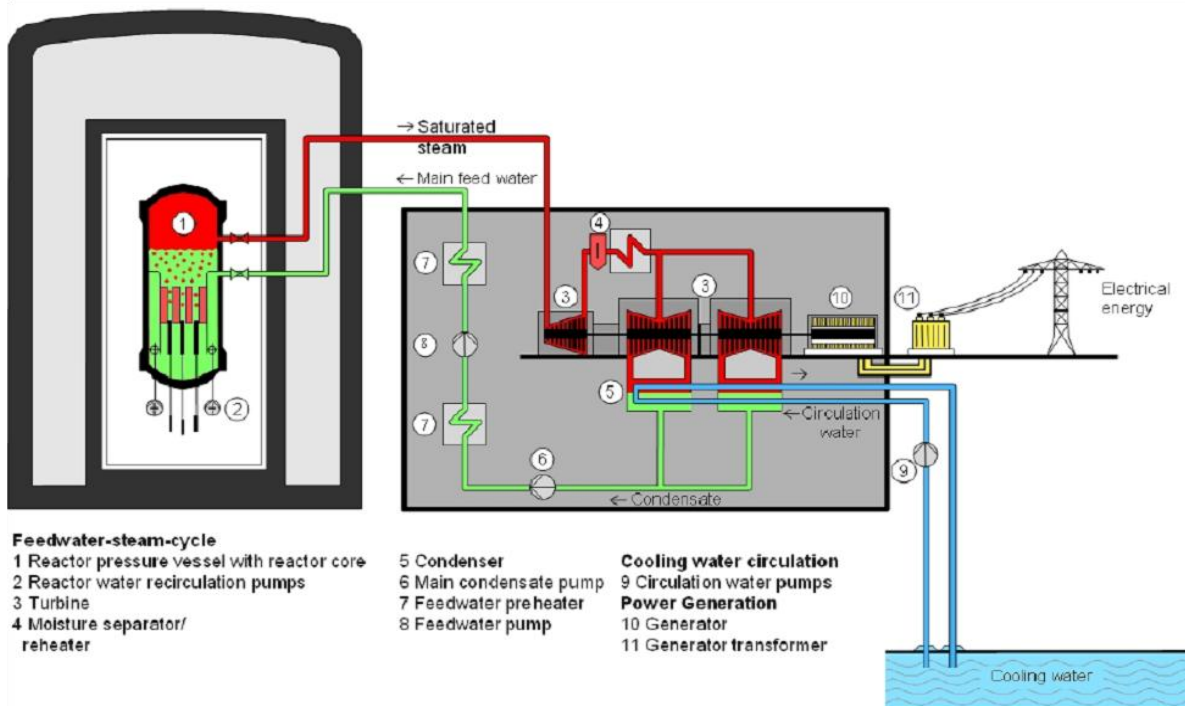


Figure 1-1: Basic diagram of the KERENA reactor [1].

1.1.2 Emergency condenser system

One of the passive safety systems of the KERENA reactor is the emergency condenser (EC) system. The EC system is an innovative concept. It passively removes excess heat and in particular the decay heat from the reactor pressure vessel (RPV) during transients and loss of coolant accidents (LOCA) without supplementary water inventory loss.

The EC system consists of four identical sub-systems which are spatially separated and can operate independently from one another. Each of them is composed of a condenser, of a steam supply line, and of a condensate return line. The steam supply line connects the RPV to the condenser and the condensate return line connects the condenser back to the RPV.

The condenser (Figure 1-2) is composed of a pre-chamber and a U-tube bundle. The pre-chamber is located in the drywell and separated into two parts. The upper-part, the steam distributor, collects the steam coming from the steam supply line and distributes it through a tube sheet to the U-tube bundle. The lower part is called the condensate collector since it collects the condensate coming from the EC U-tube bundle and conveys it to the condensate return line. The tubes are inclined so that the condensate is automatically gathered into the lower part. The entire U-tube bundle is located inside the core flooding pool which is filled with cold water.

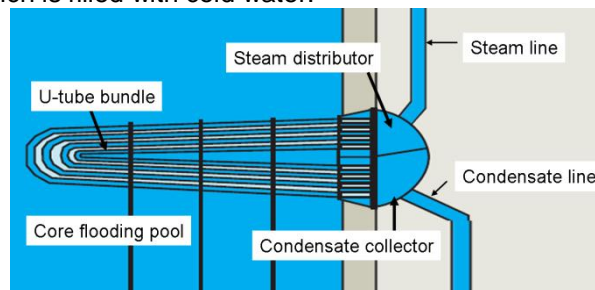


Figure 1-2: Parts of an emergency condenser sub-system: condenser (steam distributor, condensate collector, U-tube bundle), steam supply line, condensate return line.

The actuation of the EC system relies on the principle of the communicating tubes. Water levels in EC loop and on RPV side adjust themselves so that the resulting geodetic pressures equalize.

Figure 1-3 illustrates the operating modes of one EC sub-system. During power operation (Figure 1-3 on the left), water level in RPV, and thus in EC loop, is high. Steam is not in contact with the cold condenser tubes. No heat exchange occurs between the EC and the core flooding pool. No heat is removed from the RPV. In contrast, transient involving drop in water level and LOCA (Figure 1-3 on the right) induce the decrease of the water level in the EC train. Vapor gets into contact with the cold EC tubes and condensates. In the core flooding pool, water heats up and may vaporize. The condensate returns back to the RPV by gravity. The EC passively becomes active and heat is released from the RPV to the core flooding pool without loss of coolant.

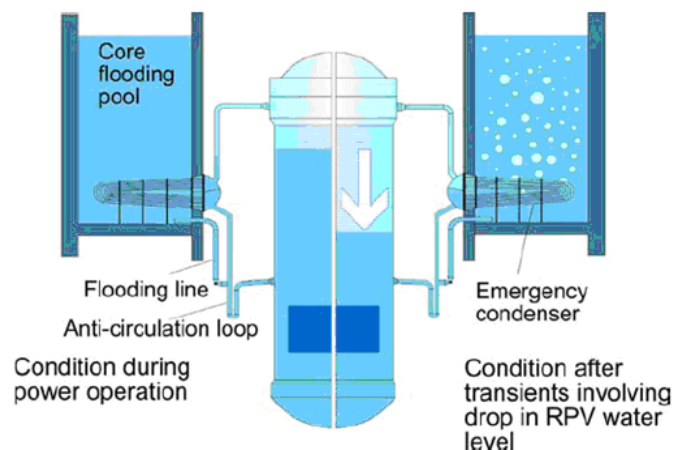


Figure 1-3: Operating modes of one of the emergency condenser sub-systems [1]. During power operation (left), no heat transfer occurs in the emergency condenser tubes. During transients involving drop in RPV water level and LOCA, steam condenses in the condenser tubes. Heat is removed from the RPV without supplementary water inventory loss.

Thus, the EC System does not change the water inventory inside the RPV in opposition to systems which limit and reduce pressure by removing coolant from the RPV. The KERENA reactor remains operating in case of incidental scenarios with small transients avoiding an emergency shutdown of the reactor (scram).

To highlight the role of the EC during large transients and LOCA in the KERENA reactor [2], three incidental scenarios are worth considering.

In the first scenario, the main heat sink (e.g. river, sea, lake, or cooling tower) is not available. The pressure increases in the RPV and a scram is actuated by the plant protection system. Rod insertion in the boiling fluid yields the collapse of the bubbles. RPV water level decreases and the EC system starts to operate. Then, RPV water level is monitored by the mass flow of either the feed water or clean up system such that EC heat removal matches the decreasing decay heat. In this manner, the RPV pressure stays constant at a nominal value.

In the second scenario, neither the main heat sink, nor the feed water is available. Large amount of heat must be removed shortly after the scram and EC capacity is not sufficient. At least one safety relief valve is opened to further reduce RPV pressure. Steam is released and EC water level decreases. After some time, the decay heat is smaller than EC heat removal and the reactor is depressurized without any further need of safety relief valve and thus loss of coolant.

The last scenario represents a LOCA. Scram and loss of coolant lower RPV and EC water levels. The EC begins to remove heat from the RPV thereby reducing the RPV pressure. The loss of coolant in the leak triggered by the pressure difference existing between the RPV and the containment also weakens. For small leakages, the pressure release is so fast that water can be pumped from the pressure suppression chambers (Figure 1-4) into the RPV to compensate the loss of coolant before safety relief valves are actuated. Thus, any supplementary loss of coolant is avoided. For severe leakages, safety relief valves are actuated. The loss of coolant in these valves also reduces by the action of the EC on the RPV pressure.

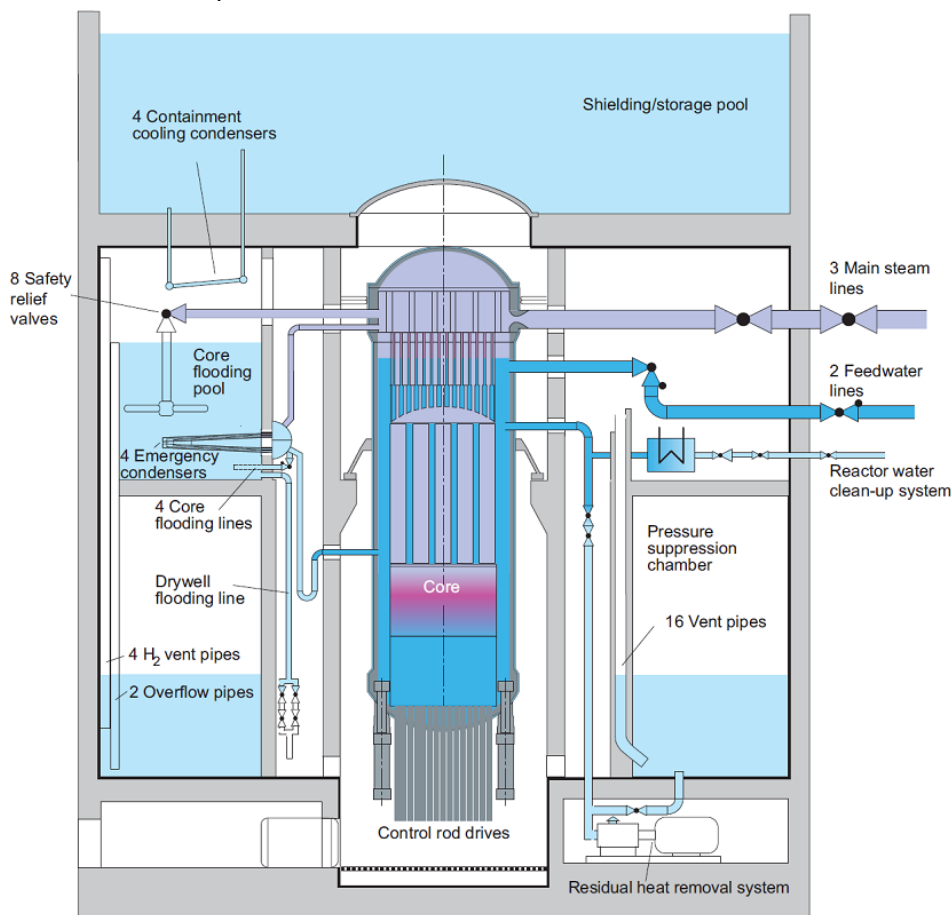


Figure 1-4: Containment and internals of the KERENA reactor [1].

1.1.3 Passive outflow reducer

The EC system is directly connected to the RPV. The failure of a part of the EC system must also be considered as a design accident. Three design accidents require consideration: the break or leakage of one condenser tube, of the steam supply line and of the EC condensate return line.

In case of the break or leakage of one condenser tube, the loss of coolant is not large and the other pipes of the bundle still work correctly. Thus, the RPV coolant inventory and the EC heat removal capacity are not significantly affected.

After the break or leakage of the steam supply line, the EC train is completely affected. To reduce the loss of coolant, a Venturi nozzle is positioned in the RPV nozzle at the beginning of the steam supply line. Parallel to that, the RPV pressure decreases fast since steam discharges from the broken pipe and the remaining three EC trains still work properly. Thus, active and passive core flooding can be actuated at low pressure before cladding heat up.

The accident involving the break or leakage of the EC condensate return line is similar to that of the steam supply line break. However, in contrast to the aforementioned scenario, the EC condensate return lines are connected at a low elevation just above the top of the core to increase EC loop geodetic pressure. As a result, the coolant is still moderately subcooled or at saturation. This is disadvantageous for two reasons. First, coolant mass flux is very high. It can exceed by several orders of magnitude vapor mass flux. Second, the loss of coolant does not induce a RPV pressure release as it would be the case with the loss of vapor. Pressure gradients remain large between downcomer and containment. Furthermore, the EC condensate return line is large to limit the flow resistance in the EC system loop. A component, called the passive outflow reducer (POR), is required to significantly limit the mass flow under these conditions.

The POR must be a compact and efficient fluidic diode. It has to fulfill conflicting requirements. First, the POR must be compact (length<1m, diameter<250mm) and perform passively without moving part. In this manner, the POR can be positioned in the heavy duty RPV nozzle of the EC condensate return line. The failure of the POR itself during KERENA operational conditions can be ruled out. Second, the POR must produce high pressure loss in one flow direction, called the backward direction. In this direction, represented on Figure 1-5 on the left, the coolant streams out of the RPV into the containment following the break of the EC condensate return line. Finally, the flow resistance in the POR in the opposite flow direction, called the forward direction, should be minimized not to jeopardize emergency core cooling. This operating mode is shown on Figure 1-5 on the right. The coolant flows from the EC to the RPV. High flow resistance would reduce EC heat removal capacity by increasing the water level in the EC tubes.

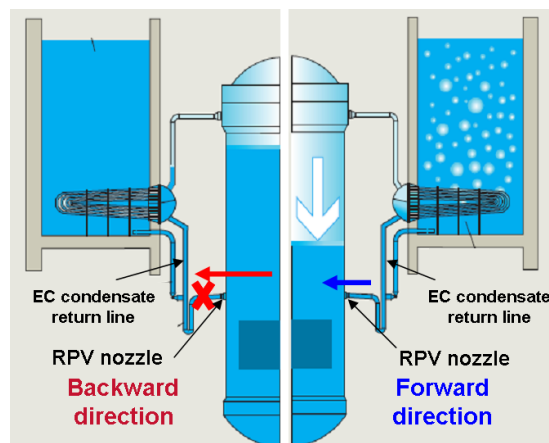


Figure 1-5: Operating modes of the POR. In case of the break of the EC condensate return line (left), the flow resistance in the POR must be high to limit the loss of coolant. This flow direction is called the backward direction. During emergency core cooling (right), the coolant flows from the EC into the RPV. In this flow direction, called the forward direction, the hydraulic loss must be minimized not to jeopardize EC heat removal capacity.

1.1.3.1 Requirement in the backward direction

In the backward flow direction, the POR must limit the loss of coolant following the break of the EC condensate return line. In this context, the most severe accident scenario is the two-full break of this

pipe. The thermohydraulic analysis of this event is performed in [3]. It indicates that the loss of coolant from the RPV should not exceed 50 tons during the first 1000 seconds. Otherwise cladding heat up could be observed. Void fraction, temperature and pressure in the downcomer at EC condensate return line height are also given in [3]. Their temporal evolution is represented for the first 1000 seconds following the break of the EC condensate return line in Figure 1-6.

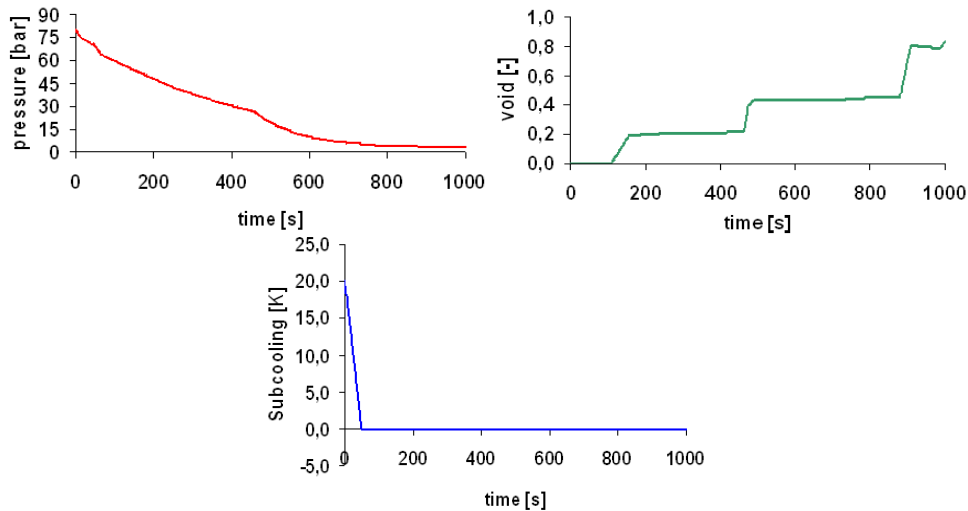


Figure 1-6: Boundary conditions at the inlet of the POR in the KERENA reactor after the break of the EC condensate return line. Pressure (top left), void (top right), subcooling (bottom) [3].

1.1.3.2 Requirement in the forward direction

In the opposite flow direction, the POR pressure loss must be minimized. All transients and LOCA of the KERENA reactor are examined in [3] to estimate the maximum authorized POR flow resistance during emergency core cooling. In the critical scenario, the mass of coolant is 45 kg/s at RPV pressure 75 bar. This critical scenario is mastered as long as the POR pressure loss does not exceed 15 kPa.

1.1.4 Vortex diodes

Vortex diodes are used [4] and developed in the nuclear industry to achieve passively and without moving part high ratios between backward and forward direction pressure losses (e.g. [5]; [6]). An example of a vortex diode is given on Figure 1-7. The flow direction is the backward direction when the coolant enters the vortex diode through the tangential ports (Figure 1-7, left). In the forward direction, the coolant enters the vortex diode through the axial port (Figure 1-7, right).

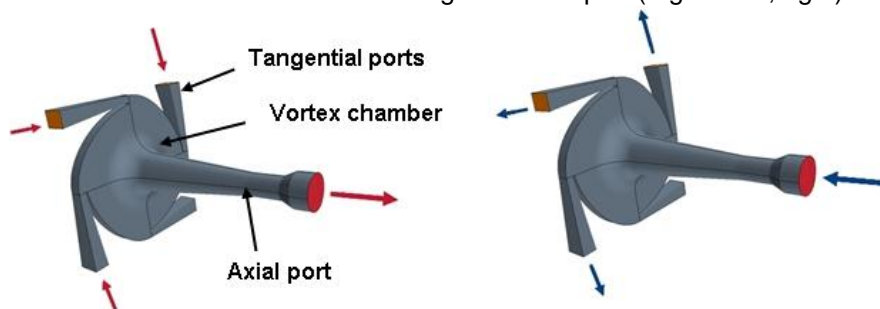


Figure 1-7: Principle of a vortex diode. Left: flow in the backward direction; right: flow in the forward direction.

1.1.4.1 Single-phase flow behavior

In incompressible single-phase flows, their principle is well known. The large flow resistance in the backward direction (Figure 1-7, Left) is produced by strong vortices induced in the vortex chamber. In a vortex diode with a vortex chamber of radius r_1 , the mass flow \dot{m} entering the tangential ports is converted into a swirl $S \propto r_1 \dot{m}$ (Figure 1-8).

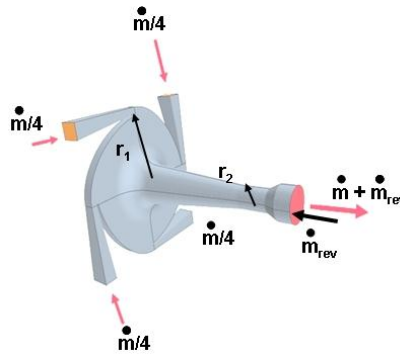


Figure 1-8: Principle of a vortex diode in the backward direction. The mass flow at the inlets is \dot{m} . The mass flow in the axial port is composed of the throughflow \dot{m} and a recirculation flow \dot{m}_{rev} . r_1 is the radius of the vortex chamber; r_2 is the radius of the axial port.

In a rough approximation the swirl is conserved down to the outlet of the vortex diode. There, the radius is $r_2 < r_1$. Consequently, the peripheral velocities increase as $\sim r_1/r_2$ and the friction loss accordingly. Moreover, due to the swirl, the pressure is smaller in the vortex core than in the periphery of the axial port. A large zone of reverse flow occurs on the vortex axis. This reverse flow reduces the effective cross section. It also causes a reverse mass flow $-\dot{m}_{rev}$ to enter in the geometry through the axial port. Then, the total mass flow leaving the geometry through the effective cross section is $\dot{m} + \dot{m}_{rev}$. Both the larger flow rate and the reduced effective cross section yield very large flow resistance. The flow resistance increases with swirl amplitude.

In the forward direction (Figure 1-7, right), no swirl is induced and the flow resistance is relatively lower.

1.1.4.2 Two-phase flow behavior

However, the efficiency of the vortex diode may decrease in the presence of a two-phase mixture. The swirl or the recirculation zones are reduced:

- Previous experiments [7] indicate that the performance of vortex diodes in the backward direction deteriorate with compressibility. Tests with steam and air in [7] or wet steam [8] show that choking is delayed and accompanied with a reduction of the fluidic diode resistance. The authors speculate that the aerodynamic blockage is swept out of the axial port as the flow becomes compressible.
- Results of [8] indicate that water slugs present at higher wetness lead to the destruction of the vortex decreasing the resistance of the vortex diode.
- Heuristic arguments in [9] explain that the expansion of the mixture at the outlet of the tangential ports destructs the vortex.
- The pressure in the core region cannot decrease below saturation pressure. If the flow already is at saturated conditions, the recirculation flow \dot{m}_{rev} is minimal.

Moreover, the mixture is no longer homogeneous at the choking cross section. If, in particular, a film of water is formed, the mass flux increases drastically.

1.2 Scope of the present study

The coolant leaving the RPV is moderately subcooled and saturated after the break of the EC condensate return line (Figure 1-6). A vortex diode may be less attractive under these conditions than with strongly subcooled coolant.

Hence, in the framework of the Ph. D., a fluidic diode for critical two-phase flows is developed. It relies on cavitation and efficient choking, instead of swirl. This fluidic diode is adapted to the KERENA boundary conditions to fulfill the POR requirements and, thus, is called the POR design or the POR in the present work. This POR design is composed of 37 parallel double-nozzle channels (Figure 1-9). These channels are shaped to achieve the following requirements:

- In the backward direction (red arrow on Figure 1-9), the POR passively limits the loss of coolant following the break of the EC condensate return line without moving part. For this

purpose, cavitation and energy dissipation are enforced in the first nozzle and the flow chokes in the second nozzle, where low sound speed and density are encountered.

- In the forward direction, i.e. during emergency core cooling, (blue arrow on Figure 1-9), the flow resistance is minimal.

The parallel channels lead to a short and compact component (length < 1m, diameter < 250mm).

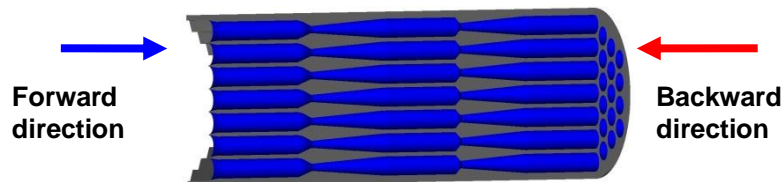


Figure 1-9: Longitudinal section of the fluidic diode adapted to KERENA reactor boundary conditions. In that case, the diode is called POR and consists of 37 channels (blue); material (grey).

Due to the simplicity of this geometry, the POR can be designed with standard system codes in the backward direction and computational fluid dynamics (CFD) codes in the forward direction.

After this innovative design was validated by experimental tests, the next objective of the Ph. D. thesis consists in developing a novel cavitation model using the stochastic-field method [10].

The simulation of cavitating flows is a challenging problem both in terms of modeling the physics and developing robust numerical methodologies. Such flows are characterized by considerable variations of the local density and involve thermodynamic phase transition. They also are inherently stochastic [11]. The turbulence interacts with the vaporous cavities and the bubble size probability density function (pdf) and nuclei number density pdf have large variance [12]; [13]. Consequently, the physical processes such as inter-phase transfers, breakup and collapse which depend upon the turbulence, number and size of vaporous cavities are fluctuating substantially. This is particularly important for nucleus growth which is highly non-linear: growth is unbounded for sufficiently large nuclei and is inhibited for small nuclei.

In spite of intensive research, available cavitation models are problem and geometry specific. They must be fitted to experimental results and thus are only valid for a small range of operating conditions and geometries. Therefore, in this thesis, emphasis is given on developing a cavitation model adequate for the simulation of cavitating flows with very different flow conditions. As an example, the POR flow behavior is investigated in both flow directions with this novel cavitation model. To achieve this objective, the present formulation distinguishes from available approaches in three different ways.

First, instead of following the individual cavities in a Lagrangian framework or the mixture in the Eulerian framework we can model the highly non-linear cavitation process using probability density functions (pdf) and pdf transport models (Figure 1-10). Pdf models are common to describe stochastic processes such as the random walk of gas molecules. As an example, relaxation to equilibrium of a fluid consisting of gas molecules is obtained from statistical mechanics in the so-called Boltzmann equation which was derived by Boltzmann in 1872. This Boltzmann equation represents the prototype of a pdf transport equation. In chemical reactions, pdf methods are commonly used to close the highly non-linear chemical source term. For this purpose, Dopazo and O'Brien [14] introduced the transport equation of the composition joint-pdf. Although the pdf transport equations are derived in an Eulerian framework, their solution generally is achieved by following particles with a Lagrangian solver in combination with Monte-Carlo methods (e.g. Pope [15] in combustion). These particles carry information on the flow properties. An Eulerian solver is needed to exploit particles statistical information. In combustion, typically an Eulerian solver is used for the flow equations, e.g. for the pressure. The coupling in an Eulerian-Lagrangian solver is complex due to the necessity to locate Lagrangian particles in the Eulerian numerical mesh. Moreover the Lagrangian method is very expensive for a good statistic and convergence. To avoid the cost and complexity of Euler-Lagrangian techniques, Valiño [10] developed the stochastic-field method to solve the pdf in a fully Eulerian framework. This new formulation has recently gained substantial interest (e.g., [16], [17], [18], [19]). In this paper, a novel cavitation model based on this stochastic-field method is derived to simulate cavitating flows. The pdf transport equation of the bubble-size pdf is solved in an Eulerian framework avoiding the complex and expensive coupling of an Eulerian-Lagrangian solver.

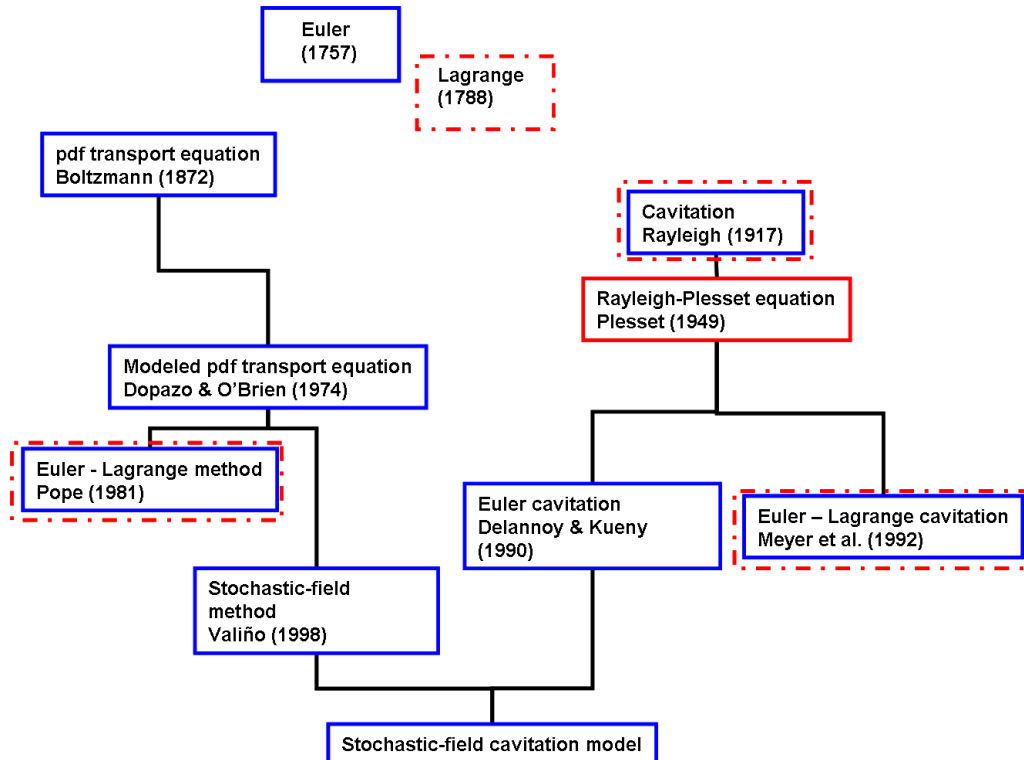


Figure 1-10: Historical context of the proposed stochastic-field cavitation model: In statistical mechanics the pdf ansatz was introduced in the 19th century by Boltzmann so that pdf transport models and corresponding numerical techniques have matured in this field. Cavitation originates from an Euler-Lagrangian point of view and currently develops in the direction of pure Eulerian pdf models. Eulerian and Lagrangian models are framed in blue and red, respectively.

Thus, the proposed cavitation model combines the advantages of Euler and Lagrange solvers in a pure Euler formulation. The probability density function of the vapor mass fraction is solved to capture the bubble size spectrum in a fully Euler framework. The wide range of bubble size spectra present at different locations can be described without excessive computational demand. Stochastic processes and highly non-linear, radius dependent phenomena can be accounted for using existing physical models available for Lagrange techniques, presumed pdf or binning methods. This cavitation model represents the first application of the stochastic-field method in multi-phase flows to capture bubble size spectra in that manner.

Second, the interfacial mass transfer mechanism is developed to include thermal, inertial and water quality effects.

Finally, the equations of state of the water-vapor mixture and constitutive relations are defined to reproduce the physics of the thermodynamic phase change.

The flow conditions in the backward direction are particularly demanding for the numerical code. Very large pressure, temperature and density gradients are encountered. With available commercial software (CFX, Fluent, Star-CCM+), no solution could be obtained. Significant modification in their code would have been required. First, the pressure, temperature and density gradients are so large that the codes become unstable. Second, the equations of state of the water-vapor mixture are not implemented. Finally, the vapor mass fraction must remain strictly positive. This requirement can not be achieved solely with a source term in the vapor mass fraction transport equation. The pressure variations encountered during the transient phase, i.e. before a statistical stationary solution is obtained, are very large. As a result, the vapor mass fraction becomes negative and the code diverges. For these reasons, the model is implemented in the state-of-the-art density-based solver SPARC [20] developed at the Karlsruhe Institute of Technology (Campus South). This code is able to cope with highly compressible flows and the necessary physical models can be implemented.

Thus, the present thesis has two main objectives:

- Presentation of this innovative multi-channel POR design;
- Presentation of this novel cavitation stochastic-field model.

1.3 Outline of the present study

The first chapters of this thesis summarize theoretical and numerical concepts applied in this thesis:

- Chapter *physics*: Coolant properties in the KERENA POR are radically different in both directions. In the forward direction, pressure variations are small and the coolant is supposed to remain in a liquid state. In the opposite direction water expands from RPV to containment pressure and reaches saturation conditions. Both single-phase and two-phase phenomena are of interest and must be considered to develop the POR design and analyze its fluidic behavior. The chapter *physics* introduces the relevant characteristics and properties of single and two-phase flows.
- Chapter *cavitation*: Cavitation is of first importance for the POR design. In the forward direction it has to be avoided. Otherwise pressure loss would increase drastically and may jeopardize EC heat removal capability. In contrast, cavitation is desired to reduce the mass flow in the backward direction. The chapter *cavitation* focuses on the physical description of the cavitation process.
- Chapter *numerical modeling*: The numerical analysis of the POR design requires some prerequisite on numerical modeling in single-phase, two-phase and cavitating flows. The chapter *numerical modeling* presents the theoretical background on the numerical techniques which are employed in this thesis.
- Chapter *stochastic*: The novel cavitation model aims to account for cavitation-turbulence interaction and to reproduce the bubble size spectra by introducing stochastic models. This chapter is dedicated to give basic prerequisite on probabilistic processes and stochastic equations and to describe one established Lagrange technique for solving velocity-composition and composition probability density function transport equations.

The following chapters describe the development, validation and analysis of the POR design and the development of the proposed cavitation model:

- Chapter *development POR*: The chapter *development POR* concentrates on the description of the development of the POR design. The numerical calculations performed to develop the POR are portrayed.
- Chapter *performance tests*: Although the design of the POR is possible with standard system codes in the BACKWARD direction, available codes are limited in several respects. They do not address directly three-dimensional effects and disregards possible mechanical, thermal or thermodynamic non-equilibrium. To validate the principle of the POR and analyze its fluidic behavior in both directions, experiments were performed at AREVA Technical Center in Karlstein under realistic boundary conditions. In the backward direction, the loss of coolant through four different channel designs was measured to assess the influence of the size and number of nozzles (one or two). In the other flow direction, the flow resistance of three different channel designs was measured to estimate the impact of the opening angles of the diffusers. The chapter *performance tests* outlines the setup and the results of these experiments.
- Chapter *stochastic-field cavitation model*: To gain more insight into the POR flow behavior, a cavitation model with stochastic fields is proposed in the framework of this thesis. The mathematical formulation of this cavitation model and validation results are presented in this chapter.
- Chapter *POR analysis*: Finally the code is used to analyze the flow behavior of one channel of the POR under cavitating conditions. The numerical results are discussed in the chapter *POR analysis*. Large eddy simulations (LES) are performed to predict the turbulent fluctuations.

Subsequently the results of the Ph. D. are summarized and discussed in the last section.

2 Physics

Coolant properties in the KERENA POR are radically different in both directions. In the forward direction, pressure variations are small and the coolant is supposed to remain in a liquid state. In the opposite direction water expands from RPV to containment pressure and reaches saturation conditions. Both single-phase and two-phase phenomena are of interest and must be considered to develop the POR design and analyze its fluidic behavior. This chapter introduces the relevant characteristics and properties of single and two-phase flows.

2.1 Single phase flows

In this chapter, governing equations and properties of single-phase flows are described in sect. 2.1.1 and sect. 2.1.2, respectively. These are prerequisite for the design and analysis of the POR geometry during emergency core cooling.

2.1.1 Governing equations

As the characteristic macroscopic quantities are much bigger than the mean free path of the molecules ($\lambda = 5 \cdot 10^{-8}$ m for air [21]) in all applications of our interest, the fluid can be described in terms of continuum mechanics: flow properties such as velocity vector $\mathbf{u} = (u_1, u_2, u_3)$, pressure p , density ρ and temperature T can be considered to be continuous functions in space $\mathbf{x} = (x_1, x_2, x_3)$ and time t .

2.1.1.1 Equations of state

An equation of state is a thermodynamic equation describing the state of matter under a given set of physical conditions. An equation of state between p , ρ and T is called thermal equation of state. For instance

$$p = \rho \mathcal{R}_g T \quad (2.1)$$

defines an ideal gas, where \mathcal{R}_g is the gas constant. When the caloric quantities, specific internal energy e , specific enthalpy h , or specific entropy s are expressed as dependent variables such as $e = e(h, s)$, the equation of state is called caloric equation of state.

The specific heat capacities at constant volume c_v and at constant pressure c_p are then defined by

$$c_v = \left(\frac{\partial e}{\partial T} \right)_v \text{ and } c_p = \left(\frac{\partial h}{\partial T} \right)_p. \quad (2.2)$$

Another important thermodynamic quantity is the speed of sound c . It represents the speed at which pressure waves propagate in the medium. The speed of sound is related to the change in pressure and density of the substance during an isentropic process:

$$c^2 = \left(\frac{\partial p}{\partial \rho} \right)_s. \quad (2.3)$$

2.1.1.2 Conservation equations

The basic assumption of continuum mechanics is that the same equations of state are valid for a material at rest or in motion. For instance it means that the internal energy of a fluid particle can be expressed purely as a function of density and entropy, not depending on motion, deformation or position of the particle.

A set of conservation equations of mass, momentum, energy, and any scalar Y representing the concentration of the species, completely describes the thermodynamic state of a fluid. In the framework of continuum mechanics, it can be written in differential form as:

Continuity equation:

$$\frac{\partial}{\partial t}(\rho) + \nabla \cdot (\rho \mathbf{u}) = 0. \quad (2.4)$$

Momentum equation also called first Cauchy's equation of motion:

$$\frac{\partial}{\partial t}(\rho \mathbf{u}) + \nabla \cdot (\rho \mathbf{u} \cdot \mathbf{u}) - \rho \mathbf{F} - \nabla \cdot \mathbf{T} = 0; \quad (2.5)$$

where $\mathbf{F} = (f_1, f_2, f_3)$ is the total volume force and $\mathbf{T} = (\sigma_{ij})$ is the stress tensor.

The stress tensor is generally divided into two parts:

$$\sigma_{ij} = -p\delta_{ij} + \tau_{ij}; \quad (2.6)$$

the first part being the hydrostatic part and τ_{ij} the deviatoric stress tensor. The angular momentum equation indicates that the stress tensor and the deviatoric stress tensor are symmetric:

$$\sigma_{ij} = \sigma_{ji}; \quad (2.7)$$

$$\tau_{ij} = \tau_{ji}. \quad (2.8)$$

The transport equation of the specific total internal energy

$$E = e + \frac{1}{2} \|\mathbf{u}\|^2 \quad (2.9)$$

is given by:

$$\frac{\partial}{\partial t}(\rho E) + \nabla \cdot (\rho \mathbf{u} E) - \rho \mathbf{F} \cdot \mathbf{u} - \nabla \cdot (\mathbf{T} \cdot \mathbf{u}) + \nabla \cdot \mathbf{q} = 0; \quad (2.10)$$

where $\mathbf{q} = (q_1, q_2, q_3)$ is the heat flux density. The energy equation can be expressed equivalently in terms of enthalpy or temperature.

The conservation law of a scalar property Y reads:

$$\frac{\partial}{\partial t}(\rho Y) + \nabla \cdot (\rho \mathbf{u} Y) = -\nabla \cdot (\mathbf{j}) + S(Y); \quad (2.11)$$

where $\mathbf{j} = (j_1, j_2, j_3)$ is the flux vector of Y and $S(Y)$ the scalar property source term.

2.1.1.3 Constitutive laws

The conservation transport equations (2.4), (2.5), (2.10) and (2.11) are generally valid for any solid or fluid. The prescription of material dependent constitutive laws describing the interactions between stress tensor and motion, between heat flux density and temperature; and between the scalar flux vector and the concentration Y ; specialize them to a given material.

The simplest constitutive law for the stress tensor of a viscous fluid is a linear dependence of the components (σ_{ij}) of the stress tensor \mathbf{T} upon the components (e_{ij}) of the deformation tensor \mathbf{S} :

$$\sigma_{ij} = -p\delta_{ij} + \lambda^* e_{kk} \delta_{ij} + 2\eta e_{ij}; \quad (2.12)$$

where the deformation tensor components are defined as:

$$e_{ij} = \frac{1}{2} \left(\frac{\partial u_j}{\partial x_i} + \frac{\partial u_i}{\partial x_j} \right). \quad (2.13)$$

The quantities λ^* and η are material-dependent scalar functions of thermodynamic quantities, e. g.

$$\eta = \eta(p, T); \quad (2.14)$$

and must be experimentally determined.

Fluids characterized by this constitutive property are called Newtonian fluids. In spite of its simplicity, this constitutive law describes remarkably well most technical fluids (including almost all gases [air, vapor, etc.] and liquids [water, oil, etc.], but also mixtures).

According to Stokes [22]

$$\lambda^* = -\frac{2}{3}\eta; \quad (2.15)$$

which means that the deviatoric stress tensor (τ_{ij}) does not contribute to the mean normal stress and its components τ_{ij} are:

$$\tau_{ij} = -\frac{2}{3}\eta e_{kk}\delta_{ij} + 2\eta e_{ij}. \quad (2.16)$$

The kinematic viscosity ν is the dynamic viscosity η scaled by the density ρ :

$$\nu = \frac{\eta}{\rho}. \quad (2.17)$$

For an isotropic material, the constitutive law of the heat flux vector \mathbf{q} can also be expressed by a linear dependence upon the temperature gradient:

$$q_i = -\lambda_T \frac{\partial T}{\partial x_i}; \quad (2.18)$$

where λ_T is a positive function of the thermodynamic properties and is named the thermal conductivity. Experiments indicate that this relationship, also known as the *Fourier* law, reproduces very accurately the real material behavior.

A constitutive law is also needed to represent the flux vector \mathbf{j} of any scalar. A gradient diffusion hypothesis is the simplest relationship:

$$j_i = -\rho D_Y \frac{\partial Y}{\partial x_i}; \quad (2.19)$$

where D_Y , the coefficient of diffusion is positive so that the quantity associated with Y is transported down the gradient intensity.

2.1.1.4 Navier-Stokes equations

Equations (2.4), (2.5) and (2.10) restricted to Newtonian fluids with the constitutive relations (2.16), (2.18) and (2.19) become the Navier-stokes equations.

2.1.1.5 Boundary conditions

To close the system of equations, initial and boundary conditions must be prescribed. The most common boundary in single-phase flows is an impenetrable wall.

At this boundary, experiments show that the velocity vector $\mathbf{u}|_w$ of Newtonian fluids at the wall matches the velocity vector of the wall \mathbf{u}_w :

$$\mathbf{u}|_w = \mathbf{u}_w. \quad (2.20)$$

2.1.2 Characteristics of single-phase flows

2.1.2.1 Fluid properties

2.1.2.1.1 Gas

Molecules in a gas are widely separated. For many applications the average distance is so large that both the attractive force between the molecules and their volume are completely negligible. The molecules move freely with the exception of occasional collisions [23]. In this case one speaks of an ideal gas and its equation of state can be deduced from kinetic considerations.

The thermal equation of state reads:

$$p = \rho R_g T. \quad (2.21)$$

The specific internal energy and enthalpy of a thermal ideal gas are function of the temperature only:

$$de = c_v dT \quad (2.22)$$

and

$$dh = c_p dT. \quad (2.23)$$

Departure from the ideal gas law arises when the distance between the molecules decreases. In that case, molecules interaction and finite volume cannot be neglected anymore since they do affect the macroscopic behavior of the gas (see sect. 2.2.1.1). To account for these effects, corrections of the ideal gas relation were derived. One of the simplest models is the *Van der Waals* equation of state:

$$\left(p + \frac{a}{v^2}\right)(v - \underline{b}) = \mathcal{R}_g T; \quad (2.24)$$

with v being the specific volume, \underline{a} a correction term to account for molecular forces and \underline{b} to account for the finite molecule size.

For a caloric ideal gas, specific heat capacities are constant so that:

$$e = c_v T \quad (2.25)$$

and

$$h = c_p T. \quad (2.26)$$

In many engineering applications, this assumption is valid. However, heat capacities increase at large temperatures due to the activation of other degrees of freedom (rotation, vibration) of the molecules.

For an ideal gas, the speed of sound can be written as:

$$c = \sqrt{\gamma \mathcal{R}_g T}; \quad (2.27)$$

with γ , called the isentropic expansion factor, being the ratio of the specific heat capacities:

$$\gamma = \frac{c_p}{c_v}. \quad (2.28)$$

In a gas, the transport of momentum, energy and species is achieved primarily by the displacement and the collisions of the randomly moving gas particles. The random motion of the particles (Figure 2-1; left), also called Brownian motion, is driven by thermal agitation and successive collisions between molecules. The characteristic quantities of this process are particles kinetic energy, or equivalently particles root-mean-square velocity $\|\mathbf{u}\|$; mean free path λ , corresponding to the mean distance between two collisions (Figure 2-1; right); and mean time τ between two collisions.

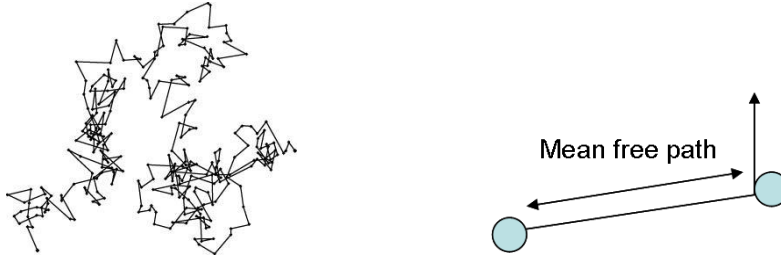


Figure 2-1: Typical Brownian motion of a gas particle (left); the mean free path is the mean value of all distances covered by any particle between two collisions (right).

Expressions of these quantities can be obtained for an ideal gas from the gas kinetic theory. The root-mean-square velocity is related to the temperature T , the gas molar mass \underline{M} and the universal gas constant $\mathcal{R} = 8.3145 \text{ J K}^{-1} \text{ mol}^{-1}$ as follows [24]:

$$\|\mathbf{u}\| = \sqrt{\frac{3\mathcal{R}T}{\underline{M}}}. \quad (2.29)$$

The mean free path is related to the temperature T , the Avogadro constant $\mathcal{N}_A = 6.022 \cdot 10^{23} \text{ mol}^{-1}$, the pressure p , the collision cross section σ_c and the universal gas constant \mathcal{R} as follows [24]:

$$\lambda = \frac{\mathcal{R}T}{\sqrt{2} \mathcal{N}_A \sigma_c p}. \quad (2.30)$$

The mean time between two collisions is given by:

$$\tau = \frac{\lambda}{\|\mathbf{u}\|}. \quad (2.31)$$

Statistical considerations indicate that the diffusion coefficients of momentum and temperature, η and λ_T respectively, are related to the characteristics of the Brownian motion ($\|\mathbf{u}\|$ and λ) [25], [26]:

$$\eta = \frac{1}{2} \rho \|\mathbf{u}\| \lambda; \quad (2.32)$$

$$\lambda_T = \rho c_v \|\mathbf{u}\| \lambda ; \quad (2.33)$$

with c_v being the specific heat capacity. Since the gas molecules are widely separated, the mean free path, thus the diffusion coefficients (eq. (2.32) and (2.33)), are large.

The Schmidt number associated to the scalar property Y :

$$\sigma_Y = \frac{\eta}{\rho D_Y} = \frac{\text{viscous diffusion rate}}{\text{molecular diffusion rate}} ; \quad (2.34)$$

defining the ratio of viscous to molecular diffusion, is generally taken to be unity [23].

Experimental values (IAPWS [27]) of the thermodynamic properties of water vapor at $p = 1\text{bar}$ and $T = 110^\circ\text{C}$ are given in Table 2-1.

	Experimental values ($p=1\text{bar}$; $T=110^\circ\text{C}$)
c	479.3 m/s
c_v	2040.0 J/(kg K)
c_p	1528.1 J/(kg K)
\mathcal{R}_g	461.6 J/(mol K)
η	$1.26 \cdot 10^{-5}$ kg/(m s)
ρ	0.57 kg/m ³
ν	$2.21 \cdot 10^{-5}$ m ² /s
λ_T	0.026 W/(m K)
γ	1.33
h	2700 kJ/kg

Table 2-1: Experimental values (IAPWS[27]) of thermodynamic properties of water vapor at $p=1\text{bar}$ and $T=110^\circ\text{C}$.

2.1.2.1.2 Liquid

A liquid is a condensed matter. In contrast to a gas, molecules are continually within the strong attractive forces of their neighbors. For non-polar substances, these attractive forces generally resume to the weak electrostatic attraction, also called London forces, which arises when neighboring molecules form temporally dipoles due to the deformation of the orbit of their electron layer [28]. For substances containing hydrogen atoms such as water, a supplementary and stronger attractive force, called hydrogen bond, exists [29]. Molecules cannot arbitrary be close due to a repulsive intermolecular force resulting from the Pauli Exclusion Principle [30]. The corresponding qualitative behavior of intermolecular potential energy as a function of the intermolecular distance is represented on Figure 2-2: The repulsive force dominates at very small intermolecular distances, while attractive forces prevail at larger distances. In contrast to gas where the intermolecular distance is so large that the potential energy is negligible in comparison to their kinetic energy, kinetic energy of liquid molecules is not sufficient for the molecules to escape from the attraction of their neighbors.

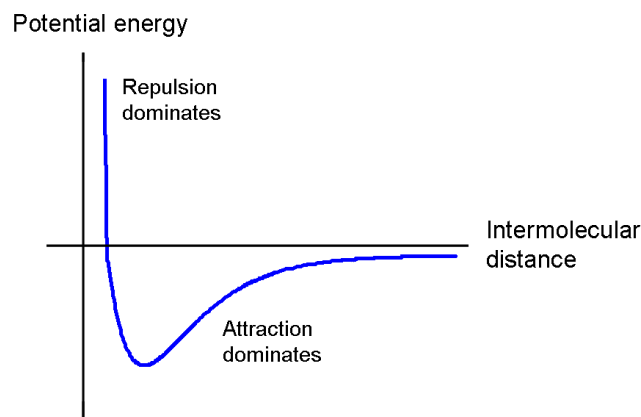


Figure 2-2: Potential energy of two particles as a function of the intermolecular distance.

Due to these intermolecular forces, density sensitivity to pressure variation is very low. According to (2.3), the speed of sound is thus very large.

No simple model exists to describe accurately liquids equation of state over large application ranges. Simple models such as the *Tait* ([31]; eq. (2.35)) or the *Tamman* ([32]; eq. (2.36)) equation of state are limited to short application ranges but are often used for water due to their simplicity.

The Tait equation of state is given by:

$$\frac{p + B_T}{p_0 + B_T} = \left(\frac{\rho}{\rho_0} \right)^{n_T}; \quad (2.35)$$

where the subscript 0 refers to normal conditions; $1/(n_T B_T)$ is the compressibility coefficient, and $B_T = 304.9 \text{ MPa}$ and $n_T = 7.15$ in the case of water. The *Tamman* equation of state ([32]) reads:

$$p + p_T = \rho K_T (T + T_T); \quad (2.36)$$

with p_T , T_T and K_T being constants derived by Tamman.

In a liquid, the molecules are close together. The mean free path is smaller than in a gas and the attractive intermolecular forces tend to reduce the mobility of the molecules. As a result, the diffusion processes driven by particles Brownian motion are weak. In contrast, direct exchange of energy between molecules lying within each other's force field is enhanced. While momentum and species transport coefficients are relatively low, thermal conductivity remains comparatively high. Similarly to gas, the Schmidt number is generally assumed to be unity [23] in liquids.

Experimental values (IAPWS [27]) of the thermodynamic properties of water are given in Table 2-2.

	Experimental values ($p=1\text{bar}$; $T=90^\circ\text{C}$)
c	1552.8 m/s
c_v	4205.0 J/(kg K)
c_p	3818.7 J/(kg K)
η	$3.14 \cdot 10^{-4}$ kg/(m s)
ρ	965.32 kg/m ³
ν	$3.26 \cdot 10^{-7}$ m ² /s
λ_T	0.67 W/(m K)
h	380 kJ/kg

Table 2-2: Experimental values (IAPWS [27]) of thermodynamic properties of water at $p=1\text{bar}$ and $T=90^\circ\text{C}$.

2.1.2.2 Turbulence

In most engineering applications, the flow is not laminar. The Reynolds number Re defined by

$$Re = \frac{\rho u L}{\eta} = \frac{\text{inertial force}}{\text{viscous force}}; \quad (2.37)$$

where L , u , η and ρ are the characteristic geometrical length and characteristic flow and fluid properties, is so high that viscous forces are not able to damp out hydrodynamic instabilities developing at the walls [33] or caused by the stretching of filament vortices [34] in the bulk. The flow is turbulent and presents typical symptoms: Disorder and efficient mixing.

2.1.2.2.1 Disorder

Flow fields such as velocity vector \mathbf{u} , pressure p , density ρ and temperature T exhibit chaotic behaviors which are never reproducible in detail (Figure 2-3 left and middle). Although details are not reproducible, flow fields averaged over large time may be very well defined and stable (Figure 2-3 right).

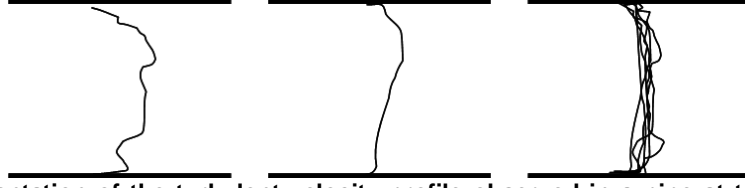


Figure 2-3: Representation of the turbulent velocity profile observed in a pipe at two arbitrary instants (left and middle) and superposition of several velocity profiles observed in the same pipe at different times (right).

Therefore, a usual method to gain insight into turbulent flows is to decompose the physical quantities into mean, denoted here with a bar, and fluctuating parts, indicated here with a prime. It is the so-called Reynolds decomposition [35]:

$$u_1 = \bar{u}_1 + u'_1; \quad u_2 = \bar{u}_2 + u'_2; \quad u_3 = \bar{u}_3 + u'_3; \quad p = \bar{p} + p'; \quad \rho = \bar{\rho} + \rho'; \quad T = \bar{T} + T', \quad \text{etc.} \quad (2.38)$$

The mean value \bar{f} of the variable f may be obtained from a time-averaging:

$$\bar{f}(x) = \frac{1}{t_1 - t_0} \int_{t_0}^{t_1} f(x, t) dt; \quad (2.39)$$

where the averaging is performed over a time interval sufficiently large so that the maximum period of the turbulent fluctuations is exceeded [35]; or from an ensemble-averaging:

$$\bar{f}(x) = \langle f(x, t) \rangle_N = \frac{1}{N} \sum_{\alpha=1}^N f^{(\alpha)}(x, t) \quad (2.40)$$

of N independent realizations (repetition of an experiment). $f^{(\alpha)}(x, t)$ is the value of one of the realizations. The mean-value obtained from the ensemble-averaging is also a random variable for a finite number N of realizations but tends towards the expectation value in the limit of $N \rightarrow \infty$:

$$\langle f(x, t) \rangle = \lim_{N \rightarrow \infty} \langle f(x, t) \rangle_N = \langle \langle f(x, t) \rangle_N \rangle; \quad (2.41)$$

according to the central limit theorem [36].

Frequency analysis of the velocity fluctuations u' in the mean flow direction is generally performed to estimate the contribution $F(n_E)$ of the frequencies between n_E and $n_E + dn_E$ to the fluctuations. Since turbulent flows fields are generally decomposed into sums of turbulent eddies, $F(n_E)$ is also the contribution of the eddies with frequencies between n_E and $n_E + dn_E$. Referring to the Taylor hypothesis [37] which assumes an equivalence between spatial and temporal frequency (wave number k_E vs. n_E), this subset of eddies is equivalent to the one with sizes between $2\pi/k_E(1 - dk_E/k_E)$ and $2\pi/k_E$.

Experimental results [38] indicate that the spectrum is continuous from the large structures (low wave numbers) to the smallest eddies. The former have the size of the characteristic geometrical length (the diameter for a pipe). The latter are as small as the Kolmogorov length scale

$$l_K \equiv \left(\frac{\nu^3}{\varepsilon} \right)^{1/4}; \quad (2.42)$$

where ε is the energy dissipation rate of the turbulent kinetic energy

$$k = \frac{1}{2} \left(\overline{u_1'^2 + u_2'^2 + u_3'^2} \right). \quad (2.43)$$

The revolution time of the smallest eddies is

$$t_K \equiv \left(\frac{\nu}{\varepsilon} \right)^{1/2}. \quad (2.44)$$

[39] first stated that energy transfer between the eddies of different sizes is not random but follow the energy cascade principle: the mean flow only feeds the bigger eddies with energy; these large eddies then transfer their energy to smaller eddies (larger wave number k_E) and so on until the smallest eddies dissipate the energy due to viscous forces.

2.1.2.2.2 Efficient mixing

The chaotic motion of the fluid particles greatly increases momentum, energy and species transport.

Considering an (idealized) incompressible turbulent flow whose velocity field is $\mathbf{u}=(u_1, u_2)$, it is possible to estimate the momentum flow through the infinitesimal surface dA of normal \mathbf{y} during the time dt [33]. Since the fluid mass flowing through dA during dt is $dA\rho u_2 dt$, the \mathbf{x} -component of the momentum flow is $dA\rho u_1 u_2$.

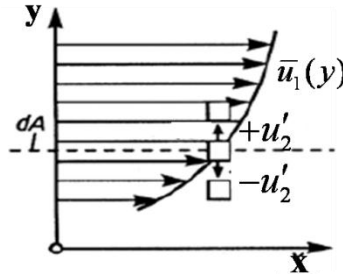


Figure 2-4: Momentum flux through infinitesimal surface dA in a turbulent flow [33].

Using the Reynolds decomposition, the average of the \mathbf{x} -component of the momentum flow is given by:

$$dA\rho\overline{u_1 u_2} = dA\rho(\overline{u_1} \overline{u_2} + \overline{u_1' u_2'}). \quad (2.45)$$

Eq. (2.45) indicates that the average momentum exchange increases due to the turbulent fluctuations in comparison to non-fluctuating (laminar) conditions. As a result, according to Newton's second law, a supplementary stress τ'_{12} arises:

$$\tau'_{12} = -\rho\overline{u_1' u_2'}. \quad (2.46)$$

For a simple shear flow (see Figure 2-4), it can easily be shown that this force is non-zero: Positive turbulent cross flow ($u_2' > 0$) transfers momentum from low to high momentum laden particles; which tends to slow down the fastest molecules ($u_1' < 0$). On the contrary, negative turbulent cross flow ($u_2' < 0$) transfers momentum from fast to slow particles; which tends to accelerate the slowest molecules ($u_1' > 0$). The fluctuations u' and v' are correlated and the average of their product is strictly negative ($\overline{u_1' u_2'} < 0$) [33].

Turbulent motion is responsible for the complex character of the flow resistance in complex geometries. On the one hand, the transition from laminar to turbulent regime leads to flow resistance increase since supplementary shear forces appear between the fluid particles. This is typically observed in simple pipes [40]. On the other hand, momentum exchange between fluid layers energizes the turbulent boundary layers. Thus, turbulent layers are able to affront larger adverse pressure gradient than laminar boundary layers thereby avoiding or reducing flow detachment and pressure head [33].

More generally, mixing is considerably enhanced by the turbulent fluctuations since these fluctuations advect fluid particles exponentially far from one another in time. As a result, fluid layers having similar properties are deformed: their interfacial area increases dramatically and fluid properties gradients tend to be accentuated, both increasing the rate of molecular mixing. This phenomenon of coarse-grained homogenization is clearly distinct from molecular mixing in such that it does not occur on a molecular level. To illustrate this two distinct processes (coarse-grained homogenization and molecular mixing), one may consider chemical species which are present in well defined globules with small interfacial area at an initial stage (Figure 2-5, bottom, left). The globules are stirred and strained under the action of the turbulent eddies and deform (Figure 2-5, bottom, from left to right); their interfacial area grows exponentially: this is the coarse-grained homogenization characteristic of turbulent flows. In contrast, the molecular mixing occurs at the interface between the globules and the remaining fluid at a molecular level due to particles Brownian motion and species gradient (Figure 2-5 top).

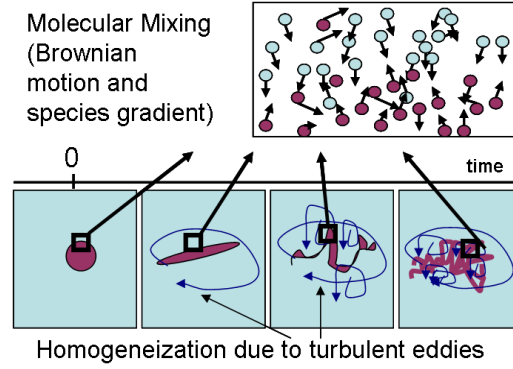


Figure 2-5: Schematic representation of molecular mixing (top) and coarse-grained homogenization (bottom) in turbulent flows.

2.1.2.3 Compressibility

A fluid is said to be incompressible when the rate of change of the density ρ following the motion is zero, that is,

$$\frac{D\rho}{Dt} = 0. \quad (2.47)$$

Using the equation of state $p = p(\rho, s)$, the variation of the density can be expressed according to the variations of pressure and entropy in a dimensionless formulation [41]:

$$\frac{1}{\rho U} \frac{L}{Dt} \frac{D\rho}{Dt} = \frac{L}{U} \frac{1}{\rho c^2} \frac{Dp}{Dt} - \frac{L}{U} \frac{1}{\rho c^2} \left[\frac{\partial p}{\partial s} \right]_p \frac{Ds}{Dt}; \quad (2.48)$$

where L and U are the characteristic length and velocity. The flow is incompressible when both terms on the right hand side of eq. (2.48) are zero.

The first and second terms represent density variation due to pressure variation and heat supply, respectively. The second term is negligible for adiabatic processes. The first term is only negligible when the speed of sound c is sufficiently large in respect to the pressure variation, which is more likely to happen in a liquid than in a gas.

A major consequence of flow compressibility is that pressure information travels relative to the medium at *finite* velocity c . For instance in a one-dimensional flow with uniform velocity u , pressure waves propagate in the upstream direction at $c - u$ and in the downstream direction at $c + u$.

For internal flows, this manifests by the choking of the flow at the smallest cross section when the pressure difference between inlet and outlet exceeds a critical value. In this case, the velocity of the fluid reaches sound speed at the smallest cross section. No information can travel upstream: the mass flow and the pressure at the choking cross section do not depend upon downstream pressure anymore [42].

The phenomenon can be accurately described by considering the steady-state conservation equations of a frictionless compressible fluid in a one-dimensional pipe with varying cross section $A(x)$. The mass conservation equation (2.4) derived with respect to the longitudinal coordinate x becomes:

$$\frac{1}{u} \frac{du}{dx} + \frac{1}{A} \frac{dA}{dx} + \frac{1}{\rho} \frac{d\rho}{dx} = 0. \quad (2.49)$$

For an isentropic flow, the definition of the speed of sound (2.3) reads:

$$c^2 = \frac{dp}{d\rho}. \quad (2.50)$$

The momentum equation (2.5) in the flow direction is:

$$\rho u \frac{\partial u}{\partial x} = - \frac{\partial p}{\partial x}. \quad (2.51)$$

Introducing the *Mach* number M :

$$M = \frac{u}{c} = \frac{\text{inertial force}}{\text{compressibility force}}; \quad (2.52)$$

the combination of equations (2.49) with (2.51) reads:

$$\frac{1}{u} \frac{du}{dx} (1 - M^2) = -\frac{1}{A} \frac{dA}{dx}. \quad (2.53)$$

For subsonic flows ($M < 1$ at the inlet), the velocity increases in the converging part of the pipe and decreases in the diverging part. Since the derivative dA/dx vanishes at the smallest cross section, either the velocity reaches a maximum $du/dx = 0$ or the Mach number M equals 1. For supersonic flows, the opposite behavior is observed. The possible flow configurations in a convergent-divergent are describes in [41].

The flow configurations happen according to the pressure ratio between inlet and outlet. Starting from a low pressure ratio and subsonic flow at the inlet of the nozzle, the flow remains subsonic in the entire nozzle. Increasing the pressure ratio leads to the acceleration of the flow until M is one at the smallest cross section. Decreasing further the downstream pressure does not lead to either mass flow increase, or pressure decrease at the choking cross section. The mass flow \dot{M} in the pipe remains equal to the critical mass flow

$$\dot{M}^* = \rho^* c^* A^*; \quad (2.54)$$

where the asterisk characterizes values of density and sound speed at the choking cross section A^* .

2.2 Two phase flows

This chapter presents the governing equations and properties of two-phase flows in sect. 2.2.1 and sect. 2.2.2, respectively. This theoretical background is needed for the design and analysis of POR geometry in particular in backward direction and for the development of the cavitation model. Indeed, after the break of EC condensate return line, the coolant expands from RPV to containment pressure. Going from subcooled conditions during the first minutes following the break to saturated conditions afterwards, the coolant vaporizes in the POR. In the opposite direction, vaporization in the POR design should be avoided. Otherwise hydraulic resistance would reduce EC heat removal capacity.

2.2.1 Governing equations

2.2.1.1 Equations of state

A given material exists in three phases – solid, liquid and gas – depending upon its thermodynamic state (Figure 2-6). Changing the thermodynamic state may lead to a phase transition where the existing phase disappears at the benefit of the other phase.

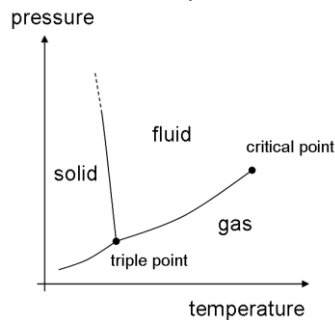


Figure 2-6: Schematic representation of water phase diagram (p, T) .

The isothermal condensation of a gas can be described on a microscopic scale as follows. The ideal gas law can accurately describe the gas behavior when the distance between the particles is sufficient. At higher pressure for a given temperature, the intermolecular potential energy gain in importance and cannot be neglected in comparison to the kinetic energy of the particles. The gas behavior departs from the ideal model (sect. 2.1.2.1.1). When the distance between the molecules further reduces, intermolecular forces become so strong that some molecules cannot escape from the interaction forces of their neighbors and start to aggregate. They form a new phase: the liquid phase. Following this agglomeration, the average distance between the molecules still moving freely increases and the pressure decreases compensating the pressure increase required to bring the molecules together. After some time, both phases reach a new thermodynamic equilibrium. Continuing to reduce the average distance between the molecules increases the proportion of the liquid phase

until the whole gas phase has condensed. Any further increase in pressure only yields very small density variation.

The isothermal condensation process is only possible at temperatures situated between triple-point and critical-point temperature. At lower temperature, thermal agitation is so low that particles aggregate in form of a solid. At temperatures above the critical-point temperature, fluid and gas phases cannot be distinguished: phase densities are equal and phase interface disappears.

Phases coexisting in equilibrium, i.e. having the same pressure (mechanical equilibrium), the same temperature (thermal equilibrium) and the same single-phase chemical potentials (thermodynamic equilibrium) [43], can be represented in (p, v) and equivalent phase diagrams (e.g. (h, s) , (T, s) , etc.).

Actually, phases in mechanical equilibrium share the same pressure only when their interface is a flat surface. In contrast to molecules situated inside the fluid phase, molecules at the interface with another phase (gas or solid) are not submitted to intermolecular forces equally from all sides. The attraction is higher in the direction of the liquid. On a macroscopic scale, this phenomenon manifests by a supplementary force, the surface tension, and a discontinuity in the pressure field. For a spherical dispersed phase, the pressure jump between dispersed phase pressure p_d and continuous phase pressure p_c can be easily expressed with the radius R of the dispersed phase and the surface tension σ :

$$p_d - p_c = \frac{2\sigma}{R}. \quad (2.55)$$

It is the so-called *Laplace* equation which indicates that the mechanical equilibrium $p_d = p_c$ is only valid for $R \rightarrow \infty$.

The gas-liquid interface increases the internal energy E_T of the system by E_σ . E_σ is proportional to the surface A_i of the interface:

$$E_\sigma = A_i \sigma. \quad (2.56)$$

Thus, E_T consists of the internal energy E_l and E_g of the liquid and gas phase, respectively; and of the interface energy E_σ :

$$E_T = E_l + E_g + E_\sigma. \quad (2.57)$$

The particular case of thermodynamic equilibrium occurs when both phases have evolved so that their chemical potentials are equal. The opposite particular case is a metastable single phase: pressure and temperature correspond to the two-phase domain but the phase is still stable against small perturbations. For example, water can withstand lower pressures than saturation pressure without vaporizing with sufficient care [44]. Only large perturbations lead to the formation of large cluster of the other phase. During the growth of the clusters, the chemical potentials of both phases evolve until they attain the same value corresponding to the stable two-phase state.

As will be described in chapter *cavitation*, highly metastable states are not common in engineering applications due to the presence of impurities in the medium (dissolved gas, particles, etc.). These impurities facilitate the formation of clusters of the other phase. However the finite time of growth of the clusters still induces a finite time-period where thermodynamic equilibrium is not realized. This is particularly important for fast transients such as flashing [45], [46] or boiling crisis [43].

2.2.1.2 Conservation equations

The local instantaneous equations of a two-phase Newtonian mixture flow are obtained in the same way as for a single-phase flow. The governing equations are the Navier-Stokes equations [47] of both phases. The subscript k indicates which phase k is involved in the balance (e.g. $k = 1, 2$ for liquid and gas phases, respectively). The six equations are:

Two mass equations

$$\frac{\partial \rho_k}{\partial t} + \nabla \cdot (\rho_k \mathbf{u}_k) = 0, \quad k = 1, 2; \quad (2.58)$$

two momentum equations

$$\frac{\partial}{\partial t} (\rho_k \mathbf{u}_k) + \nabla \cdot (\rho_k \mathbf{u}_k \cdot \mathbf{u}_k) - \rho_k \mathbf{F} - \nabla \cdot \mathbf{T}_k = 0, \quad k = 1, 2; \quad (2.59)$$

and two total energy equations

$$\frac{\partial}{\partial t}(\rho_k E_k) + \nabla \cdot (\rho_k \mathbf{u}_k E_k) - \rho_k \mathbf{F} \cdot \mathbf{u}_k - \nabla \cdot (\mathbf{T}_k \cdot \mathbf{u}_k) + \nabla \cdot \mathbf{q}_k = 0, \quad k=1,2; \quad (2.60)$$

where \mathbf{T}_k , \mathbf{F} and \mathbf{q}_k denote stress tensor, volume force vector and heat flux in the phase k .

2.2.1.3 Boundary conditions

[47] derived the jump conditions existing at the interface of the two phases:

Mass jump condition:

$$\rho_1 (\mathbf{u}_1 - \mathbf{u}_i) \cdot \mathbf{n}_1 + \rho_2 (\mathbf{u}_2 - \mathbf{u}_i) \cdot \mathbf{n}_2 = 0; \quad (2.61)$$

momentum jump condition:

$$\rho_1 (\mathbf{u}_1 - \mathbf{u}_i) \cdot \mathbf{n}_1 (\mathbf{u}_1 - \mathbf{u}_2) - \mathbf{n}_1 \cdot \mathbf{T}_1 - \mathbf{n}_2 \cdot \mathbf{T}_2 = 2H\sigma \mathbf{n}_1 + \nabla_s \sigma; \quad (2.62)$$

where $\nabla_s \equiv (\mathbf{I} - \mathbf{n}_1 \mathbf{n}_1) \cdot \nabla$ is the surface gradient operator [48], $H \equiv -\frac{1}{2} \nabla_s \cdot \mathbf{n}_1$ is the mean curvature of the interface, and the subscript i stands for the flow fields at the interface. In this expression, and the rest of the present work, surface tension variation due to temperature gradient is neglected.

Total energy jump condition:

$$\begin{aligned} & \rho_1 (\mathbf{u}_1 - \mathbf{u}_i) \cdot \mathbf{n}_1 \left(e_1 + \frac{1}{2} \mathbf{u}_1^2 \right) + \rho_2 (\mathbf{u}_2 - \mathbf{u}_i) \cdot \mathbf{n}_2 \left(e_2 + \frac{1}{2} \mathbf{u}_2^2 \right) \\ & + \mathbf{q}_1 \cdot \mathbf{n}_1 + \mathbf{q}_2 \cdot \mathbf{n}_2 - (\mathbf{n}_1 \cdot \mathbf{T}_1) \cdot \mathbf{u}_1 - (\mathbf{n}_2 \cdot \mathbf{T}_2) \cdot \mathbf{u}_2 + (2H\sigma \mathbf{n}_1 + \nabla_s \sigma) \cdot \mathbf{u}_i = 0. \end{aligned} \quad (2.63)$$

2.2.2 Characteristics of two-phase flows

2.2.2.1 Interfacial exchange

The physical properties of the two phases may differ significantly, sometimes by several orders of magnitude. See for example Table 3, where density ratios:

$$\Gamma_\rho = \frac{\rho_l}{\rho_g}; \quad (2.64)$$

viscosity ratios:

$$\Gamma_\eta = \frac{\eta_l}{\eta_g}; \quad (2.65)$$

and specific heat capacity ratios:

$$\Gamma_{c_p} = (c_p)_l / (c_p)_g \quad (2.66)$$

of steam and water are given at three different temperatures in Table 2-3.

Experimental values at saturation conditions	T=10°C	T=100°C	T=290°C
$\Gamma_\rho = \frac{\rho_l}{\rho_g}$	10630	1600	19
$\Gamma_\eta = \frac{\eta_l}{\eta_g}$	138	23	5
$\Gamma_{c_p} = \frac{(c_p)_l}{(c_p)_g}$	2.21	2.03	0.98

Table 2-3: Density, viscosity and specific heat capacity ratios for water and steam at T=10°C, T=100°C and T=290°C (Experimental values (IAPWS)[27]).

As a result, the phases tend to acquire different velocities and temperatures and to occupy the flow domain differently. This leads to mass, momentum and energy exchanges between the phases at the interface (see equations (2.61) to (2.63)) which strongly depend on the area and on the morphological configuration of the interface. Many correlations exist for spherical particles or bubbles (see chapter

cavitation) but it becomes very difficult to model these inter-phase transfers for more general interfaces. Furthermore the topological configuration of the interface itself is influenced by phase exchanges turning the analysis of two-phase flows is enormously complicated in comparison to the analysis of single-phase flows. Hence, for the sake of convenient simplification, the two-phase flows are often defined in terms of characteristic “flow patterns”.

2.2.2.2 Flow pattern

The flow patterns, or regimes, have been extensively analyzed in pipes. Since Baker [49], flow maps are drawn to represent the occurrence of the different flow regimes as a function of the superficial velocities $u_{s,k}$ of the phases (or a dimensionless form of the superficial velocities); where the superficial velocity of the phase k is defined by:

$$u_{s,k} \equiv \frac{\dot{M}_k}{\rho_k A} = \frac{\dot{V}_k}{A}; \quad (2.67)$$

where \dot{M}_k is the mass flow rate, \dot{V}_k is the volume flow rate and ρ_k the density of the phase k ; and A is the cross section of the pipe.

Typical flow patterns in vertical pipes are represented schematically in Figure 2-7. For example, bubbly flows are observed in pipes for sufficiently high water mass flux. Another type of flow regime is the stratified flow (Figure 2-8) where the liquid and the gas are well separated. It is observed at low liquid and gas mass flux in horizontal pipes [50].

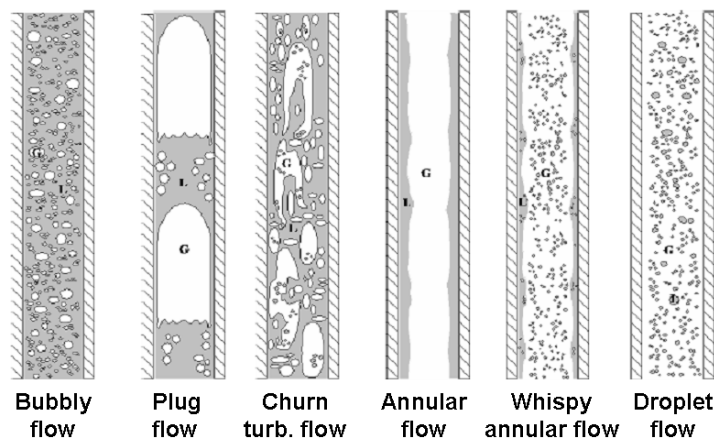


Figure 2-7: Two-phase flow regimes in vertical pipes [51].

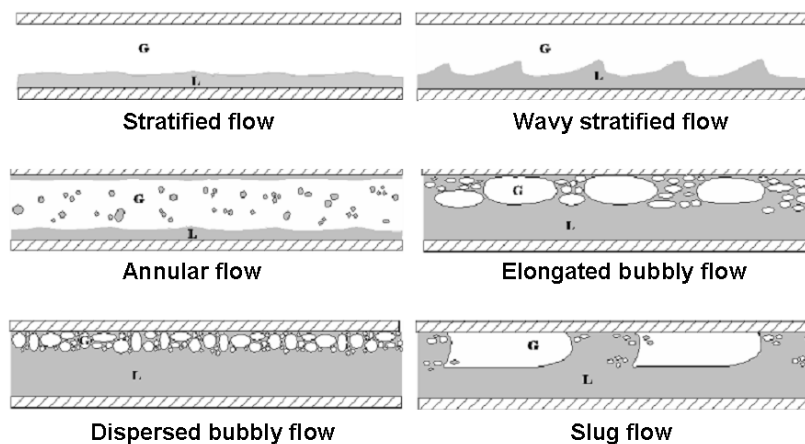


Figure 2-8: Two-phase flow regimes in horizontal pipes [51].

The transition between two flow regimes is related to interface instabilities (sect 2.2.2.4.2).

2.2.2.3 Flow resistance

Due to inter-phase momentum transfers, pressure drops in multi-phase flows are increased in comparison to single-phase flows. For very simple geometries, such as pipes, correlations are

available to account for the flow resistance increase. These correlations are function of flow parameters such as flow pattern, mass flux, void fraction and relative velocities; and of fluid properties, such as density or viscosity. [52] derived a correlation (eq. (2.69) and Table 2-4) for the two-phase multiplier ϕ_{LO}^2 which relates the two-phase pressure drop $\left(\frac{dp}{dz}\right)_{fr,2-Ph}$ to the liquid single-phase friction

pressure drop $\left(\frac{dp}{dz}\right)_{fr,l}$ along the pipe axis:

$$\left(\frac{dp}{dz}\right)_{fr,2-Ph} = \phi_{LO}^2 \left(\frac{dp}{dz}\right)_{fr,l} \quad (2.68)$$

In a pipe with vaporization, ϕ_{LO}^2 is related to the vapor mass fraction Y such as:

$$\phi_{LO}^2 = 1 + (\Gamma^2 - 1) [BY^{0.9}(1-Y)^{0.9} + Y^{1.8}]; \quad (2.69)$$

with

$$\Gamma = \left(\frac{\rho_l}{\rho_g}\right)^{0.5} \left(\frac{\mu_g}{\mu_l}\right)^{0.1}; \quad (2.70)$$

where the coefficient B depends upon Γ and the mass flux G_c in ways given by Table 2-4.

Γ	G_c	B
< 9.5	< 500	4.8
< 9.5	500 < G_c < 1900	2400 / G_c
< 9.5	> 1900	55 / $G_c^{0.5}$
9.5 < Γ < 28	< 600	520 / ($\Gamma G_c^{0.5}$)
9.5 < Γ < 28	> 600	21 / Γ
> 28		15000 / ($\Gamma^2 G_c^{0.5}$)

Table 2-4: Values of the coefficient B entering the correlation of [52] for the two-phase pressure loss as a function of Γ (eq. (2.70)) and mass flux G_c .

It should be noted that $\phi_{LO}^2 \geq 1$.

2.2.2.4 Unsteadiness

Most multi-component flows are highly unsteady flows. In addition to the turbulent fluctuations developing inside each phase (sect 2.1.2.2 and sect 2.2.2.4.1), instabilities may arise at the liquid-gas interface (sect 2.2.2.4.2). Thus, the interface itself and the liquid-gas repartition are characterized by strong fluctuations. Parallel to these microscopic manifestations of unsteadiness, macroscopic instabilities also are likely to occur in two-phase systems (sect 2.2.2.4.3).

2.2.2.4.1 Turbulence

Turbulence in two-phase flows is a very challenging topic and strongly depends on the flow pattern. For instance, in applications where both phases are well separated, such as stratified flows, some turbulence structures are still generated at the walls and in the bulk as if the phases were alone. The influence of the other phase manifests at the interface. There, the existing turbulent structures impinge and are modified; and new structures develop due to the interfacial shear stresses [53]. In applications where one of the phases is dispersed, turbulence in the continuous phase may be enhanced or reduced [54]. While the energy required to accelerate the dispersed phase tends to attenuate the turbulent fluctuations of the continuous phase, the instabilities in the wake of these particles enhance this turbulence.

2.2.2.4.2 Instabilities of the liquid-gas interface

For many gas-liquid flows and in particular for steam-water processes [55], instabilities at the interface are crucial. They develop when destabilizing forces such as velocity difference (Kelvin-Helmholtz instability [56]) and gravity (Rayleigh-Taylor instability [57]) overcome the stabilizing effect of the surface tension. Even small perturbations are accentuated thereby modifying the morphological configuration of the interface. A good example of the consequences of such interfacial instabilities is the fragmentation of droplets due to, among others, velocity difference between wave crests and surrounding medium [58].

2.2.2.4.3 Instabilities of two-phase systems

Two-phase systems instabilities are undesirable because they induce large-scale fluctuations which degrade system control and performance. Following the proposal of Boure et al [59], two-phase systems instabilities can be classified into static and dynamic instabilities. During static instabilities (e.g. Ledinegg instabilities, flow distribution instabilities, pressure drop instabilities), the system tends to jump between two equilibrium states (p' and p'' on Figure 2-9; p being unstable) due to the particular S-shape steady-state pressure-drop-flow-rate characteristic (Figure 2-9) that two-phase flow channels occasionally exhibit. In contrast, dynamic instabilities are characterized by the multiple feedbacks between flow rate, vapor generation rate and pressure drop. The most common type of dynamic instabilities in BWR is the density-wave instability. In this case, the presence of void waves delays the negative feedback mechanism of pressure drop on mass flow rate (an increase in pressure drop usually triggers a decrease in mass flow rate). With appropriate phase delay, the feedback mechanism may become positive and the perturbations (mass flow, pressure drop, void waves) become self-sustained.

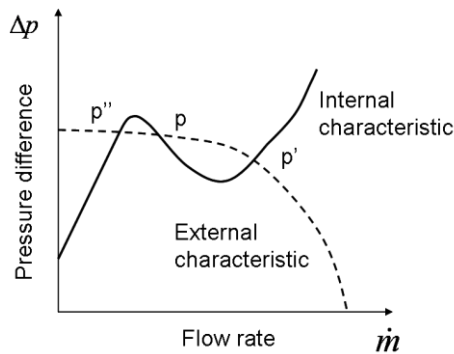


Figure 2-9: Solid line: S-shape pressure-drop-flow-rate characteristic encountered in some two-phase flow systems (internal characteristic); dashed line: pump characteristic (external characteristic); stable (p' , p'') and unstable (p) equilibrium.

2.2.2.5 Phase indicator

To completely characterize a two-phase flow field, the location of the interface between the phases has to be known. For this purpose, a binary scalar, the phase indicator or phase density function, usually is introduced to specify which phase is present at the location \mathbf{x} and at a time t . This function $P_k(x, t)$ is defined as:

$$P_k = \begin{cases} 1 & \text{if } \mathbf{x} \text{ is in phase } k \\ 0 & \text{otherwise} \end{cases} \quad (2.71)$$

As a result of the large- and small-scale instabilities, the phase indicator function is generally highly fluctuating in time and space; which complicates experimental measurement and numerical calculations (chapter *numerical modeling*).

For a gas-liquid flow, the phase-indicator, or rather the presence of liquid or gas, can be measured with miniature resistive probes [60], optical sensors [61] or hot-wire anemometers [62].

When the phase indicator of the gas phase is averaged – over the time, over a geometrical domain (cross section, volume) or over an ensemble of measurements – it is called void fraction α .

Sometimes the liquid volume fraction α_l is introduced. In this context, the gas void fraction is α_g and both quantities are related in a two-phase flow by

$$\alpha_l + \alpha_g = 1. \quad (2.72)$$

2.2.2.6 Compressibility

Two-phase mixtures are easily compressible media. The analytical derivation of the density variation relative to a pressure variation can exemplarily be accomplished for bubbly flows where all particles of the disperse phase are assumed to have the same radius R . Using the definition of sound speed (eq. (2.3)) and considering the void fraction α , the sound speed c , the density ρ and the pressure variation δp of the dispersed phase (subscript d) and of the continuous phase (subscript c) as well as the mass transferred δm from the continuous to the dispersed phase following the pressure variation; and the surface tension σ ; the speed of sound c in the media can be expressed as [12]:

$$\frac{1}{\rho c^2} = \frac{\alpha_c}{\rho_c c_c^2} + \left[\frac{\alpha_d}{\rho_d c_d^2} - \frac{\delta m}{\delta p_c} \left\{ \frac{1}{\rho_d} - \frac{1}{\rho_c} + \frac{2\sigma}{3\rho_d \rho_c c_d^2 R^2} \right\} \right] \left[1 - \frac{2\sigma}{3\rho_d c_d^2 R^2} \right]^{-1}. \quad (2.73)$$

Neglecting the mass transfer and the surface tension, equation (2.73) reduces to:

$$\frac{1}{c^2} = (\rho_d \alpha_d + \rho_c \alpha_c) \left[\frac{\alpha_c}{\rho_c c_c^2} + \frac{\alpha_d}{\rho_d c_d^2} \right]^{-1}. \quad (2.74)$$

In accordance with experimental results [63], equation (2.74) reveals that the speed of sound in a liquid-gas mixture is much smaller than in one of its constituents (Figure 2-10).

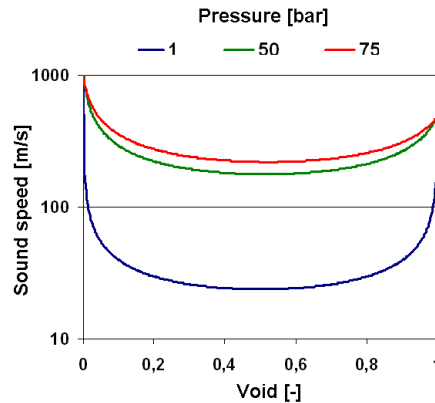


Figure 2-10: Speed of sound of a homogeneous bubbly flow water-steam mixture at $p=1$ bar, $p=50$ bar and $p=75$ bar, as a function of the void fraction at saturation conditions calculated with eq. (2.74) [12].

Taking into account phase change, the speed of sound is further reduced [31].

Thus, in two-phase flows, it is very common to reach large Mach numbers. Hence, choking flows are likely to happen in internal geometries. Furthermore, according to equation (2.54), the critical mass flow \dot{M}^* of a gas-liquid mixture is much smaller than that of the corresponding pure gas or liquid.

It should be mentioned in this regard that equation (2.54) may not directly be transposable to a two-phase choked flow, for, in contrast to single-phase flow which chokes at the smallest geometrical cross section (eq. (2.53)), a gas-liquid mixture is expected to choke at the smallest effective cross section [64], [65]. The position and size of this effective cross section is primarily affected by the interfacial coupling terms – that is, mass, momentum, and energy transfers. Furthermore the speed of sound depends upon the local void repartition (equation (2.73)), which may be inhomogeneous; and the propagation of the pressure waves may be significantly altered by interferences with bubbles [66]. Experimental observations indicate that two consecutive critical cross sections can be observed in two-phase flows, whereby only the first one limits the mass flow [67]. In spite of these differences with single-phase flows, it still is observed that the pressure at the mass flow limiting cross section remains independent of the downstream pressure under two-phase choking conditions.

3 Cavitation

The chapter *cavitation* introduces the governing equations and characteristics of cavitating flows in sections 3.1 and 3.2, respectively. On the one hand, this theoretical background is useful to develop the cavitation model. On the other hand, it provides an informative basis to apprehend under which flow conditions cavitation may be encountered in the POR, and, should the situation arise, what would be the consequences on the POR flow behavior.

3.1 Governing equations

3.1.1 Thermodynamics

Cavitation is the formation of vaporous cavities in a liquid caused by a pressure drop. Void creation starts at weak places in the fluid medium, called nuclei. If the nuclei available for the phase change are only ephemeral voids due to the thermal motion, cavitation is called homogeneous. In this case, very large tensile strengths $p_{sat} - p_{cr}$ are achieved. The tensile strength indicates at which local tension $p_{sat} - p$ the first macroscopic manifestation of cavitation is observed. This type of cavitation occurs only in very pure liquid. Otherwise, another kind of nuclei is present. These nuclei are air and vapor bubbles, either free in the flow or trapped in crevices at the surface of walls or dirt particles (Figure 3-1). Due to their presence, the liquid cannot withstand large tensile strength and the growth of void happens for local pressure around saturation pressure. It is the most common occurrence of cavitation in engineering applications. It is named heterogeneous cavitation and it will be described in detail in this section.

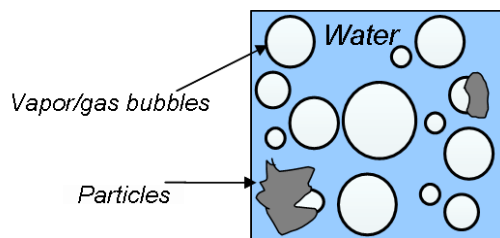


Figure 3-1: Typical impurities, also called cavitation nuclei, encountered in water.

The microscopic mechanism of cavitation can be described for an isothermal expansion as follows. The liquid phase is stretched and the average distance between the molecules increases. When the specific volume of the fluid is large enough ($v_{sat,l}(T_0)$ on Figure 3-2), some void creates inside the liquid phase which are gradually filled with fluid molecules able to escape from the diminishing attractive forces of their neighbors due to their thermal agitation. The molecules which can then move freely and independently from the other molecules inside the void form the gas phase. Following the filling of the voids with these molecules, the pressure rises compensating the pressure drop required to stretch the fluid. Thus, the intermolecular distances in the fluid reduce. After some time, both phases reach a new thermodynamic equilibrium.

The process is strongly endothermic, for energy is required to separate the fluid molecules from the attractive forces of their neighbors. This energy is the specific latent heat of vaporization l . An isothermal cavitation process ($T_0 = const$; solid line in Figure 3-2) is only possible when energy is supplied to the system from the environment. Most cavitation phenomena encountered in engineering applications are actually better approximated by an adiabatic process ($\dot{Q} = 0$; dashed line in Figure 3-2). The fluid itself has to furnish the energy. The temperature of the system tends to decrease ($T_1 < T_0$).

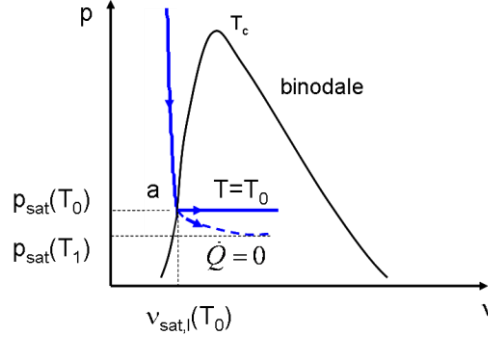


Figure 3-2: Representation of isotherm ($T_0 = \text{const}$; solid line) and adiabatic ($\dot{Q} = 0$; dashed line) cavitation in phase-diagram (p, v).

A pressure drop has a second effect on the void fraction. Not only it increases the vapor mass fraction Y but it also strongly decreases the gas-to-liquid density ratio ρ_g/ρ_l . Thus, the void fraction α , related to this gas-to-liquid density ratio and Y according to:

$$\alpha = \frac{Y}{Y + (1-Y)\frac{\rho_g}{\rho_l} S_i}; \quad (3.1)$$

where

$$S_i = \frac{u_g}{u_l} \quad (3.2)$$

is the velocity ratio between the phases; increases even though there is no interfacial mass transfer.

3.1.2 Conservation equation

In most engineering applications, the fluid is not at rest. Mechanical rotation or potential energy triggers the motion of the liquid. A pressure drop is induced where the fluid streamlines contract or inside vortices. At sufficiently low pressures the flow is cavitating. This is named hydrodynamic cavitation.

Hydrodynamic cavitation is a very complex phenomenon. The description of the flow must not only account for the formation of the vaporous cavities but also for their position, motion and interaction with the other vaporous cavities and with the liquid phase. For large void fractions, the effect the cavities have on the stretching of the fluid must be accounted for. Due to the large gas-to-fluid density ratio, small volumes of liquid are replaced by large volumes of gas during the vaporization process; initiating large deformations of fluid streamlines. Furthermore, hydrodynamic cavitation forms an inherently stochastic process since it is primarily governed by turbulence and by the probability density functions (pdf) of cavitation nuclei number density n and cavitation nuclei size R (Figure 3-3).

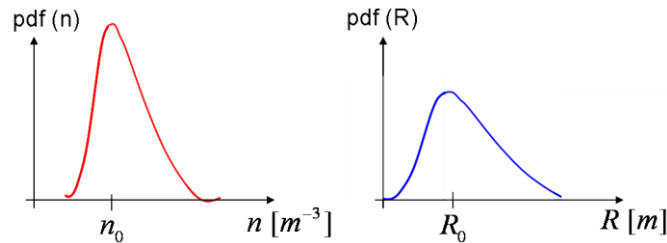


Figure 3-3: Schematic representation of probability density functions (pdf) of nuclei number density (left) and cavitation nuclei size (right); n_0 and R_0 being mean nuclei density number and mean nuclei radius, respectively.

In cavitating flows, the gas phase generally is assumed to be dispersed in the continuous liquid phase. Each cavity can be characterized by one geometry parameter ϕ (ϕ can be the cavity equivalent radius R , surface or volume), the velocity of their center of mass \mathbf{u}_g and their mean temperature T_g . Due to the stochastic nature of cavitating flows, a stochastic approach is required to capture these characteristics for the whole dispersed population. In this context, a fairly general method is to solve a

Boltzmann type equation for the distribution function $f^\phi(t, \mathbf{x}, \phi, \mathbf{u}_g, T_g)$. By definition $f^\phi d\mathbf{x}d\phi d\mathbf{u}_g dT_g$ is the probable number of cavities at time t in the phase elementary volume $dV_{sp} = d\mathbf{x}d\phi d\mathbf{u}_g dT_g$ around the point $(\mathbf{x}, \phi, \mathbf{u}_g, T_g)$.

The cavities number density is affected by break-up $\dot{S}_{break}(t, \mathbf{x}, \phi, \mathbf{u}_g, T_g, f^\phi)$ and coalescence $\dot{S}_{coal}(t, \mathbf{x}, \phi, \mathbf{u}_g, T_g, f^\phi)$ processes. It increases due to breakup and decreases due to coalescence. Parallel to that, the cavities with geometry parameter ϕ , velocity \mathbf{u}_g and temperature T_g at a position \mathbf{x} and at a time t , grow or collapse according to \dot{R}_ϕ , are submitted to forces $\mathbf{F}_{g,i}$ and are cooled or heated. Consequently, they are located at the position $\mathbf{x} + d\mathbf{x}$ at a time $t + dt$ and their geometry parameter is $\phi + d\phi$, their velocity $\mathbf{u}_g + d\mathbf{u}_g$ and their temperature $T_g + dT_g$. In analogy to sprays in combustion [68], under these conditions, the temporal evolution of the density function f^ϕ in the phase-space is given by:

$$\frac{\partial f^\phi}{\partial t} + \frac{\partial(\mathbf{u}_g f^\phi)}{\partial \mathbf{x}} + \frac{\partial(\mathbf{F}_{g,i} f^\phi)}{\partial \mathbf{u}_g} + \frac{\partial(\dot{R}_\phi f^\phi)}{\partial \phi} + \frac{\partial(\dot{T}_g f^\phi)}{\partial T_g} = \dot{S}_{break} + \dot{S}_{coal}. \quad (3.3)$$

Expressions for the different terms in equation (3.3) are generally available from experimental results for spherical bubbles. They will be discussed in the next sections.

3.1.2.1 Nuclei size distribution

In heterogeneous cavitation, the tensile strength of the liquid $p_{sat} - p_{cr}$ significantly decreases in presence of air and gas bubbles. Several experimental techniques have been developed to measure nuclei size and concentration. Results of coulter counter [69], [70], acoustic and light scattering techniques [71], liquid holograms [70] or cavitation susceptibility meter [72] indicate that liquid nuclei are strongly polydispersed. Their size can range over several orders of magnitude from micrometers to millimeters. Furthermore the nuclei population can vary significantly from one test facility to the other [73].

Analytical expressions have been suggested to represent the nuclei number density $n(R)$ [74], [75]. For instance, a lognormal function is proposed in [74]:

$$n(R) = \frac{n_0}{\sqrt{2\pi}\hat{\sigma}_R R} \exp\left(-\frac{\left(\log R/R_0\right)^2}{2\hat{\sigma}_R^2}\right); \quad (3.4)$$

where n_0 is the nuclei concentration, R is the cavitation nuclei radius; and $\hat{\sigma}_R$ and R_0 represent variance and mean value of the nuclei size distribution, respectively.

According to their definition, $n(R)$ and f^ϕ are related by:

$$n(R) = \lim_{\Delta t \rightarrow \infty} \left[\frac{1}{\Delta t} \int \left(\int_{-\infty}^{+\infty} f^\phi(t, \mathbf{x}, \phi, \mathbf{u}_g, T_g) d\mathbf{x} d\mathbf{u}_g dT_g \right) dt \right] \quad (3.5)$$

for $\phi = R$, so that $n(R)$ has to be considered as an averaged quantity [13].

Since the nuclei density strongly affects cavitation inception (see sect . 3.2.1), [76] derived a scaling law between the number of nuclei in the test loop $n_{0,test}$ and the number of nuclei present under realistic conditions $n_{0,pl}$ to account for water quality effects:

$$\frac{n_{0,pl}}{n_{0,test}} = \left(\frac{L_{test}}{L_{pl}} \right)^3. \quad (3.6)$$

In equation (3.6), L_{pl} and L_{test} are the characteristic lengths of the model and of the prototype, respectively. Practically it is very difficult to precisely estimate the nuclei concentration.

3.1.2.2 Bubble dynamic

3.1.2.2.1 Mechanical equilibrium

The mechanical equilibrium condition of a spherical nucleus can be obtained from the force balance of an infinitely thin control volume containing a segment of gas-liquid interface of surface A_i . The forces exerted by the surrounding fluid $p_\infty A_i$ and by the surface tension F_σ are balanced by the force exerted by the gas and vapor inside the nucleus $p_B A_i$:

$$p_\infty A_i + F_\sigma = p_B A_i \quad (3.7)$$

The Young-Laplace equation indicates that the surface tension σ increases the pressure acting on the nucleus owing to its interface curvature. This capillary pressure p_σ , and thus the force F_σ , is related to the nucleus radius R and the surface tension:

$$F_\sigma = p_\sigma A_i = \frac{2\sigma}{R} A_i \quad (3.8)$$

The pressure p_B inside the nucleus is the sum of the partial pressures p_g and p_G of all vaporous and gaseous species present:

$$p_B = p_g + p_G \quad (3.9)$$

The vapor phase is assumed to be saturated at all times. Thus, the vapor pressure p_g is the vapor's saturation pressure

$$p_g = p_{sat}(T_b); \quad (3.10)$$

where T_b is bubble's temperature. The pressure p_G of the residual gas is treated as an ideal gas in most cases:

$$p_G = \frac{m_G T_b \mathcal{R}_G}{\frac{4}{3} \pi R^3} \quad (3.11)$$

In that case, the mechanical equilibrium condition (3.7) for a spherical nucleus reads:

$$p_{sat}(T_b) - p_\infty = \frac{2\sigma}{R_e} - \frac{m_G T_b \mathcal{R}_G}{\frac{4}{3} \pi R_e^3} \quad (3.12)$$

In eq. (3.12), R_e is the radius of the nucleus at equilibrium.

3.1.2.2.2 Nucleus activation

According to eq. (3.12), the radius of a spherical nucleus is not uniquely determined for given mass $(m_G)_0$ of contaminant gas, bubble temperature T_b , surface tension σ and pressure p_∞ . Nuclei with two different radii R_1 and R_2 could be present in the fluid for pressures above the critical pressure

$$p_{cr} = p_{sat} - \frac{4\sigma/3}{\sqrt{\frac{9m_G T_b \mathcal{R}_G}{8\pi\sigma}}} \quad (3.13)$$

However, the mechanical equilibrium of the nuclei larger than the critical radius $R_2 > R_{cr}$:

$$R_{cr} = \sqrt{\frac{9m_G T_b \mathcal{R}_G}{8\pi\sigma}} \quad (3.14)$$

is unstable. These larger nuclei actually do not exist. In contrast, nuclei, whose radius R_1 is smaller than R_{cr} , are stable. They consistently reach another equilibrium radius when p_∞ is slowly decreased and remains above p_{cr} . When p_∞ is further decreased below p_{cr} , the nucleus is not able to find a new mechanical equilibrium. The nucleus is activated. Figure 3-4 represents stable and unstable radii for given mass $(m_G)_0$ of contaminant gas, temperature T_b , and surface tension σ .

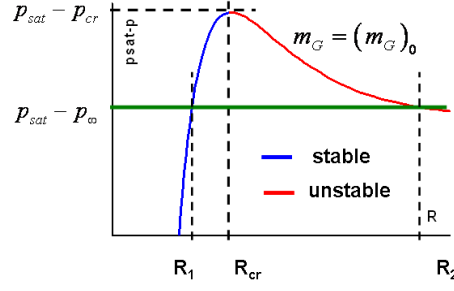


Figure 3-4: Stable R_1 and unstable R_2 nuclei equilibrium radius at a pressure p_∞ below critical pressure p_{cr} for an assumed constant contaminant gas mass $(m_G)_0$.

Following this analysis, water with large content of dissolved gas m_G possesses bigger nuclei than water with low dissolved gas content.

3.1.2.2.3 Rayleigh-Plesset equation

Once activated, vaporous cavities may grow and collapse according to the variation of fluid pressure p_∞ . Cavity's dynamics can be deduced from the combination of the mass continuity and the momentum equation of the liquid phase.

In the surrounding incompressible fluid, fluid particles volume remains unaffected by bubble radius R variation. Thus, if we consider one concentric fluid layer around the cavity defined by any two radii R_1 and R_2 ($R_2 > R_1 \geq R$), this fluid layer expands and contracts, as the bubble grows and shrinks, but its volume is conserved. The volume conservation translates into the following differential relation for the two radii $R_1 = R$ and $R_2 = r$:

$$\rho_l \dot{R} (4\pi R^2) = \rho_l \dot{r} (4\pi r^2). \quad (3.15)$$

For the fluid layer to be stretched and thinned, work is done by pressure force and energy dissipated by viscous forces. Balancing the driving force with the radial momentum and the dissipative forces of an infinitesimal thin fluid layer yields the following differential equation:

$$-\frac{1}{\rho_l} \frac{\partial p}{\partial r} = \frac{\partial u}{\partial t} + u \frac{\partial u}{\partial r} - \nu_l \left[\frac{1}{r^2} \frac{\partial}{\partial r} \left(r^2 \frac{\partial u}{\partial r} \right) - \frac{2u}{r^2} \right]. \quad (3.16)$$

Integrating eq. (3.16) from the radius R to a radius sufficiently large so that the fluid there is at rest, and using eq. (3.15), one obtains:

$$\frac{p_R - p_\infty}{\rho_l} = \frac{3}{2} \dot{R}^2 + R \ddot{R}; \quad (3.17)$$

where p_R is the pressure at the cavity interface on the fluid side.

p_R can be obtained from the force balance of an infinitely thin control volume containing a segment of gas-liquid interface. The expression is very similar to eq. (3.7) except that, in this case, a viscous force

$$F_v = \frac{4\eta_l}{R} \frac{dR}{dt} A \quad (3.18)$$

opposes resistance to radius' variation. The pressure at the interface on the fluid side is:

$$p_R = p_{sat} + p_G + \frac{F_\sigma}{A} + \frac{F_v}{A}. \quad (3.19)$$

Both equations (3.17) and (3.19) lead to the generalized Rayleigh-Plesset equation for bubble dynamics [77]:

$$\frac{p_{sat}(T_\infty) - p_\infty(t)}{\rho_l} + \frac{p_{sat}(T_b) - p_{sat}(T_\infty)}{\rho_l} + \frac{m_G T_b \mathcal{R}_G}{4\pi/3 R^3} = R \frac{d^2 R}{dt^2} + \frac{3}{2} \left(\frac{dR}{dt} \right)^2 + \frac{4\nu_l}{R} \frac{dR}{dt} + \frac{2\sigma}{\rho_l R}. \quad (3.20)$$

In contrast to nuclei activation where mass of contaminant gas and surface tension are crucial, cavity growth and collapse are primarily controlled by the external varying pressure (first term on the left hand side). An external pressure p_∞ below saturation pressure leads to an increase of bubble radius R whereas its increase above the saturation pressure yields the collapse of the cavities. For large cavities thermal effects (second term on the left) play also a crucial role. The fluid cools down during

bubble growth, for it supplies the energy required for the vaporization. A boundary layer of cold fluid develops at the periphery of the cavity. Due to the small heat capacity of the gas, the temperature in the gas phase adapts almost immediately to this temperature variation and the saturation pressure decreases. The growth rate is reduced and called thermally controlled.

3.1.2.2.3.1 Effect of mass diffusion

To solve the Rayleigh-Plesset equation, it is required to know the mass m_G of dissolved gas present in the cavity. In this context, it is useful to consider the diffusive equilibrium of a nucleus. This equilibrium condition is given by Henry's law: $co_G = H_G p_G$; (3.21)

where co_G is the concentration of dissolved gas and H_G the Henry's law constant which depends upon solute and solvent species; and temperature. p_G is defined in eq. (3.11).

[31] demonstrate that mechanical eq. (3.12) and diffusive eq. (3.21) equilibrium are always unstable: bubbles always tend to grow or resorb. An estimate of the characteristic time, also called the total resorption time, of air diffusion in absence of surface tension and negligible thickness of the concentration boundary layer is given in [78] by:

$$\tau_{res} = \frac{R_0^2}{2D_G} \frac{\rho_g}{co_s - co_\infty}. \quad (3.22)$$

In this expression, R_0 is the initial bubble radius, co_s is the initial concentration of dissolved gas, co_∞ is the concentration of dissolved gas at saturation and D_G is the coefficient of diffusivity of the gas in the water. Mass diffusion effects are negligible in most situations [31], [45]. In that case, the mass of dissolved gas m_G can be assumed to be constant. In contrast, in some particular applications such as acoustic cavitation [79], [80], the mass diffusion equation of the concentration $co(r,t)$ of gas in the liquid at time t and distance r should be solved. In spherical coordinates, this equation reads [12]:

$$\frac{\partial co}{\partial t} + \frac{dR_0}{dt} \left(\frac{R_0}{r} \right)^2 \frac{\partial co}{\partial r} = \frac{D_G}{r^2} \frac{\partial}{\partial r} \left(r^2 \frac{\partial co}{\partial r} \right); \quad (3.23)$$

with D_G being the gas mass diffusivity in water and R_0 the initial bubble radius.

3.1.2.2.3.2 Thermal effect

During the growth of the bubble, the fluid provides some energy to overcome the molecular forces so that the bubble temperature T_b differs from liquid temperature T_∞ at infinity (see section 3.1.2.2.3). To account accurately for this thermal effect in the bubble dynamics, the Rayleigh-Plesset equation must be solved with the heat diffusion equation in a coupled manner [12]. In this context, the heat diffusion equation is expressed in spherical coordinates:

$$\frac{\partial T}{\partial t} + \frac{dR_0}{dt} \left(\frac{R_0}{r} \right)^2 \frac{\partial T}{\partial r} = \frac{\alpha_{T,l}}{r^2} \frac{\partial}{\partial r} \left(r^2 \frac{\partial T}{\partial r} \right); \quad (3.24)$$

with $\alpha_{T,l}$ being the thermal diffusivity of the liquid and R_0 the bubble radius; and the heat supplied to the bubble by the fluid at the interface is related to bubble growth rate:

$$\frac{dR_0}{dt} = \frac{\lambda_{T,l}}{\rho_g l} \left(\frac{\partial T}{\partial r} \right)_{r=R_0}. \quad (3.25)$$

In eq. (3.25), $\lambda_{T,l}$ and l are liquid thermal conductivity and latent heat, respectively.

3.1.2.2.3.3 Influence of other bubbles

[81] first proposed to modify the Rayleigh-Plesset equation eq. (3.20) to account for the presence of other bubbles. For this purpose, they introduce a bubble cluster radius ΔR , which represents the distance over which bubbles may interact with each other. Assuming that the number density n of bubbles is constant, that all bubbles have the same radius R and neglecting viscous damping, surface tension and thermal effects, the modified Rayleigh-Plesset equation reads:

$$\frac{p_{sat}(T_\infty) - p_\infty(t)}{\rho_l} = \left[1 + 2\pi(\Delta R)^2 nR \right] R \frac{D^2 R}{Dt^2} + \left[\frac{3}{2} + 4\pi(\Delta R)^2 nR \right] \left(\frac{DR}{Dt} \right)^2 + 2\pi(\Delta R)^2 \frac{Dn}{Dt} R^2 \frac{DR}{Dt}. \quad (3.26)$$

In [82] and [83], the bubble cluster radius is related to the radius of the bubbles within the cluster as:

$$\Delta R = \Lambda R; \quad (3.27)$$

where $\Lambda = \text{const} \gg 1$.

3.1.2.2.3.4 Viscosity of the fluid

For very viscous fluid, [84] introduced an alternative definition of the onset of cavitation accounting not only for the normal stresses but also for the shear stresses acting on the fluid elements. In this theory, liquid breakdown may occur when the maximum of the principal component $\tilde{\tau}_{ii}$ of the stress tensor $\tau_{jk} = -p\delta_{jk} + 2\eta_1 e_{jk}$ exceeds the saturation vapor pressure:

$$\max(\tilde{\tau}_{ii}) \geq -p_{sat}. \quad (3.28)$$

3.1.2.2.3.5 Deformation

Although complex, the Rayleigh-Plesset equation has been derived for spherical bubbles and is *a priori* only valid for these particular bubbles. A criterion to assess when bubbles may deform due to their acceleration \dot{u} or growth and collapse \dot{R} can be found in [31]:

$$\rho(\dot{u}R + 3u\dot{R}) \gg \frac{2\sigma}{R}. \quad (3.29)$$

This relation indicates that bubbles deform when the maximum pressure difference due to \dot{u} or \dot{R} between two points on the interface is larger than the characteristic pressure difference $2\sigma/R$.

Surface instabilities may also cause the deformation of bubble's surface [12].

3.1.2.2.3.6 Bubble collapse

For slow pressure variations, the bubble growth rate is able to follow the pressure signal. In contrast for quick pressure variations, the bubble may continue to grow even in the compression phase due to the inertia of the fluid. In that case, the collapse of the bubble may become highly non-linear. Gas and vapor inside the cavity get strongly compressed, the bubble quickly rebounds and expands and goes through a series of secondary compressions and expansions of diminishing amplitudes [85].

Bubble collapse is associated with very high pressures, temperatures and velocities [86]. The asymptotic value of the pressure peak p_{\max} is derived in [23]:

$$p_{\max} - p_{\infty} \sim 4^{-\frac{4}{3}} \frac{p_{\infty} - p_{sat}}{\left(\frac{R_{\max}}{R_{\min}}\right)^3}; \quad (3.30)$$

where p_{∞} is pressure at infinity, R_{\max} bubble maximal (initial) radius, $R_{\min} \rightarrow 0$ bubble minimal (final) radius and p_{sat} saturation pressure. Due to the high velocity of the bubble boundary near the end of the collapse, compressibility effects could play a non-negligible role [23]. For example, [87] indicates that the lifetime of the bubble is increased due to water compressibility. Furthermore, pressure waves are observed [88] to propagate outwards, which could influence the dynamics of other bubbles or damage structure surfaces.

3.1.2.3 Coalescence

Coalescence is caused by the collision of particles. Several expressions exist for the collision frequency g_c [45]. One of them is expressed with the bubble diameter D_b , the void fraction α , the maximum packing concentration $\alpha_{\max} = 0.52$ and the bubble relative velocity U_{rel} [89]:

$$g_c = \frac{\alpha}{\alpha_{\max} - \alpha} \frac{6}{D_b} U_{rel}. \quad (3.31)$$

The frequency becomes infinite when void fraction reaches the maximum packing concentration $\alpha_{\max} = 0.52$. If the collisions are mainly attributed to the turbulent fluctuations, U_{rel} is defined as [90]:

$$U_{rel} = U_{turb} = \frac{(\varepsilon_t D_b / 2)^{1/3}}{\sqrt{2C_{am}}}. \quad (3.32)$$

In eq. (3.32), ε_l is the turbulent dissipation rate in the liquid phase and C_{am} is the added mass coefficient for which algebraic expressions are derived in [13].

Not all collisions lead to coalescence. The probability P_{col} that a collision results in coalescence is related to the film drainage time t_{dr} (time needed for the film of water situated between the bubbles to be drained) and the bubbles interaction time t_{in} by:

$$P_{col} = \exp\left(\frac{-t_{dr}}{t_{in}}\right). \quad (3.33)$$

In this expression (3.33), t_{dr} and t_{in} are defined as [90]:

$$t_{dr} = k_{dr} \frac{\rho_l U_{rel} D_b^2}{8\sigma}; \quad (3.34)$$

$$t_{in} = \frac{\pi}{4} \left(\frac{\rho_l C_{am} D_b^3}{3\sigma} \right)^{1/2}; \quad (3.35)$$

where k_{dr} is a model constant which usually has a value of 0.5 [45] and σ is the surface tension.

3.1.2.4 Break-up

Breakup occurs when deformation forces (e.g. velocity fluctuations) exceed confinement forces (typically surface tension σ). Experimental results [91] with water indicate that the frequency of breakup is a function of bubble diameter D_b , water density ρ_l , surface tension σ and liquid turbulent energy dissipation rate ε_l :

$$g_b = K_g \frac{\sqrt{\beta(\varepsilon_l D_b)^{2/3} - 12\sigma/\rho_l D_b}}{D_b}; \quad (3.36)$$

with $\beta = 8.2$ and $K_g = 0.25$. Bubbles with a diameter smaller than

$$D_c = 1.26(\sigma/\rho)^{3/5} \varepsilon_l^{-2/5} \quad (3.37)$$

do not breakup [91]. These cavities are too small to be disturbed by the velocity fluctuations.

3.1.2.5 Forces

Due to velocity, density, and pressure gradients existing between and within the phases, dispersed bubbles are submitted to numerous surface and volume forces. Most of them are summarized in Table 3-1 with their dependence on bubble radius R and on phases' relative velocity difference Δu ; their direction; their origin and the associated mechanism. Analytical expressions of some of these forces are given in appendix A.

Force	Radius dependency	Δu dependency	direction	origin	Mechanism
Drag	R^2 , C_D	u^2	Tends to u_c	Slip	Viscous, surface tension
Added mass	R^3	u	Tends to u_c	Density difference	Displacement of surrounding fluid
Buoyancy	R^3	No	Opposite to gravity	Density difference	
Wall lubrication	R^2	u^2	Repulsive	No-slip condition	Pressure difference on both side of the bubble
Wall deformation	R	no	Repulsive	Deformation of the bubble	Pressure difference due to deformation
Pressure gradient	R^3	no	Opposite to pressure gradient	Pressure gradient	
History	R^2	u		Viscous effect	Force due to lagging boundary layer development, temporal delay

Volume variation	R^3	u	Tends to u_c , if growth	Mass transfer	Momentum transfer due to mass exchange
Lift	R^3	u^2	Normal to rotation of fluid	Rotation of continuous phase	Pressure difference on bubbles' wall due to vorticity
Marangoni	R^2	No	Opposite to surface tension gradient	Surface tension gradient	
Turbulent dispersion				Concentration gradient	

Table 3-1: Forces on dispersed bubbles with their dependence on bubble radius R and on phases' relative velocity difference Δu ; their direction; their origin and the associated mechanism; u_c being the continuous phase velocity

3.1.2.6 Heat exchange

Temperature differences arise between fluid and gas phases during cavitation (sect. 3.1.2.2.3.2). As a result, heat transfer occurs between the phases.

One heat transfer mechanism is conduction. This mechanism is already discussed in sect. 3.1.2.2.3.2: The conduction can be estimated by solving the fluid temperature equation and the Rayleigh-Plesset equation in a coupled manner.

For bubbles in motion, heat transfer also occurs by convection. Exact estimation of interfacial heat exchange in this case is even more complicated. Correlations are required. The heat transfer q_b is assumed to be proportional to the temperature difference existing between the bubble and the surrounding fluid:

$$q_b = -k_b(T_b - T_f). \quad (3.38)$$

The coefficient of proportionality k_b generally is expressed with the liquid thermal conductivity $\lambda_{T,l}$ and the diameter D_b of the bubble as:

$$k_b = \frac{\lambda_{T,l}}{D_b} Nu. \quad (3.39)$$

In eq. (3.39), Nu is the Nusselt number. One correlation of the Nusselt number for a spherical bubble reads [92]:

$$Nu = 2 + 0.6Re^{0.5} Pr^{0.3} \text{ for } 0 \leq Re < 200 \quad 0 \leq Pe < 250. \quad (3.40)$$

In eq. (3.40), Pr and Pe are two dimensionless numbers called Prandtl and Peclet number, respectively. They are defined with the characteristic flow properties as:

$$Pr = \frac{\text{viscous diffusion rate}}{\text{thermal diffusion rate}} = \frac{c_p \eta}{\lambda_T}; \quad (3.41)$$

$$Pe = \frac{\text{convection rate}}{\text{thermal diffusion rate}} = Pr Re. \quad (3.42)$$

3.2 Characteristics of cavitating flows

3.2.1 Cavitation inception

Cavitation inception is primarily affected by the non cavitating pressure field [11]. Cavitating flows are observed when the local static pressure is below the saturation pressure of the fluid. This phenomenon is commonly caused by the acceleration of the fluid around solid bodies in external flows or in contractions in internal flows. Hereby the pressure p_∞ , temperature T_∞ and velocity U_∞ of the upstream flow are decisive for the occurrence or non-occurrence of cavitation. p_∞ imposes the overall pressure in the flow. When sufficiently large, the static pressure remains above saturation pressure $p_{sat}(T_\infty)$ everywhere in the flow. No cavitation occurs. T_∞ determines the value of the saturation pressure $p_{sat}(T_\infty)$. For sufficient subcooling ($T_{sat}(p_\infty) - T_\infty > 0$), $p_{sat}(T_\infty)$ is small enough so that the

static pressure remains above saturation conditions everywhere in the flow. No phase-change occurs. For sufficiently large U_∞ , the acceleration results in a large pressure drop leading to static pressures below the saturation pressure. Cavitation is observed. Thus, a dimensionless number commonly used to characterize cavitation inception is the cavitation inception number σ_{ci} defined as the particular value of the cavitation number σ_c ,

$$\sigma_c = \frac{p_\infty - p_{sat}(T_\infty)}{1/2\rho U_\infty^2}; \quad (3.43)$$

for which nucleation first occurs.

However, cavitation inception cannot accurately be described only by mean flow quantities and one dimensionless number. Boundary-layer development [93], turbulent pressure fluctuations [94] and water quality [12] also have an influence on the onset of cavitation. For example, σ_{ci} differs from one test facility to the other for the same geometry at same Reynolds numbers [12].

3.2.2 Cavitation patterns

Cavitation can appear in several macroscopic forms called cavitation patterns. On blades and in nozzles, these cavitations patterns are generally categorized into four categories: transient isolated bubbles, attached or sheet cavities, cloud cavitation and supercavities. These flow patterns are described for a hydrofoil in sections 3.2.2.1 to 3.2.2.4. These descriptions are taken from [31] to a large extent. In submerged jets, another macroscopic form of cavitation arises; which is called shear cavitation. For developed turbulent flow conditions, at given temperature and given fluid properties, the cavitation number mainly determines the nature and extension of the cavitation pattern [95]. For complex geometries, more than one of these cavitation patterns can occur simultaneously.

3.2.2.1 Transient isolated bubbles

The first manifestation of cavitation is largely influenced by the development of the boundary layer. Transient isolated bubbles are observed on blades at low angle of attack and large nuclei concentration [31] when the boundary layer is laminar whereas clusters of micro-sized vapor bubbles can be detected at larger attack angles for turbulent boundary layers [93]. The bubbles are large nuclei which start to cavitate in the low-pressure region (which may be the core of turbulent eddies in turbulent boundary layers) and are then convected downstream in higher pressure regions where they collapse (Figure 3-5).



Figure 3-5: Schematic representation of transient isolated cavitation bubbles (solid line) on a hydrofoil (blue).

3.2.2.2 Sheet cavitation

At large angles of attack or with low nuclei concentrations, cavitation onsets as an attached cavity downstream of the laminar boundary layer detachment. In turbulent boundary layers, the transient isolated bubbles are replaced by an attached cavitation sheet when the cavitation numbers reduces [93]. The attached cavity is made up of individual bubbles or consist of a vapor-filled cavity [96]. For geometries with a sharp edge the sheet cavity is fixed by the geometrical singularity. In the absence of such an element, the location of the cavity is not a priori known and will depend on surface tension effects, laminar-to-turbulent transitions and water quality [31].

The closure of the cavity region is characterized by a re-entrant jet (Figure 3-6). For thin cavities, the re-entrant jet is generally weak due to its interaction with the downward mean flow. The flow is stable and unsteadiness is limited to a small region in the rear part of the cavity. The unsteadiness of the wake is associated to high turbulent fluctuations. For thicker cavities, the momentum of the re-entrant jet is generally higher such that this re-entrant jet may reach the front section of the cavity [31].

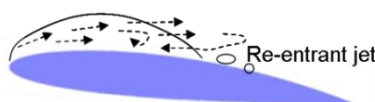


Figure 3-6: Schematic representation of sheet cavitation (solid line) on a hydrofoil (blue).

3.2.2.3 Cloud cavitation

When the impulse of the re-entrant jet is sufficient, a part of the attached cavity is separated, entrained by the downward flow and broken-up into smaller vapor bubbles and cavitating filaments (Figure 3-7). Meanwhile the part of the cavity which is still attached at the wall develops and grows until a new re-entrant jet forms and leads again to the separation of another shedding cavity. This manifestation is called cloud cavitation [31].

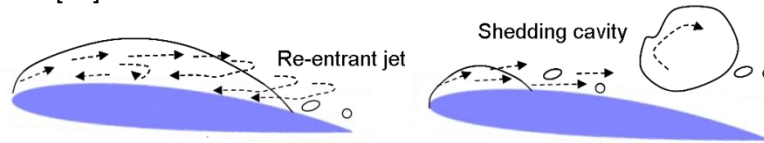


Figure 3-7: Schematic representation of cloud cavitation (solid line) on a hydrofoil (blue) at two instants: full cavity is attached (left); part of the cavity is convected downstream (right).

3.2.2.4 Supercavitation

For sufficiently low cavitation numbers, the pressure distribution on the foil produces cavities which are so long that they do not reattach on the wall anymore but close in the bulk of the flow (see Figure 3-8). These cavities are called supercavities.

The rear-part of supercavities is highly unstable with two concurring phenomena: a re-entrant jet tends to confine vapor inside the cavity while vapor and excess liquid are entrained by vortices [31].

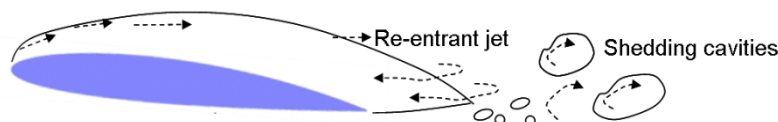


Figure 3-8: Schematic representation of supercavitation (solid line) on a hydrofoil (blue).

3.2.2.5 Shear cavitation

In submerged jets and in the wakes behind blunt bodies, vortical structures may develop [97]. As a result of the rotation of the fluid volumes, the instantaneous fluctuating pressure level may drop and differ significantly from the mean pressure [98], [99]. When the pressure in these eddies is sufficiently low during a sufficient time, nuclei grow and cavitation is observed. Industrial applications where this type of cavitation is encountered are, for example, boat propulsion or discharge control valves.

Inception of shear cavitation depends primarily on the structure of the non-cavitating flow, and water quality [100]. Shear cavitation has a non-negligible influence on the unsteadiness of the flow. For example, cavitation may affect the frequency of vortex shedding [101].

3.2.3 Effects of cavitation

Common examples of industrial components where cavitation occurs are pump impellers, bends and pipes. There cavitation is often undesirable since jets shock waves induced by bubble collapse are strong enough to produce significant noise and vibration and even damage walls. Furthermore larger flow resistance or two-phase instabilities may be encountered. However in some particular applications in the fields of medicine, water treatment or textile manufacturing, cavitation is a powerful tool to fragment or destruct molecules non-intrusively.

3.2.3.1 Surface damage

The bubble collapse close to a wall is characterized by high-velocity re-entrant jets directed towards the solid wall [102]. These jets, and the very high pressures and temperatures associated with bubble collapse (sect 3.1.2.2.3.6) may cause important surface damage (e.g. in pumps [103] and spillways [104]), noise and vibration [105]. Surface damage, noise and vibration are typically encountered with transient isolated bubbles or in the wake of sheet cavities and cloud cavitation due to the collapse of the numerous bubbles [31].

3.2.3.2 Performance breakdown

Cavitation is also undesired when it is accompanied by the alteration of the performance of the system.

On hydrofoils [106], performance reduction is intimately related to the existence and extension of cavitating regions. The lift is lowered since the pressure on the suction side does not decrease below saturation pressure. Moreover, the drag increases as a result of two-phase momentum transfers.

In nozzles, cavitation affects the flow resistance according to two mechanisms. The first mechanism consists in increased energy dissipation due to interfacial exchanges. The second phenomenon is encountered when the cavitation sheet occupies the whole cross section (Figure 3-9, (a), bottom). In that case, the flow may choke [95] and the flow resistance drastically increases. The following section summarizes the main results found in [95].

In the framework of cavitating nozzles, the cavitation number commonly is defined as [107], [108]:

$$K_{\sigma} = \frac{p_{\infty} - p_{sat}(T_{\infty})}{p_{\infty} - p_2} \quad (3.44)$$

In eq. (3.44), p_{∞} and p_2 are the pressures at the inlet and outlet of the nozzle, respectively (see Figure 3-9).

The effect of this cavitation number K_{σ} (eq. (3.44)) on the size L_{cav} of the cavity is represented schematically in Figure 3-9, (b), top. The first manifestation of cavitation occurs at K_{σ_i} . The length of the cavity grows with decreasing cavitation number. At $K_{\sigma} = K_{\sigma_{sc}}$, the cavitation sheet extends down to the outlet. The cavity tends to occupy the whole cross section with further decrease of the cavitation number.

To illustrate the effect of choking on the performance of the nozzle, the discharge coefficient C_d (eq. (3.45)) of the nozzle is represented as a function of the cavitation number K_{σ} (eq. (3.44)) in Figure 3-9, c, bottom. The discharge coefficient C_d usually is introduced to characterize the performance of a nozzle [95]. This coefficient is defined with the nozzle cross section A , the mass flow rate \dot{M} and the pressure difference existing between inlet and outlet, as:

$$C_d \equiv \frac{\dot{M}}{A\sqrt{2\rho(p_{\infty} - p_2)}} \quad (3.45)$$

While L_{cav} evolves with K_{σ} from K_{σ_i} to $K_{\sigma_{sc}}$, the performance of the nozzle significantly degrades when K_{σ} decreases below a geometry-dependent critical cavitation number K_{σ_c} [$K_{\sigma} < K_{\sigma_c}$; Figure 3-9, (a) bottom; and Figure 3-9, (c)]. K_{σ_c} may be smaller than $K_{\sigma_{sc}}$. This performance degradation occurs when the entire cross section is filled with vapor. In that case, the pressure in the nozzle can not decrease below saturation pressure. Nozzle pressure and mass flow rate \dot{M} are independent of outlet pressure p_2 . Under these conditions, C_d and K_{σ} are related as [109]:

$$C_d \propto \sqrt{K_{\sigma}}; \quad (3.46)$$

indicated by a parable on Figure 3-9, (c).

At larger cavitation number, the nozzle is only partially filled with vapor [Figure 3-9, (a), top and middle; and Figure 3-9, (b)]. Nozzle pressure and outlet pressure p_2 are identical and the discharge coefficient becomes relatively independent of the cavitation number. Instead the Reynolds number effect predominantly affects nozzle performance [109]. This regime is shown on Figure 3-9, (c) by a straight line.

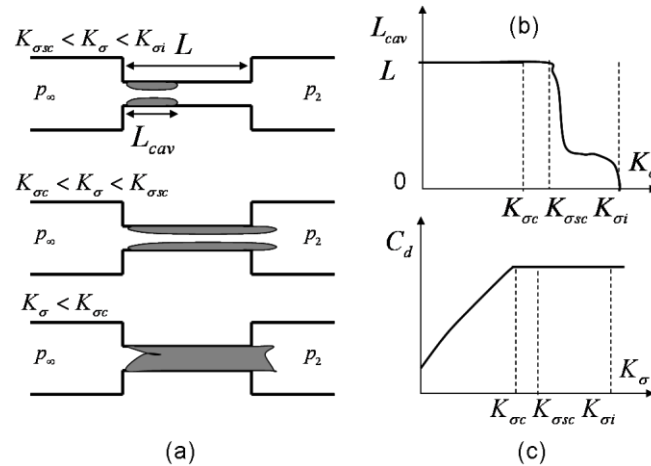


Figure 3-9: Average length of the cavitation region L_{cav} , (a) and (b); and discharge coefficient C_d , in relation to cavitation number K_σ in a straight nozzle [95].

3.2.3.3 Instabilities

In similarity to other two-phase flows, flow instabilities are another characteristic of cavitating flows. These instabilities can be localized in small regions of the flow, for example in the wake of thin cavities, thereby affecting the flow structures only locally. They can also involve the entire hydraulic system, typically when long cavities close in a region of small adverse pressure. In that case, even small pressure perturbations can significantly modify the attachment of the cavity which, in turn, impacts the pressure field in the system so that an oscillating system develops: Pressure increase yields large cavity length reduction; this, in turn, leads to a large reduction of flow blockage and momentum exchange; which finally cause the pressure to decrease in the system. The cavity grows again until the pressure increases again and the phenomenon repeats [31]. This is the typical process involved in cavitation surge [110].

3.2.3.4 Acoustic cavitation

The enormous temperatures and pressures released during bubble collapse can be utilized in many engineering fields (Medicine[111], [112], textile manufacturing [113], [114], or water treatment [115]) to fragment or destruct molecules; or to clean surfaces. For this purpose, growth and collapse of microscopic spherical bubbles are triggered by acoustic waves.

4 Numerical modeling

While the theoretical background on single-phase, two-phase and cavitating flows is presented in the preceding chapters '*physics*' and '*cavitation*', the present chapter '*numerical modeling*' describes established numerical techniques and models available to simulate these flows. These techniques and models are introduced for system codes and CFD codes since both are used for the development and analysis of the POR design. For instance, the POR flow rate in the backward direction is estimated with a system code; while the POR flow resistance during emergency core cooling is calculated with a CFD code.

First, the theoretical prerequisite on numerical techniques is outlined in section 4.1. Then, section 4.2 focuses on the models used in this work to simulate single-phase flows both with system and CFD codes. Section 4.3 describes the modeling of two-phase flows in system and CFD codes. Section 4.4 outlines three correlations available to predict the mass flux of coolant in pipes or breaks. One of these correlations is the homogeneous equilibrium model (HEM). The HEM is used for the design and analysis of the POR. Since bubbles' polydispersity is an important characteristic of cavitating flows, section 4.5 summarizes some modeling strategies currently available in CFD codes to account for it. Thereby none of these strategies is used in the present work. In section 4.6, the emphasis shifts onto the current techniques employed in the simulation of cavitating flows in CFD codes.

4.1 Numeric

The fluid dynamic governing equations (e.g. eq. (4.136), (4.139) and (4.144) in two phase flows) are highly non-linear partial differential equations (ODE) which cannot be solved analytically for complex geometries. A robust and efficient technique to solve these ODE anyway is to transform them into a system of algebraic equations which can be easily solved by numerical techniques. For this purpose, the flow variables are only calculated at discrete points in the flow domain and discrete times. The characteristic distance between two points is the mesh size Δ ; while the characteristic time increment is the time step Δt .

The transformation of a (system of) ODE into a (system of) algebraic equation(s) is called discretization. The discretization process involves the discretization of the computational domain into elementary control volumes, also called cells; and the discretization of the equations in space and time.

Different discretization techniques exist. Typically, finite-difference techniques [116] are used in system codes [117]. In CFD codes the finite volume method prevails since its formulation preserve local and, consequently, global mass conservation [118]. Nevertheless, the discretization process and the resolution of the resulting system of algebraic equations are very similar in finite-difference and finite-volume techniques. Hence, only the finite-volume approach will be presented in this work.

4.1.1 Discretization of the computational domain

The computational cells completely fill the computational domain without overlapping each other. Each cell P is characterized by its centroid \mathbf{x}_p , its volume V_p , its faces f and its neighbors N . The centroid \mathbf{x}_p is defined by:

$$\int_{V_p} (\mathbf{x} - \mathbf{x}_p) dV = 0. \quad (4.1)$$

The faces of the control volume are associated with a face area vector \mathbf{S}_f . \mathbf{S}_f points outwards from the cell, is normal to the cell and has the magnitude equal to the area of the face.

4.1.2 Discretization of a transport equation

A standard equation in fluid dynamics is the transport equation of a scalar property Y :

$$\underbrace{\frac{\partial \rho Y}{\partial t}}_{\text{temporal derivative}} + \underbrace{\nabla \cdot (\rho \mathbf{u} Y)}_{\text{convective term}} - \underbrace{\nabla \cdot (\rho D_Y \nabla Y)}_{\text{diffusion term}} = \underbrace{S(Y)}_{\text{source term}}. \quad (4.2)$$

Since the flow fields are only known at discrete points \mathbf{x}_p and \mathbf{x}_N (\mathbf{x}_N being the centroid of the neighboring cells), and discrete time t and $t + \Delta t$; equation (4.2) does not need to be satisfied locally and instantaneously. Equation (4.2) only needs to be satisfied over the control volume V_p around the point P and over the time increment Δt around the time t :

$$\int_t^{t+\Delta t} \int_{V_p} \left[\underbrace{\frac{\partial \rho Y}{\partial t}}_{\text{temporal derivative}} + \underbrace{\nabla \cdot (\rho \mathbf{u} Y)}_{\text{convective term}} - \underbrace{\nabla \cdot (\rho D_Y \nabla Y)}_{\text{diffusion term}} = \underbrace{S(Y)}_{\text{source term}} \right]. \quad (4.3)$$

4.1.2.1 Discretization in space

The spatial discretization consists in expressing the volume average of each physical process (temporal derivative, convective term, diffusion term, source term) as a function of the available discrete flow variables:

$$\int_{V_p} \frac{\partial \rho Y}{\partial t} = g_1(\rho_p, \mathbf{u}_p, p_p, T_p, Y_p, \rho_N, \mathbf{u}_N, p_N, T_N, Y_N); \quad (4.4)$$

$$\int_{V_p} \nabla \cdot (\rho \mathbf{u} Y) = g_2(\rho_p, \mathbf{u}_p, p_p, T_p, Y_p, \rho_N, \mathbf{u}_N, p_N, T_N, Y_N); \quad (4.5)$$

$$\int_{V_p} \nabla \cdot (\rho D_Y \nabla Y) = g_3(\rho_p, \mathbf{u}_p, p_p, T_p, Y_p, \rho_N, \mathbf{u}_N, p_N, T_N, Y_N); \quad (4.6)$$

$$\int_{V_p} S(Y) = g_4(\rho_p, \mathbf{u}_p, p_p, T_p, Y_p, \rho_N, \mathbf{u}_N, p_N, T_N, Y_N). \quad (4.7)$$

The functions g_1 , g_2 , g_3 and g_4 are not unique but depend on the interpolation of the available values at the cell surfaces (Figure 4-1). They strongly impact code accuracy, stability and efficiency.

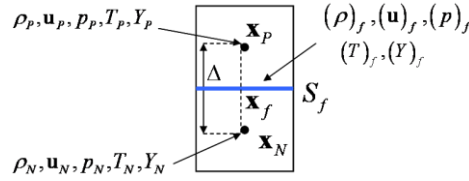


Figure 4-1: Representation of two computational cells P and N. Fluid properties are calculated in cell centroids \mathbf{x}_p and \mathbf{x}_N , and interpolated at the cell surface center \mathbf{x}_f .

Taking the diffusion term as an example, it is possible to express equation (4.6) with the Gauss theorem [119]:

$$\int_{V_p} \nabla \cdot (\rho D_Y \nabla Y) dV = \sum_f \mathbf{S}_f \cdot (\rho D_Y \nabla Y)_f = \sum_f (\rho D_Y)_f \cdot \mathbf{S}_f \cdot (\nabla Y)_f. \quad (4.8)$$

In eq. (4.8), $\mathbf{S}_f \cdot (\nabla Y)_f$ represents the scalar product of the gradient ∇Y with the face area vector \mathbf{S}_f and $(\varphi)_f$ is the value of the flow property φ at the surface center \mathbf{x}_f . Since $\mathbf{S}_f \cdot (\nabla Y)_f$ and $(\rho D_Y)_f$ are not directly available, they must be interpolated from the resolved quantities ρ_p , ρ_N , Y_p and Y_N .

The central differencing scheme (CD) calculates the property $(Y)_f$ at the center \mathbf{x}_f of the cell surface by interpolation of the values at the cells P and N which share the surface. Thereby, the ratio of the distances $\|\mathbf{x}_f - \mathbf{x}_N\|$ and $\|\mathbf{x}_p - \mathbf{x}_N\|$:

$$f_{ds} = \frac{\|\mathbf{x}_f - \mathbf{x}_N\|}{\|\mathbf{x}_p - \mathbf{x}_N\|} \quad (4.9)$$

is used as a weighting factor. Thus, the value $(Y)_f$ at surface center is given by:

$$(Y)_f = f_{ds} Y_p + (1 - f_{ds}) Y_N. \quad (4.10)$$

For a mesh with constant mesh size Δ , equation (4.10) reduces to:

$$(Y)_f = \frac{Y_p + Y_N}{2}. \quad (4.11)$$

The CD scheme obtains the gradient $(\nabla Y)_f$ at the cell surface from Y_p and Y_N . For example, in the x -direction, $\left(\frac{dY}{dx}\right)_f$ is calculated according to:

$$\left(\frac{dY}{dx}\right)_f = \frac{Y_p - Y_N}{\Delta}. \quad (4.12)$$

Considering the Taylor expansion of the function Y at the point \mathbf{x}_f , it can be shown that the approximation (4.12) is second order accurate for a constant mesh size Δ , i.e. the error scales with the square of the mesh size Δ :

$$\begin{aligned} \frac{Y_p - Y_N}{\Delta} = \frac{1}{\Delta} \left[\left(Y_f + \left(\frac{dY}{dx}\right)_f \Delta/2 + \frac{1}{2} \left(\frac{d^2Y}{dx^2}\right)_f (\Delta/2)^2 + \frac{1}{6} \left(\frac{d^3Y}{dx^3}\right)_f (\Delta/2)^3 + o(\Delta^3) \right) \right. \\ \left. - \left(Y_f - \left(\frac{dY}{dx}\right)_f \Delta/2 + \frac{1}{2} \left(\frac{d^2Y}{dx^2}\right)_f (\Delta/2)^2 - \frac{1}{6} \left(\frac{d^3Y}{dx^3}\right)_f (\Delta/2)^3 + o(\Delta^3) \right) \right] \end{aligned} \quad (4.13)$$

$$\Rightarrow \frac{Y_p - Y_N}{\Delta} = \frac{1}{\Delta} \left[\left(\frac{dY}{dx}\right)_f \Delta + \frac{1}{3} \left(\frac{d^3Y}{dx^3}\right)_f (\Delta/2)^3 + o(\Delta^3) \right] = \left(\frac{dY}{dx}\right)_f + O(\Delta^2). \quad (4.14)$$

[120] demonstrates that the accuracy of CD remains second order even on non-uniform meshes. The mesh size Δ has a significant impact on the accuracy of the solution. The discretization error is reduced by the use of finer meshes.

Second order accurate schemes represent a good compromise between accuracy, efficiency and stability. Higher order accurate schemes such as QUICK [121], involve more neighbors, and thus impose larger computational requirement; and are generally less stable; while lower order accurate schemes, such as upwind scheme [122], are more stable but the discretization errors are excessive.

4.1.2.2 Discretization in time

For the sake of clarity, the flow field quantities introduced in sect. 4.1.2.1 are given without indication on which time step the values refer to. Actually, considering the simplest case, two sets of quantities have to be considered: the “old” quantities defined at time $t = n\Delta t$ (Δt being the time step) which are available from the precedent time step n ; and the “new” quantities defined at time $t + \Delta t = (n+1)\Delta t$ which have to be calculated during the present time step $n+1$. Equation (4.3) has to be expressed with old, denoted by the superscript (n) ; or new quantities, denoted by the superscript $(n+1)$; or both.

Several formulations are used in CFD codes to discretize the equations in time. Some of them – the Euler-explicit, the Euler-implicit and the Runge-Kutta scheme – are presented in this section. For the sake of clarity, all the flow variables at the exception of the scalar property Y are assumed to be constant and the processes are assumed to be linear in Y . Under this assumption and introducing the matrix \mathcal{M}^d to represent the spatial discretization operator and the vector \mathbf{Y} consisting of the discrete values Y_p of Y in all computational cells, the spatial discretization of the physical processes (e.g. eq. (4.5) to (4.7)) in the transport equation of the scalar property can be expressed as:

$$\mathcal{M}^d \mathbf{Y}. \quad (4.15)$$

With this notation, the Euler-explicit discretization scheme is:

$$\int_t^{t+\Delta t} \mathcal{M}^d \mathbf{Y} dt = \mathcal{M}^d \mathbf{Y}^{(n)} \Delta t; \quad (4.16)$$

and the Euler-implicit discretization scheme is:

$$\int_t^{t+\Delta t} \mathcal{M}^d \mathbf{Y} dt = \mathcal{M}^d \mathbf{Y}^{(n+1)} \Delta t. \quad (4.17)$$

Both formulations are first order accurate. The error is proportional to Δt .

For the temporal derivative, the integration results in:

$$\int_t^{t+\Delta t} \int_{V_p} \frac{\partial(\rho Y)}{\partial t} dV = \int_t^{t+\Delta t} \frac{\partial}{\partial t} \left(\int_{V_p} \rho Y dV \right) dt = (\rho_p Y_p V)^{(n+1)} - (\rho_p Y_p V)^{(n)}. \quad (4.18)$$

Both Euler-implicit and Euler-explicit schemes can be used to discretize different processes in the same equation. Introducing the matrixes \mathcal{M}_1^d and \mathcal{M}_2^d associated to the spatial discretization of the processes discretized explicitly and implicitly in time, respectively, a general expression of the discrete form of equation (4.3) reads:

$$(\rho V) [\mathbf{Y}^{(n+1)} - \mathbf{Y}^{(n)}] = (\mathcal{M}_1^d \mathbf{Y}^{(n)} + \mathcal{M}_2^d \mathbf{Y}^{(n+1)}) \Delta t. \quad (4.19)$$

Similarly to the grid size Δ , the time step Δt has an influence on code accuracy.

To reduce the discretization errors, higher order schemes are available. For example, the explicit four-stage Runge-Kutta scheme is fourth-order accurate. Introducing a spatial discretization operator \mathcal{M}^d including the constant density, this scheme can be written for eq. (4.3) as:

$$Y_{(0)} = Y^{(n)}; \quad (4.20)$$

$$Y_{(1)} V = Y_{(0)} V - \frac{\Delta t}{2} \mathcal{M}^d Y_{(0)}; \quad (4.21)$$

$$Y_{(2)} V = Y_{(0)} V - \frac{\Delta t}{2} \mathcal{M}^d Y_{(1)}; \quad (4.22)$$

$$Y_{(3)} V = Y_{(0)} V - \frac{\Delta t}{2} \mathcal{M}^d Y_{(2)}; \quad (4.23)$$

$$Y_{(4)} V = Y_{(0)} V - \frac{\Delta t}{6} (\mathcal{M}^d Y_{(0)} + 2\mathcal{M}^d Y_{(1)} + 2\mathcal{M}^d Y_{(2)} + \mathcal{M}^d Y_{(3)}); \quad (4.24)$$

$$Y^{(n+1)} = Y_{(4)}; \quad (4.25)$$

where the superscript (n) denotes the time level $n\Delta t$ and the subscript (i) the internal iteration i .

4.1.3 Influence of discretization errors

During the transformation of the partial differential governing equations (e.g. (4.2)) into an algebraic system of equations (e.g. (4.19)), numerical discretization errors are introduced. As an example, the discretization error which arises from the approximation of the diffusive term (eq. (4.8)) is derived for the second order accurate CD scheme in sect. 4.1.2.1.

4.1.3.1 Dissipative errors

First order accurate schemes produce discretization errors which behave similarly to diffusive terms: these discretization errors smear out flow variable gradients. In this context, it is common to evaluate the numerical diffusion tensor Γ_N associated with the discretization operator [119]. For example, [119] shows that the numerical diffusion tensor $(\Gamma_N)_{UD}$ of the upwind differencing [118] on a uniform mesh simplifies to:

$$(\Gamma_N)_{UD} = \frac{1}{2} (\rho \mathbf{u})_f \Delta. \quad (4.26)$$

Similarly, [119] derives the numerical diffusion tensor $(\Gamma_N)_{EI}$ of the Euler-implicit temporal discretization. This numerical diffusion tensor is given by:

$$(\Gamma_N)_{EI} = \frac{\Delta t}{2} \rho |\mathbf{u}|^2. \quad (4.27)$$

Instead, the numerical diffusion tensor $(\Gamma_N)_{EE}$ of the Euler-explicit temporal discretization reads:

$$(\Gamma_N)_{EE} = -\frac{\Delta t}{2} \rho |\mathbf{u}|^2. \quad (4.28)$$

On non-orthogonal meshes, the order of discretization of the numerical schemes may be violated due to supplementary approximations. Typically, mesh skewness introduces dissipative error ([119], eq. (4.29) for the convection term) since the approximation of the flux is valid at \mathbf{f}_i , intersection of $\mathbf{x}_p - \mathbf{x}_N$ with cell surface, and not at surface center \mathbf{x}_f (see Figure 4-2).

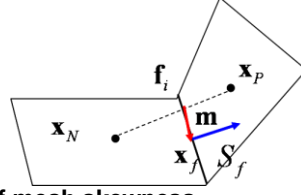


Figure 4-2: Schematic representation of mesh skewness.

The numerical diffusion tensor $(\Gamma_N)_{sk}$ arising as a result of this inaccuracy is derived in [119] for the convection term and reads, with $\mathbf{m} = \mathbf{x}_f - \mathbf{f}_i$:

$$(\Gamma_N)_{sk} = (\rho \mathbf{u})_f \mathbf{m}. \quad (4.29)$$

4.1.3.2 Dispersive errors

In contrast, the discretization errors of the second order accurate CD scheme are dispersive. They may get amplified into instabilities especially in region of large gradients (e.g. pressure shocks, stagnation region). In that case, the solution is characterized by large oscillations and unbounded scalars [119].

4.1.3.3 Artificial dissipation

To maintain the stability of the code when the fluxes are obtained with the CD scheme, artificial dissipation terms are usually included in the viscous calculations. They prevent oscillations near shocks or stagnation points. For example, the operator \mathcal{H} of the artificial dissipation is defined in [123] by [here given in two dimensions with coordinates $(\mathbf{x}_1, \mathbf{x}_2)$]:

$$\mathcal{H}(Y) = (\mathcal{H}_{x_1}^2 - \mathcal{H}_{x_1}^4 + \mathcal{H}_{x_2}^2 - \mathcal{H}_{x_2}^4)Y. \quad (4.30)$$

$\mathcal{H}_{x_1}^2$ and $\mathcal{H}_{x_1}^4$ are given by:

$$\mathcal{H}_{x_1}^2 Y = \nabla_{x_1} \left(\Lambda_{i+1/2,j} \varepsilon_{i+1/2,j}^{(2)} \right) \Delta_{x_1} Y_{i,j}; \quad (4.31)$$

and

$$\mathcal{H}_{x_1}^4 Y = \nabla_{x_1} \left(\Lambda_{i+1/2,j} \varepsilon_{i+1/2,j}^{(4)} \right) \Delta_{x_1} \nabla_{x_1} \Delta_{x_1} Y_{i,j}; \quad (4.32)$$

where i and j are associated with the \mathbf{x}_1 and \mathbf{x}_2 directions; and ∇_{x_1} and Δ_{x_1} are forward and backward difference operators in the x_1 direction. $\mathcal{H}_{x_2}^2$ and $\mathcal{H}_{x_2}^4$ have a similar expression. Thereby, the \mathbf{x}_2 coordinate replaces the \mathbf{x}_1 coordinate.

The variable scaling factor Λ is defined as:

$$\Lambda_{i+1/2,j} = \frac{1}{2} \left[(\Lambda_{x_1})_{i,j} + (\Lambda_{x_1})_{i+1,j} \right]; \quad (4.33)$$

and

$$\Lambda_{x_1} = \Phi_{x_1} \lambda_{x_1}; \quad (4.34)$$

$$\Phi_{x_1} = 1 + (\lambda_{x_1} / \lambda_{x_2})^\sigma; \quad (4.35)$$

where λ_{x_1} and λ_{x_2} are defined as:

$$\lambda_{x_1} = |u_1| + c; \quad (4.36)$$

$$\lambda_{x_2} = |u_2| + c; \quad (4.37)$$

c is the speed of sound; and the exponent σ is generally between 0 and 1. The coefficients $\varepsilon^{(2)}$ and $\varepsilon^{(4)}$ use the pressure as a sensor for shocks and stagnation points:

$$\varepsilon_{i+1/2,j}^{(2)} = K^{(2)} \max \left(\tilde{v}_{i-1,j}, \tilde{v}_{i,j}, \tilde{v}_{i+1,j}, \tilde{v}_{i+2,j} \right); \quad (4.38)$$

$$\tilde{v}_{i,j} = \left| \frac{p_{i-1,j} - 2p_{i,j} + p_{i+1,j}}{p_{i-1,j} + 2p_{i,j} + p_{i+1,j}} \right|; \quad (4.39)$$

$$\varepsilon_{i+1/2,j}^{(4)} = \max \left[0, \left(K^{(4)} - \varepsilon_{i+1/2,j}^{(2)} \right) \right]; \quad (4.40)$$

where $K^{(2)}$ and $K^{(4)}$ are model constants.

4.1.4 Solvers

4.1.4.1 Explicit solvers

The algebraic equations (4.19) can be solved directly by time-marching with a fully-explicit scheme, even if it was strongly non-linear. This is computationally advantageous since it is not necessary to inverse very large non-linear matrices; which requires much memory and costly techniques.

However, the stability of explicit schemes is limited to small time step Δt : the information should not travel over more than one cell per time step. This requirement can be formulated according to the Courant-Friedrichs-Lewy (*CFL*) number defined by

$$CFL = \frac{U_{\max} \cdot \Delta t}{\|\Delta\|}; \quad (4.41)$$

where U_{\max} is the maximal velocity (flow velocity u for pressure-based solvers or wave front velocity $|u|+c$ for density-based solvers – see sect. 4.1.5); and Δ is the length vector between the centroids of the cell P and of the neighbor cell N . The *CFL* number must be smaller than a problem dependent critical *CFL* number CFL_c for which the calculation becomes unstable:

$$CFL < CFL_c \leq 1. \quad (4.42)$$

Similarly, the von Neumann stability analysis indicates that diffusion processes impose a limit on the affordable time step. For example, the stability condition of the transport equation of a scalar property (eq. (4.2)) without convection and discretized with an explicit Euler method and CD, reads :

$$\frac{D_y \Delta t}{\Delta^2} < \frac{1}{2}. \quad (4.43)$$

For other equations or discretization schemes, the value on the right hand side of the inequality (4.43) may differ from $1/2$; and D_y may be replaced by the momentum diffusion coefficient ν .

Thus, the time step in explicit calculations has to satisfy:

$$\Delta t = \min \left(\frac{CFL_c \Delta}{U_{\max}}, \frac{\sigma_{vN} \Delta^2}{\nu} \right); \quad (4.44)$$

where σ_{vN} is a constant of order one.

4.1.4.2 Implicit solvers

The discretization in time is presented in section 4.1.2.2 assuming linear processes. A more general algebraic equation contains linear and non-linear terms. In this context, for fully- and semi-implicit numerical schemes, the algebraic equation (4.19) can be written in the matrix form with \mathcal{D} and $\underline{\mathcal{D}}$ discretization operators:

$$\mathcal{D}(Y^n, Y^{n+1}) Y^{n+1} = \underline{\mathcal{D}}(Y^n). \quad (4.45)$$

Since the direct solution of a non-linear equation is very inefficient for large matrices, the matrix \mathcal{D} is generally linearized around Y^n :

$$\mathcal{D}(Y^n, Y^n) Y^{n+1} = \underline{\mathcal{D}}(Y^n). \quad (4.46)$$

Typically, the convective term in the Navier-Stokes equations is expressed with the known fluxes. Then, eq. (4.46) is solved iteratively. For this purpose the matrix \mathcal{D} is split into two operators \mathcal{D}_1 and \mathcal{D}_2 which satisfies

$$\mathcal{D}_1 - \mathcal{D}_2 = \mathcal{D}. \quad (4.47)$$

The decomposition is not unique and largely influences the convergence of the iterative scheme:

$$Y_{p=0}^{n+1} = Y^n; \quad (4.48)$$

$$Y_{p+1}^{n+1} = \mathcal{D}_1^{-1} \left[\mathcal{D}_2(Y_p^{n+1}) + \underline{\mathcal{D}}(Y^n) \right]; \quad (4.49)$$

$$Y^{n+1} = Y_{p=N}^{n+1}. \quad (4.50)$$

p is the internal iteration incremented from 0 to N at fixed time step n . The value N of the iteration counter p in eq. (4.50) satisfies an abort criterion. For example, the variation $|Y_{N+1}^{n+1} - Y_N^{n+1}|$ is smaller than a user-defined truncation error ε_{it} :

$$|Y_{N+1}^{n+1} - Y_N^{n+1}| < \varepsilon_{it}. \quad (4.51)$$

In comparison to explicit schemes, the supplementary cost for the iterative process is compensated by the larger affordable time step, which is advantageous for long transients.

4.1.5 Solvers for coupled equations

The basic ideas of the discretization of a transport equation and the resolution of the resulting algebraic equation are presented in the preceding sections. The approach remains very similar for several equations. Nevertheless, the governing equations of single and two-phase flows are coupled. It is necessary to use dedicated numerical techniques to treat correspondingly the system of algebraic equations.

4.1.5.1 Segregated solvers

One approach is to solve the model equations sequentially. This technique is valid for processes where energy and momentum equations' coupling is weak. This is the basic idea of the segregated solvers (SIMPLE, SIMPLEC, PISO, etc.), also called pressure-based solvers. For example, the semi-implicit method for pressure linked equations (SIMPLE [124]) proceeds as follows: First the velocity field is calculated from the momentum equation. Thereby, the pressure gradient is estimated with the flow variable of the previous iteration ("old" value). Second, the pressure equation is formulated with the available velocity field and solved to obtain the new pressure distribution. Finally, the velocities are corrected with the new pressure distribution to satisfy the continuity equation. New fluxes are calculated for the next iteration. The number of correction steps required to achieve an arbitrarily precision is often problem and mesh specific.

Originally developed for incompressible flows, whose velocity field is divergence free, these pressure-based solvers have been adapted to compressible flows and in particular to two-phase flows. In essence, successive pressure corrections are used to adjust velocities and densities until the required conservation relation is satisfied [125].

These solvers have two major drawbacks. First, the conservative form of the governing equations is not strictly satisfied. This creates numerical difficulties and loss of accuracy near step gradients [126]. Second, only slow convergence rates are achieved [127].

4.1.5.2 Coupled solvers

When the interaction between the phases is very strong, or the processes have short time scales, coupled solvers are preferable [125]. Developed for compressible flows by the aerospace community, the density-based algorithms solve density, momentum and energy governing equations as a vector of equations. Cast in integral Cartesian form for an arbitrary control volume V_{cell} with differential surface area dA , the system of governing equations of a single phase flow reads:

$$\frac{\partial}{\partial t} \int_{V_{cell}} \mathbf{W} dV + \oint_{S_f} [\mathbf{F}_u - \mathbf{G}] \cdot d\mathbf{A} = \int_{V_{cell}} \mathbf{H} dV; \quad (4.52)$$

where the vectors \mathbf{W} , \mathbf{F}_u and \mathbf{G} are defined as:

$$\mathbf{W} = \begin{Bmatrix} \rho \\ \rho u_1 \\ \rho u_2 \\ \rho u_3 \\ \rho E \end{Bmatrix}, \quad \mathbf{F}_u = \begin{Bmatrix} \rho \mathbf{u} \\ \rho \mathbf{u} u_1 + p \mathbf{x}_1 \\ \rho \mathbf{u} u_2 + p \mathbf{x}_2 \\ \rho \mathbf{u} u_3 + p \mathbf{x}_3 \\ \rho \mathbf{u} E + p \mathbf{u} \end{Bmatrix}, \quad \mathbf{G} = \begin{Bmatrix} 0 \\ \boldsymbol{\tau}_{xi} \\ \boldsymbol{\tau}_{yi} \\ \boldsymbol{\tau}_{zi} \\ \boldsymbol{\tau}_{ij} u_i + \mathbf{q} \end{Bmatrix}; \quad (4.53)$$

and the vector \mathbf{H} contains source terms.

The system of partial differential equations (4.52) can be discretized in a fully-explicit manner and advanced in time with a time-marching scheme. High order accurate temporal discretization scheme

such as the fourth-order accurate Runge-Kutta scheme are generally used for this purpose. The time step is chosen according to eq. (4.44) with $U_{\max} = |u| + c$, being the maximal speed at which information travels.

The pressure and the temperature are computed from the equation of state (eos) with the conservative variables.

Supplementary equations, such as scalar property transport equations, are solved in a segregated manner.

Implicit unsteady formulations and steady formulations are other schemes available with density-based solvers. In these cases, the system of equations is linearized and solved by matrix inversion for implicit schemes; whereas the explicit time stepping and the explicit steady formulations use the preconditioning technique [92]; and the so-called dual-time stepping schemes.

4.1.6 Modeling of the boundary conditions

To reduce the computational effort, it is advantageous to limit the extent of the computational domain as much as possible. Thereby the type and the position of the boundaries largely influence the accuracy of the numerical results [128] and the stability of the code.

The spatial discretization of the governing equations is described in sect. 4.1.2.1 for internal cells, i.e. computational cells situated inside the fluid domain: the flow variables and their gradients at cell faces (e.g. $(Y)_f$ and $\left(\frac{dY}{dx}\right)_f$) are interpolated from neighboring cells. There, the number of neighbors

involved depends on the numerical scheme. In contrast, boundary cells, i.e. located at the boundaries, are missing one or more neighboring fluid cells. To use the same algorithm for boundary cells as for internal cells, supplementary cells, called halo cells, are commonly introduced. The number of halo cells depends on the discretization scheme. With the CD scheme, the halo cells mirror the first layer of cells near the boundary against the boundary face (Figure 4-3 right). Halo cells are used similarly to fluid cells except that flow variable values are not calculated but imposed at their centroid.

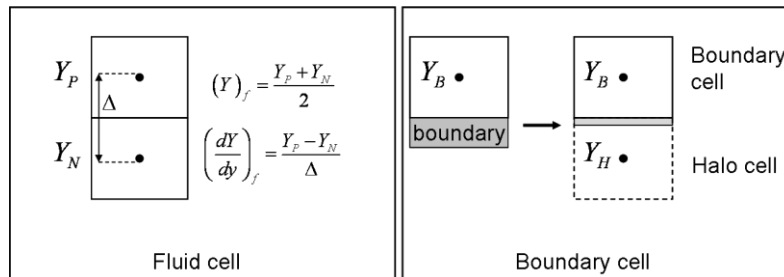


Figure 4-3: Schematic representation of fluid cell (left) and boundary cell (right) with CD scheme.

The value prescribed at the centroid of the halo cells depends on the boundary conditions. Typical boundary conditions can be categorized into wall (with no-slip or slip conditions), inlet (velocity and temperature profiles, mass flow, total pressure), symmetry, far field, and outlet (outflow, static pressure, and zero gradients). Boundary conditions which are used in this work (no-slip walls, velocity, mass flow and total pressure inlet, and outflow and static pressure outlet) will be described hereafter.

4.1.6.1 Walls with no-slip conditions

4.1.6.1.1 Momentum equation

The no-slip condition is valid at the wall for viscous fluid. In this case, the fluid has no velocity relative to the wall. Its velocity $\mathbf{u}|_w$ matches the wall velocity \mathbf{u}_w :

$$\mathbf{u}|_w = \mathbf{u}_w. \quad (4.54)$$

- shear stress and velocity vectors are parallel and unidirectional throughout the layer;
 - turbulence energy production and dissipation are balanced;
 - there is a linear variation of turbulence length scale;
- standard wall functions are used to estimate the wall shear stress. In this framework, the first computational cell is bigger (Figure 4-6 left) since it is situated in the fully turbulent layer which extends from $y^+ = 70$ to $y^+ = 300$ (see Figure 4-5). In this layer, the non-dimensional velocity u^+ defined as:

$$u^+ = \frac{u}{u_\tau}; \quad (4.59)$$

and the distance to the wall y^+ (eq. (4.57)) are related according to the logarithmic law:

$$u^+ = \frac{1}{\kappa} \ln y^+ + C^+. \quad (4.60)$$

In eq. (4.60) the constants are $\kappa = 0.41$ and $C^+ = 5.0$. Then, the wall shear stress τ_w is obtained by solving iteratively eq. (4.60) replacing u from eq. (4.59) with u_p , the velocity of the first computational cell at the wall, and y_w from eq. (4.57) with $y_{w,p}$, the distance from the wall of the first computational cell.

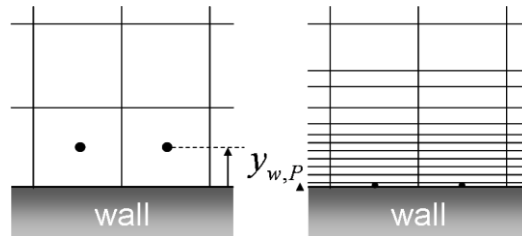


Figure 4-6: Representation of the meshes needed with wall functions (left) and resolution up to the wall (right); y_p is the distance from the wall of the first computational cell centroid.

The wall shear stress is also needed for the calculation of the turbulent properties when wall functions are used (see 4.1.6.1.3).

4.1.6.1.1.3 All- y^+ wall treatment

In commercial software, the “all- y^+ wall treatment” is available to combine the advantages of both techniques for complex geometries: The code determines which technique has to be utilized (boundary resolution or wall functions) depending on the distance from the wall of the first computational cell. Thus, it is possible to refine the mesh in regions characterized by flow detachment, stagnation, etc., so that the governing equations are solved down to wall; while the number of cells can be reduced in other regions by the use of wall functions.

4.1.6.1.2 Temperature equation

For the temperature equation, two conditions may be specified at the wall: wall heat flux or wall temperature. In the simulations presented here, the wall is adiabatic, i.e. wall heat flux \mathbf{q}_w through the boundary face is zero:

$$\mathbf{q}_w = \mathbf{0}. \quad (4.61)$$

According to Fourier’s law with constant thermal conductivity, the relation (4.61) is equivalent to:

$$\nabla T = \mathbf{0}. \quad (4.62)$$

This second relation (4.62) is satisfied by imposing the temperature of the first computational cell near the wall at the centroid of the halo cell.

4.1.6.1.3 Turbulent equations

The turbulent fluctuations vanish at the wall. Turbulent kinetic energy, specific dissipation rate and eddy viscosity are set to zero at the wall by mirroring their value from the boundary cells into the halo cells when the flow is resolved down to the wall.

In contrast, with wall functions, the first cell is situated in the fully-turbulent layer. Assuming a linear dependence of k and ω with wall distance would be too crude. Instead wall functions were derived to relate the turbulent kinetic energy and the specific dissipation rate with the distance from the wall. The values k_p and ω_p in the first computational cell are estimated from wall shear stress and distance from the wall; and imposed such as:

$$k_p = \frac{u_\tau^2}{\sqrt{\beta^*} y_{w,p}}; \quad (4.63)$$

$$\omega_p = \frac{u_\tau}{\sqrt{\beta^*} \kappa y_{w,p}}. \quad (4.64)$$

In eq. (4.63) and (4.64), β^* is a model constant.

4.1.6.2 Inlet and outlet

Inlet and outlet must reproduce the hyperbolic character of the Navier-Stokes equations. In this context, the number of variables to impose at the inlet of the computational domain is given by the number of positive local eigenvalues while the number of variables to impose at the outlet is given by the number of negative local eigenvalues. Here the local eigenvalues are defined by u , $u-c$ and $u+c$, with u and c being the local velocity and sound speed, respectively. For the calculation of the POR flow behavior, 4 variables are prescribed at the inlet and one at the outlet since subsonic conditions are encountered. The quantities which are not prescribed are extrapolated from the internal computational cells, generally assuming zero gradients between internal and boundary cells.

4.1.6.2.1 Inlet

4.1.6.2.1.1 Velocity inlet

One possible inlet boundary condition is the velocity inlet condition. In this case, velocity and temperature are prescribed at the inlet while density is extrapolated from the internal cells. If needed, turbulent parameters, chemical species or void fraction are imposed.

4.1.6.2.1.2 Mass flow inlet

Another possibility is to impose the mass flow and the temperature at the inlet of the computational domain. For an incompressible calculation, it is equivalent to the velocity inlet.

4.1.6.2.1.3 Total pressure inlet

Often total pressure and temperature are known at the inlet while the mass flow is a result of the calculation. Total stagnation pressure, total stagnation temperature and flow direction must be prescribed at the inlet.

4.1.6.2.2 Outlet

4.1.6.2.2.1 Outflow outlet

Outflow conditions can only be used in incompressible calculation when velocity or mass flow is prescribed at the inlet. A zero diffusion flux is applied to all variables at the outflow cells while an overall mass balance correction assures the conservation of mass.

4.1.6.2.2.2 Static pressure outlet

Generally, pressure outlet is known and specified at the outlet of the computational domain. Other flow variables are extrapolated from the internal cells using zero diffusion fluxes.

4.2 Modeling of single-phase flows

In system and CFD codes, the flow variables are only known at discrete points in time and space. Information on the flow variables is unavailable at any other position or time. Thus, the variations of

the flow variables over length scales smaller than the grid size and time scales smaller than the time step are unresolved.

The smallest length and time scales of the fluctuations in a single-phase turbulent flow are the Kolmogorov length l_K and time t_K , respectively. From a dimensional analysis, it is possible to estimate the number of cells required to resolve these fluctuations. In a turbulent flow of Reynolds number Re , this number of cells is of order $Re^{9/4}$ [37].

In spite of the drastic increase in computer resources during the last decades, this requirement is still beyond current computing capability in engineering applications. Small length and time scales cannot be fully resolved. Therefore, the discretized equations must be completed with models which represent the effect of this unresolved information.

4.2.1 System codes

For calculations involving long geometries and/or long transients, e.g. safety analysis in a nuclear plant reactor, it is common to discretize the equations over one-dimensional longitudinal sections. Processes such as friction, turbulence and heat transfer, which depend upon transverse gradients, must be formulated in terms of empirical transfer coefficients. These coefficients, also called correlations, must be expressed with the known quantities, i.e. the bulk properties. Experiments, available experimental data [40] or accurate numerical calculations are required to derive the correlations.

The one-dimensional conservation equations of a single-phase flow read [51]:

Mass conservation equation:

$$\frac{\partial}{\partial t} A\rho + \frac{\partial}{\partial z} \dot{M} = 0. \quad (4.65)$$

Momentum equation:

$$\frac{\partial}{\partial t} \dot{M} + \frac{\partial}{\partial z} \frac{\dot{M}^2}{A\rho} = -A \frac{\partial}{\partial z} p - P\tau_w - Ag\rho \sin \varphi_g. \quad (4.66)$$

Energy equation:

$$\frac{\partial}{\partial t} A\rho E + \frac{\partial}{\partial z} \dot{M}E = -\frac{\partial}{\partial z} \frac{\dot{M}}{\rho} p - P \frac{\dot{M}}{A\rho} \tau_w + Pq_w + A\rho Q. \quad (4.67)$$

In these equations, A is the cross section, $\dot{M} = \rho uA$ the mass flow rate, P the pipe perimeter, τ_w the wall friction coefficient, φ_g the angle existing between pipe and gravity field \mathbf{g} , q_w the heat transfer coefficient and Q the heat source term (see Figure 4-7).

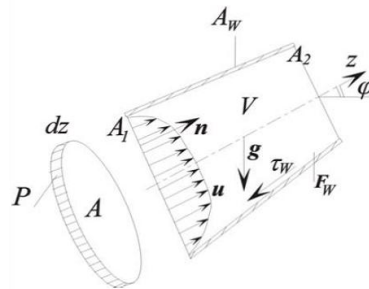


Figure 4-7: Representation of a single-phase flow in a pipe [51].

Wall friction and heat transfer coefficients must be modeled with bulk properties. A typical correlation for the wall friction is:

$$\tau_w = f(Re) \frac{1}{8} \rho u |u|; \quad (4.68)$$

where the function $f(Re)$ of the Reynolds number Re is calculated according to some assumptions on the flow conditions (turbulent or laminar), on the properties of the wall (roughness), etc. For example, the correlation of Hagen-Poiseuille [130]:

$$f(Re) = \frac{64}{Re} \quad (4.69)$$

is used for laminar flows. In contrast, the friction loss of a turbulent flow in a pipe of diameter D and roughness ε_r is better described by the correlation of Colebrook [131]:

$$\frac{1}{\sqrt{f(\text{Re})}} = -2 \log \left(\frac{2.51}{\text{Re} \sqrt{f(\text{Re})}} + \frac{\varepsilon_r}{3.7D} \right). \quad (4.70)$$

A correlation to model the turbulent heat transfer in a pipe of diameter D of a fluid of thermal conductivity λ_T is:

$$q_w = k_w (T_w - T); \quad (4.71)$$

with

$$k_w = \frac{\lambda_T}{D} Nu; \quad (4.72)$$

and [132]

$$Nu = 0.023 \text{Re}^{0.8} \text{Pr}^{1/3}. \quad (4.73)$$

For more complex geometries than simple pipes, another form of hydraulic resistance is encountered as a consequence of flow detachment, swirls, etc.: the form loss. Similarly to friction loss, correlations must be supplied to the system code to account for it.

The dissipation of energy downstream of a sudden enlargement is also a transverse process. To account for this phenomenon, a correlation must also be supplied. Considering the Carnot diffuser (see Figure 4-8, [133]), the flow detaches from the wall and large recirculation zones develop yielding high energy dissipation. The pressure recovery from section 1 to 2 is only partial and the pressure p_2 at section 2 is lower than it would have been if no energy had been dissipated.

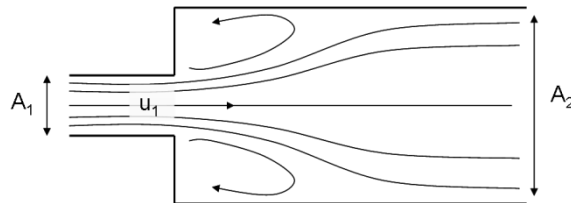


Figure 4-8: Carnot diffuser: Sudden expansion from cross section A_1 to A_2 .

For this simple configuration, an analytical expression exists [133] to estimate the hydraulic loss given two cross sections A_1 and A_2 , and a velocity u_1 at the smallest cross section A_1 :

$$\frac{\Delta p}{\frac{\rho}{2} u_1^2} = \left(1 - \frac{A_1}{A_2} \right)^2. \quad (4.74)$$

In eq. (4.74), Δp represents the difference between the (ideal) total and the Carnot diffuser pressure recovery.

A dimensionless number ζ , called the pressure loss coefficient, generally is introduced to represent the flow resistance. This coefficient is defined as the ratio between the pressure loss and dynamic pressure:

$$\zeta \equiv \frac{\Delta p}{\frac{\rho}{2} u^2}. \quad (4.75)$$

4.2.2 Computational fluid dynamics codes

Correlations are needed in system codes to represent the effect of transverse processes. When experimental data are not available for the specific flow conditions and geometry, an alternative to perform costly experiments is to use Computational Fluid Dynamic (CFD) codes. In CFD codes, the computational domain is discretized over small three dimensional computational cells. More information about the flow variables is known. However all scales of the turbulent fluctuations cannot be resolved. Models are supplied to represent the effect of these fluctuations.

4.2.2.1 Reynolds-averaged Navier-Stokes equations

In Reynolds-averaged Navier-Stokes simulations (RANS), the governing equations are time-averaged. They read:

$$\frac{\partial \bar{\rho}}{\partial t} + \frac{\partial}{\partial x_i} (\bar{\rho} u_i) = 0; \quad (4.76)$$

$$\frac{\partial}{\partial t} (\bar{\rho} u_i) + \frac{\partial}{\partial x_i} (\bar{\rho} u_i u_j) = -\frac{\partial \bar{p}}{\partial x_i} + \bar{\rho} f_i + \frac{\partial \bar{\tau}_{ji}}{\partial x_i}; \quad (4.77)$$

$$\frac{\partial}{\partial t} (\bar{\rho} E) + \frac{\partial}{\partial x_i} (\bar{\rho} u_i E) = -\frac{\partial \bar{p} u_j}{\partial x_i} + \frac{\partial \bar{\tau}_{ij} u_j}{\partial x_i} - \frac{\partial \bar{q}_i}{\partial x_i} + \bar{\rho} f_i u_i; \quad (4.78)$$

$$\frac{\partial}{\partial t} (\bar{\rho} Y) + \frac{\partial}{\partial x_i} (\bar{\rho} u_i Y) = -\frac{\partial}{\partial x_i} (\bar{j}_i) + \bar{S}(Y). \quad (4.79)$$

Assuming constant density $\rho = \bar{\rho}$ and using the Reynolds decomposition (chapter *physics*), the system of eq. (4.76) to (4.79) becomes:

$$\frac{\partial \rho}{\partial t} + \frac{\partial}{\partial x_i} (\rho \bar{u}_i) = 0; \quad (4.80)$$

$$\frac{\partial}{\partial t} (\rho \bar{u}_i) + \frac{\partial}{\partial x_i} (\rho \bar{u}_i \bar{u}_j) = \frac{\partial}{\partial x_i} (\rho \bar{u}_i \bar{u}_j - \rho \overline{u_i u_j}) - \frac{\partial \bar{p}}{\partial x_i} + \rho \bar{f}_i + \frac{\partial \bar{\tau}_{ji}}{\partial x_i}; \quad (4.81)$$

$$\frac{\partial}{\partial t} (\rho \bar{E}) + \frac{\partial}{\partial x_i} (\rho \bar{u}_i \bar{E}) = \frac{\partial}{\partial x_i} (\rho \bar{u}_i \bar{E} - \rho \overline{u_i E}) - \frac{\partial \bar{p} u_j}{\partial x_i} + \frac{\partial \bar{\tau}_{ij} u_j}{\partial x_i} - \frac{\partial \bar{q}_i}{\partial x_i} + \rho \bar{f}_i u_i; \quad (4.82)$$

$$\frac{\partial}{\partial t} (\rho \bar{Y}) + \frac{\partial}{\partial x_i} (\rho \bar{u}_i \bar{Y}) = \frac{\partial}{\partial x_i} (\rho \bar{u}_i \bar{Y} - \rho \overline{u_i Y}) - \frac{\partial}{\partial x_i} (\bar{j}_i) + \bar{S}(Y). \quad (4.83)$$

The first terms on the right-hand side of these equations represent the turbulent fluxes of momentum, energy and scalar property, respectively,

$$\rho \bar{u}_i \bar{u}_j - \rho \overline{u_i u_j} = -\rho \overline{u_i' u_j'}; \quad (4.84)$$

$$\rho \bar{u}_i \bar{E} - \rho \overline{u_i E} = -\rho \overline{u_i' E'}; \quad (4.85)$$

$$\rho \bar{u}_i \bar{Y} - \rho \overline{u_i Y} = -\rho \overline{u_i' Y'}. \quad (4.86)$$

They are not known and must be modeled: it is the closure problem.

The turbulent fluxes represent the effect of the turbulent fluctuations on the mean flow. Since one remarkable effect of the chaotic motion is to greatly increase the mixing of the fluid properties, the turbulent fluxes often are treated in analogy with the molecular diffusion processes.

For example, the turbulent momentum fluxes $-\rho \overline{u_i' u_j'}$, also called (apparent) Reynolds stresses, are represented by a linear constitutive relationship with the mean flow straining field:

$$-\rho \overline{u_i' u_j'} = \eta_t \left(\frac{\partial \bar{u}_i}{\partial x_j} + \frac{\partial \bar{u}_j}{\partial x_i} \right); \quad (4.87)$$

where η_t , the turbulent eddy viscosity, is modeled. The modeling of η_t distinguishes the numerous so-called (linear) eddy viscosity models (e.g. Baldwin-Lomax [134], Cebeci-Smith [135], Spalart-Alamaras [136], $k-\varepsilon$ [137], $k-\omega$ [138]).

In the same manner, enhanced temperature and species mixing generally are approximated by a gradient hypothesis which mimics the molecular processes. Introducing the positive turbulent thermal conductivity $(\lambda_T)_t$ and turbulent mass diffusivity $(D_Y)_t$, the turbulent fluxes of energy and scalar property are given by:

$$-\rho \overline{u_i' e'} = \rho (\lambda_T)_t \nabla \bar{T}; \quad (4.88)$$

$$-\rho \overline{u_i' Y'} = \rho (D_Y)_t \nabla \bar{Y}. \quad (4.89)$$

Instead of solving supplementary equations to determine these turbulent quantities, CFD codes commonly relate them to the momentum mixing diffusivity such as:

$$(\lambda_T)_t = \frac{c_p \eta_t}{Pr_t}; \quad (4.90)$$

$$(D_Y)_t = \frac{\eta_t}{\rho(\sigma_Y)_t}. \quad (4.91)$$

In these expressions, Pr_t and $(\sigma_Y)_t$ are turbulent Prandtl and turbulent Schmidt numbers, respectively. Most of the time, these non-dimensional terms are assumed to be constant in time and space and equal for temperature and all other scalar properties. This assumption is very crude [139] but very attractive due to its simplicity.

A major flaw of these linear eddy viscosity models is that turbulence is by definition isotropic. Flows characterized by anisotropic turbulence such as impinging, swirl and curved flows cannot be exactly predicted. Therefore, intensive research is carried out to develop anisotropic eddy viscosity models [140].

Another modeling approach inside the RANS framework is the Reynolds Stress Model equations. Transport equations of the Reynolds stresses are solved [141]. Although this approach is very promising, the modeling of unknown terms arising in these equations is difficult and calibration of model constants is, until now, only achieved for specific flows and operational ranges.

In the next two sections, the turbulent eddy viscosity models which are used in this work are outlined.

4.2.2.1.1 Spalart-Allmaras model

The Spalart-Allmaras model [136] solves the transport equation of a modified form $\tilde{\nu}_t$ of the kinematic viscosity $\nu_t = \eta_t / \rho$. Both quantities, ν_t and $\tilde{\nu}_t$, are related by a damping function f_1 such as:

$$\nu_t = \tilde{\nu}_t f_1. \quad (4.92)$$

The damping function f_1 is defined as:

$$f_1 = \frac{\left(\frac{\nu_t}{\nu}\right)^3}{\left(\frac{\nu_t}{\nu}\right)^3 + C_{v1}^3}; \quad (4.93)$$

with C_{v1} being a model constant.

The transport equation of the modified viscosity $\tilde{\nu}_t$ reads

$$\frac{D\nu_t}{Dt} = G_{\nu_t} + \frac{1}{\sigma_{\nu_t}} \left[\frac{\partial}{\partial x_j} \left\{ (\nu + \nu_t) \frac{\partial \nu_t}{\partial x_j} \right\} + C_{b2} \left(\frac{\partial \nu_t}{\partial x_j} \right)^2 \right] - Y_{\nu_t}. \quad (4.94)$$

In eq. (4.94), G_{ν_t} and Y_{ν_t} represents the production and dissipation of $\tilde{\nu}_t$, respectively; and σ_{ν_t} and C_{b2} are two model constants. The production term is given by:

$$G_{\nu_t} = C_{b1} S \nu_t; \quad (4.95)$$

where C_{b1} is a model constant and S is:

$$S = S_\Omega + \frac{\nu_t}{\kappa^2 y_w^2} f_{v2}; \quad (4.96)$$

y_w being the distance to the wall, κ the Karman constant, f_{v2} is defined by:

$$f_{v2} = 1 - \frac{\left(\frac{\nu_t}{\nu}\right)}{1 + \left(\frac{\nu_t}{\nu}\right) f_1}; \quad (4.97)$$

and

$$S_\Omega = \sqrt{2\Omega_{ij}\Omega_{ij}}; \quad (4.98)$$

Ω_{ij} being the rotation tensor:

$$\Omega_{ij} = \frac{1}{2} \left(\frac{\partial u_i}{\partial x_j} - \frac{\partial u_j}{\partial x_i} \right). \quad (4.99)$$

The dissipation term is given by:

$$Y_{\nu_i} = C_{w1} f_w \left(\frac{\nu_i}{y_w} \right)^2; \quad (4.100)$$

with

$$f_w = g_{sp} \left[\frac{1 + (C_{w3})^6}{g_{sp}^6 + (C_{w3})^6} \right]^{\frac{1}{6}}; \quad (4.101)$$

$$g_{sp} = r_{sp} + C_{w2} (r_{sp}^6 - r_{sp}); \quad (4.102)$$

$$r_{sp} = \frac{\nu_i}{S \kappa^2 y_w^2}. \quad (4.103)$$

C_{w1} , C_{w2} , C_{w3} are other model constants.

Numerical values of the model constants are summarized in Table 4-1.

C_{b1}	C_{b2}	σ_{ν_i}	C_{w1}	C_{w2}	C_{w3}	$C_{\nu1}$	κ
0.1335	0.622	2/3	$\frac{C_{b1}}{\kappa^2} + \left(1 + \frac{C_{b2}}{\sigma_{\nu_i}} \right)$ (4.104)	0.3	2.0	7.1	0.41

Table 4-1: Numerical values of the model constants in the Spalart-Allmaras model [136].

4.2.2.1.2 $k-\omega$ SST model

Another eddy viscosity model is the $k-\omega$ SST model [142]. This two-equation model solves the transport equations of the turbulent kinetic energy k (eq. (4.109)) and the scaled specific dissipation rate $\omega = \varepsilon/\beta^* k$ (eq. (4.111)), with $\beta^* = 0.09$. The eddy viscosity is calculated with k and ω according to:

$$\eta_t = \rho \frac{\tilde{a}_1 k}{\max(\tilde{a}_1 \omega, 2S F_2)}; \quad (4.105)$$

where $\tilde{a}_1 = 0.31$ is a model constant, S is an invariant measure of the strain rate and F_2 a blending function defined as:

$$F_2 = \tanh(\arg_2^2); \quad (4.106)$$

with

$$\arg_2 = \max \left(2 \frac{\sqrt{k}}{0.09 \omega y_w}, \frac{500 \nu}{\omega y_w^2} \right); \quad (4.107)$$

y_w being the distance to the wall. In the framework of the $k-\omega$ SST model, the expression of the Reynolds stresses eq. (4.87) is replaced by:

$$-\rho \overline{u_i' u_j'} = \eta_t \left(\frac{\partial \bar{u}_i}{\partial x_j} + \frac{\partial \bar{u}_j}{\partial x_i} \right) - \rho \frac{2}{3} k \delta_{ij}. \quad (4.108)$$

The transport equation of the turbulent kinetic energy reads:

$$\frac{Dk}{Dt} = \underline{\underline{P}}_k - \beta^* k \omega + \frac{\partial}{\partial x_j} \left[(\nu + \sigma_k \nu_t) \frac{\partial k}{\partial x_j} \right]; \quad (4.109)$$

where $\underline{\underline{P}}_k$ is defined as:

$$\underline{\underline{P}}_k = \min \left(\tau_{ij} \frac{\partial \bar{u}_i}{\partial x_j}, 10 \beta^* k \omega \right); \quad (4.110)$$

and σ_k is a model constant. The transport equation of the specific dissipation rate is:

$$\frac{D\omega}{Dt} = 4\tilde{\alpha}S^2 - \tilde{\beta}\omega^2 + \frac{\partial}{\partial x_j} \left[(\nu + \sigma_\omega \nu_t) \frac{\partial \omega}{\partial x_j} \right]; \quad (4.111)$$

with $\tilde{\alpha}$, $\tilde{\beta}$, σ_ω being other model constants.

The $k-\omega$ SST model combines the advantages of two other two-equation eddy viscosity models, the $k-\varepsilon$ and the $k-\omega$ models. Its blends the coefficients $C_{k-\varepsilon} = \{\tilde{\alpha}_2, \tilde{\beta}_2, \sigma_{\omega 2}, \sigma_{k2}\}$ of the $k-\varepsilon$ away from the wall to those $C_{k-\omega} = \{\tilde{\alpha}_1, \tilde{\beta}_1, \sigma_{\omega 1}, \sigma_{k1}\}$ of the $k-\omega$ close to the wall with a blending function F_1 defined as:

$$F_1 = \tanh(\arg_1^4); \quad (4.112)$$

with

$$\arg_1 = \min \left[\max \left(\frac{\sqrt{k}}{0.09\omega y_w}, \frac{500\nu}{\omega y_w^2} \right), \frac{4\sigma_{\omega 2}k}{CD_{k\omega} y_w^2} \right]; \quad (4.113)$$

and

$$CD_{k\omega} = \max \left(\frac{2\rho}{\omega} \sigma_{\omega 2} \frac{\partial k}{\partial x_j} \frac{\partial \omega}{\partial x_j}, 10^{-20} \right); \quad (4.114)$$

Thus, the coefficients $C_{SST} = \{\tilde{\alpha}, \tilde{\beta}, \sigma_\omega, \sigma_k\}$ of the $k-\omega$ SST model are given by:

$$C_{SST} = F_1 C_{k-\omega} + (1 - F_1) C_{k-\varepsilon}. \quad (4.115)$$

Numerical values of the model constants are summarized in Table 4-2.

$\tilde{\alpha}_1$	$\tilde{\alpha}_2$	$\tilde{\beta}_1$	$\tilde{\beta}_2$	$\sigma_{\omega 1}$	$\sigma_{\omega 2}$	σ_{k1}	σ_{k2}
5/9	0.44	3/40	0.0828	0.5	0.856	0.85	1

Table 4-2: Numerical values of the model constants in the $k-\omega$ SST model [142].

4.2.2.2 Large eddy simulations

In large eddy simulations (LES), the governing equations are spatially filtered: only the turbulent fluctuations which are larger than the filter width are resolved. In general the filter width matches the grid size. It is possible to apply a supplementary (larger) spatial-filter if particular mathematical or physical properties of the filtering are desired (e.g. [143], [144]). Calculations using filtered equations are called LES since the large scales are resolved. This approach supposes that the cells are sufficiently small to resolve the large turbulent scales [37]. Hence, the computation cost is quite larger than in RANS.

Mathematically the spatial filtering supposes a filter function G positive definite with characteristic filter width Δ . The spatial filter of a function f is then defined as its convolution with G according to

$$\bar{f}(\mathbf{x}, t) = \int_{\Omega} G(\mathbf{x} - \mathbf{x}'; \Delta(\mathbf{x})) f(\mathbf{x}', t) d\mathbf{x}'; \quad (4.116)$$

where Ω is the entire flow domain. The variable f is decomposed into a filtered, also called unresolved or sub-grid, variable f' and a resolved variable \bar{f} .

The filtered governing equations have exactly the same form as equations (4.80) to (4.83); but the bar now denotes spatial-filtering instead of time-averaging. Therefore, fluxes (4.84) to (4.86) are also present in the filtered equations and must be modeled. In contrast to the RANS approach, however, they only represent the turbulent transport due to the sub-grid fluctuations. This is particularly advantageous since the effect of these sub-grid fluctuations on the momentum transport are easier to model than the effect of the larger scale fluctuations. Simple sub-grid scale models in the momentum equations suffice to find good agreement [145].

The monotone integrated large eddy simulation (MILES [146]) approach and the Smagorinsky-Lilly model [147] are two common approaches to model the turbulent fluxes. The Smagorinsky-Lilly model represents the effect of the turbulent fluctuations by a subgrid-scale viscosity η_{sgs} defined as:

$$\eta_{sgs} = \rho(C_s \Delta)^2 |\bar{S}|; \quad (4.117)$$

where

$$\Delta = (V_{cell})^{1/3}; \quad (4.118)$$

$$\bar{S} = \sqrt{2e_{ij}e_{ij}}; \quad (4.119)$$

and C_s is a model constant. In contrast, the MILES approach assumes that the numerical dissipation is sufficient to represent the subgrid-scale effects.

Similarly to eddy viscosity models, it commonly is assumed that enhanced scalar property mixing due to the turbulent fluctuations can be approximated by a gradient hypothesis. Introducing the positive sub-grid thermal conductivity $(\lambda_T)_{sgs}$ and mass diffusivity $(D_Y)_{sgs}$, the turbulent fluxes of energy and scalar property are given by:

$$-\rho \overline{u_i' e'} \equiv \rho (\lambda_T)_{sgs} \nabla \bar{T}; \quad (4.120)$$

$$-\rho \overline{u_i' Y'} \equiv \rho (D_Y)_{sgs} \nabla \bar{Y}. \quad (4.121)$$

Instead of solving supplementary equations to determine $(\lambda_T)_{sgs}$ and $(D_Y)_{sgs}$, CFD codes commonly relate them to the sub-grid scale viscosity such as:

$$(\lambda_T)_{sgs} = \frac{c_p \eta_{sgs}}{\text{Pr}_{sgs}}; \quad (4.122)$$

$$(D_Y)_{sgs} = \frac{\eta_{sgs}}{\rho (\sigma_Y)_{sgs}}. \quad (4.123)$$

In these expressions, Pr_{sgs} and $(\sigma_Y)_{sgs}$ are sub-grid Prandtl and Schmidt numbers, respectively. Most of the time, these variables are assumed to be constant in time and space and equal for temperature and all scalar properties. This assumption is crude but very attractive due to its simplicity.

Since only mean values are interesting for the design of engineering components, the results of a LES are ensemble-averaged at the end of the calculations. The ensemble-averaged mean value $\langle \varphi \rangle_N$ of any flow field φ , is computed according to:

$$\langle \varphi \rangle_N = \frac{1}{N} \sum_{i=1}^N \varphi^{(i)}; \quad (4.124)$$

where $\varphi^{(i)}$ is one realization of φ .

4.3 Modeling of two-phase flows

4.3.1 Definition and properties

As discussed in chap. *physics*, the determination of the position of the interface between the two phases is crucial to accurately predict mixture macroscopic behavior. This task is particularly challenging for two reasons: On one hand, the interfacial configuration is influenced by interfacial transfers, which, in turn, are impacted by the interfacial morphology. On the other hand, length and time scales of two-phase mixtures are very disparate. For instance in cavitating flows, nuclei size may be as small as (or even smaller than) a few micrometers whereas macroscopic manifestations such as cavitation sheets are also observed. Furthermore, the interface is liable to instabilities and, thus, strongly fluctuating in time and space.

Recalling the phase indicator P_k introduced in chap. *physics*, the goal of the numerical calculations is to specify this function in time and space. For very simple flow conditions and very simple geometries, the one-fluid method is designed to capture or track the interface in time and space (e.g. [148], [149]). In this framework, all structures are described by at least a few computational cells. This requirement has also consequences on the affordable time-step due to the Courant-Friedrichs-Lewy criterion (sect.

4.1). For industrial applications, the number of cells and the time of the calculations would be prohibitive – imagine at least 4 cells for each cavitation nuclei (Figure 4-9 left). As a consequence, all structures cannot be described: only scales which are sufficiently large can be resolved whereas the rest of the scales are ensemble-, volume- and/or time-averaged (Figure 4-9 right). The averaging elements (e.g. time) is assumed to be large enough to smooth out the local variations of the properties but sufficiently small in comparison to the characteristic variation (e.g. time constant of bulk flow unsteadiness).

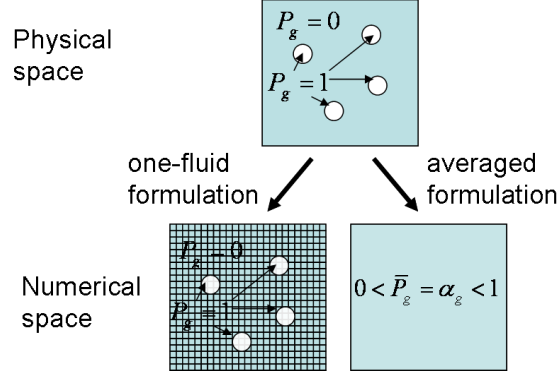


Figure 4-9: Illustration of one-fluid (bottom left) and averaged (bottom right) formulations of a dispersed flow (top): four gas bubbles (white) are dispersed in water (blue); numerical grid lines (solid lines).

In particular, the position of the interface, and thus the phase indicator P_k , is only known in averaged: \bar{P}_k , where the averaging operator $\bar{\cdot}$ represent time-, space- and/or ensemble-averaging. In this chapter, k is g for the gas phase and l for the liquid phase.

In the time-averaging framework, $\bar{P}_k(x_0)$ corresponds to the fraction of time spent by the phase k at the position x_0 during the averaging time; in the volume-averaging framework, $\bar{P}_k(t_0)$ represents the volume fraction occupied by phase k at time t_0 in the averaging volume; while $\bar{P}_k(x_0)$ is the probability of finding the phase k at the position x_0 in ensemble averaging.

\bar{P}_k commonly is called the “volume” fraction α_k of the phase k :

$$\bar{P}_k \equiv \alpha_k. \quad (4.125)$$

In this thesis, the void fraction α is the “volume” fraction of the gas phase:

$$\alpha \equiv \alpha_g. \quad (4.126)$$

More generally, for any function F associated with two-phase flows and assumed to be continuously differentiable everywhere except at the interface, a function F_k can be defined as:

$$F_k(x_0, t) = P_k(x_0, t) F \quad \begin{cases} = F(x_0, t) & \text{if } (x_0, t) \in k \\ = 0 & \text{if } (x_0, t) \notin k \end{cases}. \quad (4.127)$$

The average of the function F is \bar{F} . Using the phase density function P_k as a weighting function, the phase-average $\overline{\overline{F_k}}$ reads:

$$\overline{\overline{F_k}} \equiv \frac{\overline{P_k F_k}}{\overline{P_k}} = \frac{\bar{F}_k}{\alpha_k}. \quad (4.128)$$

A simple relation exists between average \bar{F} and phase-average quantities $\overline{\overline{F_k}}$

$$\bar{F} = \sum_{k=g}^l \bar{F}_k = \sum_{k=g}^l \alpha_k \overline{\overline{F_k}}. \quad (4.129)$$

The mass weighted mean value $\hat{\psi}$ and ψ_k of the variable per unit mass ψ are defined by:

$$\hat{\psi} = \frac{\overline{\rho \psi}}{\rho}; \quad (4.130)$$

and

$$\hat{\psi}_k = \frac{\overline{\rho_k \psi_k}}{\rho_k} = \frac{\overline{\overline{\rho_k \psi_k}}}{\overline{\rho_k}}. \quad (4.131)$$

From the definition of the mass weighted mean values, one has

$$\overline{\rho \psi} = \sum_{k=g}^l \overline{\rho_k \psi_k}; \quad (4.132)$$

so that

$$\hat{\psi} = \frac{\sum_{k=g}^l \alpha_k \overline{\rho \hat{\psi}_k}}{\sum_{k=g}^l \alpha_k \overline{\rho}} = \frac{\sum_{k=g}^l \overline{\rho_k} \hat{\psi}_k}{\sum_{k=g}^l \overline{\rho_k}}. \quad (4.133)$$

The fluctuating component can be uniquely defined such as:

$$F'_k \equiv F_k - \overline{\overline{F_k}}. \quad (4.134)$$

It obeys

$$\overline{\overline{F'_k}} = 0. \quad (4.135)$$

4.3.1.1 Governing equations

[150], [47] and [151] derived the averaged two-phase flow governing equations for time-, space-, and phase-averaging. All averaged equations have a very similar structure. Only the physical interpretation of the unresolved terms appearing in these equations differs. The time-averaging formulation [150] will be presented below.

Mass balance

$$\frac{\partial \overline{\alpha_k \rho_k}}{\partial t} + \nabla \cdot (\overline{\alpha_k \rho_k \hat{\mathbf{u}}_k}) = \dot{m}_k, \quad k = g \dots l; \quad (4.136)$$

with

$$\dot{m}_k = -\frac{1}{\Delta t} \sum_j \left\{ \frac{1}{u_{ni}} \mathbf{n}_k \cdot \rho_k (\mathbf{u}_k - \mathbf{u}_i) \right\}; \quad (4.137)$$

and

$$\sum_{k=g}^l \dot{m}_k = 0. \quad (4.138)$$

Momentum balance

$$\frac{\partial \overline{\alpha_k \rho_k \hat{\mathbf{u}}_k}}{\partial t} + \nabla \cdot (\overline{\alpha_k \rho_k \hat{\mathbf{u}}_k \hat{\mathbf{u}}_k}) = -\nabla (\overline{\alpha_k p_k}) + \nabla \cdot [\overline{\alpha_k (\mathbf{T}_k + \mathbf{T}_k^T)}] + \overline{\alpha_k \rho_k \hat{\mathbf{F}}_k} + \mathbf{M}_k, \quad k = g \dots l; \quad (4.139)$$

with

$$\mathbf{M}_k = -\frac{1}{\Delta t} \sum_j \left\{ \frac{1}{u_{ni}} \mathbf{n}_k \cdot [\rho_k (\mathbf{u}_k - \mathbf{u}_i) \mathbf{u}_k - \mathbf{T}_k] \right\}; \quad (4.140)$$

$$\mathbf{M}_m = \frac{1}{\Delta t} \sum_j \left\{ \frac{1}{u_{ni}} (2H\sigma \mathbf{n}_g + \nabla_s \sigma) \right\}; \quad (4.141)$$

$$\mathbf{T}_k^T = -\overline{\overline{\rho_k \mathbf{u}'_k \mathbf{u}'_k}}; \quad (4.142)$$

and

$$\sum_{k=g}^l \mathbf{M}_k - \mathbf{M}_m = 0. \quad (4.143)$$

Energy balance

$$\frac{\partial}{\partial t} \left[\overline{\alpha_k \rho_k \left(\hat{e}_k + \frac{\hat{\mathbf{u}}_k^2}{2} \right)} \right] + \nabla \cdot \left(\overline{\alpha_k \rho_k \left(\hat{e}_k + \frac{\hat{\mathbf{u}}_k^2}{2} \right) \hat{\mathbf{u}}_k} \right) = -\nabla \cdot [\overline{\alpha_k (\mathbf{q}_k + \mathbf{q}_k^T)}] + \nabla (\overline{\alpha_k \mathbf{T}_k \cdot \hat{\mathbf{u}}_k}) + \overline{\alpha_k \rho_k \hat{\mathbf{F}}_k \cdot \hat{\mathbf{u}}_k} + S_{Q,k}, \quad k = g \dots l; \quad (4.144)$$

with

$$S_{Q,k} = -\frac{1}{\Delta t} \sum_j \left\{ \frac{1}{u_{ni}} \mathbf{n}_k \cdot \left[\rho_k (\mathbf{u}_k - \mathbf{u}_i) \left(e_k + \frac{\mathbf{u}_k^2}{2} \right) - \mathbf{T}_k \cdot \mathbf{u}_k + \mathbf{q}_k \right] \right\}; \quad (4.145)$$

$$S_{Q,m} = \frac{1}{\Delta t} \sum_j \left\{ \frac{1}{u_{ni}} \left[(2H\sigma \mathbf{n}_g + \nabla_s \sigma) \cdot \mathbf{u}_i \right] \right\}; \quad (4.146)$$

$$\mathbf{q}_k^T = \rho_k \left(e_k + \frac{\mathbf{u}_k^2}{2} \right) \mathbf{u}'_k - \overline{\mathbf{T}_k \cdot \mathbf{u}'_k} + p_k \cdot \mathbf{u}'_k; \quad (4.147)$$

$$\hat{e}_k \equiv \hat{e}_k + \frac{(\mathbf{v}'_k)^2}{2}; \quad (4.148)$$

and

$$\sum_{k=g}^l S_{Q,k} - S_{Q,m} = 0. \quad (4.149)$$

In these expressions, u_{ni} is the normal velocity of the interface:

$$u_{ni} = \mathbf{u}_i \cdot \mathbf{n}; \quad (4.150)$$

where \mathbf{n} is the interface normal and \mathbf{u}_i is the velocity of the interface.

In the time-averaging framework, the instantaneous equations are averaged over the time Δt . During Δt , the gas-liquid interface passes a certain number of time at the location x_0 under consideration. The index of summation j in eq. (4.137), (4.140), (4.141), (4.145) and (4.146) represents the j -th passage of the interface at the location x_0 during the averaging time. \dot{m}_k , \mathbf{M}_k , \mathbf{M}_m , $S_{Q,k}$ and $S_{Q,m}$ result from the presence of the interface within the averaging time. \dot{m}_k represent the interfacial mass transfer; \mathbf{M}_k and \mathbf{M}_m are the momentum sources; and $S_{Q,k}$ and $S_{Q,m}$ are energy sources. \mathbf{T}_k^T and \mathbf{q}_k^T represent the statistical effect of two-phase and turbulent fluctuations on resolved momentum and specific total energy.

4.3.1.2 Constitutive equations

The averaging of the fluctuations has not only an impact on the conservation equations but also on the constitutive equations. [150] proposes following expressions.

The mass fraction Y_k of the phase k is given by

$$Y_k \equiv \frac{\overline{\rho_k}}{\rho} = \frac{\overline{\alpha_k \rho_k}}{\overline{\alpha_g \rho_g + \alpha_l \rho_l}} = \frac{\overline{\alpha_k \rho_k}}{\rho_m}; \quad (4.151)$$

with

$$\rho_m = \sum_{k=g}^l \overline{\alpha_k \rho_k}. \quad (4.152)$$

The mixture energy is given by:

$$e_m = \frac{\sum_{k=g}^l \overline{\alpha_k \rho_k \hat{e}_k}}{\rho_m} = \sum_{k=g}^l Y_k \hat{e}_k. \quad (4.153)$$

The mixture molecular diffusion flux $\overline{\mathbf{J}}$ can be defined as

$$\overline{\mathbf{J}} = \sum_{k=g}^l \overline{\alpha_k \mathbf{J}_k}. \quad (4.154)$$

In eq. (4.154) $\mathbf{J}_k = -\mathbf{T}_k$ is the momentum molecular flux; and $\mathbf{J}_k = \mathbf{q}_k - \mathbf{T}_k \cdot \mathbf{u}_k$ is the heat molecular flux.

The mixture mass center of velocity can be defined as:

$$\mathbf{u}_m = \frac{\sum_{k=g}^l \overline{\alpha_k \rho_k \hat{\mathbf{u}}_k}}{\rho_m} = \sum_{k=g}^l Y_k \hat{\mathbf{u}}_k; \quad (4.155)$$

and the mixture pressure as:

$$p_m = \sum_{k=g}^l \overline{\alpha_k p_k}. \quad (4.156)$$

4.3.1.3 Equation of state

[150] also derived the averaged equation of state corresponding to the specific internal energy

$$e_k = e_k(s_k, \rho_k).$$

They indicate that, in general, a simple equation of state in terms of averaged quantities does not exist because the relation between specific internal energy \hat{e}_k , entropy \hat{s}_k and density $\bar{\rho}_k$ is impacted by the effects of the fluctuations and by the interfacial transfers. This last element had already been mentioned for the determination of the speed of sound in a bubbly mixture in chap. *physics*.

4.3.1.4 Modeling of two-phase flows

\dot{m}_k , \mathbf{M}_k , \mathbf{M}_m , $S_{Q,k}$, $S_{Q,m}$, \mathbf{T}_k^T and \mathbf{q}_k^T arise from the averaging of the two-phase governing equations. These terms are expressed exactly in terms of local and instantaneous quantities. These local and instantaneous quantities are not available. Models with averaged quantities are required to represent \dot{m}_k , \mathbf{M}_k , \mathbf{M}_m , $S_{Q,k}$, $S_{Q,m}$, \mathbf{T}_k^T and \mathbf{q}_k^T . The modeling of most of these terms is very complicated. When algebraic expressions fail to satisfyingly represent interfacial and fluctuation effect, supplementary transport equations, such as particles number density transport equation [150], may be introduced in the calculation.

An alternative approach consists in considering both phases to be a continuum instead of two-interpenetrating phases. In this framework, only the three conservation equations of the mixture and the continuity equation of the gas phase need to be solved. Many, but not all, interfacial terms cancel out. This is the drift-flux model. Further assumptions on the tight-coupling of the phases, such as mechanical, thermal and thermodynamic equilibrium, reduce the drift-flux model to the homogeneous model.

4.3.2 System codes

In system codes, the equations are averaged over large computational cells. The terms arising from this averaging are extremely difficult to model. Indeed, the effect of many scales have to be modeled and the large scales are usually more difficult to characterize [152]. Therefore, in system codes, the modeling of the unresolved terms would be far too complicate and the strategy is rather phenomenological. This strategy consists in solving averaged equations whose left-hand side remains identical to eq. (4.136), (4.139) and (4.144), but equations right-hand side only incorporates ad-hoc models based on physical sounding but principally tuned to fit experimental results.

4.3.2.1 6-equations model

The most sophisticated two-phase flow modeling in commercial system codes is the 6-equation model. The phases are interpenetrating (Figure 4-10). The conservation equations of both phases are solved.

Mass conservation equations:

Gas phase

$$\frac{\partial}{\partial t} A_g \rho_g + \frac{\partial}{\partial z} \dot{M}_g = \dot{m}_g A. \quad (4.157)$$

Liquid phase

$$\frac{\partial}{\partial t} A_l \rho_l + \frac{\partial}{\partial z} \dot{M}_l = \dot{m}_l A. \quad (4.158)$$

Momentum conservation equations:

Gas phase:

$$\frac{\partial}{\partial t} \dot{M}_g + \frac{\partial}{\partial z} \frac{\dot{M}_g^2}{A_g \rho_g} = -A_g \frac{\partial}{\partial z} p_g + P_i \tau_{ig} - P_g \tau_{wg} - A_g g \rho_g \sin \varphi_g + \dot{m}_g A u_i; \quad (4.159)$$

Liquid phase:

$$\frac{\partial}{\partial t} \dot{M}_l + \frac{\partial}{\partial z} \frac{\dot{M}_l^2}{A_l \rho_l} = -A_l \frac{\partial}{\partial z} p_l + P_i \tau_{il} - P_l \tau_{wl} - A_l g \rho_l \sin \varphi_g + \dot{m}_l A u_i. \quad (4.160)$$

Energy conservation equations:

Gas phase:

$$\frac{\partial}{\partial t} A_g \rho_g E_g + \frac{\partial}{\partial z} \dot{M}_g E_g = - \frac{\partial}{\partial z} \frac{\dot{M}_g}{\rho_g} p_g - P_g \frac{\dot{M}_g}{A_g \rho_g} \tau_{wg} + P_g q_{wg} + P_i q_{ig} + A_g \rho_g Q + \dot{m}_g A l ; \quad (4.161)$$

Liquid phase:

$$\frac{\partial}{\partial t} A_l \rho_l E_l + \frac{\partial}{\partial z} \dot{M}_l E_l = - \frac{\partial}{\partial z} \frac{\dot{M}_l}{\rho_l} p_l - P_l \frac{\dot{M}_l}{A_l \rho_l} \tau_{wl} + P_l q_{wl} + P_i q_{il} + A_l \rho_l Q + \dot{m}_l A l . \quad (4.162)$$

In these equations, u_i is the interfacial velocity; τ_{ig} and τ_{il} the shear stresses in the gas and liquid phase at the interface; P_g and P_l the perimeter of the pipe in contact with the gas and liquid phase, respectively; l the specific latent heat; p_g and p_l the pressure in the gas phase and liquid phase, respectively; q_{wg} and q_{wl} the heat flux in the gas phase and liquid phase at the wall, respectively; P_i the interfacial perimeter; and q_{ig} and q_{il} the heat flux in the gas phase and liquid phase at the interface, respectively (see Figure 4-10).

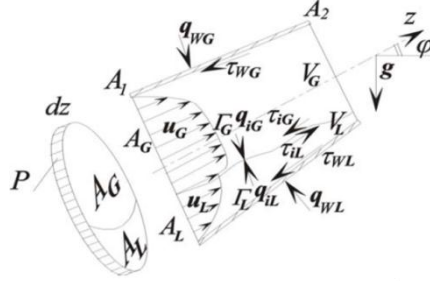


Figure 4-10: Flow variables and geometrical parameters introduced in the 6-equation model [51].

The flow variables appearing in these equations satisfy the following relations:

$$\alpha_g \equiv \alpha = \frac{A_g}{A} ; \quad (4.163)$$

$$1 - \alpha = \frac{A_l}{A} ; \quad (4.164)$$

$$Y = \frac{\dot{M}_g}{\dot{M}} ; \quad (4.165)$$

$$1 - Y = \frac{\dot{M}_l}{\dot{M}} ; \quad (4.166)$$

$$\dot{m}_g + \dot{m}_l = 0 ; \quad (4.167)$$

$$\tau_{ig} + \tau_{il} = 0 ; \quad (4.168)$$

$$P_g + P_l = P . \quad (4.169)$$

For a given geometry, A , P and φ_g are known and it is commonly assumed that both phases share the same pressure $p = p_g = p_l$. The densities are updated as a function of the pressure and enthalpies. Equations (4.157) to (4.162) are solved to obtain the temporal evolution of the longitudinal repartition of $\dot{M}(z)$, $p(z)$, $Y(z)$, $\alpha(z)$, $E_g(z)$ and $E_l(z)$. Empirical correlations are required for the unknown quantities \dot{m}_g , τ_{ig} , τ_{wg} , τ_{wl} , q_{ig} , q_{wg} , q_{wl} , P_g and P_l .

For instance, the correlation (4.68) is still valid for τ_{wg} or τ_{wl} . One correlation for the shear stress in the gas phase at the interface τ_{ig} can be expressed as:

$$F_i = \frac{\tau_{ig} P_i}{A} = R_F F_{is} + (1 - R_F) \left[(1 - E) \{ (1 - \alpha) F_{ib} + \alpha F_{ia} \} + E F_{id} \right] . \quad (4.170)$$

The coefficients R_F , F_{ia} , F_{ib} , F_{id} and F_{is} are functions of the flow regime (annular, droplet, bubbly flow) and complex function of velocity, void fraction, gravity, surface tension, etc. [153], [154].

Thermal non-equilibrium is accounted for with empirical correlations for q_{ig} and q_{il} . Finally the gas mass conservation equation is usually introduced to represent the thermodynamic non-equilibrium of the mixture:

$$\frac{\partial}{\partial t}(\alpha \rho_g) + \frac{1}{A} \frac{\partial}{\partial z}(\alpha A \rho_g u_m) + \frac{1}{A} \frac{\partial}{\partial z} \left(\alpha A \frac{\rho_g \rho_l}{\rho_m} U_{gj} \right) = \dot{m}_g. \quad (4.182)$$

A correlation for \dot{m}_g must be provided. Other empirical correlations are supplied for the unknown quantities τ_{vm} and q_w . For a given geometry, A , P and φ are known. Equations (4.171) to (4.182) are solved to obtain the temporal evolution of the longitudinal repartition of $\dot{M}(z)$, $p(z)$, $h_m(z)$ and $Y(z)$.

Although velocity and temperature differences are supplied externally, this formulation has two advantages in comparison to the 6-equation model:

- 1 - Fewer interfacial terms have to be modeled thereby reducing the risk of inaccurate modeling;
- 2 - The system of equations is more stable [64].

4.3.2.3 Homogeneous model

Assumptions of mixture thermal and mechanical equilibrium can further simplify the system of equations without losing much accuracy for bubbly or droplet flows, when the dispersed phase is finely dispersed. In that case, both phases share the same temperature and the same velocity: q_{ig} and q_{il} are identically zero and the drift velocity vanishes.

When the mass transfer is assumed to occur infinitely fast in comparison to the characteristic residence time of a fluid particle, no equation for the gas phase (4.182) is required. Y can be derived from available thermodynamic quantities (e.g. $p(z)$ and mixture enthalpy h_m). This model is called the homogeneous model. Under these assumptions, the void fraction α is obtained by:

$$\alpha = \left(1 + \frac{1-Y}{Y} \frac{\rho_g}{\rho_l} \right)^{-1}; \quad (4.183)$$

the homogeneous densities introduced in section 4.3.2.1 are equal:

$$\rho_m = \rho_l \equiv \rho_H; \quad (4.184)$$

and the conservation equations become:

Mass conservation equation:

$$\frac{\partial}{\partial t} \rho_H + \frac{1}{A} \frac{\partial}{\partial z} \dot{M} = 0. \quad (4.185)$$

Momentum conservation equation:

$$\frac{1}{A} \frac{\partial}{\partial t} \dot{M} + \frac{1}{A} \frac{\partial}{\partial z} \frac{\dot{M}^2}{A \rho_H} = - \frac{\partial p}{\partial z} - \frac{P \tau_{vm}}{A} - g \rho_H \sin \varphi. \quad (4.186)$$

Energy conservation equation:

$$\frac{\partial}{\partial t} (h_m) + \frac{1}{A} \frac{\partial}{\partial z} \dot{M} h_m = \frac{\partial p}{\partial t} + \frac{P q_w}{A} + \rho_H Q. \quad (4.187)$$

Correlations such as presented in sect. 4.2.1 are available to model τ_{vm} .

4.3.2.4 Particles density conservation equation

Two-phase flow governing equations derived until now (e.g. eq. (4.157) to (4.162)) account for the transport mechanisms of mass, momentum and energy. Unfortunately, they give no direct information on the structure of the two-phase flow. In most codes, the flow structure is estimated according to flow maps. Some other codes introduce supplementary transport equations for this purpose. Typically, codes dedicated to applications where one phase can be considered to be dispersed in the other continuous phase (e.g. flashing [155]) solve a transport equation of the number density n of dispersed particles (Figure 4-12).

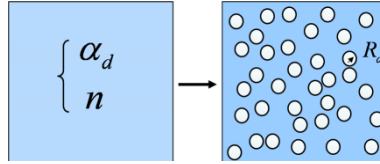


Figure 4-12: Representation of one computational cell in a two-phase flow simulation with transport equations of the volume fraction α_d and the number n_d of particles. The evaluation of the particle radius R_d , and thus of mass, momentum and heat transfers, is eased.

Knowledge on the number density n is advantageous because the radius R_d of the particles assumed to be spherical is related to n and the volume fraction α_d of the dispersed phase as follows:

$$R_d = \left(\frac{3\alpha_d}{4\pi n} \right)^{1/3}. \quad (4.188)$$

In flows with dispersed particles, all processes (forces, mass and heat exchange) are related to R_d . Thus, they can be much better described within this approach. For example, the drag force acting on one particle is (see chapter *cavitation*):

$$\mathbf{F}_D = \frac{1}{2} C_D \rho_c \pi R_d^2 (\mathbf{u}_c - \mathbf{u}_d) |\mathbf{u}_c - \mathbf{u}_d|. \quad (4.189)$$

The drag force \mathbf{f}_d acting on the dispersed phase per unit volume is then exactly (under the aforementioned assumptions):

$$\mathbf{f}_d = \frac{n}{2} C_D \rho_c \pi R_d^2 (\mathbf{u}_c - \mathbf{u}_d) |\mathbf{u}_c - \mathbf{u}_d|. \quad (4.190)$$

The conservation equation of n is derived from the conservation equation of the cavity distribution function introduced in chap. *cavitation* by integration over all particles sizes, velocities and temperatures and averaging over the computational cell. One phenomenological formulation of the conservation equation of n reads [156]:

$$\frac{\partial n}{\partial t} + \frac{1}{A} \frac{\partial}{\partial z} (n u_d A) = S_{wn} + S_{bn}. \quad (4.191)$$

In eq. (4.191), S_{wn} and S_{bn} represent the activation of the particles at the wall and in the bulk, respectively; and u_d is the velocity of the dispersed phase. Correlations for S_{wn} and S_{bn} can be found e.g. in [155], [45], [157] or [158].

4.3.3 CFD codes

In contrast to system codes, CFD codes are able to capture three dimensional effects. The terms to be modeled are directly derived from the averaging operation (see equations (4.136) to (4.144)) rather than obtained from pure phenomenological considerations. However the different approaches in CFD codes are basically the same as encountered in system codes: the 6-equation model, also called interpenetrating media formulation, is the most sophisticated model, the homogeneous model where the phases are assumed to be in equilibrium the simplest one and the drift flux model is situated in between. In this thesis, only the drift flux model is used. Thus the description restricts to the drift flux formulation in CFD codes. The readers can refer to [150], [47] for more information about the other formulations.

Similarly to system codes which include particles number density conservation equation, CFD codes can handle supplementary transport equations to describe the interfacial structure (e.g. in section 4.3.3.2). Approaches found in the literature to describe the polydispersity of the particles such as multi-group, presumed-pdf and direct quadrature method of moments are described later in section 4.5.

4.3.3.1 Drift flux model

An approximate formulation of the 6-equation model (equations (4.136) to (4.144)) consists in considering the two phases to be a continuum. The conservation equations of this continuum are obtained by summing mass, momentum and energy equations of both phases: the system of equations (4.136) to (4.144) reduces to the governing equations of the mixture:

Mixture continuity equation

$$\frac{\partial \rho_m}{\partial t} + \nabla \cdot (\rho_m \mathbf{u}_m) = 0. \quad (4.192)$$

Mixture momentum equation

$$\frac{\partial \rho_m \mathbf{u}_m}{\partial t} + \nabla \cdot (\rho_m \mathbf{u}_m \mathbf{u}_m) = -\nabla p_m + \nabla \cdot (\bar{\mathbf{T}} + \mathbf{T}^T + \mathbf{T}^D) + \rho_m \mathbf{F}_m + \mathbf{M}_m. \quad (4.193)$$

Mixture total energy equation

$$\begin{aligned} \frac{\partial}{\partial t} \left[\rho_m \left(e_m + \left(\frac{\mathbf{u}^2}{2} \right)_m \right) \right] + \nabla \cdot \left(\rho_m \left(e_m + \left(\frac{\mathbf{u}^2}{2} \right)_m \right) \mathbf{u}_m \right) = -\nabla \cdot (\bar{\mathbf{q}} + \mathbf{q}^T + \mathbf{q}^D) \\ -\nabla \cdot (p_m \mathbf{u}_m) + \nabla \cdot (\bar{\mathbf{T}} \cdot \mathbf{u}_m) + \rho_m \mathbf{F}_m \cdot \mathbf{u}_m + S_{Q,m}. \end{aligned} \quad (4.194)$$

To account for the thermodynamic non-equilibrium, the gas continuity equation is solved:

$$\frac{\partial \alpha \bar{\rho}_g}{\partial t} + \nabla \cdot (\alpha \bar{\rho}_g \mathbf{u}_m) = \dot{m}_g - \nabla \cdot (\alpha \bar{\rho}_g \mathbf{U}_{gm}). \quad (4.195)$$

The terms arising in these equations are defined as:

$$\dot{m}_g = -\frac{1}{\Delta t} \sum_j \left\{ \frac{1}{u_{ni}} \mathbf{n}_g \cdot \rho_g (\mathbf{u}_g - \mathbf{u}_i) \right\}; \quad (4.196)$$

$$S_{Q,m} = \frac{1}{\Delta t} \sum_j \left\{ \frac{1}{u_{ni}} \left[(2H\sigma \mathbf{n}_g + \nabla_s \sigma) \cdot \mathbf{u}_i \right] \right\}; \quad (4.197)$$

$$\mathbf{u}_m = \frac{\sum_{k=g}^l \alpha_k \bar{\rho}_k \hat{\mathbf{u}}_k}{\rho_m}; \quad (4.198)$$

$$p_m = \sum_{k=g}^l \alpha_k \bar{p}_k; \quad (4.199)$$

$$\bar{\mathbf{T}} = \sum_{k=g}^l \alpha_k \bar{\mathbf{T}}_k; \quad (4.200)$$

$$\mathbf{T}^T = -\sum_{k=g}^l \alpha_k \overline{\overline{\rho_k \mathbf{u}'_k \mathbf{u}'_k}}; \quad (4.201)$$

$$\mathbf{T}^D = -\sum_{k=g}^l \alpha_k \bar{\rho}_k \mathbf{U}_{km} \mathbf{U}_{km}; \quad (4.202)$$

$$\mathbf{F}_m = \frac{\sum_{k=g}^l \alpha_k \bar{\rho}_k \mathbf{F}_k}{\rho_m}; \quad (4.203)$$

$$\mathbf{M}_m = \frac{1}{\Delta t} \sum_j \left\{ \frac{1}{u_{ni}} (2H\sigma \mathbf{n}_g + \nabla_s \sigma) \right\}; \quad (4.204)$$

$$\bar{\mathbf{q}} = \sum_{k=g}^l \alpha_k \bar{\mathbf{q}}_k; \quad (4.205)$$

$$\mathbf{q}^T = \sum_{k=g}^l \alpha_k \left\{ \overline{\overline{\rho_k \left(e_k + \frac{\mathbf{u}_k^2}{2} \right) \mathbf{u}'_k - \bar{\mathbf{T}}_k \cdot \mathbf{u}'_k}} \right\}; \quad (4.206)$$

$$\mathbf{q}^D = \sum_{k=g}^l \alpha_k \left\{ \bar{\rho}_k \left(\hat{e}_k + \frac{\hat{\mathbf{u}}_k^2}{2} \right) \mathbf{U}_{km} - \bar{\mathbf{T}}_k \cdot \mathbf{U}_{km} \right\}; \quad (4.207)$$

$$e_m = \frac{\sum_{k=g}^l \alpha_k \bar{\rho}_k \left(\hat{e}_k + \frac{\hat{\mathbf{u}}_k^2}{2} \right)}{\rho_m}; \quad (4.208)$$

$$\left(\frac{\mathbf{u}^2}{2}\right)_m = \frac{\mathbf{u}_m^2}{2} + \frac{\sum_{k=g}^l \alpha_k \rho_k \frac{\mathbf{U}_{km}^2}{2}}{\rho_m}. \quad (4.209)$$

If the surface tension effect are neglected, \mathbf{M}_m vanishes and there is no direct interfacial terms in the mixture momentum equation. Considering a constant body force, we have:

$$\mathbf{F}_k = \hat{\mathbf{F}}_k = \mathbf{F}_m = \mathbf{F}. \quad (4.210)$$

The diffusion velocity of each phase \mathbf{U}_{km} is the relative velocity with respect to the mass center of the mixture:

$$\mathbf{U}_{km} = \mathbf{u}_k - \mathbf{u}_m. \quad (4.211)$$

In similarity to system codes (eq. (4.177)), a constitutive relation for $\mathbf{u}_i - \mathbf{u}_g$ must be provided.

The terms \mathbf{T}^D and \mathbf{q}^D arise from the fluctuation of the interface about the mean [150].

For the modeling of the different terms, the reader can refer to [150]. A simplified form of these equations is obtained when the mechanical and thermal non-equilibrium, gravity and the surface tension are supposed negligible. In this case, the system of equation reduces to:

Mixture continuity equation

$$\frac{\partial \rho_m}{\partial t} + \nabla \cdot (\rho_m \mathbf{u}_m) = 0. \quad (4.212)$$

Mixture momentum equation

$$\frac{\partial \rho_m \mathbf{u}_m}{\partial t} + \nabla \cdot (\rho_m \mathbf{u}_m \mathbf{u}_m) = -\nabla p_m + \nabla \cdot (\bar{\mathbf{T}} + \mathbf{T}^T) + \rho_m \mathbf{F}_m. \quad (4.213)$$

Mixture total energy equation

$$\frac{\partial}{\partial t} \left[\rho_m \left(e_m + \frac{\mathbf{u}_m^2}{2} \right) \right] + \nabla \cdot \left(\rho_m \left(e_m + \frac{\mathbf{u}_m^2}{2} \right) \mathbf{u}_m \right) = -\nabla \cdot (p_m \mathbf{u}_m) + \nabla \cdot (\bar{\mathbf{T}} \cdot \mathbf{u}_m). \quad (4.214)$$

Both phases commonly share the same pressure. To account for the thermodynamic non-equilibrium, the gas continuity equation is solved:

$$\frac{\partial \alpha \rho_g}{\partial t} + \nabla \cdot (\alpha \rho_g \mathbf{u}_m) = \dot{m}_g. \quad (4.215)$$

Constitutive properties of the mixture must also be modeled. [150] proposes for the mixture viscosity

$$\eta_m = \alpha \eta_g + (1 - \alpha) \eta_l. \quad (4.216)$$

Other models for the mixture viscosity exist such as [159]:

$$\eta_m = \alpha \eta_g + (1 - \alpha)(1 + 2.5\alpha) \eta_l. \quad (4.217)$$

4.3.3.2 Particles density transport equations

Knowledge on the two-phase flow structure enables to describe more accurately the interfacial mass, momentum and heat transfers. Similarly to system codes, CFD codes introduce supplementary transport equations for this purpose. Most of the available formulations rely on the particle density distribution $f^\phi(t, \mathbf{x}, \phi, \mathbf{u}_d, T_d)$ already introduced in chap. *cavitation* where the subscript d represents here the dispersed phase. Except with Lagrange techniques (see sect. 4.6.1), it is common to utilize a marginal particle density distribution $f'(t, \mathbf{x}, \phi)$ integrated over all velocities and temperatures:

$$f'(t, \mathbf{x}, \phi) = \iint_{\mathbf{u}_d, T_d} f^\phi(t, \mathbf{x}, \phi, \mathbf{u}_d, T_d) d\mathbf{u}_d dT_d; \quad (4.218)$$

and to introduce averaged velocities $\bar{\mathbf{u}}_d = \mathbf{u}_m$ and temperatures $\bar{T}_d = T_m$.

Basically the governing equation of the marginal particle density distribution exists in two forms depending on the interpretation of the dispersed particles. If the particles represent the entire particle population, $f'(t, \mathbf{x}, \phi)$ is governed by:

$$\frac{\partial f'}{\partial t} + \frac{\partial(\mathbf{u}_m f')}{\partial \mathbf{x}} + \frac{\partial(\dot{R}_\phi f')}{\partial \phi} = \dot{S}'_{break} + \dot{S}'_{coal}; \quad (4.219)$$

where break-up

$$\dot{S}'_{break}(t, \mathbf{x}, \phi, f') = \iint_{\mathbf{u}_d, T_d} \dot{S}_{break}(t, \mathbf{x}, \phi, \mathbf{u}_d, T_d, f^\phi) d\mathbf{u}_d dT_d$$

and coalescence

$$\dot{S}'_{coal}(t, \mathbf{x}, \phi, f') = \iint_{u_d, T_d} \dot{S}'_{coal}(t, \mathbf{x}, \phi, \mathbf{u}_d, T_d, f') d\mathbf{u}_d dT_d$$

contribute to the modification of the particles distribution.

In contrast, if the particles represent the “activated” particles, it is necessary to incorporate another source term $\dot{S}'_{ph}(t, \mathbf{x}, \phi, f')$ in the particle density number equation to account for nuclei activation:

$$\frac{\partial f'}{\partial t} + \frac{\partial(\mathbf{u}_m f')}{\partial \mathbf{x}} + \frac{\partial(\dot{R}_\phi f')}{\partial \phi} = \dot{S}'_{break} + \dot{S}'_{coal} + \dot{S}'_{ph} \quad (4.220)$$

Taking $\phi = V$ and integrating equation (4.219) or (4.220) over all bubble size, the particles number density transport equation can also be introduced in CFD codes:

$$\frac{\partial n}{\partial t} + \nabla \cdot (n \mathbf{u}_{pm}) = \int_{V_{min}}^{V_{max}} (\dot{S}'_{break} + \dot{S}'_{coal}) dV ; \quad (4.221)$$

or

$$\frac{\partial n}{\partial t} + \nabla \cdot (n \mathbf{u}_{pm}) = \int_{V_{min}}^{V_{max}} (\dot{S}'_{break} + \dot{S}'_{coal} + \dot{S}'_{ph}) dV ; \quad (4.222)$$

where

$$n(\mathbf{x}, t) = \int_{V_{min}}^{V_{max}} f'(t, \mathbf{x}, V) dV ; \quad (4.223)$$

and \mathbf{u}_{pm} is the average local particle velocity weighted by the particle number. \mathbf{u}_{pm} is defined as:

$$\mathbf{u}_{pm}(\mathbf{x}, t) \equiv \frac{\int_{V_{min}}^{V_{max}} f'(t, \mathbf{x}, V) \mathbf{u}_m(t, \mathbf{x}, V) dV}{\int_{V_{min}}^{V_{max}} f'(t, \mathbf{x}, V) dV} \quad (4.224)$$

The modeling of the source terms \dot{S}'_{break} , \dot{S}'_{coal} and \dot{S}'_{ph} is simplified by assuming particular flow conditions and processes (e.g. coalescence and break-up are binary processes [150]).

4.4 Modeling of critical two-phase mass flux

In nuclear and chemical reactor safety, the accurate prediction of the leakage mass flow rate through pipes and breaks is crucial. Despite numerous experimental and theoretical analyses, the modeling and estimation of this leakage mass flow rate is still challenging. No model exists for complex geometries and uncertainties remain, such as non-equilibrium effects. However, some models show good agreement with experimental data for specific geometries and fluid properties.

For example,

- the Bernoulli model is adapted for the prediction of the mass flux in short geometries with very strongly subcooled coolant;
- the homogeneous equilibrium model (HEM) is accurate to calculate the mass flow rate in long geometries;
- the “Henry and Fauske” model gives satisfying agreement with experimental results for short geometries and moderately subcooled or saturated coolant.

In this description, the geometries are pipes or breaks. They are said to be long when the ratio between their length L and the diameter D of their smallest cross section is larger than 20 or 30. Another geometrical parameter entering the critical mass flux models usually is the single-phase pressure loss ζ .

Figure 4-13 represents the parameters involved in the calculation of the mass flux in pipes and breaks.

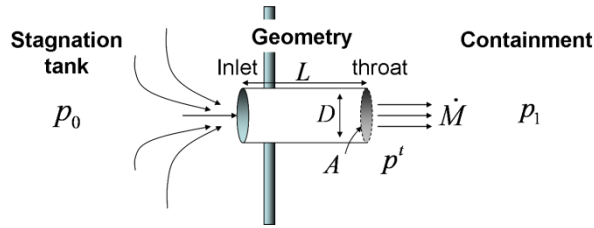


Figure 4-13: Representation of the parameters involved in the calculation of the mass flux in pipes and breaks.

Basically, the task of the model is to determine the mass flow rate \dot{M} leaving the pressure vessel given a stagnation pressure p_0 , a backpressure p_1 and thermodynamic properties such as temperature and vapor content. Most models disregard the influence of the cross section A of the geometry upon the mass flux G_c defined as:

$$G_c \equiv \frac{\dot{M}}{A}. \quad (4.225)$$

Thus, the model calculates the mass flux G_c and \dot{M} is obtained from G_c according to (4.225).

When the flow is critical, the pressure p' at geometry's throat is independent of the backpressure p_1 .

4.4.1 Bernoulli model

The Bernoulli model is adapted for the prediction of the mass flux in short geometries with very strongly subcooled coolant. Under these conditions, vaporization does not occur. The coolant is still in a liquid state at the smallest cross section. Thus, the speed of sound in the coolant is very high. Even at very high-pressure differences between the pressure vessel p_0 and the backpressure p_1 , critical conditions do not occur. The mass flux G_c is obtained from the Bernoulli equation. Since the throat pressure p' is the backpressure p_1 , this equation reads:

$$p_0 = p_1 + \frac{1}{2} \frac{G_c^2}{\rho}. \quad (4.226)$$

The density ρ is assumed constant. G_c is such that:

$$G_c = \sqrt{2\rho(p_0 - p_1)}. \quad (4.227)$$

In adiabatic irreversible flows, the single-phase pressure drop coefficient ζ is introduced to account for the pressure loss:

$$G_c = \sqrt{\frac{2\rho(p_0 - p_1)}{(1 + \zeta)}}. \quad (4.228)$$

4.4.2 Homogenous equilibrium model

The HEM model assumes mechanical, thermal and thermodynamic equilibrium of the two-phase mixture.

In geometries where the single-phase pressure loss coefficient ζ is assumed to be negligible, the flow is treated as an isentropic flow. The mass flux G_c is obtained from the two following equations:

- The first law of thermodynamics for an adiabatic flow, with the specific enthalpy h and the specific volume v is:

$$h_0 = h_2 + \frac{1}{2} G_c^2 v_2^2. \quad (4.229)$$

- The second law of thermodynamics with the specific entropy s reads:

$$s_0 = s_2. \quad (4.230)$$

In these equations, the subscript 0 refers to stagnation conditions and subscript 2 refers to the section 2 as indicated on Figure 4-14, top. The position of section 2 coincides with the throat of the geometry.

In contrast, in geometries where the single-phase pressure loss is not negligible, the flow is assumed to be isentropic only until section 2 as indicated on Figure 4-14, bottom. In this case, the position of section 2 is situated inside the geometry directly downstream of the inlet. Downstream of section 2, the flow is irreversible. The mass flux G_c is obtained from the three following equations:

- First law of thermodynamics for an adiabatic flow, with the specific enthalpy h and the specific volume v is:

$$h_0 = h_2 + \frac{1}{2} G_c^2 v_2^2. \quad (4.231)$$

- Second law of thermodynamics with the specific entropy s reads:

$$s_0 = s_2. \quad (4.232)$$

- The momentum equation is integrated along the geometry from the pressure p_2 to the throat pressure p' to account for the energy dissipated inside the geometry:

$$\zeta = 2 \int_{p'}^{p_2} \left[\frac{1}{G_c^2} + \frac{dv}{dp} \right] \frac{1}{v} dp. \quad (4.233)$$

ζ is the single-phase pressure drop coefficient from the section 2 to geometry's throat.

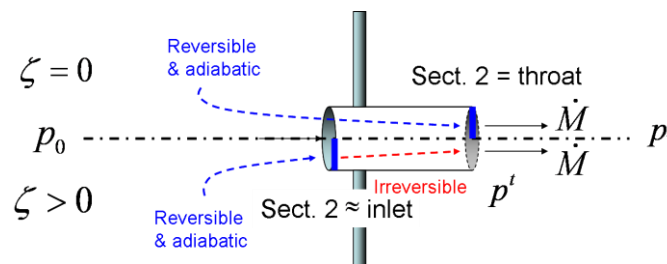


Figure 4-14: Assumptions of the HEM in critical two-phase mass flow rate calculations.

The system of equations (4.229) to (4.230) or (4.231) to (4.233) is solved numerically varying p' until G_c reaches its maximum value $G_c = G_c^*$. If the resulting p' happens to be smaller than p_1 , the flow is not critical and the calculation is performed again with $p' = p_1$ [160].

A comparison with experimental data indicates that [160]:

- The HEM with ζ -value = 0 always conservatively predicts mass flux for geometries characterized by a small ζ -value and by a ratio L/D larger than 20..30.
- The HEM very accurately predicts the critical mass flux for a wide range of flow (from strongly subcooled flow to flow with quality Y_0 up to 0.2) if the geometry is characterized by a large ζ -value.

In contrast, the HEM underpredicts the critical mass flux for geometries with L/D -ratios smaller than 20..30 when the coolant is subcooled ($T_{sat} - T_{coolant} = \Delta T = 0..40K$) or saturated with small quality ($Y_0 = 0..0.2$). In this case, the non-equilibrium ‘‘Henry and Fauske’’ model is recommended.

4.4.3 Henry and Fauske model

For shorter geometries and low vapor content, the vaporization process only partly occurs ([45], [117]) upstream of the choking section. The inter-phase mass transfer has not enough time to complete and the vapor content at the throat differs from equilibrium conditions: it is the so-called flashing delay. The non-equilibrium Henry-Fauske model accounts for this thermodynamic non-equilibrium with a model parameter [161]. In this way, it gives satisfying agreement with experiments [160] for short geometries.

4.5 Modeling of polydisperse flows

Polydisperse flows, in contrast to monodisperse flows, are characterized by particles of differing sizes (see Figure 4-15).

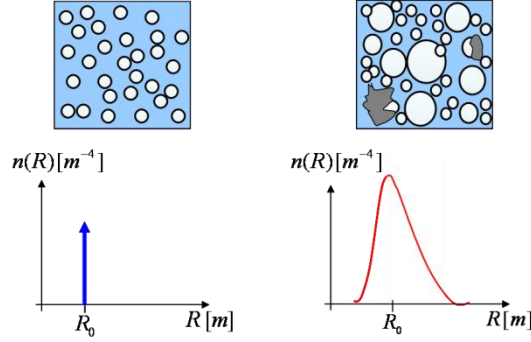


Figure 4-15: Representation of monodisperse (left) and polydisperse (right) flow; $n(R)$ being the particles number density in relation to particles radius R .

Since most interfacial processes depend on the size of the particles, it is advantageous to be able to capture the polydispersity of the flow and to treat separately particles of different size and shape. For this purpose, several techniques have been developed in CFD codes. Some of them are described in the next paragraphs. Basically, the goal of these techniques is to obtain the particles number density $n(R)$, where R is the radius of the particles. When the particles number density is accurately estimated, calculation of interfacial mass, momentum and heat transfers is greatly improved. For example, the drag force per unit volume acting on the continuous phase, which is the contribution from all droplets, can be written as:

$$\mathbf{f}_c = -\frac{1}{2} \rho_c \pi (\mathbf{u}_c - \mathbf{u}_d) |\mathbf{u}_c - \mathbf{u}_d| \int_0^{+\infty} C_D(R) n(R) R^2 dR. \quad (4.234)$$

4.5.1 Multi-group approach

In the multi-group approaches, the particles are distributed into classes, also called “bins” according to their mass, volume or diameter (Figure 4-16). The particles in each class are assumed to be identical and non-interacting with each other. Thus, a representative particle is associated to each class. For each class, it is possible to solve a transport equation in which interactions with the other classes are taken into account.

For instance, the model MUSIG [92], uses the population balance equations (4.221) of the number density in a modified form. $n(m, t)$ is the number of particles of mass m at time t . The transport equation of $n(m, t)$ is given by:

$$\frac{\partial n(m, t)}{\partial t} + \nabla \cdot [n(m, t) \mathbf{u}(m, t)] = B_B - D_B + B_C - D_C. \quad (4.235)$$

B_B , D_B , B_C and D_C respectively represent birth rate due to breakup of larger particles, death rate due to breakup into smaller particles, birth rate due to coalescence of smaller particles, and death rate due to coalescence with other particles. These rates are expressed by specific breakup or coalescence rates. For example,

$$B_B = \int_m^{\infty} g_{br, m}(\tilde{\varepsilon}, m) n(\tilde{\varepsilon}, t) d\tilde{\varepsilon}; \quad (4.236)$$

where $g_{br, m}(\tilde{\varepsilon}, m)$ represents the rate at which particles of mass m break into particles of mass $\tilde{\varepsilon}$ and $m - \tilde{\varepsilon}$. In the MUSIG model, the particles are distributed according to their mass into the bins. All particles in the bin i are assumed to have the same mass m_i . Thus, the particles of the bin i have a mass between $m_{i-1/2}$ and $m_{i+1/2}$ and the number density n_i of particles in the bin i is given by:

$$n_i(t) = \int_{m_{i-1/2}}^{m_{i+1/2}} n(m, t) dm. \quad (4.237)$$

n_i and m_i are related with the total volume fraction α_i of the particles present in the bin i as:

$$m_i n_i = \rho_g \alpha_i. \quad (4.238)$$

The governing equation of the size fraction

$$f_i = \frac{\alpha_i}{\alpha_g} \quad (4.239)$$

is given by:

$$\frac{\partial}{\partial t} (\rho_g \alpha_g f_i) + \nabla \cdot (\rho_g \alpha_g \mathbf{u}_g f_i) = S_i. \quad (4.240)$$

In eq. (4.240), all groups are assumed to share the same density ρ_g and velocity \mathbf{u}_g . The source term S_i represents the coalescence and breakup processes of the bin i :

$$S_i = B_{Bi} - D_{Bi} + B_{Ci} - D_{Ci}. \quad (4.241)$$

For example, B_{Bi} is the breakup of larger particles becoming particles of the bin i :

$$B_{Bi} = m_i \int_{m_i^{-1/2}}^{m_i^{+1/2}} B_B dm = m_i \sum_{j>i} g_{br,m}(m_j, m_i) N_j = \rho_g \alpha_g \left(\sum_{j>i} g_{br,m}(m_j, m_i) f_j \frac{m_j}{m_i} \right). \quad (4.242)$$

Expression for $g_{br,m}(m_j, m_i)$ and other frequencies needed to solve eq. (4.240) can be found in [92].

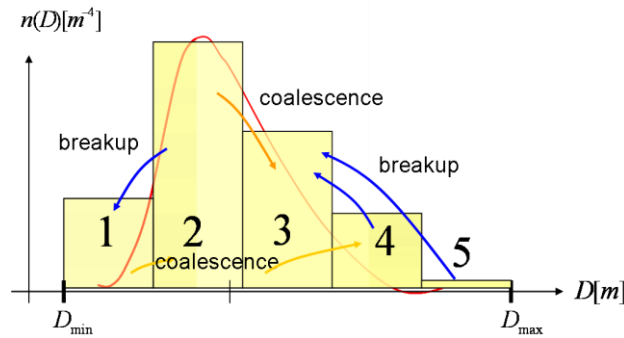


Figure 4-16: Representation of the multi-group approach MUSIG. Approximation of the particle number density distribution function (red line) in relation to particles diameter D by several bins (here 5) ranging from D_{\min} to D_{\max} . The intergroup transfers occur due to breakup and coalescence.

The segmentation in \hat{N} classes is performed by the user *a priori*, specifying the maximum D_{\max} and minimum diameter D_{\min} of the particles. The gain in accuracy resulting from the introduction of several equations may be balanced by the difficulty of inter-group transfers modeling and higher computational cost.

4.5.2 Presumed pdf approach

Although multi-group models are more complex (modeling of the intergroup transfers) and computationally more expensive (supplementary equations are solved), they are attractive in comparison to “one-group approach”. Particles of different sizes, which behave quite differently, can be treated separately. The polydispersity of the particles can be simulated. This is particularly important in engineering applications such as cavitation or sprays (e.g. [90], [162], [163]).

An alternative to account for the polydispersity of the particles is to follow the presumed probability density function (pdf) approach (Figure 4-17). In this framework, the particle distribution is assumed to have a particular pdf at any location in the flow domain and at any time – typically a gamma or a log-normal pdf. Correspondingly to this presumed pdf, the transport equations of a family of conserved scalars $S_{\hat{\gamma}}$ are derived and solved. The $S_{\hat{\gamma}}$ is known as the ‘intensity of dispersion’ [164]. It is related to the $\hat{\gamma}$ ’th moment of the particle size pdf. Solving for the $S_{\hat{\gamma}}$ ’s permits to reconstruct the local particle pdf, from which other information such as mass transfer may be derived.

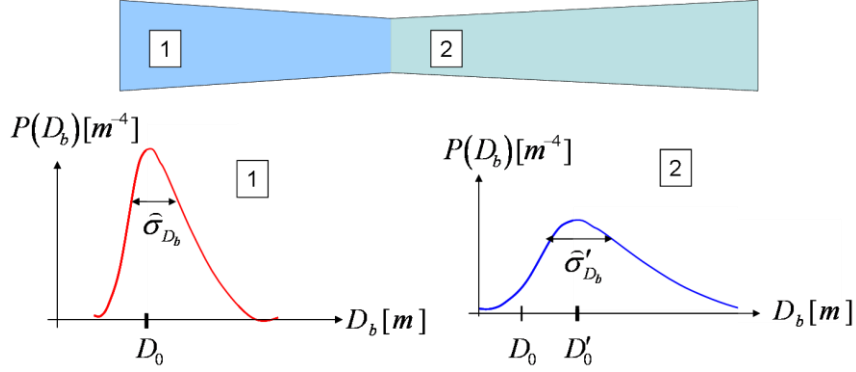


Figure 4-17: Representation of the presumed pdf approach. A particular pdf is assumed at any location in the flow domain and at any time for the particle probability density distribution function $P(D_b)$ (red line). The parameters of $P(D_b)$ are mean diameter D_0 and variance $\hat{\sigma}_{D_b}$ at the inlet of the computational domain (1). According to the ‘intensity of dispersion’ [164] $S_{\hat{\gamma}}$ transport equations, the mean diameter evolves to D'_0 and the variance to $\hat{\sigma}'_{D_b}$ at another location in the flow (2).

For a given particle size pdf $P(D_b)$, $S_{\hat{\gamma}}$ is defined as:

$$S_{\hat{\gamma}} = n \int_0^{\infty} P(D_b) D_b^{\hat{\gamma}} d(D_b) = n M_{\hat{\gamma}}; \quad (4.243)$$

where n is the particle number density, D_b the particle diameter and $M_{\hat{\gamma}}$ the $\hat{\gamma}$ 'th distribution moment. According to this definition,

$$S_0 = n; \quad (4.244)$$

$$S_1 = n D_{b,m}; \quad (4.245)$$

$$S_2 = \frac{4a_i}{\pi}; \quad (4.246)$$

$$S_0 = \frac{6}{\pi} \alpha; \quad (4.247)$$

where $D_{b,m}$ is the mean diameter; a_i is the interfacial area concentration and α is the particles volume fraction.

The governing equation for $S_{\hat{\gamma}}$ is:

$$\frac{\partial S_{\hat{\gamma}}}{\partial t} + \nabla \cdot (S_{\hat{\gamma}} \mathbf{u}_{\hat{\gamma}}) - \hat{\gamma} \dot{R}_{\hat{\gamma}-1} S_{\hat{\gamma}-1} = \varphi_{\hat{\gamma}}; \quad (4.248)$$

where

$$\dot{R}_{\hat{\gamma}} = \frac{\int_0^{\infty} P(D_b) \dot{R}(D_b) D_b^{\hat{\gamma}} d(D_b)}{\int_0^{\infty} P(D_b) D_b^{\hat{\gamma}} d(D_b)} \quad (4.249)$$

is the weighted averaged growth, and

$$\mathbf{u}_{\hat{\gamma}} = \frac{\int_0^{\infty} P(D_b) \mathbf{u}(D_b) D_b^{\hat{\gamma}} d(D_b)}{\int_0^{\infty} P(D_b) D_b^{\hat{\gamma}} d(D_b)} \quad (4.250)$$

is the weighted averaged velocity. $\dot{R}(D_b)$ and $\mathbf{u}(D_b)$ are growth and velocity of the particles of size D_b , respectively. To evaluate the source term $\varphi_{\hat{\gamma}}$, $P(D_b)$ has to be known.

If the pdf depends on two parameters D_0 and $\hat{\sigma}_{D_b}$, the distribution is uniquely defined by a combination of two moments $S_{\hat{\gamma}}$. For instance, for a log-normal pdf:

$$P(D_b) = \left(\sqrt{2\pi} \hat{\sigma}_{D_b} D_0 \right)^{-1} \exp \left[- \left\{ \ln \left(\frac{D_b}{D_0} \right) \right\}^2 / (2\hat{\sigma}_{D_b}^2) \right]; \quad (4.251)$$

$\hat{\sigma}_{D_b}$ is obtained from:

$$\hat{\sigma}_{D_b} = \left[\ln \left(\frac{6\alpha S_1}{\pi S_2^2} \right) \right]^{1/2} \quad (4.252)$$

and then, D_0 is calculated by inverting:

$$S_{\dot{\gamma}} = \frac{6\alpha}{\pi} (D_0)^{\dot{\gamma}-3} \exp \left\{ \frac{\hat{\sigma}_{D_b}^2}{2} (\dot{\gamma}^2 - 9) \right\}. \quad (4.253)$$

The success of this technique relies on the adoption of an appropriate – if any – form of the pdf [162] and on the modeling of the source term $\varphi_{\dot{\gamma}}$ [13].

4.5.3 Direct quadrature method of moments

Originated from [165], the direct quadrature method of moments (DQMOM) is a technique whose basic idea is to approximate the density number $n(D_b)$ by a summation of \underline{N} Dirac delta functions [166]:

$$n(D_b) = \sum_{q=1}^{\underline{N}} \omega_{\underline{z}_q} \delta [D_b - \underline{d}_{\underline{z}_q}]; \quad (4.254)$$

where $\omega_{\underline{z}_q}$ is the weight of the delta function centered at the characteristic particle diameter $\underline{d}_{\underline{z}_q}$ (see Figure 4-18 for a simple example).

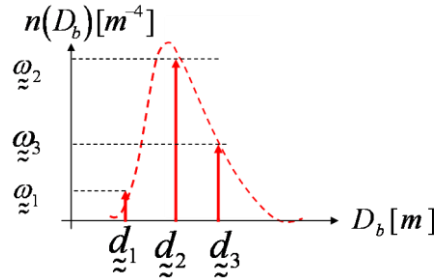


Figure 4-18: Approximation of the density number $n(D_b)$ by a summation of 3 Dirac delta functions. $\omega_{\underline{z}_q}$ ($q=1..3$) are the weight of the delta functions centered at the characteristic particle diameter $\underline{d}_{\underline{z}_q}$ ($q=1..3$).

The balance equation of the density number function $n(D_b)$ reads [167]:

$$\frac{\partial n(D_b)}{\partial t} + \nabla \cdot [n(D_b) \mathbf{u}_{D_b}] = \dot{S}(D_b); \quad (4.255)$$

where $\dot{S}(D_b)$ is the size-dependent source for coalescence and breakup and \mathbf{u}_{D_b} is the mean velocity of bubbles of size D_b . To evaluate \mathbf{u}_{D_b} , a constitutive relation is supplied or supplementary transport equations are solved [168]. By definition of \mathbf{u}_{D_b} , the mean velocity of bubbles of size $\underline{d}_{\underline{z}_q}$ is $\mathbf{u}_{\underline{d}_{\underline{z}_q}}$, also noted $\mathbf{u}_{\underline{z}_q} \equiv \mathbf{u}_q$ in the rest of this paragraph.

Inserting eq. (4.254) in eq. (4.255), the transport equations of the \underline{N} weights $\omega_{\underline{z}_q}$ and the \underline{N} weighted abscissas $\delta_{\underline{z}_q} = \omega_{\underline{z}_q} \underline{d}_{\underline{z}_q}$ are obtained:

$$\frac{\partial \omega_{\underline{z}_q}}{\partial t} + \nabla \cdot (\omega_{\underline{z}_q} \mathbf{u}_q) = S_{\omega_q}, \quad q=1, \dots, N; \quad (4.256)$$

$$\frac{\partial \delta_{\underline{z}_q}}{\partial t} + \nabla \cdot (\delta_{\underline{z}_q} \mathbf{u}_q) = S_{\delta_q}, \quad q=1, \dots, N; \quad (4.257)$$

where the source terms S_{ω_q} and S_{δ_q} satisfy:

$$(1-k) \sum_{q=1}^N \underline{d}_q^k S_{\omega_q} + k \sum_{q=1}^N \underline{d}_q^{k-1} S_{\delta_q} = \bar{S}_{m_k}, \quad k=0, \dots, 2N-1; \quad (4.258)$$

with

$$\bar{S}_{m_k} = \int_0^{\infty} D_b^k \dot{S}(D_b) d(D_b). \quad (4.259)$$

Equation (4.258) forms a linear system which, recast in a matrix form, reads:

$$\underline{\underline{\mathbf{A}}} \underline{\underline{\mathbf{x}}} = \underline{\underline{\mathbf{b}}}; \quad (4.260)$$

with

$$\underline{\underline{\mathbf{A}}} = (\underline{\underline{C}} d_{\underline{\underline{z}}}^k); \quad (4.261)$$

$\underline{\underline{C}}$ being a constant, and

$$\underline{\underline{\mathbf{x}}} = [S_{\omega_1} \dots S_{\omega_N} S_{\delta_1} \dots S_{\delta_N}]^T; \quad (4.262)$$

$$\underline{\underline{\mathbf{b}}} = [\bar{S}_{m_0} \dots \bar{S}_{m_{2N-1}}]^T. \quad (4.263)$$

$\underline{\underline{\mathbf{x}}}$ is obtained by inverting the system of equation (4.260):

$$\underline{\underline{\mathbf{x}}} = \underline{\underline{\mathbf{A}}}^{-1} \underline{\underline{\mathbf{b}}}; \quad (4.264)$$

and the transport equations (4.256) and (4.257) are solved.

Eq. (4.256) and (4.257) can also be formulated in terms of particle volume fraction α_q and effective diameter $d_{\underline{\underline{z}}_q}$ [169]:

$$\frac{\partial}{\partial t} (\alpha_q \rho_g) + \nabla \cdot (\alpha_q \rho_g \mathbf{u}_q) = \frac{\pi}{2} \rho_g d_{\underline{\underline{z}}_q}^2 S_{\delta_q} - \frac{\pi}{3} \rho_g d_{\underline{\underline{z}}_q}^3 S_{\omega_q}, \quad q = 1, \dots, N; \quad (4.265)$$

and

$$\frac{\partial}{\partial t} (\alpha_q \rho_g d_{\underline{\underline{z}}_q}) + \nabla \cdot (\alpha_q \rho_g \mathbf{u}_q d_{\underline{\underline{z}}_q}) = \frac{2\pi}{3} \rho_g d_{\underline{\underline{z}}_q}^3 S_{\delta_q} - \frac{\pi}{2} \rho_g d_{\underline{\underline{z}}_q}^4 S_{\omega_q}, \quad q = 1, \dots, N. \quad (4.266)$$

Breakup and coalescence models are recast into the DQMOM frame to evaluate (4.259).

4.6 Modeling of cavitation

Cavitation is essentially a three dimensional unsteady phenomenon, whose length scales range down to some micrometers, and primarily influenced by the development of the boundary layer and of free shear vortices (chap. *cavitation*). Its analysis is bound to fail in a system code where all information on the transverse processes is lost (sect. 4.2.1). At best, in a system code, it is possible to implement a correlation derived from experiments or CFD calculations to account for the effect of punctual cavitation on the behavior of a large and complex system (e.g. nuclear reactor plant or test section).

Although more appropriate, CFD codes are also limited to some extent and some information is lost (sect. 4.2.2). Assumptions on the flow conditions help to simplify the modeling of the governing equations. For cavitation, it is common to assume the gas phase to be finely dispersed in form of spherical cavities in the continuous liquid phase. This characteristic can be used to derive simplified governing equations of the mixture in an Euler frame. It is also possible to follow another technique, called Euler-Lagrange formulation, where the cavities are tracked with a Lagrange solver and the governing equations of the liquid phase are solved in an Euler framework.

4.6.1 Euler-Lagrange formulation

The density distribution function conservation equation defined in chap. *cavitation* describes the evolution of the cavity distribution function $f^\phi(t, \mathbf{x}, \phi, \mathbf{u}_b, T_b)$. For the sake of convenience, ϕ is taken to be the radius R of the cavities in the rest of this section.

Until now, this equation was cast in an Euler framework where the flow fields are function of time and space. For this purpose, the density function conservation equation was reduced to the density number transport equation by averaging over the cavities and introducing averaged radius, velocities and temperatures.

To avoid the loss of information on cavities' size, velocity and temperature, an alternative technique is to follow a large number of cavities. It is the so-called Lagrange technique (Figure 4-19). The dispersed phase particles are tracked from their birth (arrival in computational domain, result of coalescence/break-up) to their death (leaving the computational domain, result of coalescence / break-up). The trajectory eq. (4.267), the momentum balance eq. (4.268) and the single-bubble

dynamic eq. (4.269), typically the Rayleigh-Plesset equation [170] or one of its modified forms (e.g., [171]), are solved for individual bubbles:

$$\frac{d\mathbf{x}_b}{dt} = \mathbf{u}_b ; \quad (4.267)$$

$$m_b \frac{d\mathbf{u}_b}{dt} = \mathbf{F}_b ; \quad (4.268)$$

$$\frac{dR}{dt} = \dot{R} ; \quad (4.269)$$

$$\frac{dT_b}{dt} = \dot{T}_b . \quad (4.270)$$

Generally equation (4.270) is not considered in cavitating flows. The variation of the temperature at low pressures and low void fractions is negligible. The forces, the bubble dynamic, the break-up and the coalescence are described by adequate terms in the equations (4.267) to (4.270), typically those introduced in chap. *cavitation* sect. 1.1.2.3. Apart from the statistical error, the solution obtained from the system of cavities is equivalent to the solution of the density distribution function conservation equation.

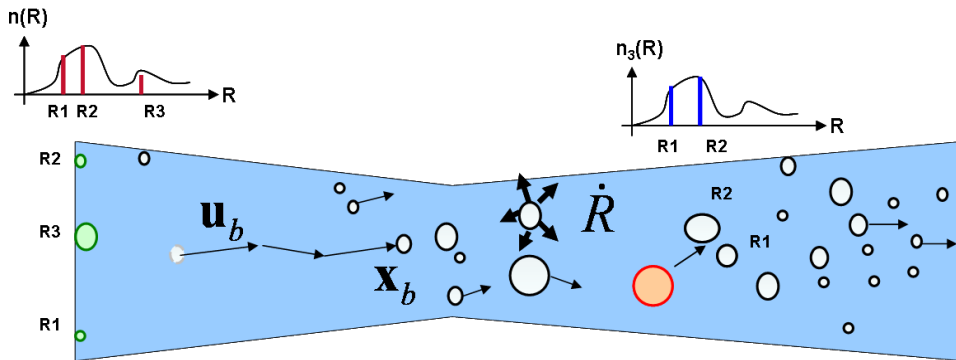


Figure 4-19: Illustration of the Euler-Lagrange approach in cavitating flows. Bubble's position \mathbf{x}_b is tracked from bubble's birth [The size of three bubbles (in green) is sampled here according to the pdf $n(R)$ at the inlet of the computational domain] to bubble's death [The death of the bubble is represented here by the breakup of the bubble (in red) into two cavities. The resulting two bubbles are sampled from the pdf $n_3(R)$]. Bubble's velocity \mathbf{u}_b and growth \dot{R} are calculated along bubble's path. An Euler solver solves the Navier-Stokes equations of the liquid phase (blue).

The description of cavitation with Monte-Carlo codes based on Lagrange techniques (e.g. [172], [173]) is attractive. The stochastic nature and the particle size dependence of the physical processes can be easily captured. The size of the cavitation nuclei is randomly sampled from a presumed pdf. The turbulent motion of the bubble is accounted for by assuming that the velocity \mathbf{u}_b consists of a mean and a turbulent fluctuation

$$\mathbf{u}_b = \bar{\mathbf{u}}_b + \mathbf{u}'_b ; \quad (4.271)$$

where \mathbf{u}'_b is sampled from a Gaussian distribution [172]. Bubble's break-up and coalescence are controlled by local quantities, e.g. bubble's size and bubble's velocity. Thereby the break-up, the coalescence and daughter bubble's size are sampled from prescribed pdf.

Coupled to the Lagrange solver which tracks the bubbles along their trajectory, an Euler solver solves the Navier-Stokes equations of the continuous liquid phase (basically eq. (4.136) to (4.144) with appropriate simplifications). This Euler solver also evaluates additional flow variables, e.g., turbulence or liquid phase velocity. By ensemble-averaging the Lagrange quantities of the N_{cell} bubbles present in each Euler computational cell, the statistical information of the Lagrange solver is exploited. For an infinite number of bubbles, the mean value of any function of the flow variables, including any non-linearity, becomes exact so that no modeling is required.

Fluid properties are evaluated with an Euler solver. Generally turbulence is predicted within the RANS approach. Liquid instantaneous and local quantities, e.g. the liquid pressure, are not available for the Lagrange solver.

The physical modeling of some processes is required. A typical example of the modeling of averaged quantities is the modeling of the pressure fluctuations in cavitating flows. These fluctuations generally

are considered to be proportional to $\rho \bar{\mathbf{u}}^{-2}$, the constant of proportionality C_t being determined semi-empirically:

$$\sqrt{\overline{p'^2}} = C_t \rho \bar{\mathbf{u}}^{-2}. \quad (4.272)$$

In case of isotropic turbulence, Hinze [174] proposed $C_t=0.7$; while for turbulent shear flows, the coefficient C_t is larger [31]. Then the effective liquid pressure is estimated by:

$$p_\infty(t) = \bar{p}_\infty(t) - C_t \frac{2}{3} \rho_l k_l. \quad (4.273)$$

Furthermore, the particle position $\mathbf{x}_p = (x_p, y_p, z_p)$ generally does not coincide with the Euler grid point $\mathbf{x}_{cell} = (x_l, y_m, z_n)$ (Figure 4-20). The interpolation of the Euler flow fields at the Lagrange particle positions are based on the use of local approximations. Typically, the velocity $\mathbf{u}_f(x_p, y_p, z_p, t)$ of the fluid at the particle position $\mathbf{x}_p = (x_p, y_p, z_p)$ is expressed as a weighted summation over the grid (whose grid points coordinates are x_l , y_m and z_n). The basis functions f_l , g_m and h_n and the coefficients a are introduced for this purpose [125]. Thus, \mathbf{u}_f is estimated by:

$$\mathbf{u}_f(x_p, y_p, z_p, t) = \sum_{x_l} \sum_{y_m} \sum_{z_n} a(x_l, y_m, z_n, t) f_l(x_p) g_m(y_p) h_n(z_p). \quad (4.274)$$

This interpolation is associated to additional operations and interpolation errors, which are strongly affected by the choice of the basis functions and coefficients. For parallel computation, the coupling is even more difficult and usually associated with very poor performance due to imbalanced particle concentration in the flow [175], [176].

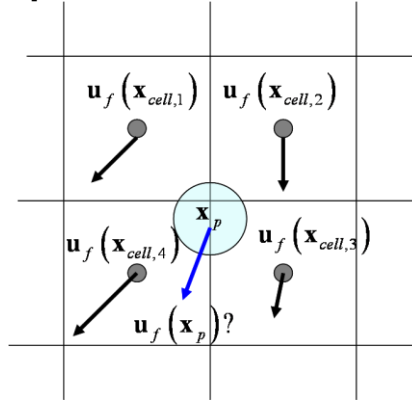


Figure 4-20: Interpolation in Euler-Lagrange simulations: Velocity field $\mathbf{u}_f(\mathbf{x}_{cell,i})$ of the fluid phase is known at the Euler grid points but unknown at the particle position \mathbf{x}_p .

To represent the properties of the whole population [177] and have a sufficiently smooth void-fraction profile to assure convergence of the Euler solver [178], the number of bubbles must be large. To increase the statistic representativeness of the results, stochastic statistic approximation methods such as the discrete bubble model can be used. In this case, the total bubble population is represented by a number of parcels, each containing a large number of identical non-interacting bubbles, and the trajectory and momentum equations are solved for each parcel. In spite of this amelioration, Euler-Lagrange simulation of coupled multiphase flows with strong interaction between the continuous fluid phase and the dispersed particle phase belongs to the application with the highest demand on computational resources. They generally are used for two-phase flows with low void fractions.

4.6.2 Euler formulation

In the Euler formulation, the flow variables are expressed as flow fields which are function of time and space. In cavitating flows, this formulation requires the averaging of the bubbles properties over the bubble population. Thus, information on the bubble size pdf and on the velocities of the different bubbles is not available without further ado. In spite of this inaccuracy, this approach is advantageous for two reasons. First, Euler simulations require modest computational resources in comparison to Euler-Lagrange calculations. Second, Euler codes are very robust.

In cavitating flows, water and vapor are usually assumed to be in mechanical and thermal equilibrium since bubbles are finely dispersed in the liquid phase. Water and vapor share same velocity, pressure and temperature. They are treated as a continuum. In this framework, two models exist to describe the water-vapor mixture: the drift flux model and the homogeneous model. The distinction between both models relies on the treatment of the thermodynamic behavior of the mixture. The drift flux accounts for the thermodynamic non-equilibrium by solving the transport equation of the vapor mass fraction whereas the homogeneous model estimates the void fraction from mixture properties (energy, pressure, etc.).

4.6.2.1 Homogeneous model

The homogeneous model supposes that the interfacial mass transfer is infinitely fast. Under this assumption, the local pressure has an instantaneous effect on the density of the mixture. Thus, in this model, the density can be expressed as a function of the pressure [95]:

$$p(\rho_m) = \tilde{p}_{l,s} + \frac{\rho_g - \rho_l}{\rho_g \rho_l} \frac{1}{(\rho_l c_l)^{-2} + (\rho_g c_g)^{-2}} \log \left[\left(\frac{\tilde{c}_m \rho_m}{c_l \rho_l} \right)^2 \right]. \quad (4.275)$$

In eq. (4.275), $\tilde{p}_{l,s}$ is the pressure at which the liquid starts to turn into vapor and \tilde{c}_m is the speed of sound of the mixture; both being model constants which are tuned to fit experimental results. An alternative is to obtain the void fraction α from mixture properties, typically mixture internal energy ρe per unit volume [179] (eq. (4.276)) or mixture density [180] (eq. (4.277)):

$$\alpha = \frac{\rho e - \rho_{sat,l} e_{sat,l}}{\rho_{sat,g} e_{sat,g} - \rho_{sat,l} e_{sat,l}}; \quad (4.276)$$

or

$$\alpha = \frac{\rho_{sat,l} - \rho}{\rho_{sat,l} - \rho_{sat,g}}. \quad (4.277)$$

Although this modeling cannot describe liquid quality effects and metastable conditions, it is often used in numerical simulations due to its simplicity.

4.6.2.2 Rayleigh-Plesset

The drift flux model considers the finite growth rate of the cavities by introducing the void fraction transport equation (eq. (4.215)). The source term of this supplementary equation represents the interfacial mass transfer \dot{m}_g . \dot{m}_g (see eq. (4.278)) involves local and instantaneous quantities such as interface surface, velocities etc. which are not available:

$$\dot{m}_g = -\frac{1}{\Delta t} \sum_j \left\{ \frac{1}{u_{ni}} \mathbf{n}_g \cdot \rho_g (\mathbf{u}_g - \mathbf{u}_i) \right\}. \quad (4.278)$$

The modeling of \dot{m}_g with resolved quantities is required. In cavitating flows, this modeling usually is based on the Rayleigh-Plesset equation.

In this context, the source term \dot{m}_g reflect the fact that the vapor phase consists of a finite number of vaporous cavities. The gas phase commonly is represented by n_0 monodisperse bubbles, i.e. they all have the same radius R_0 . The vapor void fraction α_g is then given by:

$$\alpha_g = n_0 \frac{4\pi}{3} R_0^3. \quad (4.279)$$

\dot{m}_g is easily obtained from R_0 when the variation of n_0 and ρ_g are disregarded. In that case, the mass transfer \dot{m}_g is given by:

$$\dot{m}_g = \frac{d}{dt} (\rho_g \alpha_g) = \frac{d}{dt} \left(\rho_g n_0 \frac{4\pi}{3} R_0^3 \right) = \rho_g n_0 4\pi R_0^2 \frac{dR_0}{dt}. \quad (4.280)$$

In general, the growth rate dR_0/dt of R_0 is derived from a simplified form of the Rayleigh-Plesset equation where the inertial, thermal and surface effects are neglected. Under these assumptions, $\frac{dR_0}{dt}$ is given by:

$$\begin{aligned}\frac{dR_0}{dt} &= \sqrt{\frac{2}{3} \frac{p_{sat}(T_l) - p_l}{\rho}} \quad \text{for } p_{sat}(T_l) - p_l > 0; \\ \frac{dR_0}{dt} &= -\sqrt{\frac{2}{3} \frac{|p_{sat}(T_l) - p_l|}{\rho}} \quad \text{for } p_{sat}(T_l) - p_l < 0.\end{aligned}\quad (4.281)$$

Thus, the mass transfer eq. (4.280) reduces to:

$$\begin{aligned}\dot{m}_g &= \rho_g n_0 4\pi R_0^2 \sqrt{\frac{2}{3} \frac{p_{sat}(T_l) - p_l}{\rho}} \quad \text{for } p_{sat}(T_l) - p_l > 0; \\ \dot{m}_g &= -\rho_g n_0 4\pi R_0^2 \sqrt{\frac{2}{3} \frac{|p_{sat}(T_l) - p_l|}{\rho}} \quad \text{for } p_{sat}(T_l) - p_l < 0;\end{aligned}\quad (4.282)$$

where R_0 and n_0 are model parameters.

The Rayleigh-Plesset equation is generally used in this simplified form because its full expression is not adapted to Euler codes. An additional solver is needed to resolve the acceleration term and bubbles radius is not a Euler conserved quantity. Moreover, the timescale of the Rayleigh-Plesset equation differs significantly from the macroscopic time-scale.

Although \dot{m}_g is derived on equivalent physical grounding for all models based on the Rayleigh-Plesset equation, many differing expressions exist for this term in the literature. Some (e.g. [181]) considers n_0 to be defined per unit of water volume instead of mixture volume; others (e.g. [182], [95]) modify n_0 to take into account coalescence or flow conditions; while (e.g. [183], [171]) integrate a velocity potential to represent the influence of other cavities on bubbles growth. Usually growth and collapse (eq. (4.282)) are also scaled by ad-hoc coefficients C_{vap} and C_{cond} [e.g. [92]]. The model parameters R_0 , n_0 , C_{vap} and C_{cond} vary from one application to the other to palliate the inaccuracy of the physical model. Vaporization and condensation rates \dot{m}_g may differ by several orders of magnitude [95].

One promising strategy to improve the modeling and to renounce to ad-hoc coefficients is to consider the polydispersity of the bubble distribution. A first attempt can be found in [184] where the DQMOM (sect. 4.5.3) is introduced to simulate cloud cavitation.

5 Probability density function approach

The proposed cavitation model aims to account for cavitation-turbulence interaction and to reproduce the bubble size spectrum by introducing stochastic models. This technique is based on the proposition of Valiño [10] to solve the modeled composition probability density function (pdf) transport equation. Before this technique is discussed in chapter *stochastic-field cavitation model*, the present chapter is dedicated to give basic prerequisite on probabilistic processes (section 5.1) and stochastic equations (section 5.2), to indicate when stochastic modeling is adequate (section 5.3) and to present exact and modeled pdf transport equations of fluid dynamics (section 5.4). Section 5.4 is of particular interest since it presents the modeled composition pdf equation which is solved in the cavitation model. Finally in section 5.5, one established Lagrange technique for solving the velocity-composition and composition pdf transport equations is described. Other properties of random variables and stochastic processes are given in appendix B.

5.1 Stochastic processes

5.1.1 Introduction

In turbulent flows, the flow variables (e.g. T) are highly fluctuating quantities. Measurement under the same flow conditions at the same location but at different times, or repetitions of the measurement under the same flow conditions at the same location and at the same time, does not deliver a single value T_0 but a range of values $T_{\min} \leq T \leq T_{\max}$.

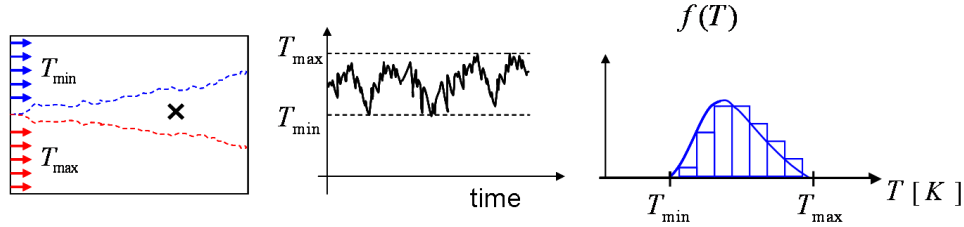


Figure 5-1: Schematic representation of the turbulent mixing of two fluid layers (left), one being hot (T_{\max}), the other cold (T_{\min}); time-evolution of the temperature (middle); and temperature pdf (right) at the location marked by a cross.

The flow variables are better described in terms of statistics.

5.1.1.1 Cumulative distribution function

For instance, considering the measurement is performed a sufficient number of times at the same location x_1 and at the same time t_1 , it is possible to estimate the probability for $T(x_1, t_1)$ to take a value below T_1 :

$$P\{T(x_1, t_1) \leq T_1\}. \quad (5.1)$$

Varying T_1 from T_{\min} to T_{\max} , we obtain the distribution function $F_{T(x_1, t_1)}(T)$ of the random variable $T(x_1, t_1)$, defined as:

$$F_{T(x_1, t_1)}(T_1) = P\{T(x_1, t_1) \leq T_1\}. \quad (5.2)$$

5.1.1.2 Probability density function

Under the same assumptions, it is also possible to estimate the probability for $T(t_1)$ to take a value between T_1 and $T_1 + dT$ ($P\{T_1 \leq T(x_1, t_1) \leq T_1 + dT\}$). For dT sufficiently small and varying T_1 from T_{\min} to T_{\max} , we obtain the probability density function $f_{T(x_1, t_1)}(T)$ of the random variable $T(x_1, t_1)$. $f_{T(x_1, t_1)}(T)$ is the derivative of the distribution function $F_{T(x_1, t_1)}(T)$:

$$f_{T(x_1, t_1)}(T_1) = \frac{dF_{T(x_1, t_1)}(T_1)}{dT}. \quad (5.3)$$

In this context, we are dealing with first order statistics in time and space since only one time and one point are considered in the statistics.

5.1.1.3 Higher order statistics

If we want to have a finer description of the flow variable, it is possible to repeat a measurement under the same flow conditions at the same location x_1 but at two different times t_1 and t_2 ; and to estimate the probability for $T(x_1, t_1)$ to take a value below T_1 ; while $T(t_2)$ takes a value below T_2 . This analysis results in second order statistics.

Without further assumption on $T(x, t)$, this procedure should be repeated for the n th order distribution or density function for any n and time t_1, \dots, t_n to obtain the complete description of the stochastic process $T(x_1, t)$.

5.1.2 Definition and notation

5.1.2.1 Stochastic variable

The flow variable T is a stochastic process $\tilde{\mathbf{T}}(x_1, t)$ at any point x_1 in the flow; i.e. a family of time functions $T(x_1, t, \xi_i)$ where each member $T(x_1, t, \xi_i)$ is determined by the outcome ξ_i of an experiment \mathcal{E} and evolves according to some rule [185].

For a specific location x_1 , the stochastic process $\tilde{\mathbf{T}}(x_1, t)$ has four meanings [185] (Figure 5-2):

- 1- a family of time functions (t variable, ξ_i variable)
- 2- a single time function (t variable, ξ_i fixed)
- 3- a random variable (t fixed, ξ_i variable)
- 4- a number (t fixed, ξ_i fixed)

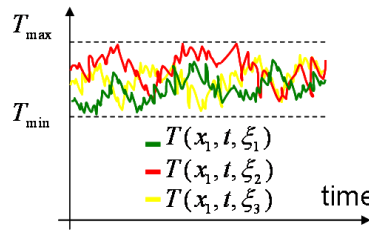


Figure 5-2: Schematic representation of the stochastic process $\tilde{\mathbf{T}}(x_1, t)$ with the time evolution of three member functions.

For a specific location x and time t , $\tilde{\mathbf{T}}(x, t)$ is a random variable. The distribution $F_{T(x,t)}(T)$ and density function $f_{T(x,t)}(T)$ of this random variable will in general depend on x and t . Therefore, denoting by $F_{\tilde{\mathbf{T}}}(T; x, t)$, or simply $F(T; x, t)$ when there is no risk of confusion, the distribution of the stochastic process $\tilde{\mathbf{T}}(x, t)$; we have:

$$F(T; x, t) = P\{\tilde{\mathbf{T}}(x, t) \leq T\}. \quad (5.4)$$

Given a position x and a time t , $F(T; x, t)$ is the probability of the event $\{\tilde{\mathbf{T}}(x, t) \leq T\}$ consisting of all outcomes ξ_i such that at the specified time t and location x , the functions $\tilde{\mathbf{T}}(x, t)$ do not exceed the given number T .

The corresponding probability density function (pdf) $f_{\tilde{\mathbf{T}}}(T; x, t)$ (or $f(T; x, t)$) is obtained by differentiating with respect to T :

$$f(T; x, t) = \frac{\partial F(T; x, t)}{\partial T}. \quad (5.5)$$

5.1.2.2 Joint statistics

Considering the two random variables $\tilde{\mathbf{T}}(x,t)$ and $\tilde{\mathbf{V}}(x,t)$ given a position x and a time t , the joint-distribution $F_{\tilde{\mathbf{T}}\tilde{\mathbf{V}}}(T,V;x,t)$ is the probability of the event $\{\tilde{\mathbf{T}}(x,t) \leq T\} \cap \{\tilde{\mathbf{V}}(x,t) \leq V\}$. The joint-pdf $f_{\tilde{\mathbf{T}}\tilde{\mathbf{V}}}(T,V;x,t)$, (or $f(T,V;x,t)$), is such that the probability of the event $\{T \leq \tilde{\mathbf{T}}(x,t) \leq T+dT\} \cap \{V \leq \tilde{\mathbf{V}}(x,t) \leq V+dV\}$ for $dT \rightarrow 0$ and $dV \rightarrow 0$ is $f(T,V;x,t)dTdV$.

These definitions can be extended to an arbitrary number of stochastic processes; typically scalar properties such as chemical species mass fractions.

5.1.3 Markov process

To reduce the complexity of statistical modeling, stochastic processes are generally assumed to be Markov processes: their statistical properties in the future are uniquely determined from the present regardless of the past; they have no memory [186]. In terms of probability, the stochastic process $\tilde{\mathbf{x}}(t)$ is a Markov process if for every n and $t_1 < t_2 \dots < t_n$:

$$P[\tilde{\mathbf{x}}(t_n) \leq x_n | \tilde{\mathbf{x}}(t_{n-1}), \dots, \tilde{\mathbf{x}}(t_1)] = P[\tilde{\mathbf{x}}(t_n) \leq x_n | \tilde{\mathbf{x}}(t_{n-1})]. \quad (5.6)$$

This property permits to calculate all higher-order statistics when the initial pdf $f(x_0; t_0)$ and the conditional density function $f(x_1; t_1 | x_0; t_0)$, also called transitional density function; are known. The transitional density function represents the probability for $\tilde{\mathbf{x}}(t)$ to take a value x_1 at a time t_1 assuming that the value of $\tilde{\mathbf{x}}(t)$ at a time t_0 was x_0 .

5.1.3.1 White noise

The Gaussian white noise is a particular Markov process. It is stationary, i.e. its density function $f(x,t)$ is time-independent:

$$f(x,t) = f(x); \quad (5.7)$$

and its autocorrelation function $R(t_1, t_2)$ is zero everywhere except for $t_1 = t_2$. Figure 5-3 represents one member function of the white noise process ξ .

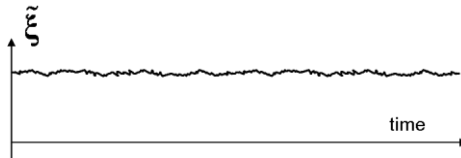


Figure 5-3: Schematic representation of a member function of the white noise process ξ .

5.1.3.2 Random walk

Another simple Markov process $\tilde{\mathbf{x}}(t)$ is the random walk. This process can be defined as follows [185]: every T seconds, the next step of finite fixed length s is tossed: if the outcome is head then the step is to the right, otherwise to the left. Thus, each function $\tilde{\mathbf{x}}(t, \xi)$ has a staircase form with discontinuities at the points $t = nT$. Figure 5-4 represents one member function $\tilde{\mathbf{x}}(t, \xi_1)$ of the random walk process $\tilde{\mathbf{x}}(t)$.

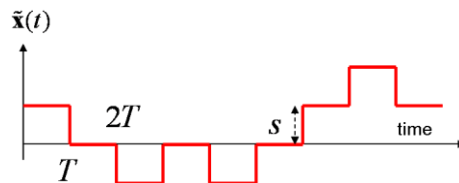


Figure 5-4: Representation of one realization $\tilde{\mathbf{x}}(t, \xi_1)$ of the random walk process $\tilde{\mathbf{x}}(t)$.

5.1.3.3 Wiener-Levy process

The Wiener-Levy process $\tilde{w}(t)$, also known as Brownian motion, is the limiting case of the random walk where the size step s and the time step T both tend to zero such that:

$$s^2 = DT. \quad (5.8)$$

In eq. (5.8), D is a constant value. It can be shown that this process ($\tilde{w}(t) = \lim_{s,T \rightarrow 0} \tilde{x}(t)$, where $\tilde{x}(t)$ is a random walk and (5.8) is satisfied) is a family of continuous functions. Figure 5-5 represents four member functions of the Wiener-Levy process $\tilde{w}(t)$.

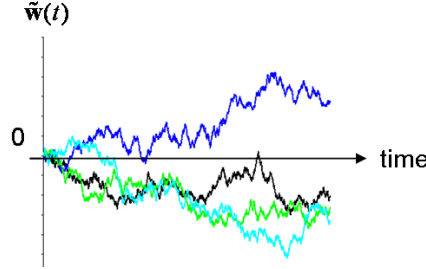


Figure 5-5: Representation of four member functions of the Wiener-Levy process $\tilde{w}(t)$.

The Wiener-Levy process $\tilde{w}(t)$ is also a Markov process. Its expectation value is zero and its variance is Dt :

$$E[\tilde{w}(t)] = 0; \quad (5.9)$$

$$E[\tilde{w}^2(t)] = Dt. \quad (5.10)$$

Furthermore, $\tilde{w}(t)$ is normally distributed such that its density function is given by:

$$f(w;t) = \frac{1}{\sqrt{2\pi Dt}} e^{-w^2/2Dt}. \quad (5.11)$$

As a Gaussian process, the Wiener-Levy process is completely determined by its mean value and its covariance.

For the rest of this chapter, it is important to note that, if $\tilde{\xi}$ is a white noise, the stochastic process

$$\tilde{y}(t) = \int_0^t \tilde{\xi}(\tau) d\tau \quad (5.12)$$

is a Wiener-Levy process.

5.2 Stochastic equations

5.2.1 Master equation

A Markov-process $\tilde{x}(t)$ can be completely determine by its initial pdf $f(x_0; t_0)$ and its transition density function $f(x_1; t_1 | x_0; t_0)$. However, these functions cannot be chosen arbitrarily; they must satisfy a.o. the Chapman-Kolmogorov equation [187]:

$$f(x; t | x_0; t_0) = \int f(x; t | x_1; t_1) f(x_1; t_1 | x_0; t_0) dx_1. \quad (5.13)$$

This equation states that the probability to go from $(x_0; t_0)$ to $(x; t)$ is the sum over all intermediate $(x_1; t_1)$. A graphical representation of eq. (5.13) [188] is given on Figure 5-6 where the probability to go from $(x_0; t_0)$ to $(B; t)$ where B is a interval of \mathbb{R} is the sum over all intermediate $(dx_1; t_1)$.

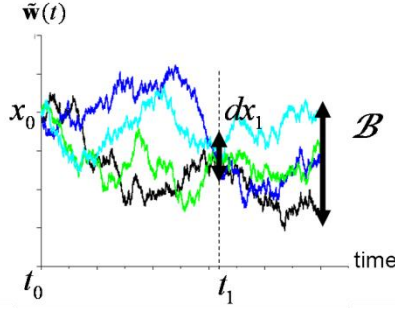


Figure 5-6: Illustration of the Chapman-Kolmogorov equation [188].

A differential form of this relation (5.13) is the Master equation [187]:

$$\frac{\partial}{\partial t} f(x; t | x_0; t_0) = \int w(x | x', t) f(x'; t | x_0; t_0) dx' - \int w(x' | x, t) f(x; t | x_0; t_0) dx'. \quad (5.14)$$

In equation (5.14), $w(x | x', t)$ is defined as the transition rate, the probability per time unit, for a transition from x' to $x \neq x'$ at time t . $w(x | x', t)$ has to be known from a physical context. The Master equation provides the evolution of the density function $f(x, t)$ with prescribed initial pdf $f(x, t = 0)$.

The Master equation can be interpreted as a local balance for the probability density [187]. For example, the conditional density function $f(x; t | x_0, t_0) \equiv f(ns; t | n_0s, t_0)$, $n \in \mathbb{Z}$, of the random walk (step length s) at the level n increases due to the transition from levels $n \pm 1$ to level n but decreases following the opposite transition. Furthermore, the probability to be at the level n and $n \pm 1$ is $f(ns; t | n_0s, t_0)$ and $f((n \pm 1)s; t | n_0s, t_0)$, respectively. Thus, the variation of $f(ns; t | n_0s, t_0)$ is given by:

$$\frac{\partial}{\partial t} f(ns; t | n_0s, t_0) = [w_+(n-1) f((n-1)s; t | n_0s, t_0) + w_-(n+1) f((n+1)s; t | n_0s, t_0)] - [w_+(n) + w_-(n)] f(ns; t | n_0s, t_0) \quad ; \quad (5.15)$$

where $w(n|n-1) = w_+(n-1)$; $w(n|n+1) = w_-(n+1)$; $w(n+1|n) = w_+(n)$ and $w(n-1|n) = w_-(n)$ (Figure 5-7). Clearly, (5.15) is the discrete form of the Master equation (5.14) for a one-step process.

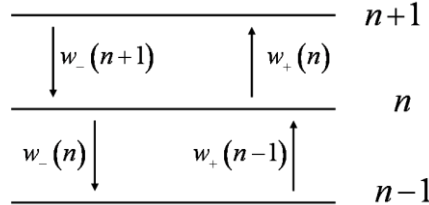


Figure 5-7: Schematic representation of a one-step jump process with transition rate w_+ and w_- [187].

5.2.2 Fokker-Planck equation

The Master equation is particularly well suited for birth and death problems; e.g. to investigate properties at a molecular level in gas dynamics. Larger scales are considered in fluid dynamics and an approximation of the Master equation for small transition step $x - x'$ generally is more adequate. This approximation called the Fokker-Planck equation (FPE) is obtained from a Taylor expansion (named Kramers-Moyal in this particular application) of the Master equation about x' until second order terms [189].

The Fokker-Planck equation of the conditional density function $f(x; t | x_0, t_0)$ reads:

$$\frac{\partial}{\partial t} f(x; t | x_0, t_0) = -\frac{\partial}{\partial x} [A(x, t) f(x; t | x_0, t_0)] + \frac{1}{2} \frac{\partial^2}{\partial x^2} [B(x, t) f(x; t | x_0, t_0)]. \quad (5.16)$$

The corresponding equation for the marginal pdf $f(x; t)$ is simply [189]:

$$\frac{\partial}{\partial t} f(x; t) = -\frac{\partial}{\partial x} [A(x, t) f(x; t)] + \frac{1}{2} \frac{\partial^2}{\partial x^2} [B(x, t) f(x; t)]. \quad (5.17)$$

The first and second terms on the right hand side represent the drift and the diffusion of the density function, respectively [190].

The correspondence Master equation / FPE can be illustrated by the correspondence random walk / Wiener-Levy process. Considering the example of section 5.1.3.2, the random walk transition probability per unit time is $w_-(n) = w_+(n) = 1/T$. Introducing this quantity into the Master eq. (5.15) and expanding the resulting expression up to second order in s for small s , one obtains the following FPE [190]:

$$\frac{\partial}{\partial t} f(x, t | x_0, t_0) = (s^2/T) \frac{\partial^2}{\partial x^2} f(x, t | x_0, t_0). \quad (5.18)$$

Introducing D such as eq. (5.8) is satisfied (infinitely small time and length steps), eq. (5.18) becomes the diffusion equation:

$$\frac{\partial}{\partial t} f(x, t | x_0, t_0) = D \frac{\partial^2}{\partial x^2} f(x, t | x_0, t_0); \quad (5.19)$$

whose solution is the Wiener-Levy process:

$$f(x; t | 0; 0) = \frac{1}{\sqrt{2\pi Dt}} e^{-x^2/2Dt}. \quad (5.20)$$

Figure 5-8 represents the probability density function of a Wiener-Levy process at four different times.

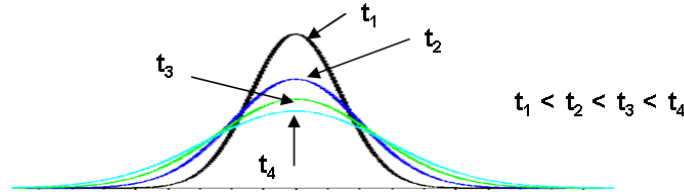


Figure 5-8: Probability density function of a Wiener-Levy process at four different times.

5.2.3 Ito formulation

For complex geometries or complex FPE, the Ito formulation is generally more practicable. Basis for the Ito stochastic differential equation (SDE) is the Langevin SDE consisting of an ordinary differential equation (ODE) in which a rapidly and irregularly fluctuating random function of time occurs. Typically in the form:

$$\frac{d\tilde{\mathbf{x}}}{dt} = a(\tilde{\mathbf{x}}, t) + b(\tilde{\mathbf{x}}, t) \tilde{\xi}(t); \quad (5.21)$$

where $\tilde{\mathbf{x}}(t)$ is the variable of interest, $a(\tilde{\mathbf{x}}, t)$ and $b(\tilde{\mathbf{x}}, t)$ are known functions and $\tilde{\xi}(t)$ is the rapidly fluctuating quantity idealized as a white noise (sect. 5.1.3.1).

From a mathematical point of view, (5.21) is not very satisfactory [190]. An integral formulation using property (5.12) of the Wiener-Levy process $\tilde{\mathbf{w}}(t)$ is more rigorous. One of these integral formulations is the Ito formulation. In this framework, $\tilde{\mathbf{x}}(t)$ obeys the Ito SDE written as [190]:

$$d\tilde{\mathbf{x}} = a(\tilde{\mathbf{x}}, t) dt + b(\tilde{\mathbf{x}}, t) d\tilde{\mathbf{w}}(t); \quad (5.22)$$

if for all t and t_0

$$\tilde{\mathbf{x}}(t) = \tilde{\mathbf{x}}(t_0) + \int_{t_0}^t a(\tilde{\mathbf{x}}, t') dt' + \int_{t_0}^t b(\tilde{\mathbf{x}}, t') d\tilde{\mathbf{w}}(t'). \quad (5.23)$$

It can be shown that the Ito SDE

$$d\tilde{\mathbf{x}}(t) = A(\tilde{\mathbf{x}}(t), t) dt + \sqrt{B(\tilde{\mathbf{x}}(t), t)} d\tilde{\mathbf{w}}(t) \quad (5.24)$$

is equivalent to the FPE (5.17) [190].

This is advantageous because Monte-Carlo procedures [190] can be employed to solve the Ito SDE. For example, the Cauchy-Euler method can be used to construct a solution (Figure 5-9). Considering the discretized form of the SDE (5.22) at the mesh of points t_i ($t_0 < \dots < t_i < \dots < t_n$):

$$\tilde{\mathbf{x}}_{i+1} = \tilde{\mathbf{x}}_i + a(\tilde{\mathbf{x}}_i, t_i) \Delta t_i + b(\tilde{\mathbf{x}}_i, t_i) \Delta \tilde{\mathbf{w}}_i; \quad (5.25)$$

where $\tilde{\mathbf{x}}_i = \tilde{\mathbf{x}}(t_i)$, $\Delta t_i = t_{i+1} - t_i$ and $\Delta \tilde{\mathbf{w}}_i = \tilde{\mathbf{w}}(t_{i+1}) - \tilde{\mathbf{w}}(t_i)$; $\tilde{\mathbf{x}}_{i+1}$ is calculated from $\tilde{\mathbf{x}}_i$ by adding a deterministic term $a(\tilde{\mathbf{x}}_i, t_i)\Delta t_i$ and a stochastic term $b(\tilde{\mathbf{x}}_i, t_i)\Delta \tilde{\mathbf{w}}_i$.

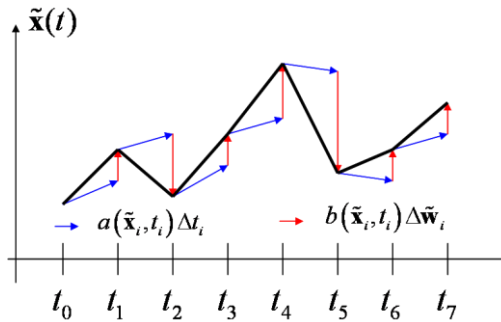


Figure 5-9: Construction of one solution of the Ito SDE $d\tilde{\mathbf{x}} = a(\tilde{\mathbf{x}}, t)dt + b(\tilde{\mathbf{x}}, t)d\tilde{\mathbf{w}}(t)$ with the Cauchy-Euler method.

The solution is obtained for sufficiently small time step and repeated for an infinite number of trajectories. The statistic of the trajectories governed by (5.24) provides an equivalent statistical information as delivered by the analytical solution of (5.17).

From this analysis, the physical meaning of terms $A(\tilde{\mathbf{x}}(t), t)$ and $B(\tilde{\mathbf{x}}(t), t)$ in the FPE can be better described: $A(\tilde{\mathbf{x}}(t), t)$ corresponds to a deterministic drift; while the diffusion term $B(\tilde{\mathbf{x}}(t), t)$ represents the stochastic fluctuations.

As an example, the diffusion eq. (5.19) proposed in its FPE formulation is equivalent to the Ito SDE:

$$d\tilde{\mathbf{x}} = \sqrt{2D}d\tilde{\mathbf{w}}(t). \quad (5.26)$$

Eq. (5.26) represents the trajectory $\tilde{\mathbf{x}}(t)$ of Brownian particles agitated through the turbulent velocity field (if D is the turbulent diffusion coefficient) or thermal fluctuations (if D is the molecular diffusion coefficient) and deviated as a result of collision with the other particles.

Figure 5-10 illustrates the correspondence between the Master equation, the Fokker-Planck equation and the Ito formulation.

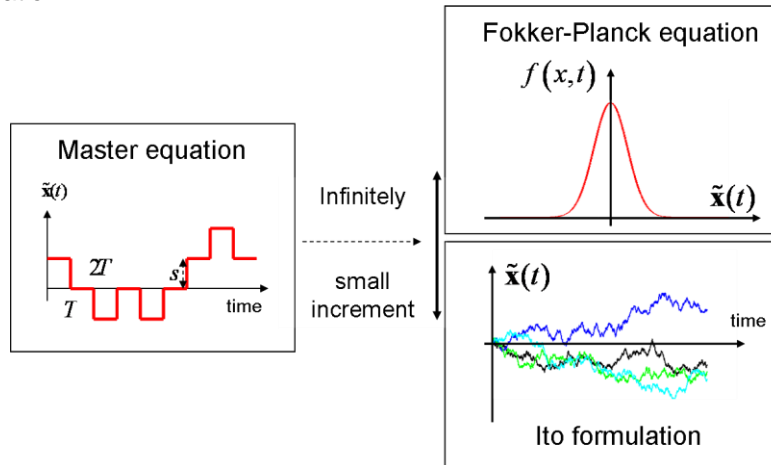


Figure 5-10: Illustration of the relation between Master equation (fig. on the left: random walk), Fokker-Planck equation (fig. on the top right: analytical solution of diffusion equation – density function of Wiener-Levy process) and Ito formulation (fig. on the bottom right: four particle trajectories of eq. (5.26)).

5.3 Modeling with stochastic processes

5.3.1 Principle

A dynamical system generally is governed by processes with very different time scales. If the Master equation or FPE associated to the system is not already known, random fluctuations commonly are

introduced in system's ODE to represent variables which are much faster than the variables of interest. The ODE becomes a SDE which can be interpreted as an Ito SDE.

Then, it is possible either to solve the Ito SDE, for example with Monte-Carlo techniques, or to solve the corresponding FPE if an analytical solution exists. This modeling is also called adiabatic elimination since it is equivalent to assume that the slow variable remains constant during the relaxation of the fast variable [190].

5.3.2 Example

For example, considering the Brownian motion of particles (eq. (5.26)) due to thermal motion, the variable of interest is the position $\tilde{\mathbf{x}}(t)$ of the particles. The velocity varies very fast between two collisions and is generally unobservable. Particles velocity is replaced by a white noise process.

5.3.3 Limitation

In contrast to the molecular motion, the modeling of the turbulent motion with a Markovian process requires more attention. Modeling of the velocity by a fast varying process is valid as long as the observation times dt are much larger than the characteristic time scale T_L of the velocity $\tilde{\mathbf{u}}(t)$ of the particles [186]:

$$dt \gg T_L ; \quad (5.27)$$

where T_L is defined as the integral of the normalized autocorrelation R_L of $\tilde{\mathbf{u}}(t)$ (see Figure 5-11, [186]):

$$T_L = \int_0^{\infty} R_L(\tau) d\tau . \quad (5.28)$$

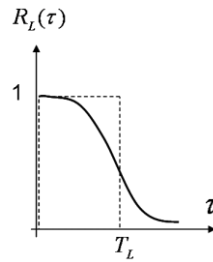


Figure 5-11: Illustration of the normalized autocorrelation function $R_L(\tau)$ of particle velocity, T_L being the integral time scale [186].

As long as eq. (5.27) is satisfied, the process is observed in its diffusive regime and the coefficient of turbulent diffusion D_t in homogeneous turbulence can be related to the variance and characteristic time of the velocity field [186]:

$$D_t = E[\tilde{\mathbf{u}}'^2] T_L . \quad (5.29)$$

In contrast, when the observation time do no longer satisfy eq. (5.27), it is erroneous to represent the velocity by random fluctuations. If no model exist elsewhere, it is necessary to solve the governing equation of the particle velocity. In that case, Thomson [191] showed that the most general form of the velocity equation is an Ito SDE:

$$d\tilde{\mathbf{u}} = \tilde{\mathbf{a}}(\tilde{\mathbf{u}}, \tilde{\mathbf{x}}, t) dt + \sqrt{C_0 \varepsilon} d\tilde{\mathbf{w}}(t) ; \quad (5.30)$$

where C_0 is the universal constant derived by Kolmogorov [192] and ε is the mean turbulent dissipation rate.

In this probabilistic model, the acceleration is considered to be an external variable varying faster than $\tilde{\mathbf{u}}(t)$ and thus represented by random fluctuations. $\tilde{\mathbf{x}}(t)$ is obtained by integration in time and its variance becomes

$$\hat{\sigma}_x^2 = 2E[\tilde{\mathbf{u}}'^2] T_L \left[dt - T_L \left(1 - \exp\left(-\frac{dt}{T_L}\right) \right) \right] . \quad (5.31)$$

For $dt \gg T_L$, eq. (5.31) provides the diffusion regime with:

$$\hat{\sigma}_x^2 = 2E[\tilde{\mathbf{u}}'^2]T_L dt = 2D_t dt ; \quad (5.32)$$

while for smaller time, eq. (5.31) indicates the particles have essentially a straight-line motion [189]:

$$\hat{\sigma}_x \approx \sqrt{E[\tilde{\mathbf{u}}'^2]} dt . \quad (5.33)$$

These results are valid as long as the observation time is larger than the acceleration characteristic time:

$$T_a = \int_0^\infty R_{\tilde{\mathbf{a}}}(s) ds . \quad (5.34)$$

In equation (5.34), $R_{\tilde{\mathbf{a}}}$ is the normalized autocorrelation of the particle acceleration.

5.4 Pdf transport equations

5.4.1 Principle

We have seen in chapter *numerical modeling* that, in spite of the drastic increase in computer resources during the last decades, local and instantaneous equations in high-Reynolds flows require resolution of small length and time scales beyond current computing capability. Averaging is required, i.e., time-averaging in Reynolds-Averaged Navier-Stokes Simulations (RANS) or spatial-filtering in Large Eddy Simulations (LES). This averaging leads to open terms for any non-linear process $f(\varphi)$ function of the flow variable φ , since:

$$\langle f(\varphi) \rangle - f(\langle \varphi \rangle) \neq 0 . \quad (5.35)$$

In eq. (5.35), $\langle \cdot \rangle$ represents the averaging operator. Closure of open terms exploits mean (RANS) or filtered (LES) quantities to reproduce the effect of the unresolved scales.

5.4.1.1 Stochastic model

Many years of intensive turbulence research emphasize the challenge of closing highly non-linear terms. Therefore, the strategy of the pdf transport method introduced by Dopazo and O'Brien [14] is different. To avoid the loss of information due to the averaging, the flow field variables are represented by stochastic processes. The joint-pdf transport equation (5.40) or (5.42) of these stochastic processes is modeled and solved; thereby reproducing the statistics of the original governing equations.

This technique is very attractive since one has access to all moments (see *moments* in appendix B) of the quantities involved in the pdf (typically velocities and/or scalar properties) so that a.o. non-linear source terms appear in closed form and do not need modeling (see *expectation value* in appendix B).

5.4.1.2 Velocity-composition vs. composition pdf

Basically, two pdf transport equations can be found in the literature. If one is concerned with velocity and scalar composition statistics, the pdf transport equation of the velocity-composition joint-pdf $f_{\tilde{\mathbf{u}}\tilde{\boldsymbol{\psi}}}(\mathbf{V}, \boldsymbol{\psi}; \mathbf{x}, t)$ is derived. If, in contrast, only composition statistics is of interest, the pdf transport equation of the composition joint-pdf $f_{\tilde{\boldsymbol{\psi}}}(\boldsymbol{\psi}; \mathbf{x}, t)$ is derived.

In these expressions, vectors of stochastic processes are introduced. The components of these vectors are stochastic processes. For a given position \mathbf{x} and given time t , $\tilde{\mathbf{U}}(\mathbf{x}, t)$ is the stochastic velocity vector. Its components $\tilde{U}_i(\mathbf{x}, t), i=1..3$ are stochastic processes. The same applies for $\tilde{\boldsymbol{\phi}}(\mathbf{x}, t)$ the scalar properties vector. For a given position \mathbf{x} and given time t , each of its components $\tilde{\phi}_\alpha(\mathbf{x}, t), \alpha=1..N_\phi, N_\phi$ being the number of scalars, is a stochastic process.

In this context, $f_{\tilde{\mathbf{u}}\tilde{\boldsymbol{\psi}}}(\mathbf{V}, \boldsymbol{\psi}; \mathbf{x}, t) d\mathbf{V} d\boldsymbol{\psi}$ is the probability of the event:

$$\{V_i \leq \tilde{U}_i(\mathbf{x}, t) \leq V_i + dV_i, i=1..3\} \cap \{\psi_\alpha \leq \tilde{\phi}_\alpha(\mathbf{x}, t) \leq \psi_\alpha + d\psi_\alpha, \alpha=1..N_\phi\} ; \quad (5.36)$$

for $(d\mathbf{V}, d\boldsymbol{\psi}) \rightarrow (\mathbf{0}, \mathbf{0})$ where $\mathbf{V} = (V_i)$, $i = 1..3$ and $\boldsymbol{\psi} = (\psi_\alpha)$, $\alpha = 1..N_\phi$; at position \mathbf{x} and time t .

However, all flow information, typically pressure, is not obtained with the velocity-composition joint-pdf or the composition joint-pdf. Other equations need to be solved in parallel. One common approach is to use an Euler solver for this purpose.

5.4.2 Derivation

The transport equation of the one-point one-time joint-pdf $f_{\tilde{\mathbf{u}}\tilde{\boldsymbol{\phi}}}(\mathbf{V}, \boldsymbol{\psi}; \mathbf{x}, t)$ is obtained by averaging the material derivative of the so called fine-grained velocity-composition (first order) pdf $f_{\tilde{\mathbf{u}}\tilde{\boldsymbol{\phi}}}^+(\mathbf{V}, \boldsymbol{\psi}; \mathbf{x}, t)$. $f_{\tilde{\mathbf{u}}\tilde{\boldsymbol{\phi}}}^+(\mathbf{V}, \boldsymbol{\psi}; \mathbf{x}, t)$ is defined as [193]:

$$f_{\tilde{\mathbf{u}}\tilde{\boldsymbol{\phi}}}^+(\mathbf{V}, \boldsymbol{\psi}; \mathbf{x}, t) \equiv \delta(\tilde{\mathbf{U}}(\mathbf{x}, t) - \mathbf{V}) \cdot \delta(\tilde{\boldsymbol{\phi}}(\mathbf{x}, t) - \boldsymbol{\psi}) = \prod_{i=1}^3 \delta(\tilde{U}_i(\mathbf{x}, t) - V_i) \prod_{\alpha=1}^{N_\phi} \delta(\tilde{\phi}_\alpha(\mathbf{x}, t) - \psi_\alpha); \quad (5.37)$$

where N_ϕ is the number of scalar properties $\tilde{\phi}_\alpha(\mathbf{x}, t)$. Thus, $f_{\tilde{\mathbf{u}}\tilde{\boldsymbol{\phi}}}^+$ is a $(3 + N_\phi)$ -dimensional delta function at $\{\mathbf{V} = \tilde{\mathbf{U}}(\mathbf{x}, t), \boldsymbol{\psi} = \tilde{\boldsymbol{\phi}}(\mathbf{x}, t)\}$ in the $\mathbf{V} - \boldsymbol{\psi}$ sample space, at every position \mathbf{x} and time t .

$f_{\tilde{\mathbf{u}}\tilde{\boldsymbol{\phi}}}^+(\mathbf{V}, \boldsymbol{\psi}; \mathbf{x}, t)$ is very useful since it possesses the two properties:

$$\langle f_{\tilde{\mathbf{u}}\tilde{\boldsymbol{\phi}}}^+(\mathbf{V}, \boldsymbol{\psi}; \mathbf{x}, t) \rangle = f_{\tilde{\mathbf{u}}\tilde{\boldsymbol{\phi}}}(\mathbf{V}, \boldsymbol{\psi}; \mathbf{x}, t); \quad (5.38)$$

$$\langle \theta(\mathbf{x}, t) f_{\tilde{\mathbf{u}}\tilde{\boldsymbol{\phi}}}^+(\mathbf{V}, \boldsymbol{\psi}; \mathbf{x}, t) \rangle = \langle \theta(\mathbf{x}, t) | \tilde{\mathbf{U}}(\mathbf{x}, t) = \mathbf{V}, \tilde{\boldsymbol{\phi}}(\mathbf{x}, t) = \boldsymbol{\psi} \rangle f_{\tilde{\mathbf{u}}\tilde{\boldsymbol{\phi}}}(\mathbf{V}, \boldsymbol{\psi}; \mathbf{x}, t); \quad (5.39)$$

$\theta(\mathbf{x}, t)$ being an arbitrary function. Definition and properties of the conditional average are given in appendix B.

5.4.3 Velocity-composition joint-pdf transport equation

The transport equation of the one-point one-time velocity-composition joint-pdf $f_{\tilde{\mathbf{u}}\tilde{\boldsymbol{\phi}}}(\mathbf{V}, \boldsymbol{\psi}; \mathbf{x}, t)$ reads [193]:

$$\begin{aligned} & \overbrace{\frac{\partial \rho f_{\tilde{\mathbf{u}}\tilde{\boldsymbol{\phi}}}}{\partial t} + \frac{\partial \rho V_i f_{\tilde{\mathbf{u}}\tilde{\boldsymbol{\phi}}}}{\partial x_i}}^1 + \overbrace{\left(\rho g_i - \frac{\partial \langle p \rangle}{\partial x_i} \right) \frac{\partial f_{\tilde{\mathbf{u}}\tilde{\boldsymbol{\phi}}}}{\partial V_i}}^2 + \overbrace{\frac{\partial \rho S_\alpha(\boldsymbol{\psi}) f_{\tilde{\mathbf{u}}\tilde{\boldsymbol{\phi}}}}{\partial \psi_\alpha}}^3 \\ & = \underbrace{\frac{\partial}{\partial V_i} \left[\left\langle \left(-\frac{\partial \tau_{ji}}{\partial x_j} + \frac{\partial p'}{\partial x_i} \right) \middle| \mathbf{V}, \boldsymbol{\psi} \right\rangle f_{\tilde{\mathbf{u}}\tilde{\boldsymbol{\phi}}} \right]}_4 + \underbrace{\frac{\partial}{\partial \psi_\alpha} \left[\left\langle \frac{\partial}{\partial x_i} \left(\rho D_\alpha \frac{\partial \phi_\alpha}{\partial x_i} \right) \middle| \mathbf{V}, \boldsymbol{\psi} \right\rangle f_{\tilde{\mathbf{u}}\tilde{\boldsymbol{\phi}}} \right]}_5. \end{aligned} \quad (5.40)$$

In contrast to the classical approach where the Navier-Stokes equations are averaged, the calculation of the pdf transport equation permits to obtain all moments of the processes $\tilde{\mathbf{U}}(\mathbf{x}, t)$ and $\tilde{\boldsymbol{\phi}}(\mathbf{x}, t)$.

In this context, term 1 which represents the change of rate and convection of the pdf, can be calculated with known flow variables and does not require modeling. Term 2 represents the effect of the mean pressure on the pdf. This term is also known because the mean pressure $\langle p \rangle$ can be calculated according to the following Poisson equation [189]:

$$-\frac{1}{\rho} \nabla^2 \langle p \rangle = \left\langle \frac{\partial \tilde{U}_i}{\partial x_j} \frac{\partial \tilde{U}_j}{\partial x_i} \right\rangle = \left\langle \frac{\partial \tilde{U}_j}{\partial x_i} \right\rangle \left\langle \frac{\partial \tilde{U}_j}{\partial x_i} \right\rangle + \frac{\partial \langle \tilde{u}_i \tilde{u}_j \rangle}{\partial x_i \partial x_j}; \quad (5.41)$$

where all flow variables are known. Term 3 represents the source term of the scalar properties equation. It is closed since all flow variables are known. Thus, any source term, including any non-linearity can be calculated without modeling. This is one of the great advantages of the method. Term 4 represents the conditional expectations of the viscous terms and the fluctuating pressure. A model is required to account for this term. Term 5 represents the conditional expectation of the scalar molecular transfer. A model is also required to account for this term.

Term 4 and 5 must be modeled with known flow variables because the joint-pdf $f_{\tilde{\mathbf{u}}\tilde{\phi}}(\mathbf{V}, \boldsymbol{\psi}; \mathbf{x}, t)$ provides no information on the gradient of the fluctuating pressure, of the viscous terms and of the scalar properties. For these terms to be closed in a pdf approach, one should come up with a closure equation for higher-order pdf [186].

5.4.4 Composition pdf transport equation

Integration of eq. (5.40) over the velocities provides the one-point one-time pdf transport equation of the composition pdf $f_{\tilde{\phi}}(\boldsymbol{\psi}; \mathbf{x}, t)$ [193]:

$$\overbrace{\frac{\partial \rho f_{\tilde{\phi}}}{\partial t}}^6 + \overbrace{\frac{\partial \rho \langle \tilde{\mathbf{U}}_i \rangle f_{\tilde{\phi}}}{\partial x_i}}^7 + \overbrace{\frac{\partial \rho S_\alpha(\boldsymbol{\Psi}) f_{\tilde{\phi}}}{\partial \psi_\alpha}}^8 = - \overbrace{\frac{\partial}{\partial x_i} \left[\langle u'_i | \boldsymbol{\Psi} \rangle \rho f_{\tilde{\phi}} \right]}^8 + \overbrace{\frac{\partial}{\partial \psi_\alpha} \left[\left\langle \frac{\partial}{\partial x_i} \left(\rho D_\alpha \frac{\partial \phi_\alpha}{\partial x_i} \right) \middle| \boldsymbol{\Psi} \right\rangle f_{\tilde{\phi}} \right]}^9. \quad (5.42)$$

In that case, all moments of the process $\tilde{\phi}(x, t)$ are known but the pdf equation does not provide any information on the moments of the velocity field $\tilde{\mathbf{U}}(x, t)$. The first moment (mean velocity $\langle \tilde{\mathbf{U}} \rangle$) of components $\langle \tilde{\mathbf{U}}_i \rangle$, $i=1..3$) and, as we will see later, information on the turbulent scales are supposed to be obtained elsewhere, e.g., with an Euler solver.

In this context, term 6 which represents the change of rate and convection of the pdf, can be calculated with known flow variables and does not require modeling. Term 7 represents the source term of the scalar equation. It is closed since the statistic of the scalars is known. Thus, the source term in the scalar equations, including any non-linearity, can be calculated without modeling. This is one of the great advantages of the method. Term 8 represents the conditional expectation of the fluctuating velocity, which is not available from the composition pdf $f_{\tilde{\phi}}(\boldsymbol{\psi}; \mathbf{x}, t)$. A model is required to account for this term. Term 9 represents the conditional expectation of the scalar molecular transfer. A model is also required to account for this term.

5.4.5 Modeling of open terms

In this thesis' framework, the composition pdf is of particular interest. Thus, models description will only be discussed in the context of the composition pdf; while the reader is invited to refer to established material (e.g. [189]) for more information on the velocity-composition joint-pdf.

5.4.5.1 Turbulent transport

The composition pdf only provides information on the statistic of the scalar properties. The conditional average of the velocity fluctuations is not available and must be modeled. Commonly, a gradient hypothesis is used to represent the effect of these fluctuations on the transport of the scalar pdf. Thus, in a RANS approach, term 8 is modeled as follows [193]:

$$-\frac{\partial}{\partial x_i} \left[\langle u'_i | \boldsymbol{\Psi} \rangle \rho f_{\tilde{\phi}} \right]^m = \frac{\partial}{\partial x_i} \left[(D_\alpha)_i \frac{\partial \rho f_{\tilde{\phi}}}{\partial x_i} \right]; \quad (5.43)$$

where $(D_\alpha)_i$ is the turbulent scalar diffusivity; while in a LES calculation, the modeling of term 8 is:

$$-\frac{\partial}{\partial x_i} \left[\langle u'_i | \boldsymbol{\Psi} \rangle \rho f_{\tilde{\phi}} \right]^m = \frac{\partial}{\partial x_i} \left[(D_\alpha)_{sgs} \frac{\partial \rho f_{\tilde{\phi}}}{\partial x_i} \right]; \quad (5.44)$$

where $(D_\alpha)_{sgs}$ is the sub-grid scalar diffusivity. Eq. (5.43) and (5.44) are modeled equations denoted by equal superscript "m".

As discussed in chapter *numerical modeling*, $(D_\alpha)_i$ and $(D_\alpha)_{sgs}$ generally are assumed to scale with the eddy viscosity. Turbulent and sub-grid viscosity are not provided by the composition pdf transport equation. Other equations need to be solved (e.g. RANS equations with adequate turbulent modeling or LES equations with adequate sub-grid turbulence modeling).

5.4.5.2 Molecular transport

Probably the weakest element in the pdf approach is that term 9 in eq. (5.42):

$$\frac{\partial}{\partial \psi_\alpha} \left[\left\langle \frac{\partial}{\partial x_i} \left(\rho D_\alpha \frac{\partial \phi_\alpha}{\partial x_i} \right) \middle| \Psi \right\rangle f_{\tilde{\phi}} \right] \quad (5.45)$$

representing the transport of the pdf under the action of molecular diffusivity is not known: The conditional expectation of the scalar molecular transfer is not available since the pdf contains only one-point statistics. A model is thus required to account for this term.

Modeling of (5.45) is quite complicated. Indeed, molecular mixing occurs at the smallest length scales [194] and has a two-fold action [193]: it disperses the scalar in the physical space while it decreases scalar variance in the composition space (Figure 5-12).

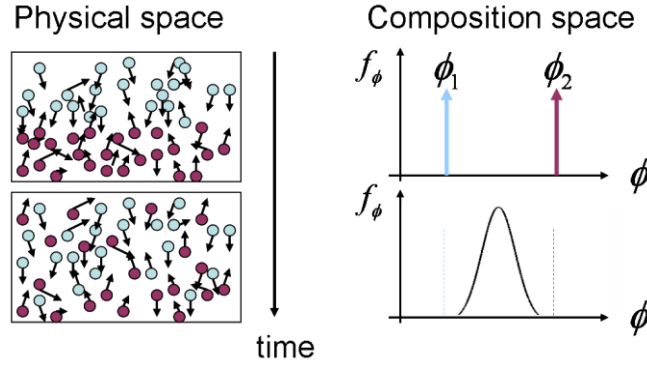


Figure 5-12: Illustration of molecular mixing: dispersion in the physical space (left) and variance reduction in the composition space (right).

A model for (5.45) should fulfill several criteria (e.g. [189], [195]). Among others, the mean value of the scalar property should not be modified; the variance of the scalar property must decrease; and the pdf should relax to Gaussianity in homogeneous turbulence.

The dispersion in the physical space generally is caused by the mean scalar molecular flux [193]. It commonly is modeled by a deterministic molecular diffusion term:

$$\frac{\partial}{\partial \psi_\alpha} \left[\left\langle \frac{\partial}{\partial x_i} \left(\left\langle \rho D_\alpha \frac{\partial \phi_\alpha}{\partial x_i} \right\rangle \right) \middle| \Psi \right\rangle f_{\tilde{\phi}} \right]^m = \frac{\partial}{\partial x_i} \left[D_\alpha \frac{\partial \rho f_{\tilde{\phi}}}{\partial x_i} \right]. \quad (5.46)$$

In contrast, variance reduction in the composition space is due to the fluctuating scalar molecular transport [193]. In this thesis, the interaction by exchange with the mean (IEM), also called return-to-the-mean model, is used to model this phenomenon as follows:

$$\frac{\partial}{\partial \psi_\alpha} \left[\left\langle \frac{\partial}{\partial x_i} \left(\rho D_\alpha \frac{\partial^2 \phi_\alpha}{\partial x^2} - \left\langle \rho D_\alpha \frac{\partial \phi_\alpha}{\partial x_i} \right\rangle \right) \middle| \Psi \right\rangle f_{\tilde{\phi}} \right]^m = \frac{\partial}{\partial \psi_\alpha} \left[\frac{1}{2} \frac{(\psi_\alpha - \langle \tilde{\phi}_\alpha \rangle)}{\tau_\phi} \rho f_{\tilde{\phi}} \right]. \quad (5.47)$$

Scalar fluctuations relax to the mean value $\langle \tilde{\phi}_\alpha \rangle$ of the components $\tilde{\phi}_\alpha$ of $\tilde{\phi}$. τ_ϕ is the relaxation time which usually scales with the turbulent time scale τ_t :

$$\tau_\phi = \frac{\tau_t}{C_\phi}; \quad (5.48)$$

where C_ϕ is a model constant.

Turbulent time scale τ_t is not provided by the composition pdf equation. Other equations are solved; for instance LES equations, where τ_t is the sub-grid mixing time scale defined as [152]:

$$\tau_t = \frac{\langle \rho \rangle \Delta^2}{\eta + \eta_{sgs}}. \quad (5.49)$$

The IEM simulates flow realization interaction through mean fields and not through direct flow realizations interaction (such as in Curl model [15]). Despite its simplicity, it possesses the three most essential characteristics of a mixing model [193]: the mean value of the scalar property is not modified; the variance of the scalar property decays; and the scalar remains bounded.

5.5 Lagrange approach for pdf equations

5.5.1 Monte-Carlo Lagrange

Both velocity-composition and composition pdf transport eq. (5.40) and (5.42) are FPE. Since analytical expressions are in general not available, the usual technique developed in [15] is to consider the equivalent Ito formulation. A Lagrange solver is employed with Monte-Carlo techniques to follow notional particles which carry flow information according to the specific stochastic Ito SDE. The Monte-Carlo technique is particularly well suited for such complex problems in multi-dimensional spaces.

5.5.2 Particle equations for the composition-pdf

Using eq. (5.43) [or (5.44)], eq. (5.46) and eq. (5.47) in eq. (5.42) to model term 8 and 9, respectively, the modeled composition pdf is defined by:

$$\overbrace{\frac{\partial \rho f_{\phi}}{\partial t} + \frac{\partial \rho \langle \tilde{\mathbf{U}}_i \rangle f_{\phi}}{\partial x_i}}^6 + \overbrace{\frac{\partial \rho S_{\alpha}(\boldsymbol{\Psi}) f_{\phi}}{\partial \psi_{\alpha}}}_{7} = \overbrace{\frac{\partial}{\partial x_i} \left[D'_{\alpha} \frac{\partial \rho f_{\phi}}{\partial x_i} \right]}^8 + \overbrace{\frac{1}{2} \frac{\partial}{\partial \psi_{\alpha}} \left[\frac{(\psi_{\alpha} - \langle \tilde{\phi}_{\alpha} \rangle)}{\tau_{\phi}} \rho f_{\phi} \right]}^9; \quad (5.50)$$

where D'_{α} is the combined molecular and turbulent scalar diffusivity.

Equivalence between FPE and Ito formulation allows solving the modeled composition pdf (5.50) with Lagrange techniques. In this context, the pdf is represented by N notional particles at each Euler computational nodes. The particles are modified at each time step to simulate the FPE (5.50). The notional particles are characterized by their mass, their position x_i^* , velocity $\langle \tilde{\mathbf{U}}_i \rangle^*$ and scalar properties $\phi^* = (\phi_{\alpha}^*)$ in a composition pdf. With standard stochastic methods [189], the governing equations of these notional particles can be derived from the pdf equation (5.50).

The trajectory x_i^* of a notional particle is given by [193]:

$$dx_i^* = \langle \tilde{\mathbf{U}}_i \rangle^* dt + (\partial_{x_i} D'_{\alpha})^* dt + \sqrt{2D'_{\alpha}} dW_i, \quad i=1..3; \quad (5.51)$$

and the scalar property ϕ_{α}^* evolves according to [193]:

$$d\phi_{\alpha}^* = S_{\alpha}(\phi^*) dt - 1/2 (\phi_{\alpha}^* - \langle \phi_{\alpha} \rangle) / \tau_{\phi} dt. \quad (5.52)$$

The asterisk refers to any notional particle, dt is a time increment, and W_i a Wiener process which reflects the random walk due to turbulence.

5.5.3 Euler solver

In parallel, a Euler solver is used to describe the fluid system by its Euler velocity and pressure field, $\langle \tilde{\mathbf{U}}(x,t) \rangle$ and $\langle p(x,t) \rangle$, respectively; and to gather the statistical information needed for the particle trajectories (Figure 5-13), for example the mean density $\langle \rho \rangle$. For the composition pdf eq. (5.42), the Euler solver must also deliver information on turbulent scales (see sect. 5.4.5).

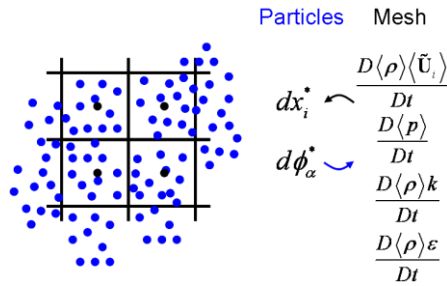


Figure 5-13: Coupling Lagrange (particles) and Euler solver (mesh) for a composition pdf within the pdf transport method.

5.5.4 Euler-Lagrange coupling

Similarly to Lagrange techniques used in cavitating flows, one of the biggest difficulties in the Lagrange pdf method results from the coupling between Lagrange and Euler solver. Complex algorithms for the interpolation and averaging of the flow variables must be developed as well as to ensure consistency between both formulations. The next paragraphs describe some characteristic of Euler-Lagrange solver coupling in the Lagrange pdf transport method.

5.5.4.1 Binning

In the pdf approach, the Euler mesh usually is used for the binning of the particles. This binning process is based on spatial proximity.

5.5.4.2 Interpolation error

In general particle position does not coincide with Euler control volume centroid (Figure 5-13), so that particle variables must be interpolated onto the Euler mesh. Truncation and approximation errors arise; which limits the accuracy of the numerical schemes to be first order accurate in time and space [196].

5.5.4.3 Statistical error

The ensemble-averaging is performed over the particles present in the Euler control volume. It would provide an exact estimation of the mean value if the number of particles was infinite. In practice, a compromise between accuracy and efficiency must be found since the computational cost increases approximately linearly with the number of particles. Thus, the statistical error is of order $N_p^{-1/2}$, with N_p being the number of particles present inside the control volume [193].

5.5.4.4 Code stability

The number of particles has also an influence on the stability of the code. Noise can be critical for the convergence of the Euler solver, and thus of the whole calculation. It is desirable to have approximately the same number of particles in each computational cell, independently of the cell volume, to ensure an approximately uniform distribution of statistical error [193].

The optimal number of particles is obtained with specialized algorithms. It can be improved for steady problems with internal loops and iterations between Lagrange and Euler solver. For unsteady problems, there is no other solution than increasing the number of particles and setting very small time step to ensure code stability [194].

5.5.4.5 Consistency

Since, in the framework of this method, Euler and Lagrange solvers provide some information twice (e.g. velocity in the velocity-composition pdf equation approach); it is essential to verify that both solvers deliver the same information. For instance, it must be ensured that the mean continuity and momentum equation are also satisfied by the velocity field of the particles. This need of consistency does not only translate into supplementary constraints on the particle system but also on the numerical schemes [193].

6 Development of the passive outflow reducer

The preceding chapters provide an informative basis about the physical processes affecting the passive outflow reducer (POR) flow behavior; and about the numerical models used in the POR analysis and the cavitation model development. The present chapter concentrates on the description of the development of the POR design. First, a short introduction (section 6.1) recalls the background of the POR. Then, section 6.2 and 6.3 depict the numerical calculations performed to develop the POR in backward and forward directions, respectively. Finally, section 6.4 explains the way how a compact design is obtained.

6.1 Introduction

In the boiling water reactor KERENA, increased safety and reduced costs are achieved with a smart combination of active and passive safety systems. One of these passive systems is the emergency condenser (EC). The EC passively removes excess heat and in particular the decay heat from the reactor pressure vessel (RPV) during transients and loss of coolant accidents (LOCA) without supplementary water inventory loss.

Water level in the EC condenser tubes is coupled to RPV water level according to the principle of communicating tubes. During a LOCA or a transient with RPV water level drop, EC water level sinks and steam gets in contact with the cold condenser surface. In this way, heat is removed passively through steam condensation. The condensate returns to the RPV through the EC condensate return line. A break of this EC return line must be considered as a design accident. The POR is crucial to ensure that the KERENA reactor returns to a stable and safe state in case of this accident scenario.

The POR is positioned in the reactor nozzle at the end of the EC condensate return line. It limits the loss of coolant from the RPV passively without moving part before other passive and active systems refill the core with coolant. The requirements concerning the POR are conflicting. On the one hand, the mass flow leaving the RPV has to be limited in case of the break of the EC condensate return line. On the other hand, POR flow resistance in the opposite flow direction, from the EC to the RPV, should not decrease EC heat removal capacity. Furthermore, the component must be compact ($L < 1\text{m}$, diameter $< 250\text{mm}$) and easily manufactured.

In the framework of this Ph. D., a new POR design composed of 37 parallel double-nozzle channels (Figure 1-9) is developed. The system is first designed to provide sufficient flow resistance in the backward direction (red arrow on Figure 1-9) using a system code (section 6.2). Afterwards, it is optimized to minimize the flow resistance in the forward direction (blue arrow on Figure 1-9) with CFD software (section 6.3). Both requirements can be fulfilled with one single pipe of about 6 meters length. In order to assure compactness of the component, this parallel disposition is developed (section 6.4).



Figure 6-1: Longitudinal section of POR - 37 channels (blue); material (grey).

6.2 Backward direction

In the backward direction, the objective is to design a geometry limiting the coolant loss to 50 tons during the first 1000 seconds after the double-ended break of the EC condensate return line. Hereby, the boundary conditions at the POR inlet are known from a safety analysis calculation of the KERENA reactor [3] (see chapter *introduction*).

The first step consists in choosing an adequate numerical tool to calculate the leakage flow rate. As discussed in the chapter *numerical modeling*, no universal model exists to calculate this flow rate but some models show good agreement with experimental data for specific geometries and fluid properties: The Bernoulli model provides good results for short geometries with a very strongly subcooled coolant; the homogeneous equilibrium model (HEM) correctly predicts the mass flow rates

in long geometries for a wide range of flow conditions; and the “Henry-Fauske” model is recommended for short geometries with moderately subcooled or saturated coolant. Here, “long geometry” signifies that the length L of this geometry is at least 20 or 30 times larger than the diameter D of the choking cross section of the geometry.

A comparison of the mass flow rates predicted by these three models indicates that the mass flow rate, at given boundary conditions, calculated with the HEM is lower than with the other models. This comparison suggests that the outflow rates are lower in long geometries than in short geometries. This observation has two consequences for the POR design: First, the POR geometry is designed as to be a long geometry; second, the HEM is used to calculate the leakage mass flow rate in the POR.

According to the HEM, the mass flow rate is determined by the area of the choking cross section and the single-phase pressure loss coefficient (ζ -value) upstream of this cross section. A design with a large choking cross section fulfills the LOCA requirement as long as the single-phase pressure loss upstream of this cross section is sufficient. In the POR design, a large cross section is advantageous since it minimizes the flow resistance during emergency core cooling. To produce a sufficient single-phase pressure loss upstream of the POR choking cross section, the idea is to place a sudden enlargement, also called a Carnot diffuser (Figure 6-2).

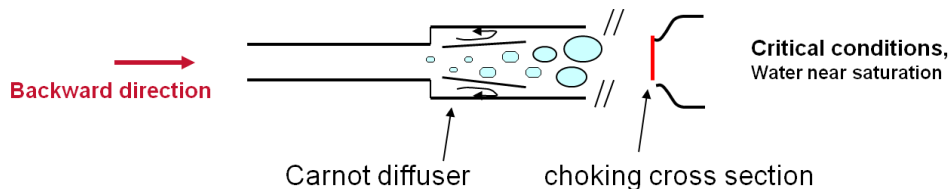


Figure 6-2: Principle of the POR design in the backward direction: a Carnot diffuser positioned upstream of the choking cross section (red).

The Carnot diffuser is a simple single-phase fluidic diode. In contrast to a straight pipe, it produces larger pressure loss in one direction than in the opposite direction. An analytical expression of the Carnot diffuser pressure loss coefficient exists (see chapter *numerical modeling*). According to this expression, it is possible to achieve $\zeta = 0.67$ with a sudden expansion from DN77 to DN180. This is particularly advantageous since the HEM calculation indicates that the LOCA requirement is mastered with a choking nozzle DN77 and a single-phase pressure loss coefficient $\zeta = 0.67$ upstream.

In the Carnot diffuser, energy is dissipated primarily in the recirculation zones downstream of the expansion. Hence, the choking cross section is positioned sufficiently far from the expansion to ensure that these recirculation zones, and thus the pressure loss, are not reduced. Theoretically the pipe situated between the expansion and the choking cross section must be $10D_0$ long, whereby D_0 is the smallest diameter of the Carnot diffuser [40].

Finally, for a valid design calculation (choking cross section DN77 and $\zeta = 0.67$ upstream of this cross section), one must ensure that the flow effectively chokes in the assumed choking cross section (red cross section on Figure 6-2). To rule out the occurrence of choking in the smallest cross section of the Carnot diffuser, the following model implemented into a FORTRAN program is developed for geometries consisting of two consecutive small cross sections with an intermediate enlargement (Figure 6-3).

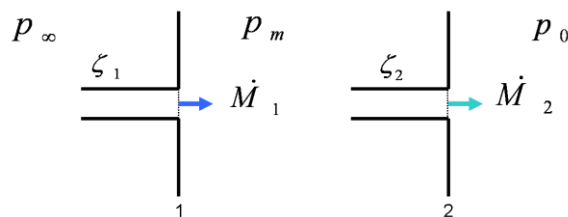


Figure 6-3: Modeling of geometries consisting of two small cross sections (1 and 2); pressure loss coefficients upstream of the cross sections 1 and 2 are ζ_1 and ζ_2 , respectively; mass flow rates in cross sections 1 and 2 are \dot{M}_1 and \dot{M}_2 , respectively; p_∞ , p_m and p_0 are total pressures at geometry inlet, between the smallest cross sections and geometry outlet, respectively.

In this model, the intermediate pressure p_m establishing between the nozzles is varied according to the secant method [197] until the mass flow rates \dot{M}_1 and \dot{M}_2 in cross sections 1 and 2, respectively, become equal (Figure 6-4 (a)). Fluid properties (void fraction α_m , temperature T_m , etc.) between the nozzles are updated according to the value of the pressure p_m . For a prescribed p_m , \dot{M}_1 and \dot{M}_2 are calculated according to HEM (Figure 6-4 (b)). Thereby, the pressure loss is assumed to arise from the friction at pipe walls. Hence, ζ_1 and ζ_2 are estimated with the Colebrook correlation (see chapter *numerical modeling*). The HEM correlation distinguishes between choked and non-choked flow. For this purpose, HEM calculates the critical pressures p_{m1}^* and p_{m2}^* corresponding to stagnation pressures p_∞ and p_m , respectively, and compare them to the outlet pressures. Taking the first nozzle as an example, $p_{m1}^* > p_m$ signifies choking. In the non-choked flow ($p_{m1}^* \leq p_m$), the mass flow rate \dot{M}_1 also depends on backpressure p_m .

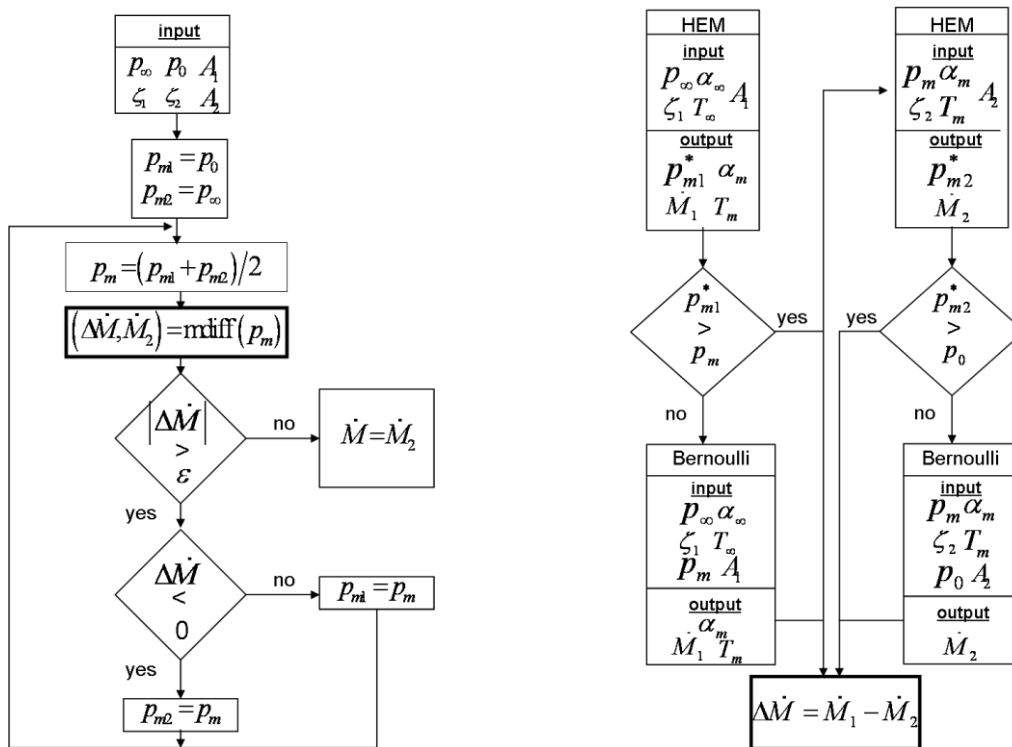


Figure 6-4: Flow diagram of the routines used to estimate critical cross sections in a serial arrangement of two cross sections. On the left: variation of p_m according to secant method [197]. The variation is stopped when mass flow rates difference is smaller than a prescribed ε_{it} . On the right: estimation of mass flow rates \dot{M}_1 and \dot{M}_2 in both sections with HEM.

As an example, mass flow rates \dot{M}_1 and \dot{M}_2 are given as a function of the varying pressure p_m in Figure 6-5. Under critical conditions, \dot{M}_1 is equal to the critical mass flow rate $(\dot{M}_1)^*$ and independent of the pressure p_m . Under sub-critical conditions, \dot{M}_1 , indicated by $(\dot{M}_1)_B$ in Figure 6-5, depends on p_m . The intersection of the curves gives the calculated flow conditions: pressure $(p_m)_0$ establishing within the enlargement and $(\dot{M})_0$ the resulting mass flow rate.

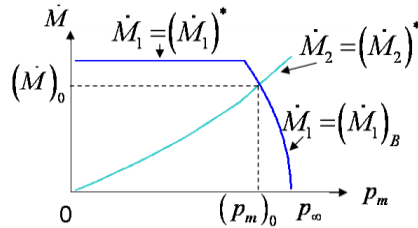


Figure 6-5: Mass flow rates \dot{M}_1 and \dot{M}_2 as a function of the varying pressure p_m ; \dot{M}_1 under critical conditions $(\dot{M}_1)^*$ is independent of the pressure p_m whereas it depends on p_m under sub-critical conditions $(\dot{M}_1)_B$; curves intersection gives calculate flow conditions: pressure $(p_m)_0$ establishing between the cross sections and $(\dot{M})_0$ resulting mass flow rate.

For the particular case displayed on Figure 6-5, the flow is subcritical in the first cross section and critical in the second cross section although the first cross section is 2.25 times smaller than the second cross section. Since this phenomenon is observed under all KERENA LOCA conditions for two identical cross sections, it is assumed that, for a design with two identical cross sections, choking takes place in the second cross section.

6.3 Forward direction

Safety analysis calculations [3] indicate that the POR flow resistance must not exceed 15 kPa at $\dot{M} = 45 \text{ kg/s}$ and system pressure 75bar to guarantee adequate EC heat removal for the KERENA reactor to return to a safe and stable state for all KERENA transients and LOCA. According to the LOCA calculation with the HEM (section 6.2), a long geometry with a choking cross section DN77 and an enlargement from a pipe DN77 to a pipe DN180 masters the LOCA (Figure 6-2). Typically, a geometry consisting of a Carnot diffuser followed by an abrupt contraction (Figure 6-6) fulfills these geometrical requirements. However, the flow resistance in the forward direction is equally high and exceeds the KERENA POR requirement during emergency core cooling.

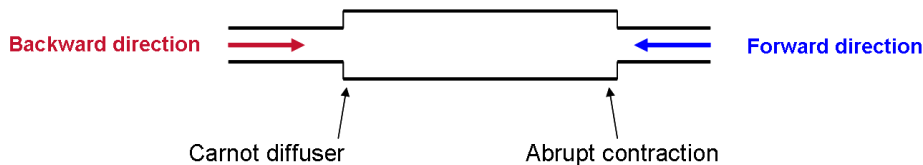


Figure 6-6: Geometry fulfilling backward requirement: Carnot diffuser and abrupt contraction.

The Carnot diffuser also generates large form loss in the counter direction which is known as “Borda opening” pressure loss [133]. To reduce forward direction flow resistance, it is necessary to modify the shape of the Carnot diffuser to avoid a flow detachment in the forward direction. One possibility is to replace the Carnot diffuser by a short Venturi-nozzle (Figure 6-7). With this design modification, flow detachment and pressure loss are strongly reduced during emergency core cooling.

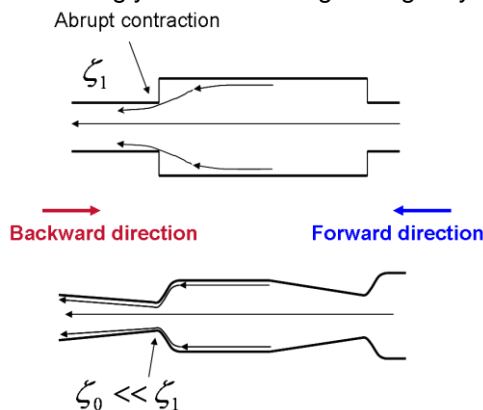


Figure 6-7: Schematic representation of fluid streamlines in an abrupt contraction (top) and a short Venturi-nozzle (bottom); flow detachment and pressure loss are strongly reduced in the Venturi-nozzle.

However, in the backward direction, the pressure loss downstream of a Venturi-nozzle is lower than downstream of a Carnot diffuser. Estimated with a CFD calculation, the pressure loss coefficient of a Venturi-nozzle in the backward direction amounts to $\zeta_{LOCA} = 0.4$. To fulfill the LOCA requirement with this pressure loss coefficient, the HEM shows that the smallest cross section must be further reduced to DN75. To increase conservatism, the smallest and largest sections are designed DN74 and 200, respectively.

Thus, a geometry consisting of two consecutive Venturi nozzles (Figure 6-8), called double-nozzle or double Venturi-nozzle design in the rest of this thesis, also satisfies the LOCA requirement. Its smallest and largest cross sections are DN74 and 200, respectively.

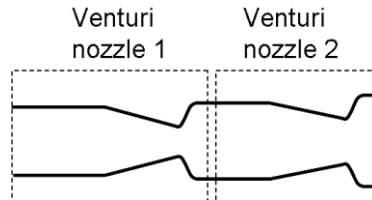


Figure 6-8: Design with two consecutive Venturi nozzles (called double-nozzle or double Venturi-nozzle design in the rest of this thesis).

Transition sections are necessary between the tubes of diameter DN74 and the tubes of diameter DN200 (see Figure 6-8). Optimizing the shape of this double-nozzle design in the forward direction primarily consists in finding the optimal convergence and opening angles $\alpha = \alpha_{opt}$ (see Figure 6-9) of these transition sections.

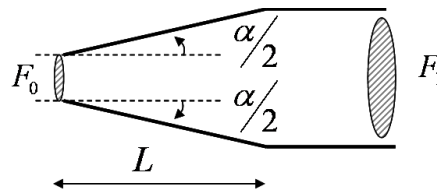


Figure 6-9: Characteristic dimensions for transition sections such as diffusers and contractions.

This optimal angle represents the best compromise between friction and form losses (Figure 6-10). For small α , the cross sectional area is smaller in averaged. Thus, the friction loss coefficient ζ_{fr} is high. In contrast, for large α , the flow detaches and the turbulence is enhanced. The form loss coefficient ζ_{exp} is large. The optimal convergence/opening angle α_{opt} , yields a minimal total flow resistance coefficient ζ .

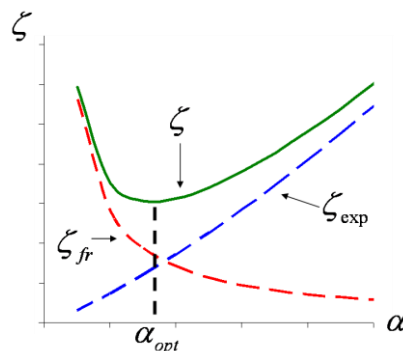


Figure 6-10: Schematic representation of total ζ , friction ζ_{fr} , and form ζ_{exp} loss coefficients in a diffuser in relation to its opening angle α ; α_{opt} being the opening angle at which total flow resistance coefficient is minimal.

Unfortunately, α_{opt} is largely affected by upstream flow conditions such as shape of the boundaries, boundary layer thickness, shape of the velocity profile, degree of turbulence, flow regime both in the boundary layer and in the main flow; and flow compressibility [40]. For example, a tube with constant cross section positioned directly upstream of the diffuser inlet tends to thicken the boundary layer, and thus enhances the risk of flow detachment. The resulting flow resistance increase depends on the

length of the tube positioned upstream of the diffuser but also on the diffuser opening angle. This phenomenon is illustrated on Figure 6-11. The pressure loss coefficient through a diffuser without straight tube is ζ_0 ; while the same diffuser has a pressure loss coefficient ζ when a straight tube is positioned upstream of its inlet. The ratio k_d defined as

$$k_d \equiv \frac{\zeta}{\zeta_0} \quad (6.1)$$

is formed to assess the influence of the straight tube on the flow resistance in the diffuser. Figure 6-11 summarizes data from [40] for diffusers with opening angle $\alpha = 4^\circ$ (blue), $\alpha = 8^\circ$ (red) and $\alpha = 12^\circ$ (green). The flow resistance in a diffuser with an opening angle of 12° is more than doubled at low Reynolds number when a straight tube is positioned upstream of its inlet. The length of the straight tube in this example is $l_0 = 2D_0$, where D_0 is the diameter of the smallest cross section.

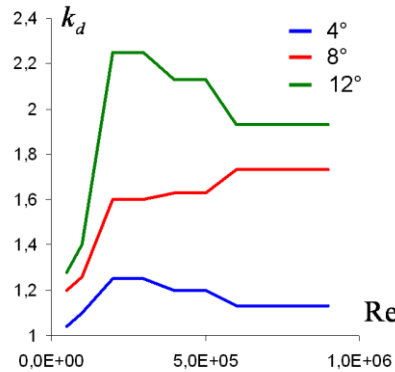


Figure 6-11: Representation of k_d , proportionality factor between the pressure losses in diffusers without and with straight tube for three opening angles $\alpha = 4^\circ$ (blue), $\alpha = 8^\circ$ (red) and $\alpha = 12^\circ$ (green).

The downstream flow conditions also influence the optimal opening angle. In the KERENA reactor, the POR is positioned inside the RPV nozzle. The downward flow of the downcomer may yield flow detachment in the second diffuser if this angle is too large.

In this context, three-dimensional calculations are necessary to optimize the geometry. CFD simulations are carried out with the commercial software STAR-CCM+. The numerical domain consists of a double-nozzle geometry connected to a vessel with downward flow.

The setup of the CFD calculations is summarized in the following:

- Turbulence is predicted with $k-\omega$ SST model of Menter [142]. This turbulence model combines advantages of $k-\omega$ model near walls and of $k-\varepsilon$ model in flow bulk.
- The “All y^+ ” wall treatment switching from viscous sublayer resolution to wall functions according to y^+ -values is adopted to reduce computation time. Since the geometry is designed to avoid flow detachment, the error associated with wall law functions should be limited.
- A steady, segregated solver is employed.
- Water is considered to have constant density and constant temperature.
- The mesh consists of trimmed cells [129] in the bulk and of prism cells [129] near the walls (Figure 6-12). An analysis of the sensitivity of the results on mesh size shows that the discretization errors are in an acceptable range (The difference between the pressure losses calculated on this mesh and on a twice finer mesh is maximum 3%).
- To speed up the calculations, a 60° channel section with periodic boundary conditions is analyzed instead of the complete cross section. Although the flow resistance can be underestimated in this configuration, a sensitivity analysis indicates that the error is limited to about 6%. Therefore, it is neglected during this basic design phase.
- Boundary conditions: The flow at the inlet has a constant velocity profile; flow variables are extrapolated from the computational domain at geometry outlet; no-slip condition at the walls and periodic boundary conditions on the lateral sides of the 60° channel section are imposed.

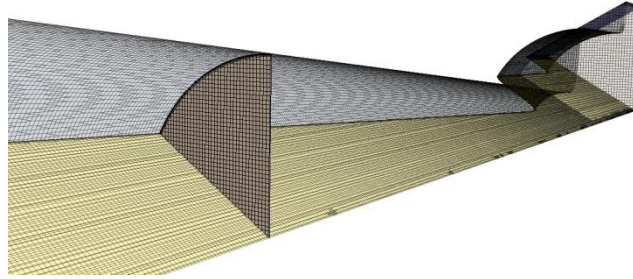


Figure 6-12: Section of the mesh used for the design of the POR in the forward direction.

Resulting from this optimization phase, the double-nozzle design consists of the following parts (Figure 6-13):

- the inlet section (I) homogenizes the flow;
- the contractions (II and V) limits flow resistance and static pressure decrease. They are based on the 5th order polynomial found in [198]. This contraction minimizes boundary layer thickness so that the flow is less liable to detach in the diffuser. This shape also limits the static pressure decrease occurring at the smallest cross sections. This is advantageous to avoid cavitation.
- the diffusers (III and VI) avoid flow detachment and high friction loss with 7° opening angle;
- the cylinder (VII) and the contraction (VIII) assure that the flow in the diffuser (VI) does not detach due to the downward flow of the downcomer.

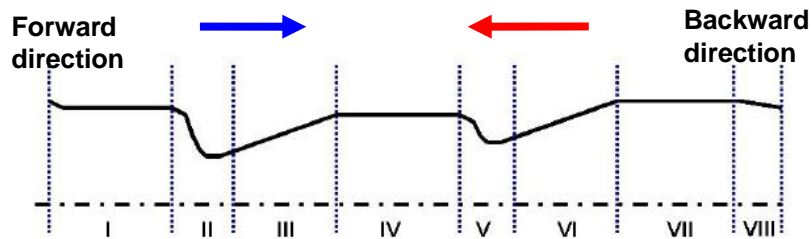


Figure 6-13: Flow sections of a double-nozzle design [inlet (I), outlet (VIII), contractions (II and V) and diffusers (III and VI)].

The CFD calculation indicates that this optimized double-nozzle fulfills the requirement in the forward direction. The calculated pressure loss amounts to 12.5kPa at POR design point (45kg/s at 75bar).

6.4 Size reduction

Calculations performed in sections 6.2 and 6.3 indicate that a POR consisting of a single channel with 2 optimized Venturi-nozzles DN74 and a long intermediate pipe DN200 satisfies the requirements in backward and forward directions. However, with a length of about 6 m, this design is too long.

As a consequence, the following more compact design is developed. The idea is to increase the number of channels to N^2 , to downscale each of them by N , and to connect them in parallel. This results into:

- All the cross section areas of the channels are divided by N^2 .
- The minimal total cross section remains DN74.
- The pressure loss coefficient approximately remains the same in each channel.
- The mass flow rate in each channel is divided by N^2 .

This geometry with N^2 parallel channels downscaled by N has two equivalent minimal cross sections DN74 and the same pressure loss. It can therefore meet LOCA requirement as well.

To position the POR in the RPV nozzle, the POR must be shorter than one meter. Scaling it from six to one meter implies to increase the number of pipes to $6^2 = 36$, whereby each pipe has smallest cross sections DN12.17. A honeycomb-like disposition with 37 channels is proposed for the new design (see Figure 6-14).

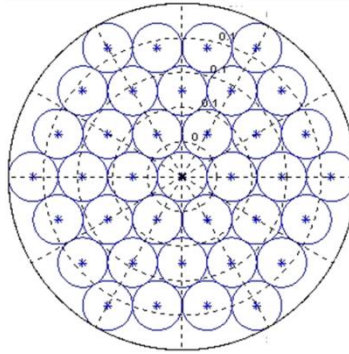


Figure 6-14: Honeycomb-like disposition with 37 channels.

This yields a cluster with 250mm diameter and 900mm length which conveniently fits into the heavy duty reactor pressure vessel nozzle assuring no failure of the passive outflow reducer.

7 Performance tests

To validate the principle of the POR design and analyze its fluidic behavior in both directions, experiments are performed at AREVA Technical Center in Karlstein under realistic boundary conditions. In the backward direction, the loss of coolant through four different channel designs is measured to assess the influence of the size and number of smallest cross sections. In the other flow direction, the flow resistance of three different channel designs is measured to estimate the impact of the opening angles of the diffusers. This chapter *performance tests* outlines the setup and the results of the experiments. Backward and forward directions are treated separately in section 7.2 and 7.3, respectively. In section 7.4, the experimental results are exploited to calculate the performance factor of the POR. Principal information and outlook of this chapter are given in section 7.5.

7.1 Introduction

The new POR design is developed with numerical tools. The HEM is used to estimate the loss of coolant occurring after the break of the EC condensate return line. Single-phase CFD calculations are exploited to minimize the flow resistance during emergency core cooling. Since these models are limited in several respects (see chapter *numerical modeling*), experiments are performed in both directions under realistic plant conditions to validate the POR design at AREVA Technical Center in Karlstein ([199]; [200]).

7.2 Backward direction

The POR is designed to meet the functional requirement in the backward direction with the HEM correlation. The HEM very accurately predicts the critical mass flux for a wide range of flow conditions (from strongly subcooled flow to flow with quality Y_0 up to 0.2) when the geometry is characterized by a large ζ - value [160]. However this modeling does not address directly three-dimensional effects and disregards possible mechanical, thermal or thermodynamic non-equilibrium. Furthermore, it does not reproduce unsteady phenomena. For instance, calculations performed with an unsteady 6-equation system code (RELAP) indicate that, under certain flow conditions, both nozzles interact giving birth to strong mass flow oscillations at low frequency ($\sim 1Hz$) (Figure 7-1).

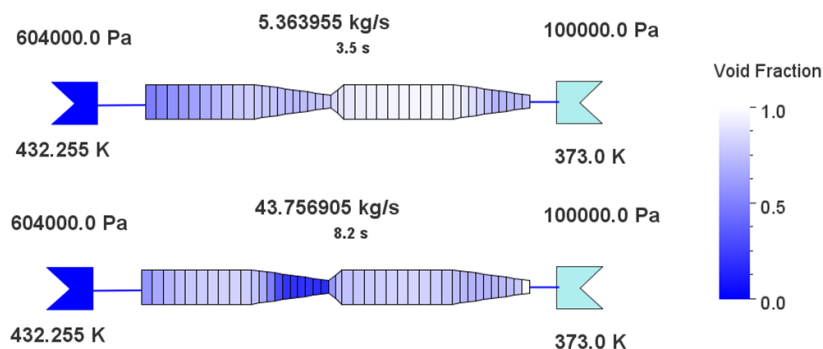


Figure 7-1: Graphical representation of the result of a transient RELAP calculation with inlet pressure 60.4bar and outlet pressure 1bar: the double-nozzle design is colored with void fraction. Strong mass flow oscillations are encountered at steady boundary conditions: (top): very low mass flow at time 3.5s, (bottom) high mass flow at time 8.2s.

In this context, experiments are required to validate the POR design, i.e. to answer the following questions:

- What is the real benefit of positioning a first small cross section upstream of the choking cross section in the backward direction?
- Which smallest cross section area is required to sufficiently limit the loss of coolant for the KERENA reactor to remain in a safe and stable state after the break of the EC condensate return line?
- Do mass flow oscillations occur as a result of small cross sections interaction?

Experiments shall also be exploited to develop a correlation which can be implemented in the safety analysis code RELAP to represent the effect of the POR on the KERENA reactor transients (section 7.2.2.4); and to validate a new cavitation model (chap. *stochastic-field cavitation model*).

7.2.1 Experimental setup

To investigate the general fluid dynamic behavior of double-nozzle channels, four different geometries are tested in the backward direction (Table 7-1): The double-nozzle channels A and B; and the single-nozzle channels C and D. Geometry A is one channel of the KERENA POR; geometry B is similar but with smaller smallest cross sections. Geometry C and D have the same smallest cross section but the straight tube downstream of this cross section is longer in geometry D than in geometry C.

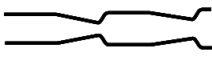
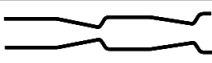
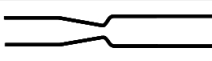
Geometry		Smallest cross section	Number of tests
A- double nozzle		12.17	8
B- double nozzle		11.51	4
C- single nozzle		12.17	3
D- single nozzle		12.17	4

Table 7-1: Geometries tested in the backward direction.

To ease the experimental setup between tests, the geometries consist of interchangeable modules which are assembled leak-proof. Photographs (Figure 7-2) show two of these modules. The transverse pipes are ports for pressure and temperature sensors.



Figure 7-2: Photographs of two of the interchangeable modules assembled leak-proof to form the tested geometries; transverse pipes are ports for pressure and temperature sensors.

The experimental setup [199] used to simulate the backward conditions consists of an accumulator tank which discharges hot water through the geometries into a condensation pool. A schematic representation of the experimental setup is given on Figure 7-3.

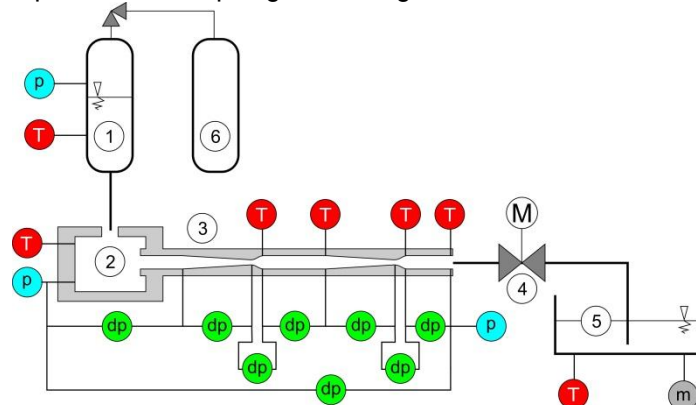


Figure 7-3: Schematic representation of the experimental setup in the backward direction; 1: accumulator tank, 2: connection tank, 3: tested geometry, 4: servo valve, 5: condensation pool.

Pressure in the accumulator tank (1) is imposed by the pressurizer tank (6). The geometry (3) which is tested is connected upstream to a connection tank (2). The test begins when the servo valve (4) opens. Water flows from the accumulator tank through the geometry into a condensation tank (5). The thermo-fluidic conditions present in the downcomer after the break of the EC return line are reproduced at the inlet of the geometries in the tank (2) at quasi steady-state conditions. A photograph of the experimental test stand is presented on Figure 7-4. The isolating coat around the nozzle is removed for the photograph.



Figure 7-4: Photograph of the experimental test stand in the backward direction; isolating coat envelops the connection tank but is removed from around the nozzle.

The four geometries are tested at different pressures (from 5 to 75 bar) and temperatures (from 3K to 40K subcooling). The break mass flow rate is estimated with the temporal variation of the mass of the condensation pool. Pressure (p), pressure difference (dp) and temperature (T) are measured among others along the channels (Figure 7-4).

7.2.2 Experimental results

For none of the tests, high amplitude low frequency mass flow oscillations are observed. Thus, the instabilities monitored in the system code calculations (Figure 7-1) have no physical but numerical origins. No interaction occurs between the smallest cross sections and POR flow rates and loads remain constant under given boundary conditions.

7.2.2.1 Pressure distribution

A typical pressure distribution along a double-nozzle channel is given on Figure 7-5.

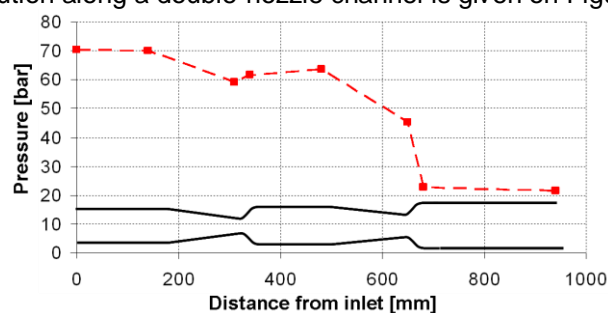


Figure 7-5: Pressure distribution along a double-nozzle channel.

In the first section (up to 200mm), wall shear friction and entrance form loss slightly decrease the static pressure. A larger static pressure drop occurs in the contraction (350mm) mainly due to a dynamic pressure rise. Downstream of the expansion (between 350 and 500mm) the pressure recovery occurs only partially because the flow detaches from the wall and large amounts of energy are dissipated in the recirculation zones. In the second contraction, static pressure fall is amplified which suggests that larger void content, and thus larger velocities and larger flow resistance, are involved. Downstream of the second cross section, no pressure recovery is observed and the pressure remains at saturation conditions.

7.2.2.2 Influence of inlet pressure

A comparison of this pressure distribution (red curve on Figure 7-6) with the one of a test at lower inlet pressure (orange curve on Figure 7-6) indicates that, in this particular case, inlet pressure does not significantly modify the static pressure evolution. A closer look at the data points out that pressure gradients are smaller at lower inlet pressure. This suggests that the mass flow is lower. Available mass flow measurements confirm this assumption: Mass flows measured during the first and second tests are 4.2 and 3.8 kg/s, respectively.

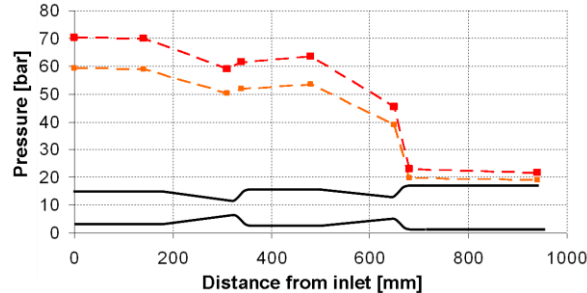


Figure 7-6: Pressure distribution along a double-nozzle channel at two different inlet pressures.

7.2.2.3 Influence of inlet temperature

Comparison between pressure distributions and mass flow rates of the first test (red curve on Figure 7-7; $\dot{M} = 4.2 \text{ kg/s}$) with those of a third test (blue curve on Figure 7-7; $\dot{M} = 7.3 \text{ kg/s}$) proves that a lower pressure at the inlet does not necessarily imply a lower mass flow rate. Despite a lower inlet pressure, the mass flow rate is larger during the third test than during the first test.

In fact, the experimental results of these two tests illustrate the impact of coolant subcooling on the magnitude of the critical two-phase mass flow rates. The subcooling is larger during the third test ($\Delta T = 40 \text{ K}$) than during the first test ($\Delta T = 9 \text{ K}$). Due to the larger coolant subcooling, coolant vaporization is mitigated upstream of the choking cross section. As a result, the flow resistance arising from two-phase interactions is reduced and the speed of sound at the choking cross section is larger. These two phenomena contribute to the larger critical flow rate.

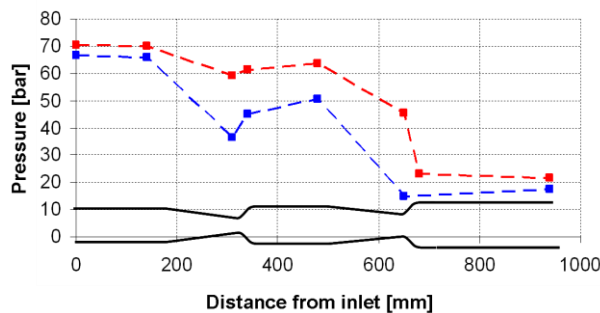


Figure 7-7: Pressure distribution along a double-nozzle channel at two different inlet pressures and subcooling.

7.2.2.4 Mass flow rate

As illustrated by the former paragraphs, an adequate representation of the experimental results addresses both inlet pressure and inlet subcooling. Same inlet pressure but different subcooling may induce large discrepancies between critical two-phase flow rates.

Since the POR and each of its double-nozzle channels are developed with the HEM correlation, this correlation should describe the flow characteristic of channel A and B correctly. One assumption of this model is that the mixture has enough time, and thus the geometry is long enough, to relax to equilibrium. If the geometry is too short, water and steam are not in equilibrium and the measured mass flow is larger than expected.

The experimental results for the four geometries are displayed in Figure 7-8 as a function of inlet pressure. The mass flow rates are normalized by the theoretical mass flow rate predicted by the HEM at same inlet pressure and subcooling. This normalization has the advantage that consequences of

inlet subcooling on mass flow rate are accounted for. Since the HEM accurately predicts the mass flow rate through long straight pipes, the ordinate also gives the ratio between the experimental (through the tested geometries) and the theoretical mass flow rate through a long pipe with constant cross section. The cross section of this pipe with constant cross section equals the smallest cross section of the tested geometries. A ratio which is bigger than one indicates that the mass flow rate is larger through the tested geometry than through a long pipe with constant cross section.

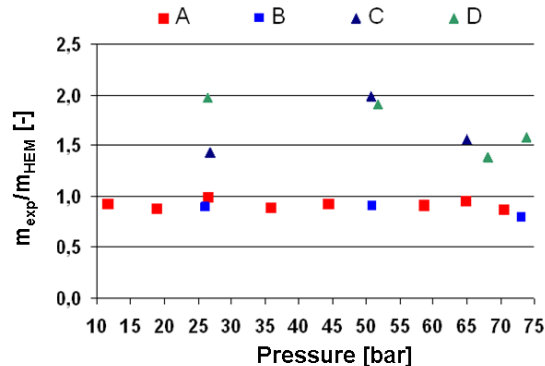


Figure 7-8: Ratio between the experimental mass flow rate measured through the geometries and the theoretical mass flow rate calculated through a long pipe with constant cross section.

Mass flow rates through the single-nozzle designs C and D are much bigger than what would be expected through a long pipe with constant cross section. In contrast mass flow rates through the double-nozzle designs A and B are smaller. From Figure 7-8 it is qualitatively obvious that the use of double-nozzle designs helps reducing the mass flow rate resulting from the break of the EC return line in comparison to single-nozzle designs.

Quantitative information on the total loss of coolant through a double-nozzle design is obtained when the pressure loss coefficient ζ used within the HEM is tuned to fit experimental results. For example HEM with $\zeta = 0.1$ reproduces all experimental results for the design A. This suggests that the fluidic behavior of A is well described by the HEM with $\zeta = 0.1$. Thus, the HEM with $\zeta = 0.1$ can be used to estimate the total coolant loss through the channel A during the whole LOCA (Boundary conditions are extracted from safety analysis calculations for the KERENA reactor [3]).

An extrapolation to 37 identical pipes indicates that the new POR design masters the LOCA requirement (Figure 7-9). Figure 7-9 also shows that the loss of coolant can be reduced up to 50% by the use of a double-nozzle design instead of a single-nozzle design.

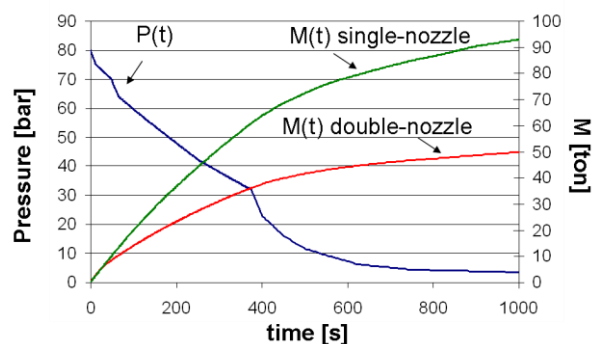


Figure 7-9: Pressure evolution in the downcomer at POR inlet (blue curve); and integral loss of coolant with POR (red curve) and with 37 parallel single-nozzle channels (green curve); during the first 1000s after the break of the EC condensate return line.

7.3 Forward direction

The POR is designed to limit the flow resistance in the forward direction with single-phase constant-density CFD simulations since water flows mostly with large subcooling from the EC into the POR. The effects of the turbulent fluctuations on the mean flow are modeled within the RANS approach. For attached flow, such as encountered in straight pipes and contractions or diffusers with small angles, RANS models are known to be very reliable. However, they often fail to correctly predict detaching flows. As a result of turbulence modeling uncertainties, these flows may be described as non-

detaching flows in the calculation. In this case, the calculated flow resistance is largely underestimated and does not correspond to reality at all. This is troublesome for the POR development since it is not possible to determine precisely which opening angle is optimal for the POR diffusers. This optimal angle is sufficiently large for the POR geometry to be short and the friction loss minimized but sufficiently small for the flow not to detach. To estimate accurately the correct opening angle, a double-nozzle design is tested alternatively with three different diffuser opening angles. Tests are performed under realistic plant conditions for two of these geometries. With the other geometry, experiments are carried out at lower pressures and temperatures. Experimental results should also be useful to validate CFD calculations [201].

To assess the risk of cavitation and the impact of cavitation on the POR fluidic behavior in the forward direction, one test is also performed at high mass flow rate and very low subcooling. Experimental results concerning this experiment are treated in section 7.3.2.3 separately from the other experimental data and shall be exploited to validate the new cavitation model (chap. *POR analysis*).

7.3.1 Experimental setup

For the tests in the forward direction, three different geometries (Table 7-2) are alternatively inserted in the existing KATHY loop [199]. Geometry A is one channel of the POR; while geometries B and C possess diffusers with smaller and larger opening angles, respectively.

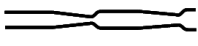
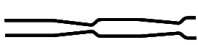
Geometry		Diffuser opening angle	Number of tests
A- POR channel		7	18
B- Smaller diffuser opening angle		5	18
C- Larger diffuser opening angle		12	6

Table 7-2: Geometries tested in the forward direction.

The flow resistance in the channels is measured at imposed mass flow rates. Geometries A and B are tested under realistic plant conditions (at the exception of the test performed to evaluate the impact of cavitation on POR flow behavior): Inlet pressure ranges from 10 to 75 bars; while inlet subcooling spans from -3 to -7K. The geometry C is tested with cold coolant at 10 bars. The experimental setup dedicated to the tests in the EC direction is described on Figure 7-10. The pump (1) enforced a steady state mass flow through the geometry (3). The temperature is regulated by the heat exchanger (2) and the pressure by the pressurizer tank (5). The tank (4) is connected at the outlet of the channel to simulate the downcomer. Pressure (p), pressure difference (dp) and temperature (T) are measured along the geometry.

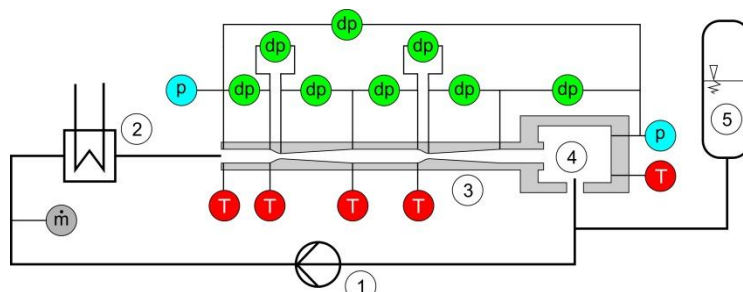


Figure 7-10: Schematic representation of the experimental setup in the forward direction; 1: pump, 2: heat exchanger, 3: tested geometry, 4: connection tank, 5: pressurizer tank.

7.3.2 Experimental results

7.3.2.1 Flow behavior of POR channel

7.3.2.1.1 Pressure loss

A graphical representation of the experimental results obtained with geometry A at POR design point and two other flow conditions at 75bar is displayed in Figure 7-11. The flow resistance is given as a function of the mass flow rate.

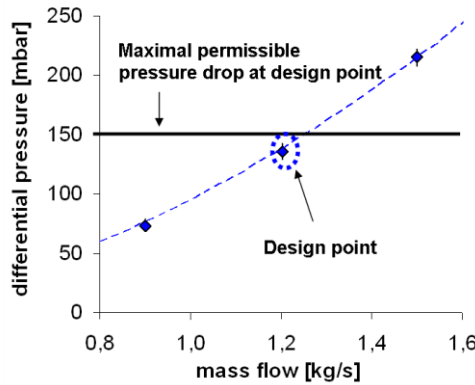


Figure 7-11: Measured pressure drop (diamond) at POR design point (dashed circle) and two other flow conditions at 75 bar; the solid line represents the maximum permissible pressure drop at design point mass flow.

Assuming that the coolant distributes homogeneously in the 37 channels, the flow resistance at design point is obtained from experimental data for geometry A at $\dot{M} = 45/37 \text{ kg/s} = 1.22 \text{ kg/s}$ and 75 bar. In this case the pressure loss is 13,9kPa, i.e. below the maximal authorized flow resistance of 15kPa. Hence, the POR design fulfills the requirement in the forward direction.

7.3.2.1.2 Pressure loss coefficient

The flow resistance induced in the EC system loop tends to decrease EC heat removal capacity. To account for the effect of the POR pressure drop on KERENA transients and LOCA, it is necessary to estimate the POR flow resistance under all possible flow conditions. Analysis of available experimental data on geometry A suggests that a constant pressure loss coefficient $\zeta = 0.20$ (related to the smallest cross section) conservatively represents the POR pressure loss during all measured flow conditions (Figure 7-12).

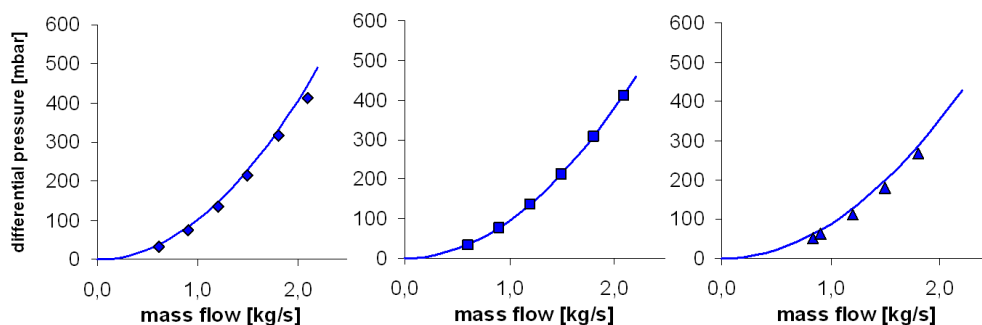


Figure 7-12: Measured (diamonds: 75 bar; squares: 50 bar and triangles: 25 bar) and calculated (solid line: pressure loss coefficient 0.20) flow resistance in geometry A (POR channel) in relation to mass flow.

7.3.2.2 Influence of opening angles

Although the POR flow resistance is acceptably small, it could be advantageous to further reduce the flow resistance and the component length by using diffusers with larger opening angles. Diffusers with smaller opening angles could help reduce form losses. Although the opening angle of the diffuser is crucial for the flow resistance during emergency core cooling, it is expected to have only a negligible impact on the POR flow behavior in the backward direction.

7.3.2.2.1 Smaller opening angles

The comparison between the pressure loss in geometries A and B (Figure 7-13) indicates that smaller opening angles yield larger flow resistance. The form loss reduction is compensated by larger friction losses.

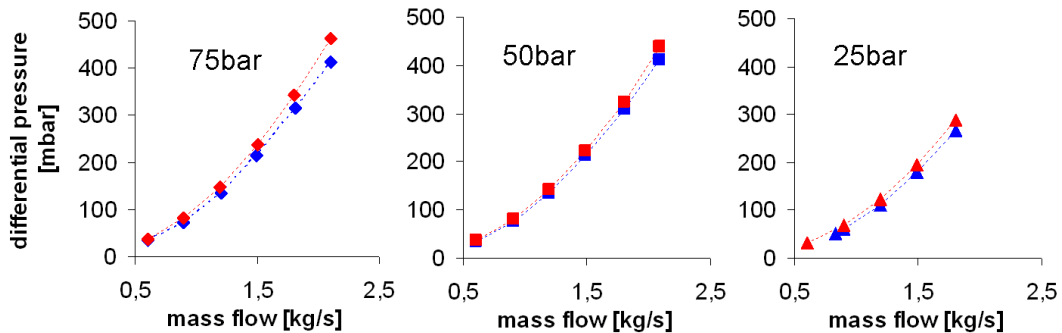


Figure 7-13: Measured flow resistance at 75 bar (left), 50 bar (middle) and 25 bar (right) in geometries A (blue) and B (red) plotted as a function of mass flow.

7.3.2.2.2 Larger opening angles

Since experiments with geometry A and C are performed under different flow conditions, it is necessary to display the experimental results in a non-dimensional form, e.g. the pressure loss coefficient in relation to the Reynolds number (Figure 7-14).

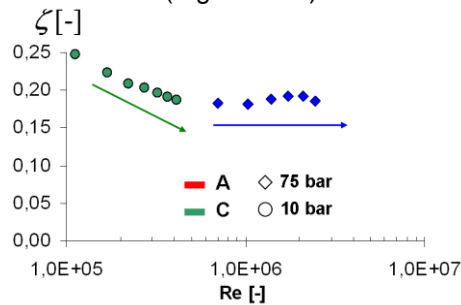


Figure 7-14: Pressure loss coefficients in geometries A (blue) and C (green) at 75 bar (diamond) and 10 bar (circle), respectively.

At low Reynolds numbers, the flow resistance coefficient is high. Increasing the Reynolds number lowers the flow resistance coefficient (green arrow on Figure 7-14). At sufficiently high Reynolds numbers, an approximately constant pressure drop is observed (blue arrow on Figure 7-14). This qualitative flow behavior is close to the behavior of the friction loss in straight tubes and characteristic for separation-free diffusers [40].

The analysis of the flow resistance in the first and second nozzle of geometry C shows that high flow resistance coefficients are only detected in the first nozzle whereas pressure drop coefficients in the second nozzle are lower and approximately constant (Figure 7-15), although both nozzles are geometrically identical.

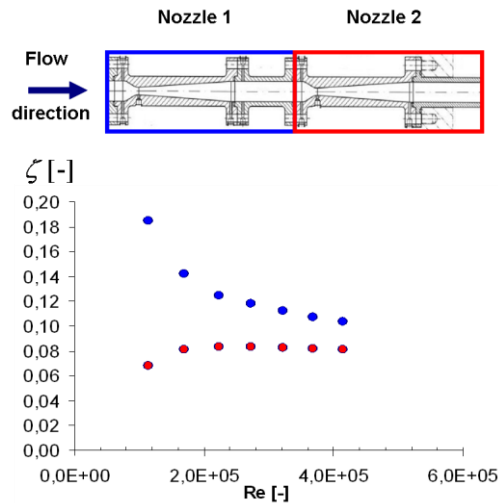


Figure 7-15: Flow resistance coefficients in first (blue) and second (red) nozzle of geometry C.

More generally with all geometries (A, B and C), the pressure loss coefficients observed in the second nozzle are smaller than those measured in the first nozzle. The difference between the pressure losses in the first and second nozzle diminishes at high Reynolds number. The flow resistance in the second nozzle shows the same behavior at low Reynolds numbers as at high turbulent Reynolds numbers.

Using data available in [40] for separation-free diffusers, the pressure drop coefficient in a theoretical double-nozzle design is estimated at all Reynolds numbers and compared to the experimental results for geometry C (Figure 7-16). The theoretical double-nozzle design is assumed to consist of two separation-free diffusers with opening angles of 12°. The second diffuser is supposed to have a constant pressure loss corresponding to fully-turbulent conditions. The comparison suggests that geometry C performs better than this theoretical geometry. Therefore, at high Reynolds numbers, the flow resistance coefficient of geometry C should also be lower than that of the theoretical geometry, i.e. below 0.196. Since geometry C is shorter than geometry A and its pressure loss coefficient ζ_C is expected to be lower than that of geometry A ($\zeta_C < 0.196 < \zeta_A = 0.20$), it could be beneficial to use diffusers with opening angles of 12° (geometry C) instead of 7° (geometry A) to reduce POR length and flow resistance.

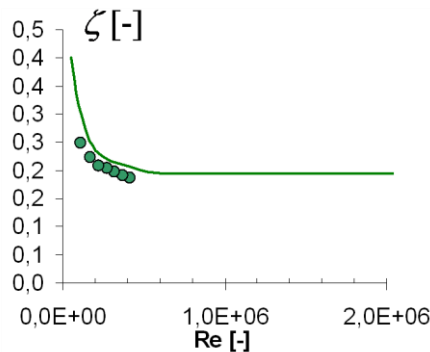


Figure 7-16: Comparison between measured pressure loss coefficient in geometry C (circle); and theoretical pressure loss coefficient in a double-nozzle design (solid line) estimated with data available in [40] for separation-free diffusers.

However, Figure 7-17 indicates that the pressure loss coefficient is not only a function of the Reynolds number but also of the system pressure.

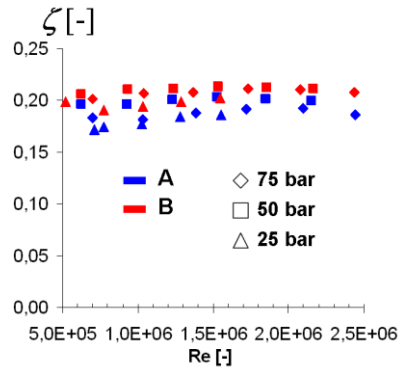


Figure 7-17: Pressure loss coefficients in geometry A (blue) and B (red) at 75 bar (diamond), 50 bar (square) and 25 bar (triangle).

CFD calculations calibrated with the available experimental results are required to estimate the flow behavior of geometry C at high Reynolds numbers and high system pressures.

7.3.2.3 Cavitation

To assess the consequence of cavitation on the POR fluidic behavior, one test is performed with decreasing subcooling. The mass flow $\dot{M} = 1.8 \text{ kg/s}$ is imposed at system pressure 50 bar. The temporal variation of the pressure loss measured during this test is presented in Figure 7-18. The flow resistance remains almost constant until 200s at its single-phase value ($dp = dp_0$); after that, it starts to increase, first moderately ($dp < 1.4 dp_0$), then drastically after 400s.

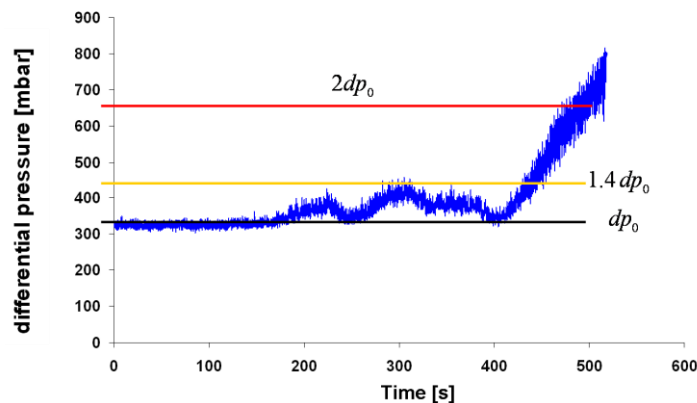


Figure 7-18: Temporal evolution of the flow resistance in one POR channel with varying subcooling; dp_0 being the single-phase flow resistance.

The moderate flow resistance increase probably occurs when the first cavities and cavitation sheets develop at the smallest cross section. The momentum exchange between the new vapor phase and the liquid phase yields the pressure drop increase observed between 200s and 400s. The drastic increase after 400s may be induced by the blockage of the cross section by a large cavitation sheet.

To estimate under which conditions cavitation occurs in the forward direction, the temperature of the coolant is measured at four positions along the POR channel (Figure 7-10). These temperature measurements indicate that the subcooling is low and of order of the measurement uncertainty ($\pm 1.5 \text{ K}$) when the flow resistance increases. In that case, it is not possible to determine exactly the coolant subcooling corresponding to this flow resistance rise. A conservative representation of the experimental results is necessary and given in Figure 7-19. There, the maximal subcooling is displayed in yellow and the flow resistance in blue. The maximal subcooling is about 2K when the flow resistance starts to increase.

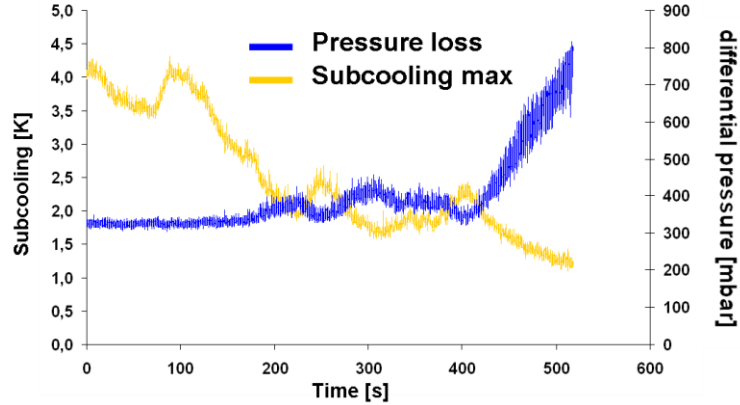


Figure 7-19: Temporal evolution of the maximal subcooling at POR inlet (yellow) and the resulting POR flow resistance (blue).

7.4 Performance factor

A fluidic diode is usually characterized by its performance factor. This performance factor Σ_R is defined as the ratio between the resistance coefficient K_1 in the direction where the high flow resistance is achieved and the resistance coefficient K_2 in the opposite flow direction [6]:

$$\Sigma_R = \frac{K_1}{K_2}. \quad (7.1)$$

These resistance coefficients are defined in both directions as the ratio between the pressure difference existing between the inlet and the outlet of the diode and the dynamic pressure at the inlet of the fluidic diode [6]:

$$K = \frac{p_{inlet} - p_{outlet}}{\frac{\dot{M}^2}{2\rho A^2}}. \quad (7.2)$$

In eq. (7.2), p_{inlet} and p_{outlet} are the pressure at the inlet and outlet of the diode, respectively; A is the cross section of diode's inlet, ρ is the density of the fluid at diode's inlet and \dot{M} is the mass flow rate.

In the forward direction, the resistance coefficient defined as (7.2) is proportional to the single-phase pressure loss coefficient defined in section 7.3.2.1.2. The scaling factor between both coefficients is the square of the ratio between the POR inlet cross section and POR smallest cross section. Thus, within the POR operation range, the POR resistance coefficient in the forward direction is low ($K_2 = 10.7$) and approximately constant (section 7.3.2.1.2).

In contrast, the POR resistance coefficient in the opposite flow direction defined as (7.2) does not scale with the pressure loss coefficient defined in section 7.2.2.4. Nevertheless, it can be determined with available experimental results. For this purpose, the pressure at the outlet of the POR channel in the backward direction is assumed to be the atmospheric pressure. Coolant subcooling at the inlet of the POR significantly affects this resistance coefficient K_1 (Figure 7-20). K_1 is high at low subcooling and decreases with increasing subcooling.

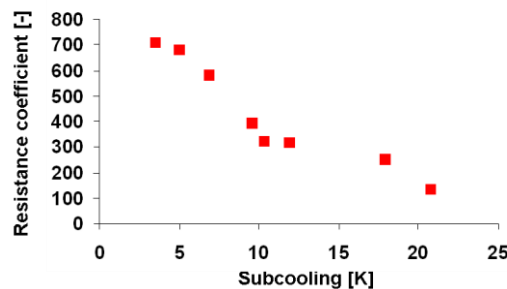


Figure 7-20: Resistance coefficient in the backward direction of one POR channel as a function of coolant's subcooling.

The performance factor Σ_R of the POR is represented in Figure 7-21 as a function of the coolant subcooling. In this context, the coolant subcooling is at the inlet of the POR channel in the backward direction. Σ_R attains remarkable values at low subcooling (70 at subcooling 4K); and decreases with increasing subcooling (about 15 at subcooling 21K).

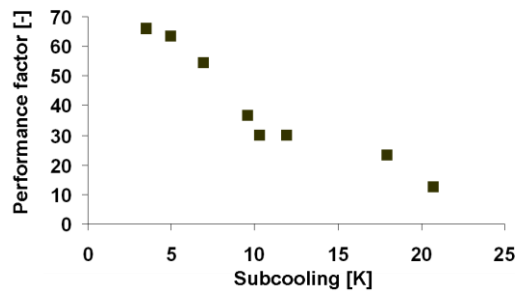


Figure 7-21: Performance factor of one POR channel as a function of coolant's subcooling (subcooling in the backward direction).

7.5 Conclusion

Experiments with single channels are performed in both directions under realistic boundary conditions to validate the principle of the new design and to adapt the numerical tools to the geometry and flow conditions.

Experimental results in the backward direction indicate that the double-nozzle design does reduce the loss of coolant in comparison to a single-nozzle design. Assuming a homogeneous distribution of the flow inside the 37 identical POR channels enables to extrapolate the experimental data to the POR design. This assumption is conservative since the flow resistance is expected to be minimal in that case. This extrapolation to a bundle of 37 POR channels confirms that the new POR design fulfills the LOCA requirement. To account for the POR in the backward direction in safety analysis codes, comparison with experiments suggests that the POR outflow can be represented by the HEM correlation with a pressure loss coefficient $\zeta = 0.1$.

Experiments in the other flow direction show that the flow resistance in the POR is sufficiently small to ensure adequate heat removal by the EC system. Experimental data available at low Reynolds numbers and low system pressure suggests that it could be possible to further reduce the pressure loss and the size of the component by increasing the opening angle of the diffusers. This improvement should not significantly modify the POR flow behavior in the other flow direction. CFD calculations calibrated with available experimental results will be carried out in the forward direction to assess the flow behavior of a bundle of 37 identical parallel POR channels.

Finally, comparison of experimental data in both flow directions shows that the ratio between the resistance coefficient in the backward direction and the resistance coefficient in the opposite direction amounts up to 70.

8 Stochastic-field cavitation model

This chapter is devoted to the description, the validation and the analysis of the cavitation model developed during this thesis. The introduction (section 8.1) summarizes some important issues about cavitation, cavitation modeling and more generally numerical modeling. Section 8.1 also presents the major novelty of the model: the adaptation of the stochastic-field method (SFM) to cavitating flows. With this technique, the spectrum of the size of the vaporous cavities is obtained in a fully Euler framework and physical processes which were, until now, only compatible with complex and costly Lagrange Monte-Carlo techniques are included in the Euler calculations. Most of these issues are already discussed in the preceding chapters but are repeated here to clearly portray the background and the objectives of this novel cavitation model. Section 8.4 briefly introduces the numerical setup and the numerical code used to implement this cavitation model. Section 8.5 recapitulates model's governing equations. Some of these equations are derived in the framework of this Ph. D. to increase the accuracy of available models. A particular attention is devoted to define the interfacial mass transfer (section 8.5.6). Section 8.6 concentrates on two validation cases found in the literature and discusses some properties of the stochastic-field method.

8.1 Introduction

8.1.1 Background

Experimental tests were performed under realistic plant conditions (up to 75bar and 290 °C) at the AREVA Technical Center in Karlstein to validate the principle of an innovative fluidic diode for critical two-phase flows, called the passive outflow reducer (POR). They indicate that very high backward-to-forward flow resistance ratios are achieved with the POR. Furthermore, the POR fulfills the requirements of the KERENA reactor in both backward and forward directions (chapter *performance tests*).

Since experiments are very costly under such pressures and temperatures, the test matrix was simplified to the analysis of the most crucial parameters. In the backward direction, these parameters are the size of the minimal cross sections and the number of minimal cross sections (one or two). In the other flow direction, the critical parameter is the opening angle of the diffusers. All other parameters, e.g. the length of the pipe between the two smallest cross sections, were hold fixed during the experiments.

The high pressure and temperature gradients complicate the measurement. First, the channels are made of thick walls of steel to resist to these pressure gradients. No optical measurement is possible. Thus, non-intrusive techniques such as particle image velocimetry (PIV) could not be used to obtain velocity profiles in the POR geometry. Similarly, non-intrusive methods such as gamma-densitometry could not be used to obtain void profiles and flow patterns. The thickness of the wall would have significantly deteriorated the accuracy of the measurements. Second, pressure and temperature sensors must be able to measure under a large range of conditions. A good trade-off between robustness and cost of the measurement sensors are obtained at the expense of the accuracy. Although this accuracy is sufficient to analyze the POR flow behavior under its operating conditions, it was not adequate to exactly estimate when cavitation occurs in the POR in the forward direction (see chapter *performance tests*).

In this context, it is of great benefit to have a numerical code. More insight into the POR flow behavior can be gained and the effect of other geometrical or physical parameters, such as the length of the POR channels, can be analyzed at a low cost. However, the requirements on a numerical code able to simulate the flow in both POR directions are severe. The simulation of cavitating and flashing flows is a challenging problem both in terms of modeling the physics and developing robust numerical methodologies. Such flows are inherently stochastic [11]. They primarily are governed by turbulence and the probability density functions (pdf) of cavitation nuclei number density n and cavitation nuclei size R have a large variance. Cavitating flows also are characterized by considerable variations of the local density and involve thermodynamic phase transition.

8.1.2 Euler vs. Euler-Lagrange method

Two numerical techniques prevail in CFD codes for the treatment of cavitating and turbulent flows. One of them is the so-called Euler method; the other one is the Euler-Lagrange method. Principle, advantages and drawbacks of these methods are already discussed in the chapter *numerical modeling* and *stochastic* but are briefly repeated here for clarity.

8.1.2.1 Euler method

The Euler method describes the flow variables in terms of time and space dependent fields. The governing equations are expressed in this framework and must be averaged because the resolution of the small length and time scales of the flow variables is beyond current computing capability. The averaging leads to an open term for any non-linear process S function of the flow variable ψ_α :

$$\langle S(\psi_\alpha) \rangle - S(\langle \psi_\alpha \rangle) \neq 0; \quad (8.1)$$

where $\langle \cdot \rangle$ represents the averaging operator. To obtain a solution of the averaged equation, the closure of these open terms is needed. This closure exploits mean (RANS) or filtered (LES) quantities to reproduce the effect of the unresolved scales.

In fluid dynamics, three types of open terms generally arise from the averaging:

- The Reynolds stresses in the momentum equations;
- The turbulent flux of the scalar property in scalar property transport equations; and
- The source term in scalar property transport equations.

For cavitation, the source term in the vapor mass fraction conservation equation is the interfacial mass transfer.

Models for the averaged non-linear terms in the momentum equations are available (Reynolds stresses). In the RANS approach, supplementary equations generally are introduced to calculate the eddy viscosity. In LES calculations, simple algebraic expressions are sufficient to obtain the sub-grid viscosity since modeled scales have short length and time scales and have less influence on the sub-grid-flux.

Usually, the transport of the scalar property by the turbulent fluctuations is modeled by a gradient-hypothesis. The turbulent flux is proportional to the gradient of the mean scalar property. Thereby, the constant of proportionality is the turbulent mass diffusivity which is proportional to the turbulent viscosity.

In contrast, models for the averaged non-linear source term in scalar property transport equations are, in general, not available. Many years of intensive turbulence research emphasize the challenge of closing these highly non-linear terms. In cavitation, an algebraic model based on mean/filtered quantities (usually vapor and liquid mass fractions, density and pressure) often fails to universally describe the effect of the fluctuations on the inter-phase mass transfer. This explains why the source terms of the vapor mass fraction equation found in the literature (e.g., [202], [203], [204]) may differ by several orders of magnitude; each model being calibrated to reproduce experimental results and thus adapted for specific conditions and geometry.

In addition, the Euler method is not suited to incorporate stochastic processes (such as coalescence, breakup or nucleus size spectrum in cavitating flows).

By contrast, Euler solvers are very efficient and robust (in comparison to Euler-Lagrange methods). They are much less demanding on computation power and system resources; and can address more easily compressibility and large density ratios.

8.1.2.2 The Euler-Lagrange method

The Euler-Lagrange method consists in the coupling of an Euler solver with a Lagrange solver. The Lagrange solver tracks bubbles (in cavitating flow modeling) or notional particles (in turbulent flow modeling). In combination, Monte-Carlo techniques are used to sample the bubbles/particles and the occurrence of the events impacting their life (e.g. breakup, coalescence in cavitating flows) from prescribed probability density functions.

The Euler solver solves the Navier-Stokes equations of the continuous phase and evaluates additional flow variables, e.g., turbulence or velocities. By ensemble-averaging the Lagrange quantities of the N bubbles/particles present in each Euler computational cell, statistical information of the Lagrange solver is exploited.

Thus, the simulation with Monte-Carlo codes based on Lagrange techniques is attractive. Stochastic nature and particle size dependence of the physical processes occurring in cavitating flows can be easily captured. More generally, the Lagrange approach proves to be very successful to close highly-non linear source terms. For an infinite number of realizations (bubbles/particles), the ensemble averaged of any function of the flow variables, including any non-linearity, becomes exactly the mean value of the function so that no modeling is required.

By contrast, the Euler-Lagrange formulation is balanced by the typical Euler-Lagrange solver coupling difficulties. An Euler-Lagrange simulation of coupled multiphase flow with strong interaction between the continuous fluid phase and the disperse particle phase is restricted due to its extreme computational resources demand. On the one hand, the number of bubbles/samples must be large to represent the properties of the whole population [177], and to assure the convergence of the Euler solver [178]. On the other hand, very poor performance for parallel computation can often be encountered in Lagrange solvers due to imbalanced particle concentration [175], [176]. Moreover, Euler-Lagrange solver coupling requires complex algorithms and introduces interpolation errors which may reduce the order of accuracy of the scheme to the first order.

8.1.2.3 Conclusion

Figure 8-1 represents schematically the performance of Euler and Euler-Lagrange codes for cavitating/turbulent flows according to their stability, efficiency and accuracy. “Notes” are given to both solver types. Thereby, 10 corresponds to a code perfectly robust/efficient/accurate while 0 represents a very bad code. The codes behave quite differently: Euler codes are stable and efficient while Euler-Lagrange codes can describe accurately the physical processes. In contrast, Euler-Lagrange are less stable and very resource demanding while Euler codes may be deficient in accuracy.

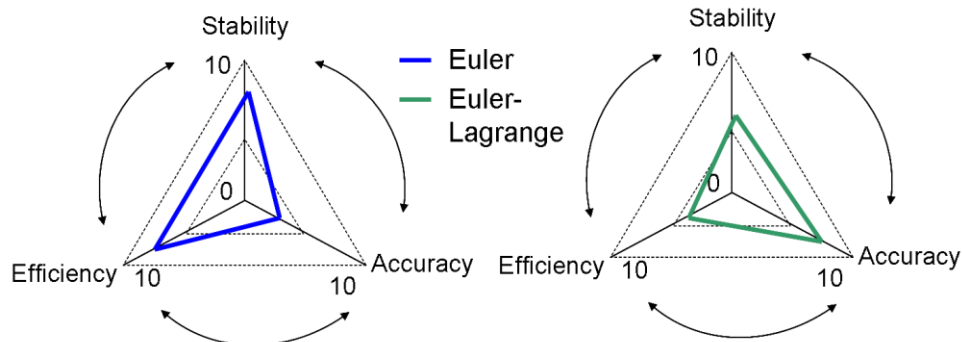


Figure 8-1: Illustration of the performance of Euler (blue, left) and Euler-Lagrange (green, right) codes according to their stability, efficiency and accuracy in the simulation of cavitating/turbulent flows. 10 corresponds to a code perfectly robust/efficient/accurate while 0 represents a very bad code.

8.2 Objective of the model

The cavitation model should provide accurate results in both POR flow directions. For this purpose, the code must be able to cope with highly compressible flows, large void fractions and reproduce the stochastic nature of cavitating flows. None of the cavitation models available in the Euler or the Euler-Lagrange formulation fulfills all criteria.

The flow conditions represent severe constraints on the numerical code, in particular in the backward direction. Under these conditions, an Euler method is more adequate. Therefore, in this thesis, the emphasis is placed on the improvement of the accuracy of Euler codes in the simulation of cavitating flows. A novel cavitation model is proposed to combine the advantages of the Lagrange technique with those of the Euler technique into a fully Euler framework. With this model, it is possible to simulate cavitation under very differing flow conditions at affordable computational resources.

Figure 8-2 illustrates this objective. The stability and efficiency of the Euler formulation in the simulation of cavitating flows is preserved while its accuracy is improved.

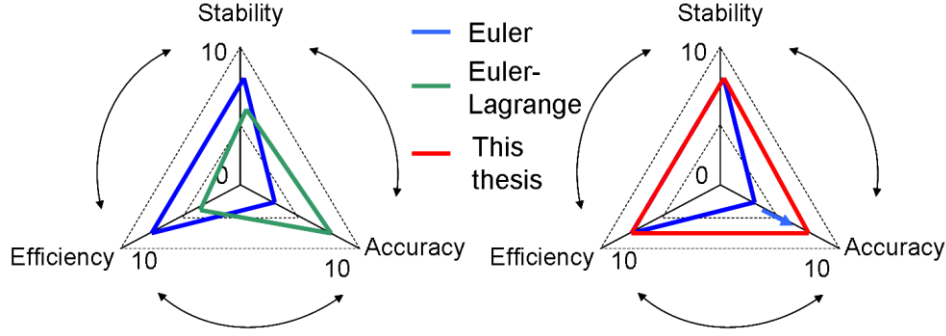


Figure 8-2: Illustration of the performance of the novel cavitation (red, right), Euler (blue, left and right) and Euler-Lagrange (green, left) codes according to their stability, efficiency and accuracy in the simulation of cavitating flows. 10 corresponds to a code perfectly robust/efficient/accurate while 0 represents a very bad code.

To simulate the flashing of the coolant in the backward direction, a caloric equation of state (eos) is derived and fluid properties are implemented as a function of the temperature over wide application ranges. A particular effort is undertaken to ensure that the code remains efficient and stable in spite of these modifications. Code efficiency is particularly important since the flow conditions (high speed, low compressibility) already impose very small time steps, and thus long calculation times.

Numerical schemes and other physical models (e.g. turbulence) are “state-of-the-art”. The discretization in time is performed with the fourth stage Runge-Kutta explicit scheme. This scheme is fourth order accurate. The central difference scheme with artificial dissipation SWITCH [123] is used for the spatial discretization. This numerical scheme is second order accurate everywhere except at large density jumps (A modification of the sensor (eq. 1.38 in chapter *numerical modeling*) was needed to ensure code stability).

8.3 Derivation of the model

8.3.1 Stochastic-field method

The cavitation model is based on the stochastic-field method (SFM) introduced by Valiño [10]. This technique recently has gained much interest (e.g., [205], [16], [17], [18], [19]) since it enables to solve the modeled composition pdf transport equation in a fully Euler framework. The modeled transport equation of the composition joint-pdf $f_{\tilde{\phi}}$ is given by:

$$\frac{\partial \rho f_{\tilde{\phi}}}{\partial t} + \overbrace{\frac{\partial \rho u_i f_{\tilde{\phi}}}{\partial x_i}}^1 + \overbrace{\frac{\partial \rho S_\alpha(\boldsymbol{\psi}) f_{\tilde{\phi}}}{\partial \psi_\alpha}}^2 = \overbrace{\frac{\partial}{\partial x_i} \left[D'_\alpha \frac{\partial \rho f_{\tilde{\phi}}}{\partial x_i} \right]}^3 + \overbrace{\frac{1}{2} \frac{\partial}{\partial \psi_\alpha} \left[\frac{(\psi_\alpha - \langle \tilde{\phi}_\alpha \rangle)}{\tau_\phi} \rho f_{\tilde{\phi}} \right]}^4. \quad (8.2)$$

In eq. (8.2), $f_{\tilde{\phi}}$ is the composition joint-pdf of the (stochastic) scalar properties $\tilde{\phi} = (\tilde{\phi}_\alpha)$, $\alpha = 1..N_\phi$, with N_ϕ the number of scalar properties; $\mathbf{u} = (u_i)$ is the mean velocity, D'_α is the combined molecular and turbulent scalar diffusivity coefficient; $S_\alpha(\boldsymbol{\psi})$ is the source term with $\boldsymbol{\psi} = (\psi_\alpha)$ being the sample space at every position \mathbf{x} and time t ; and $\langle \tilde{\phi}_\alpha \rangle$ is the mean value of the stochastic process $\tilde{\phi}_\alpha$.

Term 1 represents the convection of the pdf. It can be calculated with known flow variables and does not require modeling. Term 2 is the source term of the transport equation. Any function of the instantaneous flow variable $\boldsymbol{\psi}$, including any non-linearity, can be calculated without modeling. This is one of the great advantages of the method. Term 3 represents the effect of the turbulent fluctuating velocity and of the molecular transport on the dispersion of the scalar in the physical space. It is modeled with the gradient hypothesis. Term 4 represents the effect of the molecular transport on the scalar properties in the composition space modeled with the interaction by exchange with the mean (IEM) (chapter *stochastic*).

The basic idea of the SFM is to represent the pdf by \underline{N} stochastic fields (SF) $\phi^k = (\phi_\alpha^k)$, $k \in 1..\underline{N}$ (see Figure 8-3); continuous and differentiable in space and continuous in time [10]:

$$f_{\tilde{\phi}}(\Psi; \mathbf{x}, t) = \frac{1}{\underline{N}} \sum_{k=1}^{\underline{N}} \delta[\Psi - \phi^k(\mathbf{x}, t)] \equiv \langle \delta[\Psi - \phi^k(\mathbf{x}, t)] \rangle. \quad (8.3)$$

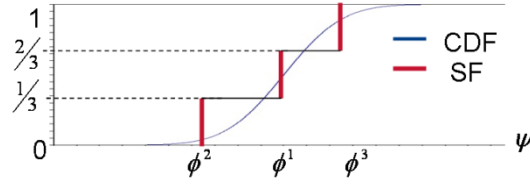


Figure 8-3: Representation of the cumulative density function (CDF) of a Gaussian scalar $\tilde{\phi}$ with three stochastic fields ϕ^1 , ϕ^2 and ϕ^3 . These stochastic fields are equiprobable. The exact CDF is the blue solid line; the approximated CDF is of staircase form with three steps (in red).

With standard stochastic calculus techniques, Valiño [10] derived the governing equations of these fields from the pdf transport equation (8.2). The governing equation of the scalar ϕ_α^k , $k = 1..\underline{N}$, $\alpha = 1..N_\phi$, is given by:

$$d\phi_\alpha^k = \underbrace{-u_i \frac{\partial \phi_\alpha^k}{\partial x_i} dt}_{1} + \underbrace{S(\phi^k) dt}_{2} + \underbrace{\frac{\partial}{\partial x_i} \left(D'_\alpha \frac{\partial \phi_\alpha^k}{\partial x_i} \right) dt}_{3} + \underbrace{\sqrt{2D'_\alpha} \frac{\partial \phi_\alpha^k}{\partial x_i} dW_i^k}_{4} - \frac{1}{2} \frac{(\phi_\alpha^k - \langle \phi_\alpha \rangle)^2}{\tau_\phi} dt. \quad (8.4)$$

In eq. (8.4) $\mathbf{u} = (u_i)$ is the mean velocity, D'_α is the combined molecular and turbulent diffusivity, W_i^k is a Wiener process, independent for each spatial component i but constant in space; and $\langle \phi_\alpha \rangle$ is the mean value of the scalars ϕ_α^k over the \underline{N} stochastic fields.

The system of stochastic partial differential equations (8.4) is an Ito formulation of the Fokker-Planck equation (8.2). This system provides equivalent statistical information as the pdf transport equation (8.2).

Quoting Valiño [10], “those \underline{N} stochastic fields are not any particular realization of the real field, but constitute a stochastic system allegedly equivalent” to (8.2). “They represent possible particular scalar values for each value of \mathbf{x} and t ”.

As in the stochastic Lagrange pdf techniques (chapter *stochastic*), non-linear processes, in particular the source terms, are closed. The estimation of mean-values becomes very accurate for a sufficient number of realizations. Due to the pure Euler formulation, the computational cost and the complexity of this method is substantially reduced in comparison to the stochastic Lagrange methods.

8.3.2 Cavitation and stochastic fields

8.3.2.1 Stochastic-field equations

In the simulation of cavitating flows within an Euler approach, water and vapor are usually assumed to be in mechanical and thermal equilibrium. The bubbles are finely dispersed in the liquid phase. Water and vapor share the same velocity, pressure and temperature. They are treated as a continuum. Various approaches exist to define the thermodynamic behavior of the mixture (e.g. [202], [206], [207], [208], [209], [210], [211] or [212]). For the analysis of the POR, in particular in the backward direction, the consideration of the thermodynamic non-equilibrium is essential. To account for the finite time of cavities' growth, the transport equation of the vapor mass fraction Y is generally solved:

$$\frac{\partial}{\partial t}(\rho Y) + \nabla \cdot (\rho \mathbf{u} Y) = -\nabla \cdot (\mathbf{j}) + S(Y); \quad (8.5)$$

where \mathbf{j} is the mass flux vector of Y and $S(Y)$ is the interfacial mass transfer.

Within the SFM, eq. (8.5) is replaced by a system of \underline{N} stochastic-field equations (Eq. (8.4) with $\phi^k = (Y^k) = Y^k$) to obtain the vapor mass fraction pdf. The equation of the field Y^k , $k = 1..N$, reads:

$$dY^k = -u_i \frac{\partial Y^k}{\partial x_i} dt + S(Y^k) dt + \frac{\partial}{\partial x_i} \left(D'_Y \frac{\partial Y^k}{\partial x_i} \right) dt + \sqrt{2D'_Y} \frac{\partial Y^k}{\partial x_i} dW_i^k - 1/2 \frac{(Y^k - \langle Y \rangle)}{\tau_Y} dt. \quad (8.6)$$

The velocity $\mathbf{u} = (u_i)$ is obtained from the Navier-Stokes equations. D'_Y and τ_Y are obtained from the turbulence model. According to (8.3), the vapor mass fraction pdf can be obtained from the fields Y^k such as:

$$f_Y(y; \mathbf{x}, t) = \frac{1}{\underline{N}} \sum_{k=1}^{\underline{N}} \delta[y - Y^k(\mathbf{x}, t)] \equiv \langle \delta[y - Y^k(\mathbf{x}, t)] \rangle. \quad (8.7)$$

Then, the vapor mass fraction $Y(\mathbf{x}, t)$ is simply:

$$Y(\mathbf{x}, t) = \int_{-\infty}^{\infty} y f_Y(y; \mathbf{x}, t) dy = \frac{1}{\underline{N}} \sum_{k=1}^{\underline{N}} y \delta[y - Y^k(\mathbf{x}, t)] = \frac{1}{\underline{N}} \sum_{k=1}^{\underline{N}} Y^k(\mathbf{x}, t). \quad (8.8)$$

Any function of the flow variable Y , typically the source term $S(Y)$, can be expressed with the fields Y^k in exact form:

$$S(Y)(\mathbf{x}, t) = \int_{-\infty}^{\infty} S(y) f_Y(y; \mathbf{x}, t) dy = \frac{1}{\underline{N}} \sum_{k=1}^{\underline{N}} S(y) \delta[y - Y^k(\mathbf{x}, t)] = \frac{1}{\underline{N}} \sum_{k=1}^{\underline{N}} S(Y^k(\mathbf{x}, t)). \quad (8.9)$$

8.3.2.2 Benefits

The stochastic-field cavitation model proposed in the framework of this thesis uses the SFM technique in two different ways to improve the accuracy of the Euler code:

- First, the highly non-linear source term $S(Y)$ present in the vapor mass fraction equation appears in closed form. This corresponds to the common application of the SFM which has shown very successful in other applications (e.g. in reacting flows).
- Second, the bubble size pdf is obtained by geometrical consideration from the vapor mass fraction pdf. For this purpose, the vapor is assumed to be finely dispersed in the continuous water phase in form of a finite number of spherical cavities. This assumption is commonly made in cavitating flows.

As far as the author knows, the proposed cavitation model is the first application of the SFM for the description of the bubble size spectrum. This application gives birth to a particularly powerful modeling tool in multi-phase flows in a fully Euler framework; as it will be explained in the following for cavitation.

8.3.2.3 Conceptual framework

In the present model, the stochastic fields represent possible particular values of the vapor mass fraction for each value of \mathbf{x} and t . In cavitating flows, the vapor phase consists of finely dispersed cavities. Thus, the vapor mass fraction can be interpreted as being the vapor mass fraction of one particular bubble:

- Considering a fluid containing n cavities per unit volume, it is always possible to divide each unit volume into n volumes containing exactly one bubble (see Figure 8-4).
- Then, each stochastic field represents the vapor mass fraction of one of these volumes, i.e. of one of the bubbles present in the unit volume.

By definition (8.3), the stochastic fields are equiprobable. Each particular bubble is considered to represent $1/\underline{N}$ of the bubbles present in the unit volume. Within this framework, the radius R^k of each of these “representative” bubbles can easily be derived from the mass fraction Y^k and the number n of cavities per unit volume:

$$R^k = \left(\frac{3\rho Y^k}{4\pi\rho_g n} \right)^{\frac{1}{3}}. \quad (8.10)$$

The spectrum of the size of all possible particular bubbles for each value of \mathbf{x} and t is obtained for a sufficient number of realizations.

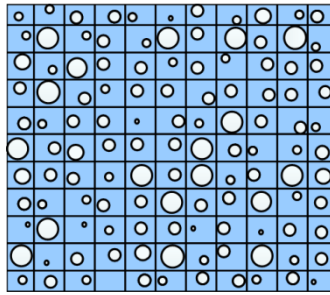


Figure 8-4: A unit volume of the vapor-water mixture containing n cavities can be subdivided into n elementary units. Each of these units contains exactly one vaporous cavity.

The cavity size spectrum can be used at any iteration and position to calculate accurately the physical processes occurring in cavitation flows. Typically, the proposed cavitation model uses the bubble size spectrum to estimate the mass transfer. Other non-linear phenomena such as forces can also be estimated with the radius pdf.

This spectrum can be also applied to model the transfers occurring between the different bubbles. For example, the implementation of the stochastic break-up and coalescence would simply require estimation of break-up and coalescence frequencies. All existing physical models available for Lagrange techniques, presumed pdf or binning methods can be easily extended to the stochastic-field formulation.

In contrast to other Euler methods developed to obtain bubble size spectrum, the binning is dynamic and adapts to the flow conditions.

8.3.3 Mass transfer

Within the SFM, the difficulty of modeling the *averaged* mass transfer with averaged flow variables disappears. Nevertheless, the instantaneous and local mechanism of interfacial mass transfer must still be provided.

In cavitating flows, the Rayleigh-Plesset equation in its original version or in a modified form (chapter *cavitation*), consensually is used to represent the dynamic of the vaporous cavities.

In an Euler framework, a very simplified form of the Rayleigh-Plesset equation, called the Rayleigh equation [213], usually is applied. Since this simplified form neglects surface tension and mass of dissolved gas, water quality effect can not be accounted for. In the same manner, thermal effects commonly are disregarded.

On the contrary, the present cavitation model is based on a modified form of the Rayleigh-Plesset equation which takes into consideration these determinant phenomena.

8.3.4 Summary of the model

The pure Euler stochastic fields describing the vapor mass fraction pdf are used to close the highly non-linear mass exchange between water and vapor and improve the formulation of cavitation mass transfer mechanism.

The source term is derived from the Rayleigh-Plesset equation. The vapor phase is represented by a finite number of vaporous cavities. The size pdf of these cavities can directly be derived from the vapor mass fraction pdf. The dependence of the physical processes upon the cavity size can be addressed. For instance, nuclei are activated only when the pressure decreases below their threshold pressure. Thus, small and large nuclei are activated separately.

This method combines the advantages of Euler and Lagrange formulations to obtain accurate results with a stable and efficient numerical code.

This new concept in two-phase flows is implemented into the state-of-the-art compressible code SPARC [20]. This density-based code can handle large density ratios and Mach numbers as encountered in cavitating flows. Reynolds-averaged Navier-Stokes (RANS) and Large Eddy Simulations (LES) are performed for the prediction of turbulence.

This chapter is organized as follows. In section 8.4 and 8.5, the solver SPARC and the governing equations implemented in the code are presented. In section 8.6 numerical results are compared to experimental results and some properties of the stochastic fields are discussed.

8.4 Solver SPARC

It was already emphasized that the flow conditions are particularly challenging for the numerical code in the backward direction. The coolant expands from the high pressure vessel into the containment through the POR. Subcooled at the inlet of the POR; the coolant starts to vaporize inside the POR and chokes at the second smallest cross section. The flow is characterized by large density, pressure and temperature gradients; and by a strong imbalance between regions with large void fraction and other with almost no void fraction.

Under these conditions, an Euler method appears to be adequate. However, even for an Euler solver, these conditions are demanding. Codes are generally adapted to specific conditions. Typically they are specialized for single-phase high-speed compressible flows or for two-phase low-velocity flows; and they cannot provide any (physical) solution outside of their domain of specification.

For the analysis of the POR, a code capable of handling two-phase high speed compressible flows is required. Starting from a solver specialized in single-phase high-speed compressible flows; the first and necessary step consists in implementing thermal and caloric eos valid for the two-phase mixture. This step requires important modifications of the numerical code. The access to the code of commercial software is limited. Therefore, the density-based code SPARC [20] is adopted for the calculations.

8.5 Governing equations

Water and vapor are assumed to be in mechanical and thermal equilibrium. They are described as a continuum by mixture's three dimensional Navier-Stokes equations. This approach is acceptable in cavitating flows where the vapor phase is finely dispersed in the continuous water phase (at least at an early stage). The objective is, among others, to simulate flashing conditions. The vapor mass fraction pdf transport equation is included in the set of transport equations to account for the flashing delay.

8.5.1 Equations of state

In two-phase flow simulations with density-based codes, the eos basically are required to calculate the pressure p , the temperature T (eventually the specific enthalpy h) and the vapor mass fraction Y from the conserved variables. These primitives flow variables are required in the transport equations and for the calculation of the constitutive properties and speed of sound.

Since the calculation of primitive variables is performed at any iteration in any cells, simple analytical eos are advantageous. Large simulation speed up and improved code stability are expected in comparison to techniques which access tabulated eos and liquid-vapor thermodynamic tables.

However, simple analytical eos covering the wide range of pressures (from almost $0Pa$ to $75bar$) and temperatures (from $293K$ to about $575K$) involved are not always available in the literature. Furthermore caloric eos is erroneous in most cavitation models. The error associated to these caloric eos does not have much influence on the results at low pressures but yields unphysical results at larger pressures.

Thus, one part of the development of the cavitation model is to collect in the literature or derive simple analytical eos covering the range of flow conditions occurring in both POR directions. Flow properties whose variation significantly impacts the numerical results are also implemented as a function of the temperature.

8.5.1.1 Vapor

8.5.1.1.1 Thermal equation of state

Similarly to other cavitation models, vapor is modeled as an ideal gas. Its thermal eos is given by:

$$p = \rho_g \mathcal{R}_g T ; \quad (8.11)$$

with $\mathcal{R}_g = 461.5 \text{ J/(kg K)}$.

8.5.1.1.2 Caloric equation of state

Vapor may have the same specific internal energy e_g at two different temperatures $T_2(e_g)$ and $T_1(e_g)$. This characteristic is prejudicial for the stability of the code. Standard methods, typically Newton methods, are unable to distinguish the physical $T_2(e_g)$ from the unphysical $T_1(e_g)$ solution. The determination of the temperature from the specific internal energy with the numerical method may be wrong. The numerical solution may be $T_1(e_g)$ instead of $T_2(e_g)$. In that case, the other flow variables calculated with the temperature $T_1(e_g)$ also become unphysical. The code becomes unstable and no solution is obtained. In order to avoid this difficulty, the specific internal energy of the vapor is approximated by a simple bijective function. The temperature of vapor is uniquely defined for a given specific internal energy e_g .

The caloric equation of state is expressed in the form:

$$e_g = K_{v,v}(T). \quad (8.12)$$

In eq. (8.12), $K_{v,v}(T)$ is a simple bijective function of T :

$$K_{v,v}(T) = K_{v,1} \sqrt{T_c - T} + K_{v,3} ; \quad (8.13)$$

where T_c is the critical temperature. $K_{v,1}$ and $K_{v,3}$ are two constants chosen such that (8.12) provides a good approximation of e_g in the domain of interest. Although better approximations exist, this solution has the advantage to allow fast and stable simulations.

The vapor heat capacity $(c_p)_g$ is assumed to be constant.

8.5.1.2 Water

8.5.1.2.1 Thermal equation of state

The eos of water is described by the model of Tamman [32]:

$$p + p_T = \rho_l K_T (T + T_T). \quad (8.14)$$

In the present work, model constants p_T and T_T are set to their standard values derived by Tamman [32]:

$$p_T = 1944.61 \text{ MPa} ; \\ T_T = 3837 \text{ K} .$$

The model constant K_T is modified to fit water properties (obtained from IAPWS [27]) over large pressure and temperature ranges (until at least 75 bar):

$$K_T (T^\circ\text{C}) = \begin{cases} 1.6 \cdot 10^{-3} T^2 - 5.78 \cdot 10^{-2} T + 472.22 & \text{J/(kgK) if } T < 220^\circ\text{C} \\ 9.893 \cdot 10^{-1} T + 315.61 & \text{otherwise} \end{cases}$$

8.5.1.2.2 Caloric equation of state

The derivation of the caloric eos of the water phase is based on the same principle as discussed in section 8.5.1.1.2 for the caloric eos of the gas phase. A simple bijective function $K_{v,l}(T)$ of T :

$$K_{v,l}(T) = K_{v,2} \sqrt{T_c - T} + K_{v,3} \quad (8.15)$$

is introduced to approximate liquid specific internal energy e_l :

$$e_l = K_{v,l}(T) . \quad (8.16)$$

Although better approximations exist, this solution has the advantage to allow fast and stable simulations.

Similarly to $(c_p)_g$, vapor heat capacity $(c_p)_l$ is assumed to be constant.

8.5.1.3 Mixture

8.5.1.3.1 Thermal equation of state

The mixture density is expressed as a linear combination of the density, ρ_l and ρ_g , of water and vapor respectively, with the void fraction α :

$$\rho = \alpha\rho_g + (1-\alpha)\rho_l . \quad (8.17)$$

Following the work of [214], the eos (8.18) of a locally homogeneous gas-liquid medium is written with (8.11), (2.36) and (8.17) as:

$$\rho = \frac{p(p+p_T)}{K_T(1-Y)p(T+T_T) + \mathcal{R}_g Y(p+p_T)T} . \quad (8.18)$$

The speed of sound in the mixture is derived from this equation [214]. It is displayed at three pressures 1bar, 50bar and 75bar in Figure 8-5. The speed of sound obtained with Brennen's model [12] is also represented in Figure 8-5 with dashed lines. This model is compared to experimental results in [63] and show remarkable agreement.

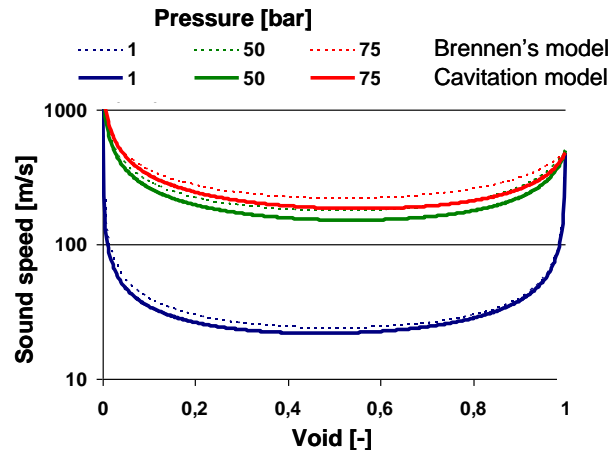


Figure 8-5: Mixture sound speed at three pressures 1bar, 50bar and 75bar. Dashed lines: model of Brennen [12]; solid lines: equation of state used in the simulations.

8.5.1.3.2 Saturation conditions

Saturation conditions (pressures and temperatures) are calculated with the polynomials of [215].

8.5.1.3.3 Caloric equation of state

The contribution of the surface tension energy to the specific internal energy of the system e is negligible in comparison to the contribution of liquid and vapor specific internal energies, e_l and e_g , respectively. Under this assumption, the specific internal energy e of the system consists of the specific internal energy e_l and e_g of the liquid and gas phase, respectively; in proportion to their respective mass fraction:

$$e = Ye_g + (1-Y)e_l . \quad (8.19)$$

This representation enables to reproduce correctly the thermal behavior of the two-phase mixture. For example, an isothermal vaporization of the liquid phase in a static two-phase mixture requires heat from the surrounding. The internal energy of the mixture increases. A graphical representation of this

phenomenon is given on Figure 8-6. The specific internal energy of the mixture is calculated according to the caloric eos implemented in the cavitation model. When the fluid vaporizes, the vapor mass fraction increases. Here as an example, the vapor mass fraction increases from 0.3 to 0.5. At constant temperature T , this vapor mass fraction rise induces an increase of the specific internal energy of the mixture from e_1 to e_2 .

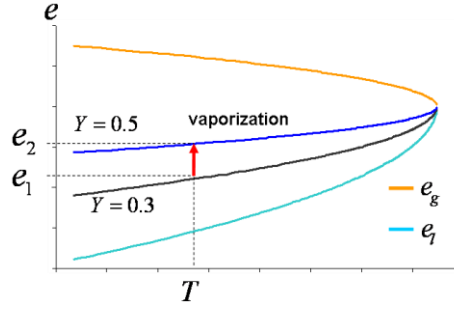


Figure 8-6: Illustration of the effect of an isothermal vaporization on the specific internal energy e of the mixture at the temperature T . The vapor mass fraction of the mixture increases from $Y = 0.3$ to $Y = 0.5$.

Vapor heat capacity $(c_p)_g$ and water heat capacity $(c_p)_l$ are mass weighted to obtain the heat capacity c_p of the mixture:

$$c_p = Y(c_p)_g + (1-Y)(c_p)_l. \quad (8.20)$$

8.5.2 Navier-Stokes equations

The three dimensional Navier-Stokes equations of the water-vapor mixture are solved to simulate the evolution of vapor-water mixture.

Continuity equation:

$$\frac{\partial}{\partial t}(\rho) + \nabla \cdot (\rho \mathbf{u}) = 0. \quad (8.21)$$

Momentum equation:

$$\frac{\partial}{\partial t}(\rho \mathbf{u}) + \nabla \cdot (\rho \mathbf{u} \cdot \mathbf{u}) - \nabla \cdot \mathbf{T} = 0. \quad (8.22)$$

Specific total energy equation:

$$\frac{\partial}{\partial t}(\rho E) + \nabla \cdot (\rho \mathbf{u} E) - \nabla \cdot (\mathbf{T} \cdot \mathbf{u}) + \nabla \cdot \mathbf{q} = 0. \quad (8.23)$$

In eq. (2.4) to (2.10), \mathbf{u} is the mixture velocity, ρ is the mixture density, $E = e + \frac{1}{2} \|\mathbf{u}\|^2$ is the mixture specific total energy, \mathbf{T} is the mixture stress tensor and \mathbf{q} is the mixture heat flux density. Gravity force is neglected.

Expressions for \mathbf{T} and \mathbf{q} are given in section 8.5.3.

8.5.3 Constitutive laws

The water-vapor mixture is assumed to be a Newtonian fluid. The experimental determination of its molecular viscosity is difficult. Its molecular viscosity is largely influenced by the structures of the two-phase flow, such as cavities radius, cavities density number, cavities shape [216]. Thus, several expressions exist to represent the molecular viscosity as a function of the void fraction. In this work, the molecular viscosity is expressed according to the formula found in [159]:

$$\eta = (1 - \alpha)(1 + 2.5\alpha)\eta_l + \alpha\eta_g. \quad (8.24)$$

The viscosity of the mixture is given on Figure 8-7 as a function of the void fraction.

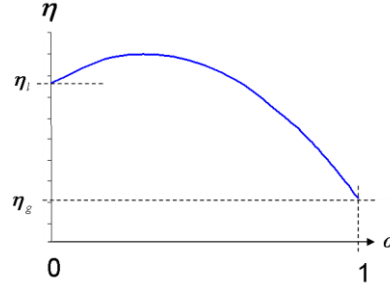


Figure 8-7: Viscosity η of the mixture as a function of the void fraction α . The viscosity η_l and η_g of the liquid and gas phase, respectively, are assumed to remain constant for this representation.

The heat flux density \mathbf{q} is modeled by Fourier's law. The mixture thermal conductivity λ_T is given by:

$$\lambda_T = \frac{c_p \eta}{\text{Pr}}; \quad (8.25)$$

where Pr is the mixture Prandtl number defined as:

$$\text{Pr} = Y \text{Pr}_g + (1 - Y) \text{Pr}_l; \quad (8.26)$$

with Pr_g and Pr_l being vapor and liquid Prandtl numbers, respectively.

8.5.4 Turbulent velocity fluctuations

To account for the effect of the turbulent fluctuations, both RANS and LES calculations are performed. Within the RANS approach, the one equation Spalart-Allmaras model is used; while the MILES and the High Pass Filter (HPF) Smagorinsky [217] approaches are employed in the LES simulations.

LES is a promising tool to capture interaction between turbulence and cavitation. In LES simulations, interaction between eddies and vaporous cavities larger than the filter width are accurately captured. This is attractive because, in cavitation, only the slowest turbulent pressure scales are capable to activate the nuclei. The pressure must remain below nucleus pressure threshold during a sufficient time period for the nucleus to have the time to grow.

8.5.5 Stochastic-field Method

The stochastic-field method is presented in section 8.3.1. \underline{N} equations are solved to obtain the vapor mass fraction pdf. The transport equation of the field Y^k , $k = 1..N$, reads:

$$dY^k = -u_i \frac{\partial Y^k}{\partial x_i} dt + S(Y^k) dt + \frac{\partial}{\partial x_i} \left(D'_Y \frac{\partial Y^k}{\partial x_i} \right) dt + \sqrt{2D'_Y} \frac{\partial Y^k}{\partial x_i} dW_i^k - 1/2 \frac{(Y^k - \langle Y \rangle)}{\tau_Y} dt. \quad (8.27)$$

The velocity \mathbf{u} of components u_i , $i = 1..3$, is obtained from the Navier-Stokes equations.

τ_Y is the relaxation time which usually is assumed to be proportional to the turbulent time scale τ_t :

$$\tau_Y = \frac{\tau_t}{C_Y}; \quad (8.28)$$

where $C_Y = 2.0$ is a model constant. Information on the turbulent scales τ_t is obtained from the Spalart-Allmaras model in RANS calculations and from the HPF Smagorinsky model [217] in LES calculations. $S(Y^k)$ is the interfacial mass transfer. The total diffusion coefficient D'_Y consists of the molecular and turbulent diffusion coefficients of the scalar Y . For example, the molecular mass diffusion coefficient is D_Y and defined with the Schmidt number σ_Y as follows:

$$D_Y = \frac{\eta}{\rho \sigma_Y}. \quad (8.29)$$

The model of $S(Y)$ is discussed in the next section.

8.5.6 Mass transfer modeling

Within the SFM, the difficulty of modeling the *averaged* mass transfer with averaged flow variables disappears. Nevertheless, the instantaneous and local mechanism $S(Y)$ of interfacial mass transfer must still be provided.

The Rayleigh-Plesset equation (RP) is considered to represent accurately the evolution of a spherical vapor bubble. However, to solve exactly this equation, temperature and gas diffusion equations should be solved in a coupled manner. Furthermore, in cavitating flows, the dynamic of the bubble is modified by the interaction with the surrounding bubbles and surrounding moving liquid. The assumptions of the RP may not all be valid. Moreover, an additional solver is required in Euler codes, in particular to account for the inertial term of the RP. Finally, the smallest time scale of the bubble dynamic is significantly smaller than the smallest time scale of the flow.

Therefore, the model of the mass transfer mechanism remains an approximation of the real process. This model should represent an optimal trade-off between efficiency and accuracy. In this thesis, the mass transfer mechanism implemented in the code SPARC is based on the following assumptions:

- 1) The vapor phase consists of a finite number of finite size cavities;
- 2) The radius of the vaporous cavities evolves according to a simplified form of the RP.

8.5.6.1 Finite number of finite size cavities

The vapor phase consists of a finite number n of finite size cavities per unit volume of the mixture.

The initial number n_0 of cavities (nuclei) per unit volume depends on water quality. It varies from one test facility to the other. If no experimental data is available, n_0 is a model constant.

8.5.6.1.1 Correlation used in this thesis

In this thesis, the number n of cavities per unit volume is related to the average void fraction to simulate coalescence and breakup:

$$n(\alpha) = \frac{n_0 + 1}{2} - \frac{n_0 - 1}{2} \tanh[5(\alpha - 0.4)]. \quad (8.30)$$

A graphical representation of this expression is displayed on Figure 8-8.

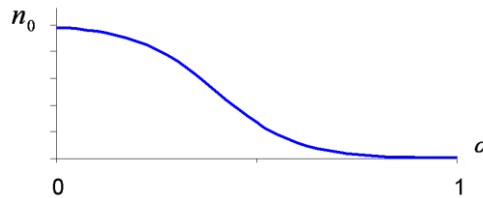


Figure 8-8: Number density n of cavities in relation to the average void fraction α .

Eq. (8.30) is a very crude representation of the phenomena of break and coalescence. A more accurate picture of the physics of these phenomena would be obtained by solving (a) transport equation(s) of the number density n .

8.5.6.1.2 Derivation of this correlation

This expression correctly reproduces the trend of the variation of n with α . It is based on a very simplified version of the conservation equation of the number density:

$$\frac{\partial n}{\partial t} = S_b + S_c; \quad (8.31)$$

where S_b and S_c are breakup and coalescence sources, respectively. Correlations for S_b and S_c are given in the chapter *cavitation*. They are repeated here for convenience.

- Coalescence is caused by the collision of particles. Several expressions exist for the collision frequency g_c [45]. One of them is expressed with the bubble diameter D_b , the void fraction α , the maximum packing concentration $\alpha_{\max} = 0.52$ and the bubble relative velocity U_{rel} [89]:

$$g_c = \frac{\alpha}{\alpha_{\max} - \alpha} \frac{6}{D_b} U_{rel}. \quad (8.32)$$

If the collisions are mainly attributed to the turbulent fluctuations, U_{rel} is defined by [90]:

$$U_{rel} = U_{turb} = \frac{(\varepsilon_l D_b / 2)^{1/3}}{\sqrt{2C_{am}}}; \quad (8.33)$$

where ε_l is the turbulence dissipation rate in the liquid phase and C_{am} is the added mass coefficient for which algebraic expressions are derived in [13].

Not all collisions lead to coalescence. The probability P_{col} that a collision results in coalescence is related to the film drainage time t_{dr} (time needed for the film of water situated between the bubbles to be drained) and the bubbles interaction time t_{in} . These characteristic times are defined as [90]:

$$t_{dr} = k_{dr} \frac{\rho_l U_{rel} D_b^2}{8\sigma}; \quad (8.34)$$

$$t_{in} = \frac{\pi}{4} \left(\frac{\rho_l C_{am} D_b^3}{3\sigma} \right)^{1/2}. \quad (8.35)$$

The probability P_{col} that a collision results in coalescence is such that:

$$P_{col} = \exp\left(-\frac{t_{dr}}{t_{in}}\right). \quad (8.36)$$

In eq. (3.34) k_{dr} is a model constant which usually has a value of 0.5 [45] and σ is the surface tension.

- The breakup of the bubbles occurs when deformation forces (e.g. velocity fluctuations) exceed confinement forces (typically surface tension σ). In [91], Martinez-Bazan et al. indicate that bubbles with a diameter smaller than

$$D_c = 1.26(\sigma/\rho)^{3/5} \varepsilon_l^{-2/5} \quad (8.37)$$

do not breakup.

For very small void fractions, the cavities are too small to be disturbed by the velocity fluctuations. They do not breakup (eq. (3.37)). Eq. (8.32) suggests that the frequency of collision is very weak. They do not coalesce. Thus, the number of cavities does not vary in time. When the void fraction tends to α_{\max} , the coalescence frequency is infinite. α_{\max} represents the maximum void fraction with rigid spheres. However, the probability that the collision leads to coalescence reduces (eq. (8.36)). Moreover it can not be ruled out that cavities deform. Therefore, the number of cavities strongly decreased near α_{\max} but not necessary equals one. For large void fractions, the probability is large to have only one cavity per unit volume of mixture.

8.5.6.2 Mass transfer and SFM

Each stochastic field Y^k is considered to represent one particular bubble at each iteration and computational cell. Considering a fluid containing n bubbles per unit volume; the radius R^k of this representative bubble can be easily derived from the mass fraction Y^k :

$$R^k = \left(\frac{3\rho Y^k}{4\pi\rho_g n} \right)^{1/3}. \quad (8.38)$$

8.5.6.3 Simplified form of the Rayleigh-Plesset equation

8.5.6.3.1 Preliminary discussion

The original RP is derived for a single spherical bubble. The radius of the spherical bubble evolves according to the pressure gradient existing between bubble's internal pressure, i.e. $p_{sat}(T)$ ignoring dissolved gas and surface tension; and the pressure $p_{l,\infty}$ in the liquid infinitely far from the bubble:

$$p_{sat}(T) - p_{l,\infty} . \quad (8.39)$$

In Euler cavitation models, the pressure at infinity $p_{l,\infty}$ of single-bubble theory (eq. (8.39)) is replaced by the average pressure p_{cell} of the mixture in the cell:

$$p_{l,\infty} \equiv p_{cell} . \quad (8.40)$$

Since this assumption may appear rather crude, this paragraph proposes a starting analysis to which extent this assumption is valid (Figure 8-9).

The first step in this analysis is to distinguish the liquid pressure $p_{l,cell}$ in the cell from the liquid pressure $p_{l,\infty}$ at infinity and to investigate the difference between them. For example, Fuster and Colonius [218] show that, for a small number of bubbles whose size is comparable to the cell size, p_l differs from $p_{l,\infty}$. The surrounding bubbles induce disturbances. Supplementary equations and supplementary terms in the RP are required to account for these disturbances. Nevertheless, Fuster and Colonius [218] indicate that when the number of small bubbles (small compared to the mesh size) is large, the contribution of the other bubbles is negligible and $p_{l,cell} \approx p_{l,\infty}$.

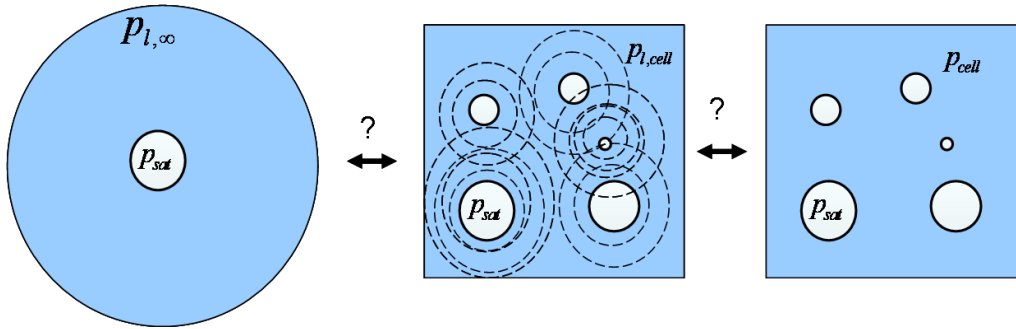


Figure 8-9: Illustration of the preliminary discussion about the validity of the Rayleigh-Plesset equation in the present formulation.

Neglecting these disturbances under all conditions, the discussion consists in comparing

$$p_{sat}(T) - p_{cell} ; \quad (8.41)$$

with

$$p_{sat}(T) - p_{l,cell} . \quad (8.42)$$

One approach to compare these two expressions (8.41) and (8.42) is to consider the correlation of Ishii [150] for the pressure of a two-phase mixture. This formula states that the pressure p of the mixture is the volume weighted pressure of both phases:

$$p_{cell} = \alpha p_{sat}(T) + (1 - \alpha) p_{l,cell} . \quad (8.43)$$

Expression (8.41) can be formulated with the mixture pressure p_{cell} defined in (8.43) as:

$$p_{sat}(T) - p_{cell} = p_{sat}(T) - [\alpha p_{sat}(T) + (1 - \alpha) p_{l,cell}] = (1 - \alpha) [p_{sat}(T) - p_{l,cell}] . \quad (8.44)$$

From (8.44), it is observed that the error between (8.41) and (8.42) is of order $O(\alpha)$. Prosperetti gives the same result in [219]. For small void fraction α , both expressions are equivalent. In contrast, for larger void fraction, eq. (8.44) indicates that the implementation of the RP with the mixture pressure p_{cell} may be inaccurate.

Finally it should be stressed here that the RP accounts for the thermodynamic non-equilibrium of the phases. Although the phases share the same pressure and the same temperature; they may have different chemical potentials. In that case, the mass transfer occurs between the phases as to equalize the potentials. Typically, the chemical potential of water becomes higher than that of vapor when the pressure of the mixture decrease below saturation conditions (see Figure 8-10) Thus, phase change starts in direction of the more stable gas phase. In the RP, this phenomenon is represented by a positive pressure difference:

$$p_{sat}(T) - p > 0. \quad (8.45)$$

Vaporization ends when the chemical potentials of both phases are equal. The phases are in thermodynamic equilibrium at saturation conditions (pressure and temperature). Similarly in the RP, vaporization stops when

$$p_{sat}(T) - p = 0. \quad (8.46)$$

In that case, the pressure, and thus the temperature, reaches saturation conditions.

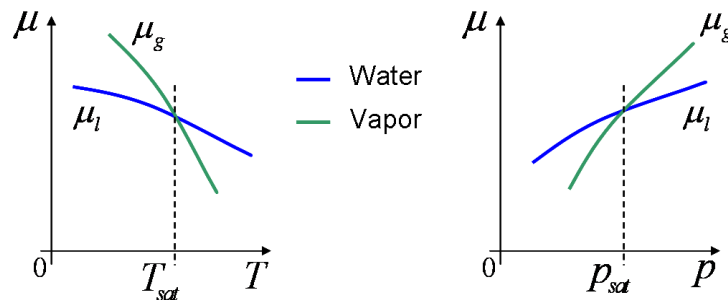


Figure 8-10: Chemical potentials of water and vapor as a function of temperature (left) and pressure (right).

8.5.6.3.2 Assumptions

A simplified form of the RP is developed. The mass transfer $S(Y)$ is decomposed into a condensation part $S_-(Y)$ and a vaporization part $S_+(Y)$. $S_-(Y)$ is defined on the interval $]p_{sat}, +\infty[$; while $S_+(Y)$ on the interval $]-\infty, p_{sat}]$.

Assumptions for the derivation of the model are:

- 1) On bubble motion:
 - a. No gravity effect
 - b. Spherical symmetry
 - c. Inertial effects are approximated
- 2) On liquid behavior:
 - a. Single component fluid
 - b. Newtonian fluid
 - c. Viscosity η_l is neglected
- 3) On vapor behavior:
 - a. Viscosity η_g is neglected
 - b. Density $\rho_g \ll \rho_l$
 - c. Presence of contaminant gas mass m_G
 - d. Mass diffusion of contaminant gas neglected
 - e. The vapor pressure is the saturation pressure of the mixture (temperature-dependent)
- 4) On interface behavior:
 - a. (Constant) surface tension is not neglected
- 5) On bubbles interaction
 - a. No interaction

These assumptions are common for cavitation models based on the RP and implemented in Euler solvers except assumptions 3)c, 3)e and 4)a.

8.5.6.3.3 Water quality effect

8.5.6.3.3.1 Mass of dissolved gas

Assumptions 3)c and 4)a are used to estimate the nuclei equilibrium radius R_e from the steady-state formulation of the RP at $p_{l,\infty} = p_{sat}(T)$:

$$p_{sat}(T) - p_{l,\infty} = \frac{2\sigma}{R_e} - \frac{m_G T \mathcal{R}_G}{\frac{4}{3}\pi R_e^3} = 0 \Rightarrow R_e = \sqrt{\frac{3m_G T \mathcal{R}_G}{8\pi\sigma}}. \quad (8.47)$$

Similarly to n_0 , m_G represents water quality effects. Water with larger mass of dissolved gas is characterized by a larger equilibrium radius. In this work, the geometry possesses only one inlet and water quality is assumed to be constant. The mass of contaminant gas is assumed constant in space and time (assumption 3)d). The dependence of R_e on the temperature is neglected. The temperature T in eq. (8.47) is assumed to be the temperature at the inlet of the computation domain.

For complex geometries with several inlets, the transport equation of the mass of dissolved gas m_G could be solved to account for the mixing of fluids characterized by different qualities. R_e would be calculated in any cell according to (8.47).

The interfacial mass transfer is expressed to ensure that vaporous cavities do not become smaller than the initial nuclei after collapse.

8.5.6.3.3.2 Initial nucleus size spectrum

The radius R^k calculated from the vapor mass fraction according to eq. (8.38) is not directly used for the calculation of the interfacial mass transfer.

The number and the size repartition of the nuclei importantly impact the cavitation process. A simple routine estimates if the cavity of size R^k belongs to the ensemble of cavitation nuclei. In that case, the cavity size is sampled from a prescribed lognormal distribution. Otherwise, the cavity already is an activated nucleus and its radius R^k is not modified by the routine.

8.5.6.3.3.3 Nuclei activation

Assumption 4)a is important to represent the activation of the nuclei. In this cavitation model, the pressure must decrease below nucleus pressure threshold p_{cr} to activate the nucleus. Thus, vaporization starts only when the pressure p is below:

$$p_{cr} = p_{sat}(T) - \frac{4\sigma}{3R}; \quad (8.48)$$

R being the radius of the nucleus. The source term $S_+(Y)$ is zero otherwise; i.e. the nucleus is stable.

8.5.6.3.4 Thermal effects

To account for thermal effects (see chapter *cavitation*), the saturation pressure is implemented as a function of the varying temperature (Assumption 3)e) (section 8.5.1.3.2).

Hence, the source term in the RP is given by:

$$\sqrt{\frac{3}{2} \frac{|p_{sat}(T) - p|}{\rho_l}}$$

correctly reduces when water vaporizes since the saturation pressure decreases.

Furthermore, pressure and temperature reach the correct saturation conditions at equilibrium:

$$p = p_{sat}(T); \quad (8.49)$$

$$T = T_{sat}(p). \quad (8.50)$$

8.5.6.3.5 Inertial effect

Inertial effects are represented in the Rayleigh-Plesset equation by the acceleration term. This term cannot be directly solved with an Euler code and requires an additional solver. Furthermore, the time scale of the bubble collapse is much smaller than that of the flow. To avoid the complexity of the coupling and extremely large computation times, the inertial effects are represented in the present formulation by a condensation parameter $C_{cond} = 1/750$. C_{cond} reduces the condensation rate in comparison to the vaporization rate.

An illustration of this modeling is given on Figure 8-11. The diagram on the top represents the size of a single bubble moving in a fluid from abscissa $x = -0.02$ to $x = 0.16$. The growth of the bubble is assumed to have no influence on the pressure field of the fluid. This pressure field is displayed in Figure 8-11, bottom. It varies along the abscissa. The bubble enters at $x = -0.01$ a domain where the pressure is below saturation pressure and starts to grow. At $x = 0.03$ the bubble exits this region and enters a region where the pressure field is above the saturation pressure. Due to the inertial effects, the bubble does not immediately shrink. It shrinks abruptly with a certain time delay. Then, the bubble rebounds until it reaches its initial value. The exact equation of this complex phenomenon is the Rayleigh-Plesset equation (in blue on Figure 8-11). A simplification of the Rayleigh-Plesset equation is the Rayleigh equation. The Rayleigh equation neglects among others inertial effects. The growth calculated with this simple equation (black solid line on Figure 8-11) does not differ significantly from the growth calculated with the Rayleigh-Plesset equation. However, the collapse of the bubble is noticeably different. To improve the modeling avoiding a complex coupling with an additional solver, the condensation term of the Rayleigh equation is scaled in this cavitation model (red curve on Figure 8-11).

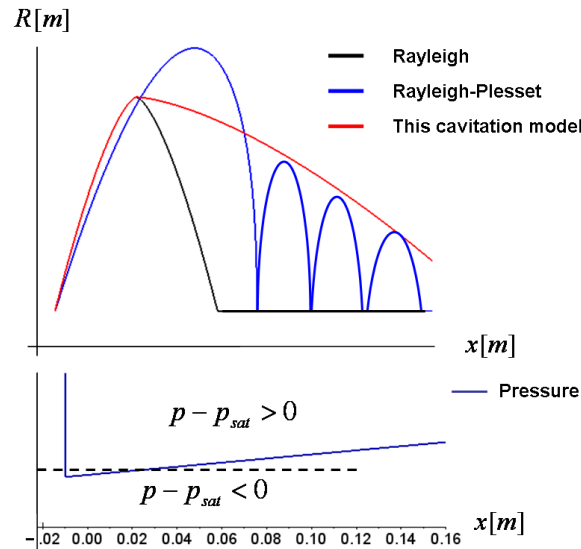


Figure 8-11: Illustration of inertial effects. The diagram on the top represents the radius of a single bubble moving in a fluid from abscissa $x = -0.02$ to $x = 0.16$. The growth of the bubble is assumed to have no influence on the pressure field of the fluid. The pressure field of the fluid is displayed in the figure on the bottom. It varies along the abscissa. Three relations are used to estimate the growth of the bubble. Displayed in black, the Rayleigh equation neglects inertial effects. In blue, the Rayleigh-Plesset equation is the exact solution of the bubble growth. The cavitation model used in this thesis (in red) scales the condensation term of the Rayleigh equation to reproduce inertial effects.

8.5.6.4 Source term

The derivation of the source term relies on the RP. The source term of the stochastic-field vapor mass fraction equations can be related to the growth of the cavities:

$$\frac{DY^k}{Dt} = \frac{D}{Dt} \left(\frac{\rho_g}{\rho} n \frac{4\pi}{3} (R^k)^3 \right) = \frac{\rho_g}{\rho} 4\pi n (R^k)^2 \frac{DR^k}{Dt} = S(Y^k). \quad (8.51)$$

In eq. (8.51), the relation between the mass fraction Y^k and the radius R^k :

$$Y^k = \frac{\rho_g}{\rho} n \frac{4\pi}{3} (R^k)^3; \quad (8.52)$$

is used. Furthermore, the effect of the temporal variation of the cavity number and densities are neglected.

Similarly, the equilibrium vapor mass fraction representing the mass fraction of the bubbles which have the radius R_e (sect. 8.5.6.3.3.1) is given by:

$$Y_e = \frac{\rho_g}{\rho} n \frac{4\pi}{3} (R_e)^3. \quad (8.53)$$

The expression for $S_+(Y^k)$ is:

$$S_+(Y^k) = (36\pi n)^{1/3} (\rho_g)^{1/3} (\rho Y^k)^{2/3} \sqrt{\frac{2}{3\rho_l}} \sqrt{\max\left[p_{sat}(T) - p - \frac{4\sigma}{3R^k}, 0\right]}. \quad (8.54)$$

The expression for $S_-(Y^k)$ is:

$$S_-(Y^k) = \begin{cases} S_-^1(Y^k) & \text{if } Y < Y_{eq} \\ S_-^2(Y^k) & \text{if } Y \geq Y_{eq} \end{cases}; \quad (8.55)$$

with

$$S_-^1(Y^k) = \frac{\rho}{\tau_{nuc}} (Y_e - Y^k); \quad (8.56)$$

$$S_-^2(Y^k) = -C_{cond} (36\pi n)^{1/3} (\rho_g)^{1/3} (\rho Y^k)^{2/3} \sqrt{\frac{2}{3\rho_l}} \sqrt{\max[p - p_{sat}(T), 0]}; \quad (8.57)$$

where τ_{nuc} is a model time-constant.

8.6 Validation cases

8.6.1 Flow patterns downstream of a sudden expansion

8.6.1.1 Experimental setup

The experiments of Attou et al. [67] are used to validate qualitatively the code. In these experiments, the phenomenon of double-choking in critical two-phase flows is investigated. A steady-state critical vapor-water flow is observed in a horizontal relief line. This relief line is characterized by a sudden enlargement of the cross section. The pressure is 6bar and the temperature ranges from subcooled to saturated conditions.

The walls of the test section are transparent. In this manner, the flow patterns downstream of the enlargement can be observed. The influence of the subcooling on these flow patterns is stressed by the experimenters.

8.6.1.2 Objective

The test stand of Attou et al. [67] is a very long geometry. A quantitative validation of the cavitation model with these experiments would require far too long computation time. To avoid this inconvenience, these experimental results are used to validate only qualitatively the code.

For this purpose, the influence of the subcooling on the flow pattern is investigated numerically. The qualitative validation consists in comparing the flow patterns obtained in the experiments and in the numerical calculations.

8.6.1.3 Comparison between numerical and experimental results

8.6.1.3.1 Fluid largely subcooled

Attou et al. [67] first describe the characteristics of the flow pattern of a largely subcooled fluid. These characteristics are:

- The streamlines of the central flow remain parallel to the pipe axis at the vicinity of the enlargement.
- The reattachment point is located well beyond the sudden enlargement.

- The confined free jet pattern is axisymmetric.
- The central flow seems conical with a small opening angle.
- A high density of small bubbles is observed at the jet boundary.

A similar flow pattern is observed in the numerical calculation under the same flow conditions (see Figure 8-12).

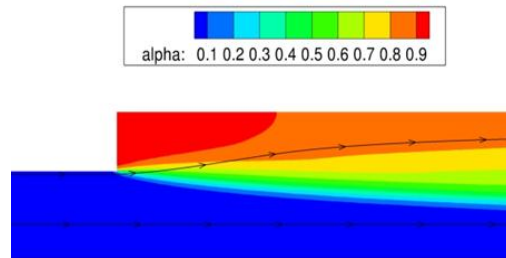


Figure 8-12: Flow pattern of a largely subcooled fluid downstream of an enlargement with the cavitation model. Streamlines are represented by solid lines with arrows. Only one half of the enlargement is represented.

8.6.1.3.2 Fluid near saturation

In contrast, the flow pattern of a fluid near saturation downstream of an enlargement is characterized by [67]:

- The streamlines of the central flow diverge strongly from the pipe axis close to the enlargement.
- The separation zone does not exist practically. The reattachment is located at a very small distance from the enlargement.

A similar flow pattern is observed in the numerical calculation under the same flow conditions (Figure 8-13).

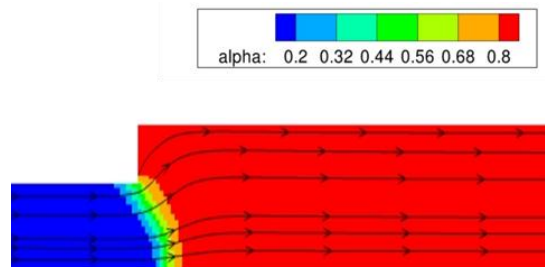


Figure 8-13: Flow pattern of a fluid near saturation downstream of an enlargement with the cavitation model. Streamlines are represented by solid lines with arrows. Only one half of the enlargement is represented.

8.6.1.3.3 Fluid at saturation

A two-phase mixture at saturation is also investigated by Attou et al. [67]. In this case, the flow pattern has a similar structure as observed in subcritical incompressible flows [67]:

- The reattachment point is situated downstream of the enlargement.
- The composition of the separated zone and central flow are similar.

A similar flow pattern is observed in the numerical calculation with a two-phase mixture (Figure 8-14).

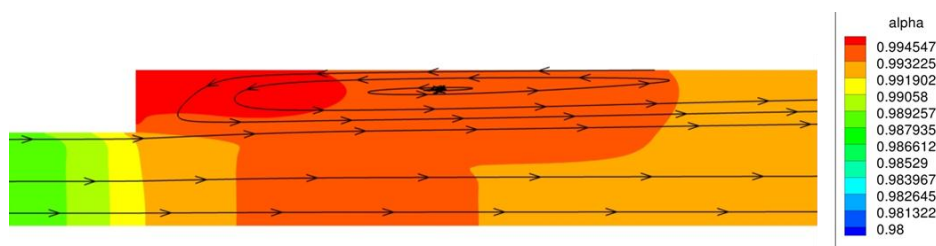


Figure 8-14: Flow pattern of a two-phase mixture downstream of an enlargement with the cavitation model. Streamlines are represented by solid lines with arrows. Only one half of the enlargement is represented.

8.6.2 Cavitation sheet

8.6.2.1 Experimental setup

For the validation of the code, it is advantageous to have measured void and velocity profiles. Experiments with detailed data in cavitation flows are rare. One available experimental study of cavitation with detailed information on the flow structure can be found in [220]. Thus, the experimental results of Barre et al. [220] are exploited to validate the novel cavitation model. In these experiments, an attached cavitation sheet develops in the venturi type test section CREMHYG (Institut national polytechnic Grenoble). The upper and lower walls of the test section are designed to reproduce cavitating flows on the blades of space turbopump inducers. The cross sections are rectangular and their sizes at inlet and throat are 50x44 mm² and 43.7x44 mm², respectively. The convergence and divergence angles are 4.3° and 4°, respectively.

The visualization of the cavitation sheet is possible through the transparent walls on the side. The test section is equipped with pressure and temperature sensors as well as a double optical probe. The double optical probe is used to evaluate the void fraction and velocity field inside the cavity at five horizontal positions.

A free surface tank imposes the reference pressure in the loop. The flow rate is enforced by a circulating pump. For the selected operating point, the pressure in the tank is $p = 0.713$ bar and the volume flow rate is $\dot{V} = 23.75$ dm³/s. In that case, a cavity develops downstream of the contraction. The length L_{cav} of this cavity is about 80 mm.

8.6.2.2 Previous numerical analysis

Other numerical analyses of these experiments can be found in [179] and [221]. In both numerical investigations vapor and water are considered to form a compressible mixture. In [179] the barotropic state law of Delannoy et al. [222] is used. Mixture's density and local static pressure are explicitly linked. Turbulence is modeled by the Yang-Shih $k-\varepsilon$ model [223] with extended wall functions [179]. Steady and unsteady calculations are performed. In [221], the transport equation of the vapor mass fraction is solved but turbulence is neglected.

8.6.2.3 Numerical setup

8.6.2.3.1 Numerical mesh

The test section is modeled with block-structured meshes. Both two-dimensional and three-dimensional simulations are performed. The Spalart-Allmaras model is used for the two-dimensional analysis. The LES simulation is performed with the MILES approach for the three-dimensional analysis.

The meshes are refined

- at the contraction;
- downstream of the contraction; and
- at the walls.

Far upstream and downstream of the contraction, the cells are stretched out to increase the damping of the disturbances. In this manner, increased code stability and faster statistical convergence are obtained.

In RANS simulations, the mesh globally is refined until the length of the cavitation sheet remains similar in the mesh under consideration and in a finer mesh.

In the LES calculation, the $x+$, $y+$ and $z+$ values of the mesh correspond to the usually recommended values in LES calculations [37]. The $x+$, $y+$ and $z+$ values are the non-dimensional sizes of the first cells at the wall in the flow direction, normal to the wall and transverse to the flow direction, respectively.

8.6.2.3.2 Boundary conditions

Figure 8-15 represents the computational domain and the boundary conditions. Walls have non-slip conditions and are adiabatic. The temperature and the velocity components are imposed at the inlet. Thereby, the velocity is steady-state and normal to the boundary surface. Its magnitude is calculated according to the experimental volume flow rate. The pressure is prescribed at the outlet. No experimental data are available on the value of this pressure. The pressure is varied until a cavitation sheet of about 80mm is observed.

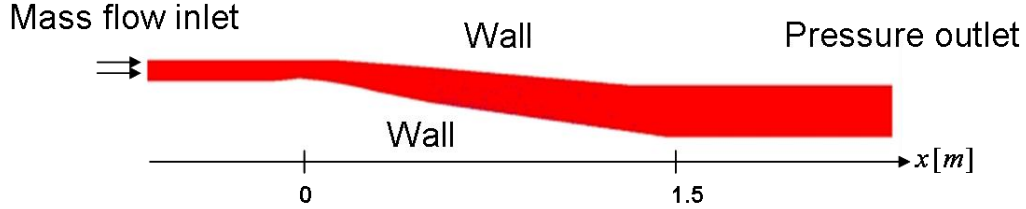


Figure 8-15: Representation of the computational domain and boundary conditions. $x=0m$ is the position of the contraction.

8.6.2.4 Objective

The present investigation focuses on:

- The behavior of the stochastic fields;
- The validation of the cavitation model;
- The information obtained with the stochastic-field method.

8.6.2.5 Preliminary discussion

8.6.2.5.1 Turbulence model and stochastic fields

The vapor mass fraction pdf results among others from the turbulent fluctuations. Each stochastic field represents one realization of this pdf at every position and time; and the ensemble of the stochastic fields is an approximation of the vapor mass fraction pdf on the sub-grid scale. In this context, it is of interest to analyze the influence of the turbulence model on the stochastic fields.

The transport equation of a stochastic field Y^k is already given in section 8.3.2.1 but repeated here for convenience:

$$dY^k = -u_i \frac{\partial Y^k}{\partial x_i} dt + S(Y^k) dt + \overbrace{\frac{\partial}{\partial x_i} \left(D'_Y \frac{\partial Y^k}{\partial x_i} \right) dt}^1 + \overbrace{\sqrt{2D'_Y} \frac{\partial Y^k}{\partial x_i} dW_i^k - 1/2 \frac{(Y^k - \langle Y \rangle)^2}{\tau_Y} dt}^2. \quad (8.58)$$

The influence of the unresolved turbulent fluctuations appears in the two modeled terms: Term 1 represents the effect of the turbulent fluctuations on the transport of the vapor mass fraction in the physical space. Term 2 represents the effect of the molecular transport on the scalar properties in the composition space.

8.6.2.5.1.1 Turbulent transport

The transport of Y^k by the turbulent fluctuations is modeled according to the gradient hypothesis. The combined molecular and turbulent mass diffusivity coefficient D'_Y is a measure of the mixing of the stochastic field Y^k on the sub-grid scale. This coefficient is larger in RANS simulations than in LES simulations since all turbulent fluctuations are modeled in the RANS approach. Therefore, the modeled stochastic contribution

$$\sqrt{2D'_Y} \frac{\partial Y^k}{\partial x_i} dW_i^k \quad (8.59)$$

is expected to have more impact in a RANS simulation than in a LES calculation.

8.6.2.5.1.2 Molecular mixing in the composition space

In the present implementation of the model, the turbulent time scale τ_t is expressed with the grid size Δ , the average density $\langle \rho \rangle$, the molecular viscosity and the modeled viscosity η_{mod} :

$$\tau_t = \frac{\langle \rho \rangle \Delta^2}{\eta + \eta_{\text{mod}}} . \quad (8.60)$$

This modeling is usual in most LES calculations (e.g. [19]). In that case, the modeled viscosity η_{mod} is the sub-grid scale viscosity η_{sgs} .

In contrast, in a RANS framework, the time scale τ_t is the inverse of the turbulent specific dissipation rate ω :

$$\tau_t = \omega^{-1} . \quad (8.61)$$

Thus, τ_t can be calculated with the turbulent kinetic energy k and the turbulent energy dissipation rate ε or directly with the turbulent specific dissipation rate ω . These turbulent flow variables are available in the typical two-equation eddy viscosity models such as $k-\varepsilon$ or $k-\omega$. However, these eddy viscosity models are not available in the present code for two-phase flows. Hence the model (8.60) is used instead with the eddy viscosity $\eta_t = \eta_{\text{mod}}$. In that case, however, the turbulent time scale depends on the mesh size; while all other flow variables become independent of the mesh size when the mesh is sufficiently fine.

8.6.2.5.1.3 Molecular mixing and bubbles

The IEM is used to model the molecular mixing of the vapor mass fraction. An investigation on the validity of this model is not included in the scope of this work. However, the mixing of bubbles may follow another dynamic than the mixing of chemical species. For example, the mixing of polydisperse bubbles does not (necessarily) induce the reduction of the variance of the bubble size pdf in a homogeneous turbulent flow.

8.6.2.6 Influence of the number of stochastic fields

As a Monte-Carlo technique, the statistical error should reduce with increasing number of fields. More precisely, this statistical error should be of order $O(1/\sqrt{N})$ with N fields. In this work, no quantitative estimation of the impact of the number of fields is performed under real flow conditions. However, a simple example is presented in this paragraph to illustrate the effect of an increase of the number of stochastic fields.

In this simple example, five calculations are performed under the same flow conditions but with a number of stochastic fields differing from one calculation to the other:

- One stochastic field in the first calculation;
- Four stochastic fields in the second calculation;
- Eight stochastic fields in the third calculation;
- Sixteen stochastic fields in the fourth calculation; and
- Twenty stochastic fields in the fifth calculation.

The computational domain corresponds to the test stand of Barre et al. [220]. The flow conditions used in these simulations do not represent the experimental flow conditions. They are selected to illustrate the behavior of the stochastic fields as simply as possible. The mesh is coarse and the turbulence very low. In this manner, the turbulent time scale calculated according to (8.60) is very large and the fields relax to the mean value only after a very long time.

The calculations are performed as follows. The pressure of the fluid is initialized at atmospheric conditions and the fluid velocity is zero. The cavities are nuclei sampled from a lognormal pdf. At time $t=0s$, water enters the computational domain with a velocity $10m/s$. The pressure of the fluid decreases after the moving liquid reaches the divergent part of the test stand. The largest nuclei are activated and start to grow. An attached cavitation sheet develops downstream of the smallest cross section.

The stochastic fields are monitored at a given location inside the cavitation sheet. The evolution of these fields is presented on Figure 8-16 for the first (left) and the fifth (right) calculations. In the first calculation, the stochastic field starts to grow until it attains a constant value $R = 4.5 \cdot 10^{-4} m$. In the other simulation, only some fields grow and attain a constant value. These fields represent the large activated nuclei. The other fields remain sampled from the lognormal distribution. They represent the inactivated nuclei.

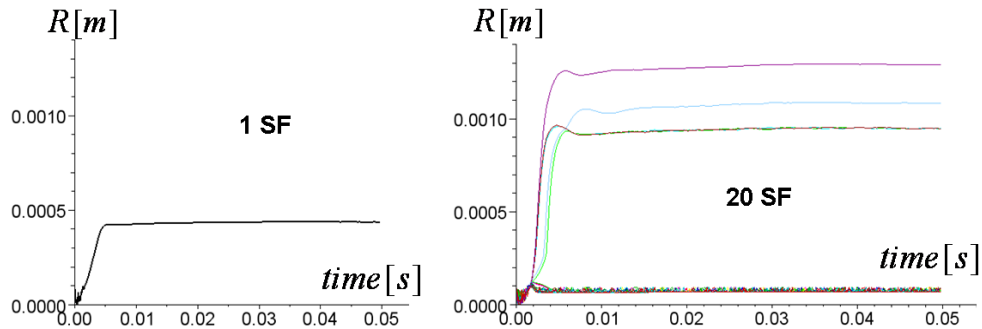


Figure 8-16: Evolution of the stochastic fields in a simulation with one stochastic field (left) and 20 stochastic fields (right).

At any time, the mean value of the stochastic radius R^k , $k = 1..N$, is the mean radius of the cavities in the cell under consideration. The comparison between the mean radii obtained in the five calculations is displayed on Figure 8-17. The mean radius attains an equilibrium size in each calculation. This size differs from one calculation to the other. With an increase of the number of stochastic fields, the mean radius tends to a constant value. The difference in the equilibrium radii is almost negligible between the fourth and fifth calculations. With eight fields the approximation of the mean radius is still very good while the error is large with fewer fields.

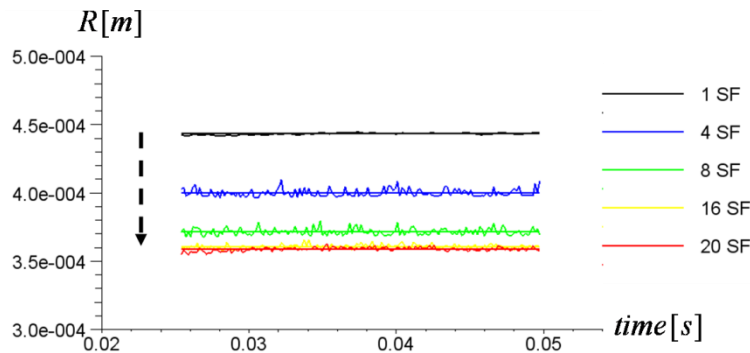


Figure 8-17: Reduction of the statistical error with an increasing number of fields. The mean radius of the bubbles in a cavitation sheet is estimated with 1/4/8/16/20 stochastic fields. The arrow indicates that this mean value tends to a constant value with an increasing number of fields.

8.6.2.7 Comparison between numerical and experimental results

According to the simple example of the preceding section, eight fields represent a good compromise between accuracy and efficiency. Thus, in the rest of this thesis, the calculations are performed with 8 stochastic fields to accurately capture the vapor mass fraction pdf and the bubble size spectrum at a reasonable cost. This number of fields is also generally recommended in the simulation of combusting flows.

8.6.2.7.1 Two-dimensional simulations

In spite of the shortcoming described in section 8.6.2.5.1.2, two-dimensional simulations are performed with the Spalart-Allmaras model. These simulations have the advantage to be faster than expensive LES calculations.

Two RANS simulations are performed. The first simulation reproduces the experimental conditions of Barre et al. [220]. The second is performed with a lower pressure outlet. As a result, the cavitation sheet becomes unstable at its rear end. Some results of this second calculation are discussed in section 8.6.2.7.1.4.

In the RANS calculations, it is necessary to increase the nuclei density number to $n_0 = 10^{10} m^{-3}$ to obtain numerical results in agreement with experimental data. The equilibrium vapor mass fraction is set to 10^{-7} in both calculations.

8.6.2.7.1.1 Qualitative validation

Similarly to the experimental results, the numerical results indicate that an attached cavitation sheet develops in the divergent section. In Figure 8-18, the cavitation sheet obtained in the calculation is shown. It is characterized by the density of the vapor-water mixture. There, a density below $900 kg/m^3$ indicates the presence of vapor.

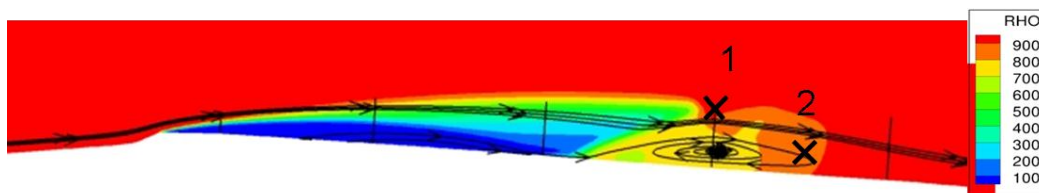


Figure 8-18: Numerical results for the attached cavitation sheet observed in Barre et al. [220]. The cavitation sheet is characterized by the vapor-water mixture density, where a density below $900 kg/m^3$ indicates the presence of vapor. Streamlines are shown; vertical lines represent experimental measurement positions; and at the locations marked 1 and 2 bubble size pdf are numerically sampled.

8.6.2.7.1.2 Velocity profiles

Experimental data on the velocity field are available inside the cavitation at five longitudinal positions indicated by vertical lines in Figure 8-18. The calculated velocity profiles (solid lines in Figure 8-19) are in good quantitative agreement with the experimental results (triangles in Figure 8-19). These experimental results are described in [220]. There, Barre et al. [220] present their experimental data (blue triangles) and compare them to the results of Stutz et al. [224] (orange triangles) obtained for the same experiment some years before.

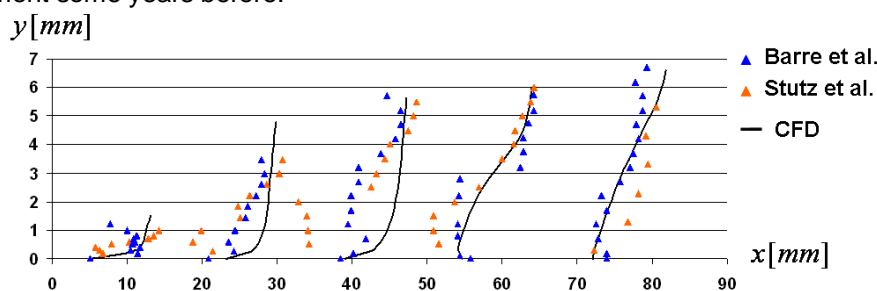


Figure 8-19: Measured (triangles: Barre et al. [220] and Stutz et al. [224]) and calculated (solid lines) velocity profiles inside the cavitation sheet at the five longitudinal positions indicated by solid lines in Figure 8-18.

Although the agreement is rather good, the calculation underestimates the flow detachment at the second and third position. This discrepancy is caused by the turbulence modeling.

8.6.2.7.1.3 Void profiles

The void profiles measured at the five longitudinal positions in the cavitation sheet indicated by the vertical lines in Figure 8-18 are also available in [220]. Calculated (solid line in Figure 8-20) and measured (blue triangle in Figure 8-20) void fraction profiles are in good quantitative agreement.

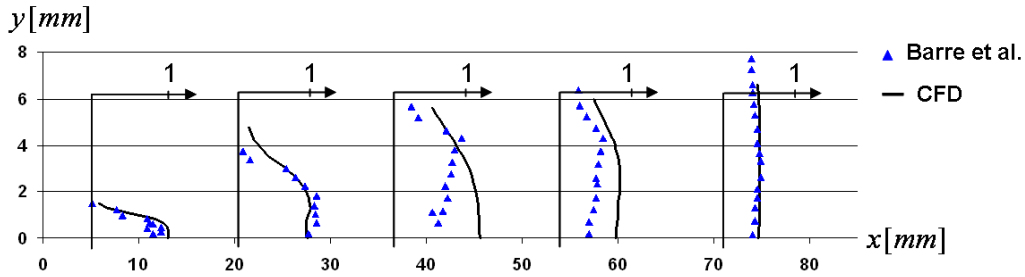


Figure 8-20: Measured (triangles: Barre et al. [220]) and calculated (solid lines) void fraction profiles inside the cavitation sheet at the five longitudinal positions indicated by solid lines in Figure 8-18.

8.6.2.7.1.4 Bubble size spectrum

Figure 8-21 gives an example of the evolution of the 8 radii at one location in the computational domain. In that case, the location is marked by 1 in Figure 8-18.

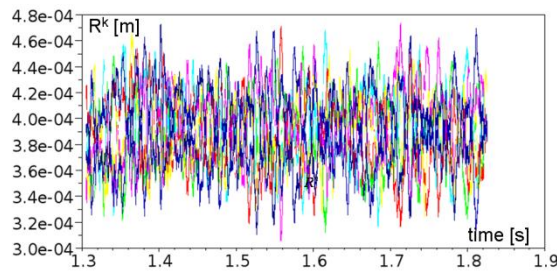


Figure 8-21: Radius-size R^k statistical probability (time history) of the 8 stochastic fields calculated at location 1 in Figure 8-18.

With the proposed modeling, the bubble size pdf at any location can be obtained from the evolution of the stochastic field. The bubble size pdf obtained at two locations in the nozzle are represented in Figure 8-22. On the left hand side, the pdf obtained at the location marked by 1 in Figure 8-18 is displayed. On the right hand side, the pdf obtained at the location marked by 2 in Figure 8-18 is displayed. At both positions, near Gaussian distributions are observed.

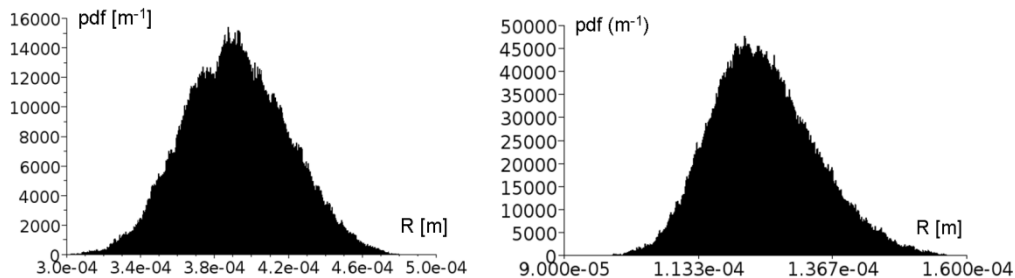


Figure 8-22: Calculated bubble size pdf in a stable cavitation sheet at locations 1 (left) and 2 (right) marked in Figure 8-18.

When reducing the outlet pressure in the numerical simulation, the cavity becomes unstable at its rear end. In this case, the pdf associated to the location 1 and 2 are displayed on Figure 8-23 on the left and Figure 8-23 on the right, respectively. The evolution of the stochastic fields (Figure 8-24) is strongly non-Gaussian. The turbulent fluctuations and the macroscopic cavitation sheet unsteadiness are superimposed. In particular, at location 1, the bubble size pdf (on Figure 8-23, left) would be better approximated by a 4-modal distribution.

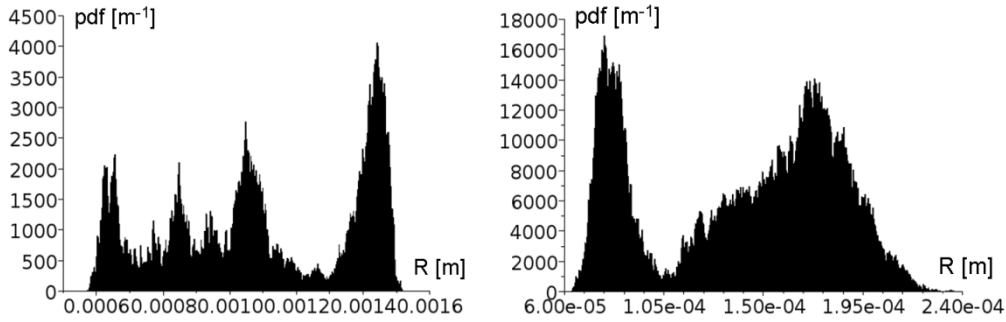


Figure 8-23: Calculated bubble size pdf at locations 1 (left) and 2 (right) marked in Figure 8-18 in an unstable cavitation sheet.

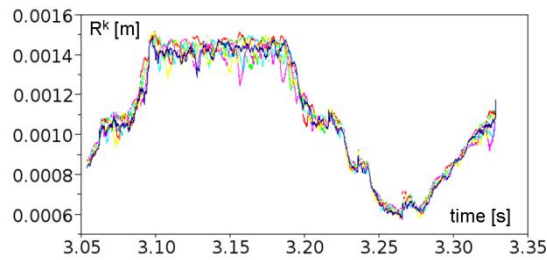


Figure 8-24: Radius-size R^k statistical probability (time history) of the 8 stochastic fields calculated at location 1 in Figure 8-18.

8.6.2.7.1.5 Stochastic fields

A snapshot of one of the stochastic fields is displayed in Figure 8-25 (bottom) with the corresponding pressure field (top). This snapshot is extracted from the calculation performed under the flow conditions described in [220]. In that case, the cavitation sheet is stable. The stochastic fields observed are also stable.

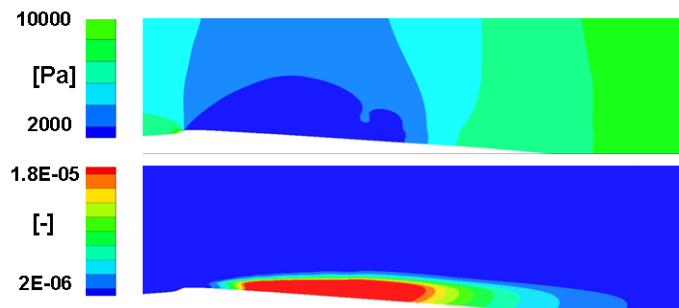


Figure 8-25: Snapshot of one of the stochastic fields observed in the calculation of a stable cavitation sheet (bottom) and the corresponding pressure field (top). The flow direction is from the left to the right.

All stochastic fields have a similar behavior. They do not immediately increase in the region where the pressure is below the saturation pressure (below 2400Pa). A slight delay is observed corresponding to the time necessary for the bubbles to grow. Then, the stochastic fields slowly decrease in the region of pressure above the saturation pressure. The bubbles require a finite time to collapse.

The finite time of bubble collapse is also observed in the experiments (Figure 8-26). This time is primarily influenced by the inertial effects (section 8.5.6.3.5).

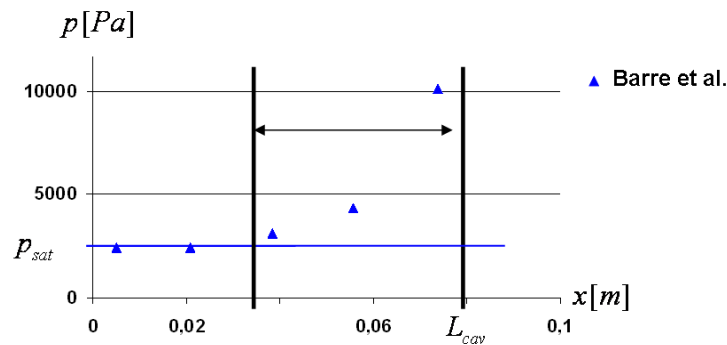


Figure 8-26: Experimental pressure measurement of Barre et al. [220] as a function of the distance from the contraction. The arrow symbolizes the domain where the cavitation sheet is observed despite pressures above the saturation pressure.

8.6.2.7.2 Three-dimensional simulations

Two dimensional calculations are performed to analyze the behavior of the stochastic fields. However, the time constant of the turbulent fluctuations is not physically correct and three dimensional effect are disregarded. The same experiment is simulated with a LES in a three-dimensional mesh.

In the LES calculation, the number density is set to $n_0 = 10^7 \text{ m}^{-3}$ and the equilibrium vapor mass fraction to 10^{-7} .

8.6.2.7.2.1 Qualitative behavior

The same qualitative behavior is observed in the LES calculation. An attached cavitation sheet develops in the Venturi-like test section. The intensity of the density field is fluctuating but the length of the cavitation sheet remains approximately constant (Figure 8-27 and Figure 8-28).



Figure 8-27: Representation of a density iso-surface ($\rho = 900 \text{ kg/m}^3$) obtained in the LES calculation of the stable cavitation sheet. The flow conditions and the geometry are those described in [220].

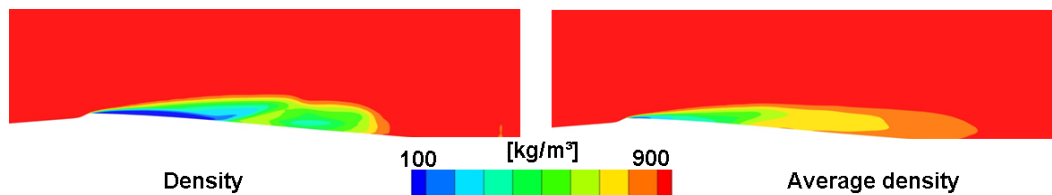


Figure 8-28: Numerical results of the LES calculation of an attached cavitation sheet. The cavitation sheet is characterized by the instantaneous density (left) and average density (right) of the vapor-water mixture. A density below 900 kg/m^3 indicates the presence of vapor.

8.6.2.7.2.2 Velocity profile

The calculated ensemble-averaged velocity profiles at the five longitudinal positions indicated by vertical lines in Figure 8-18 are in good agreement with the experimental results of Barre et al. [220] and Stutz et al. [224]. The calculated velocity profiles are represented by solid lines in Figure 8-29 and the experimental results by triangles. The flow detachment is better predicted in this LES calculation than in the RANS simulation presented in section 8.6.2.7.1.2.

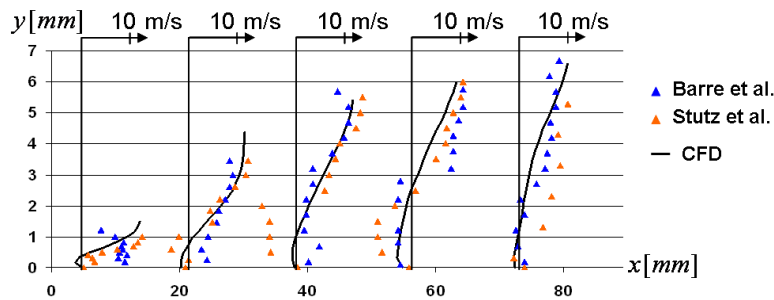


Figure 8-29: Measured (triangles: Barre et al. [220] and Stutz et al. [224]) and calculated (solid lines) velocity profiles inside the cavitation sheet at the five longitudinal positions indicated by solid lines in Figure 8-18.

8.6.2.7.2.3 Void profile

The calculated ensemble-averaged void profiles at the five longitudinal positions indicated by vertical lines in Figure 8-18 are in good agreement with the experimental results of Barre et al. [220]. The calculated void profiles are represented by solid lines in Figure 8-30 and the experimental results by triangles. The void fraction is slightly over-predicted at the rear part of the cavitation sheet.

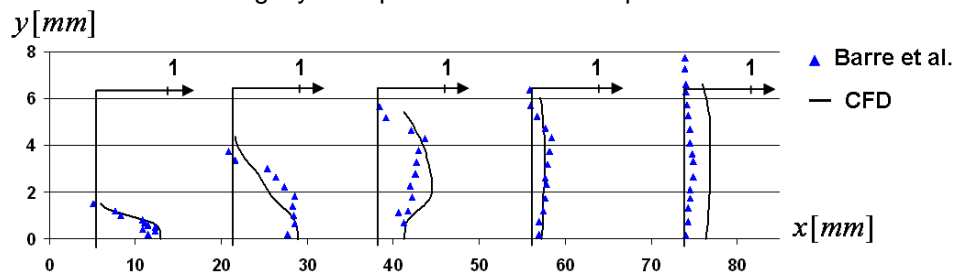


Figure 8-30: Measured (triangles: Barre et al. [220]) and calculated (solid lines) void fraction profiles inside the cavitation sheet at the five longitudinal positions indicated by solid lines in Figure 8-18.

8.6.2.7.2.4 Pressure profile

Pressure measurement data are also available on the bottom side of the test stand. Both experimental and calculated mean pressures are compared in Figure 8-31. The agreement between both pressure distributions is relatively good.

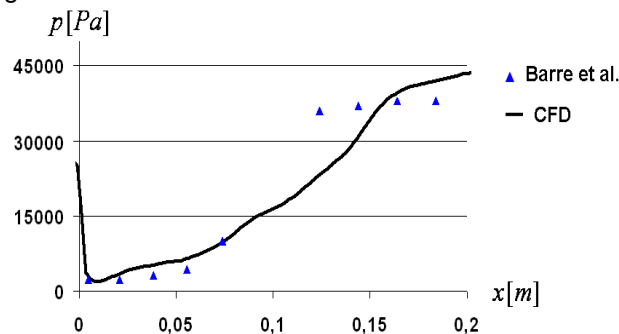


Figure 8-31: Comparison between measured (triangle: Barre et al. [220]) and calculated (solid line) pressure distribution at the bottom side of the test stand. The abscissa is 0 at the contraction.

8.6.2.7.2.5 Bubble size spectrum

The bubble size spectra obtained in the RANS and LES calculations can not be compared. The number of nuclei has a direct influence on the size of the cavities. In the RANS calculations, the initial number of cavities is thousand times larger than in the LES calculation. Thus, the bubbles in the RANS simulations are expected to have a smaller radius (see eq. (8.38)). Moreover, as it is discussed in sect. 8.6.2.5.1.2, the RANS simulations are performed with a turbulent time scale which does not correspond to the physical time scale.

The evolution of the stochastic fields at four different locations in the cavitation sheet is represented on Figure 8-32 to Figure 8-35. These four locations are marked on Figure 8-36. The bubble size spectrum significantly differs from one location to the other. The bubble size spectra at location 3 and 4 tend to a Gaussian distribution.

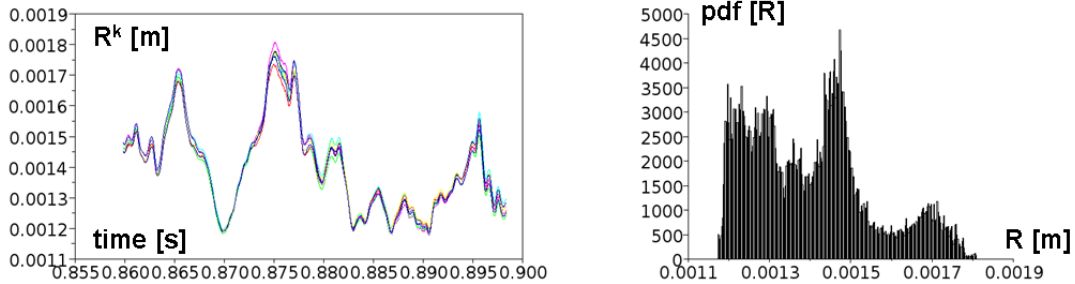


Figure 8-32: Radius-size R^k statistical probability (time history) of the 8 stochastic fields (left) and bubble size spectrum (right) at the location 1 marked in Figure 8-36.

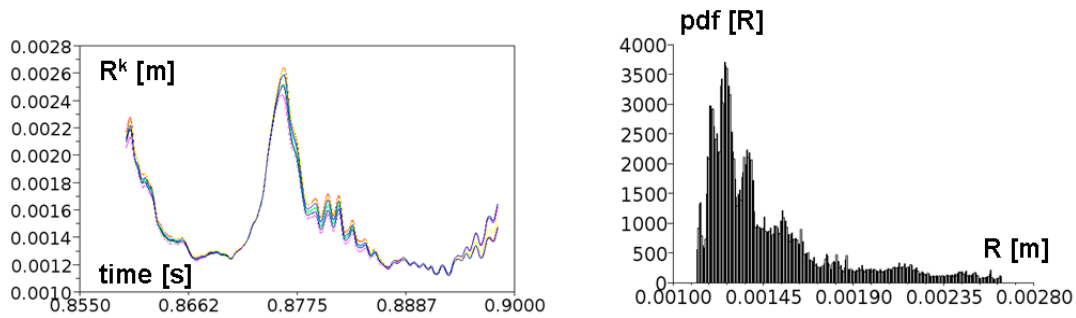


Figure 8-33: Radius-size R^k statistical probability (time history) of the 8 stochastic fields (left) and bubble size spectrum (right) at the location 2 marked in Figure 8-36.

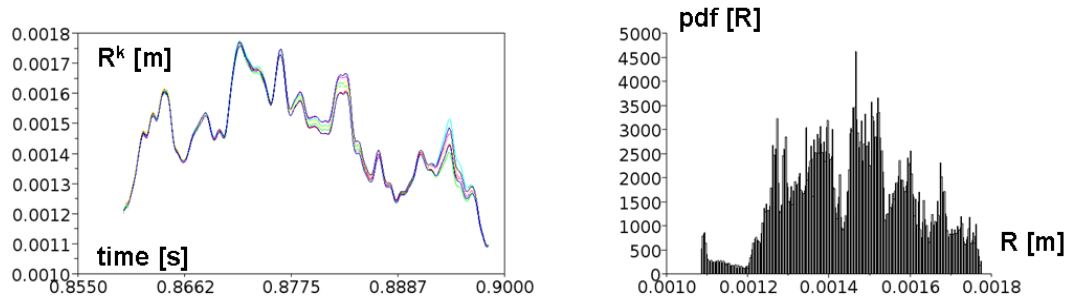


Figure 8-34: Radius-size R^k statistical probability (time history) of the 8 stochastic fields (left) and bubble size spectrum (right) at the location 3 marked in Figure 8-36.

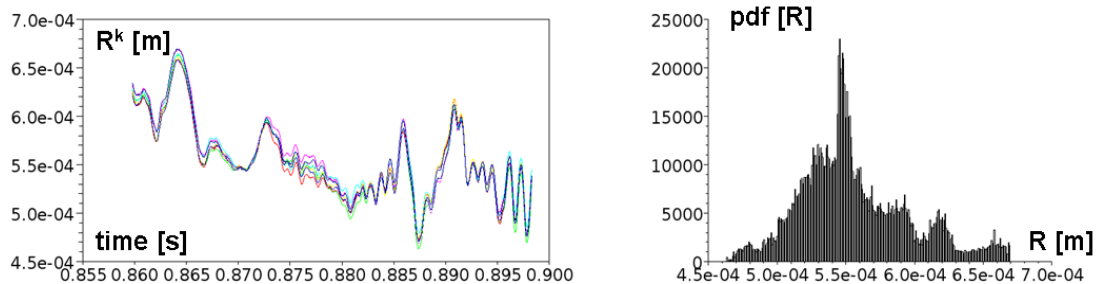


Figure 8-35: Radius-size R^k statistical probability (time history) of the 8 stochastic fields (left) and bubble size spectrum (right) at the location 4 marked in Figure 8-36.

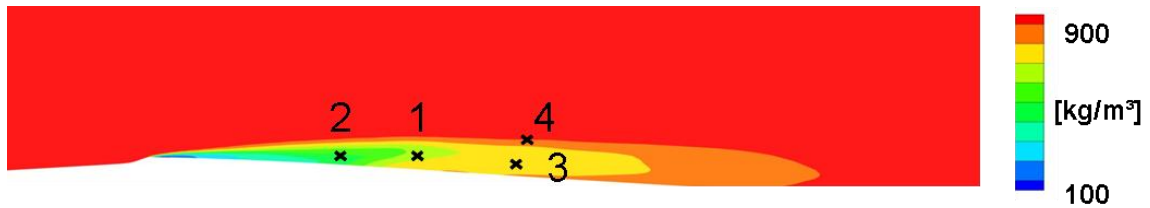


Figure 8-36: Average density of the vapor-water mixture. A density below 900kg/m³ indicates the presence of vapor. The locations marked 1, 2, 3 and 4 are the positions where the bubble size pdf are numerically sampled.

8.6.2.7.2.6 Stochastic fields

In contrast to the RANS simulations, the stochastic fields are strongly fluctuating in the LES calculation although the cavitation sheet is stable. Figure 8-37 shows seven snapshots of the stochastic field Y^5 taken at different times. On these selected snapshots, the field Y^5 attains its maximal value at different positions in the cavitation sheet. At some instant, the largest vapor mass fraction is at the front end of the cavitation sheet. This phenomenon corresponds to large bubbles present near the contraction. Their pressure threshold is lower and they need less time to grow. At other times, the maximum vapor mass fraction is in the middle of the cavitation sheet or at its rear end.

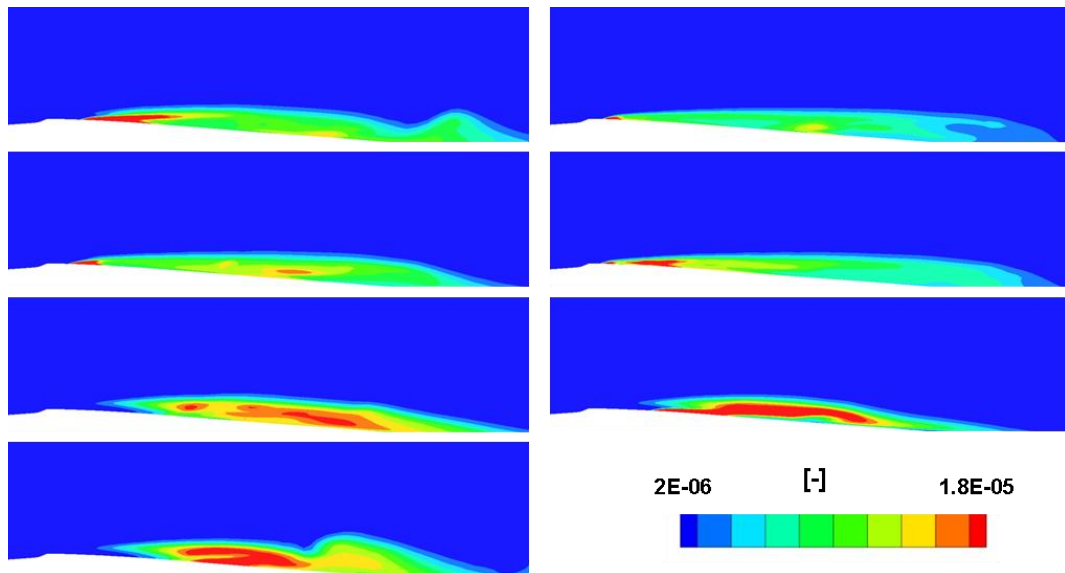


Figure 8-37: Instantaneous values of the stochastic field Y^5 at seven different times (LES calculation of a stable cavitation sheet).

The ensemble-averaged value of this stochastic field Y^5 is given in Figure 8-38. The maximal vapor mass fraction is situated in the middle and at the front end of the cavitation sheet.

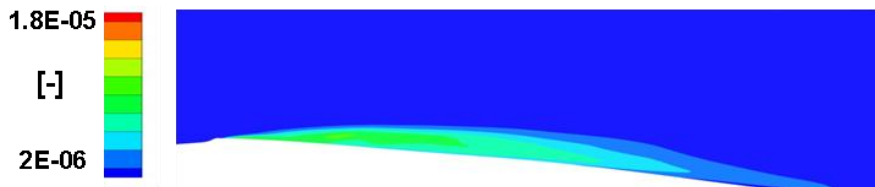


Figure 8-38: Ensemble-averaged values of the stochastic field Y^5 (LES calculation of a stable cavitation sheet).

A non-negligible amount of vapor is found further upstream than in the RANS calculations. This phenomenon is caused by the difference in the initial number of nuclei. The bubbles are smaller in the RANS calculations than in the LES calculation. As a result, their pressure threshold is lower and they need more time to grow.

9 POR analysis

This chapter presents the numerical analysis of the passive fluidic diode, also called POR design. The cavitation model described in the preceding chapter is employed to investigate the flow behavior of one channel of the POR in both flow directions under cavitating conditions. The first section places emphasis on the efficiency of the double-nozzle design in the backward direction. For this purpose, three LES simulations are performed to analyze the effect of the first nozzle and the influence of the subcooling on the mass flow rate. In the second section, the analysis focuses on the opposite flow direction. The effect of cavitation on the pressure loss in one POR channel is investigated with the help of two LES calculations.

9.1 Backward direction

The objective of this section is three-folds.

- First, the numerical code is validated against experimental results. For this purpose, two LES are performed with one channel of the POR under differing flow conditions.
- Second, the principle of the double-nozzle design is investigated. The numerical results obtained with one POR channel are compared to the numerical results obtained with a single-nozzle design.
- Finally, the influence of the subcooling on the efficiency of the POR is analyzed. The numerical results of two LES calculations with differing coolant subcooling are compared.

9.1.1 Validation of the code

In the precedent chapter, the code is validated qualitatively with the experiments of Attou et al. [67] and quantitatively with the experiments of Barre et al. [220]. In this chapter, the experimental data of two tests performed in Karlstein are exploited to validate the code and analyze the flow behavior of the POR in the backward direction.

9.1.1.1 Numerical mesh

The computational mesh is a three-dimensional block-structured mesh consisting of about 550 000 cells. In spite of the mesh refinement at the walls, the y^+ values are larger than those usually recommended in LES calculations [37]. For example, y^+ values up to 115 may be encountered locally. The mean y^+ value is about 40. In contrast, the mesh is sufficiently fine to resolve the largest fluctuating scales in the bulk. The maximal ratio between the sub-grid scale viscosity and the laminar viscosity is about 7 in the computational domain.

Far upstream and downstream of the smallest cross sections; the cells are stretched out to increase the damping of the disturbances. In this manner, increased code stability and faster statistical convergence are obtained.

9.1.1.2 Boundary conditions

Walls have non-slip conditions and are adiabatic. The total pressure and the temperature at the inlet and the pressure at the outlet of the double-nozzle design are known from the experiments. They are imposed at the boundaries of the computational domain (Figure 9-1).

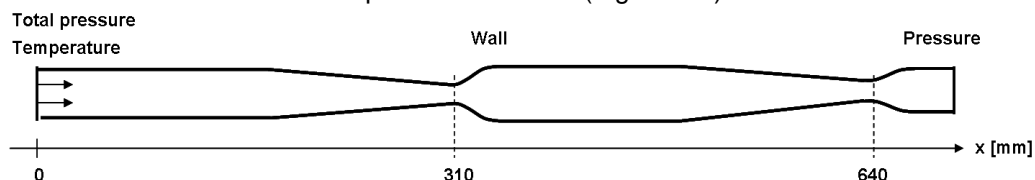


Figure 9-1: Representation of the computational domain and boundary conditions in the backward direction. $x=0\text{mm}$ is the position of geometry inlet.

The variations of the flow properties along the POR channel are presented in this section in diagrams. The abscissa of these diagrams represents the distance from the inlet of the geometry. As an example, the first smallest cross section is situated at 310mm of the inlet of the geometry and the second smallest cross section at 640mm (Figure 9-1).

The velocity is assumed to be normal to the boundary at the inlet. This modeling represents an approximation of the experimental conditions. Entrance pressure loss and disturbances associated to the sudden contraction (Figure 9-2) are neglected.

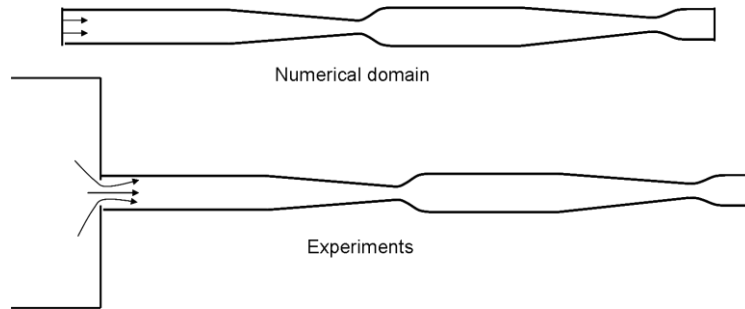


Figure 9-2: Illustration of the modeling of the inlet boundary. In the numerical domain (top), the velocity is assumed to be normal to the inlet. In contrast, in the experiments (bottom), the inlet velocity profile is disturbed by the sudden contraction.

In all calculations, the equilibrium vapor mass fraction is set to 10^{-7} and the number density to $n_0 = 10^7 \text{ m}^{-3}$. This numerical setup is exactly the same as for the validation case described in chapter *stochastic-field cavitation model*.

9.1.1.3 Turbulence model

The High Pass Filter Smagorinsky turbulence model [217] is used for the modeling of the sub-grid scales.

9.1.1.4 Numerical versus experimental results

In the first validation case, the coolant is characterized by a subcooling of 11K. The pressure at the inlet is 70.3 bar and the pressure at the outlet is 22.24 bar. The resulting mass flow rate is $\dot{M} = 4.2 \text{ kg/s}$. The pressure measured along the POR channel during the experiment is represented by squares on Figure 9-3. On the same figure, the pressure distribution obtained in the bulk with the proposed cavitation model is the blue solid line.

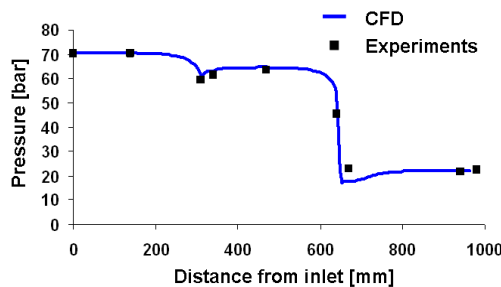


Figure 9-3: Comparison between numerical and experimental pressure distribution along a POR channel in case of moderately subcooled (11K) coolant in the backward direction.

The agreement between the numerical and experimental results is satisfactory. The agreement between measured and calculated mass flow rates is also very good since the cavitation model predicts a mass flow rate of $\dot{M} = 4.28 \text{ kg/s}$.

In the second validation test, the coolant is characterized by a subcooling of 4K. The pressure at the inlet is 65.7 bar and the pressure at the outlet is 16.9 bar. The resulting mass flow rate is $\dot{M} = 3.10 \text{ kg/s}$. Also in that case, the agreement between the numerical and experimental results is satisfactory. The pressure distribution along the POR design obtained in the calculation (solid line on Figure 9-4) is consistent with the experimental results (squares on Figure 9-4). The numerical code slightly overestimates the mass flow rate ($\dot{M} = 3.38 \text{ kg/s}$). As a result, the static pressure decrease at

the first smallest cross section is also overpredicted. This static pressure decrease primarily is induced by an increase of the dynamic pressure.

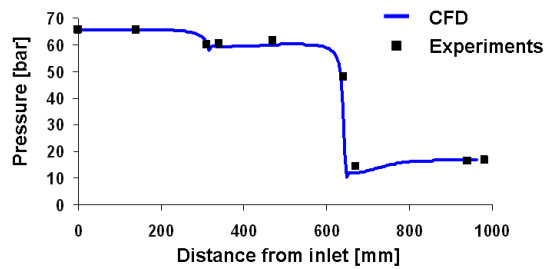


Figure 9-4: Comparison between numerical and experimental pressure distribution along a POR channel in case of slightly subcooled (4K) coolant in the backward direction.

9.1.2 Principle of the double-nozzle design

In the backward direction, a double-nozzle design significantly reduces the mass flow rate in comparison to a single-nozzle design. For the tests performed in Karlstein, this mass flow rate reduction ranges between 30% and 50% (chapter *performance tests*).

To analyze precisely the mechanism yielding this mass flow reduction, two LES simulations are performed. The boundary conditions are identical in both simulations. However, the geometry in the first simulation is a single-nozzle design while the geometry in the second simulation is a double-nozzle design.

The simulation involving the double-design is already described in section 9.1.1.4. The coolant is characterized by a subcooling of 11K. The pressure at the inlet is 70.3 bar and the pressure at the outlet is 22.24 bar. The resulting mass flow rate is $\dot{M} = 4.2 \text{ kg} / \text{s}$. The mesh used in this simulation is described in section 9.1.1.1.

The numerical mesh used to represent the single-nozzle design possesses the same characteristics with fewer cells.

9.1.2.1 Single-nozzle design

An illustration of the computational domain used to represent the single-nozzle design is given in Figure 9-5. The geometry consists of one nozzle of the POR channel.

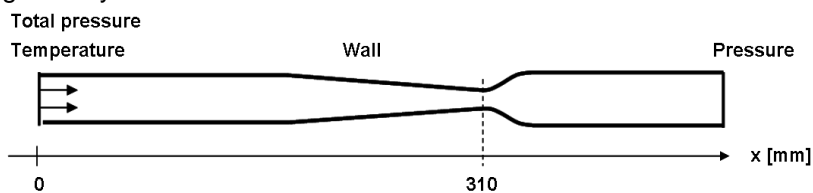


Figure 9-5: Illustration of the computational domain used to represent the single-nozzle design. $x=0\text{mm}$ is the position of geometry inlet.

9.1.2.1.1 Validation

No experimental data are available to validate this numerical calculation. However, the calculated mass flow rate ($\dot{M} = 5.9 \text{ kg} / \text{s}$) is about 30% larger than the mass flow rate obtained with a double-nozzle ($\dot{M} = 4.2 \text{ kg} / \text{s}$) under the same flow conditions. This result matches available experimental data (section 9.1.2).

9.1.2.1.2 General flow behavior

Figure 9-6 on the left represents the distribution of the calculated pressure (blue solid line), saturation pressure (black solid line) and vapor mass fraction (green solid line) in the bulk along the single-nozzle design. The smallest cross section is situated at 310mm from the inlet. Figure 9-6 on the right

represents the calculated velocity (blue solid line), speed of sound (black solid line) and vapor mass fraction (green solid line) in the bulk along the single-nozzle design.

The pressure starts to decrease in the contraction as a result of the acceleration of the fluid. At some point in the contraction, the pressure is below the saturation pressure. The coolant starts to vaporize. The fluid accelerates even more yielding a further decrease of the static pressure. This mechanism is self-sustained. The coolant drastically vaporizes, the velocity significantly increases and the pressure abruptly reduces. The vaporization of the coolant also causes a rapid drop of the speed of sound in the mixture. Near the smallest cross section, the coolant velocity is as high as the speed of sound. The flow chokes.

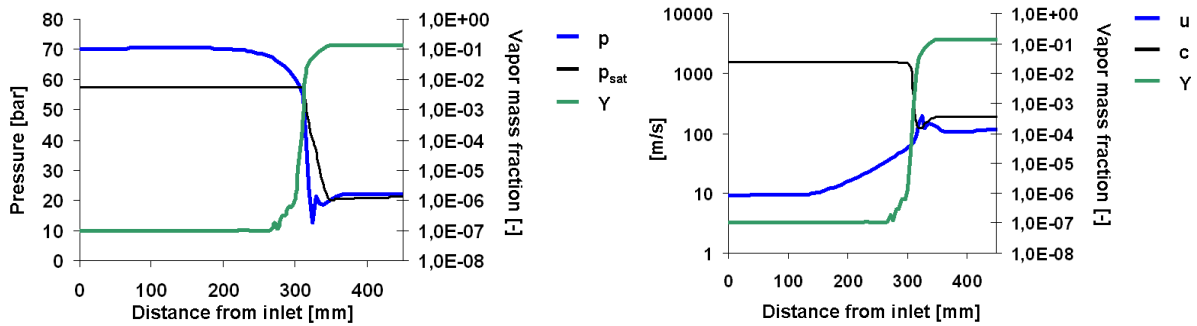


Figure 9-6: Pressure (blue solid line, left), saturation pressure (black solid line, left), vapor mass fraction (green solid line), velocity (blue solid line, right) and sound speed (black solid line, right) in the bulk along a single-nozzle in case of moderately subcooled (11K) coolant.

9.1.2.1.3 Choking

The choking cross section does not coincide with the smallest cross section (Figure 9-7, left).

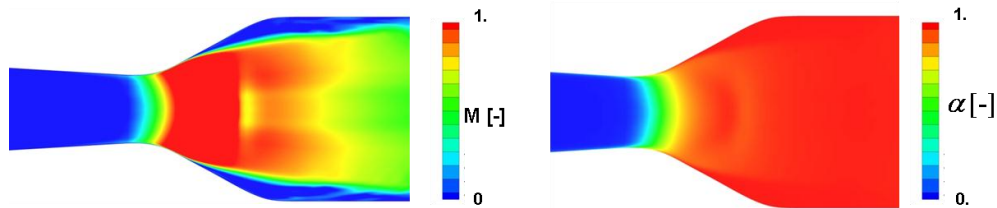


Figure 9-7: Contour plot of the Mach number (left) and vapor mass fraction (right) in the single-nozzle design in case of moderately subcooled (11K) coolant.

Apart from boundary effect, the choking cross section rather corresponds to an iso-surface of the void fraction (Figure 9-7, right).

Although the void fraction is almost constant over the choking cross section, the other flow properties may significantly vary. Mean values of the calculated density ρ^* , speed of sound c^* , pressure p^* and void fraction α^* at the choking cross section are given in Table 9-1.

ρ^*	300 kg/m ³
c^*	118 m/s
p^*	30 bar
α^*	0.67

Table 9-1: Mean values of the density ρ^* , speed of sound c^* , pressure p^* and void fraction α^* at the choking cross section of the double-nozzle design in case of moderately subcooled (11K) coolant.

9.1.2.2 Double-nozzle design

The flow behavior of the double-nozzle design is investigated under the same flow conditions. The numerical results of this calculation are presented in this section.

9.1.2.2.1 General flow behavior

Figure 9-8 represents the mean pressure distribution (blue solid line), saturation pressure (black solid line) and vapor mass fraction (green solid line) in the bulk of the POR channel.

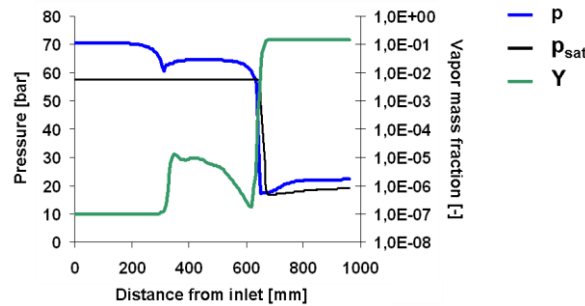


Figure 9-8: Pressure (blue solid line), saturation pressure (black solid line) and vapor mass fraction (green solid line) in the bulk along the POR channel in case of moderately subcooled (11K) coolant in the backward direction.

In the first section (up to 200mm), the wall shear friction slightly decreases the static pressure. A larger static pressure drop occurs in the contraction (310mm) mainly due to a dynamic pressure rise. Downstream of the expansion (between 350 and 500mm), the pressure recovery occurs only partially. The flow detaches from the wall and large amounts of energy dissipate in the strongly fluctuating jet (Figure 9-9).

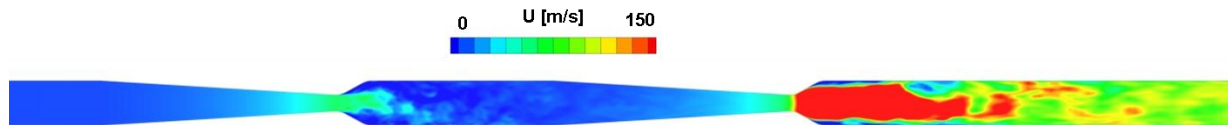


Figure 9-9: Instantaneous velocity field in one POR channel in case of moderately subcooled (11K) coolant in the backward direction.

In average, the reattachment point is situated at a small distance from the enlargement (Figure 9-10). The pressure recovery is maximal near this reattachment point.

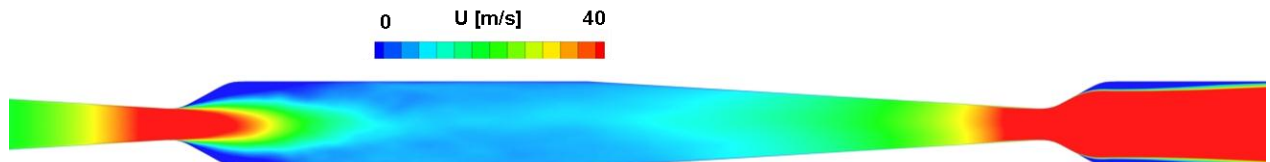


Figure 9-10: Mean velocity field in one POR channel in case of moderately subcooled (11K) coolant in the backward direction.

The same self-sustained mechanism is observed in the second contraction of the double-nozzle design as in the nozzle of the single-nozzle design. The coolant drastically vaporizes (Figure 9-8 and Figure 9-16), the velocity increases significantly (Figure 9-10 and Figure 9-11) and the static pressure fall is amplified. The vaporization of the coolant also has an effect on the speed of sound in the mixture (black solid line, Figure 9-11). This speed of sound drastically reduces with a vapor content rise (green solid line). In the second nozzle, the velocity of the coolant (blue solid line) reaches the speed of sound. The flow chokes.

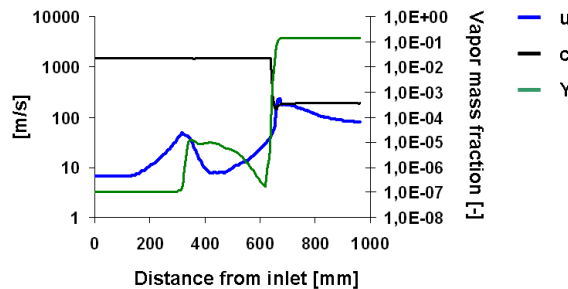


Figure 9-11: Velocity (blue solid line), sound speed (black solid line) and vapor mass fraction (green solid line) in the bulk along the POR channel in case of moderately subcooled (11K) coolant in the backward direction.

9.1.2.2.2 Choking

Figure 9-12 shows the instantaneous Mach number in the second nozzle. The Mach number reaches one at the smallest cross section and increases downstream up to about 1.4 before it decreases to subsonic conditions at the outlet. In contrast to other flow properties, the location of the choking cross section does not fluctuate much.

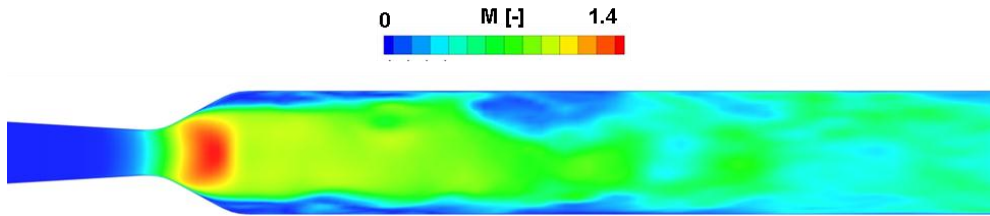


Figure 9-12: Instantaneous Mach number field in the second nozzle in case of moderately subcooled (11K) coolant in the backward direction.

A close up on the second smallest cross section is given in Figure 9-13. Similarly to the single-nozzle design, the choking cross section does not coincide with the smallest cross section but rather with an iso-surface of the void fraction.

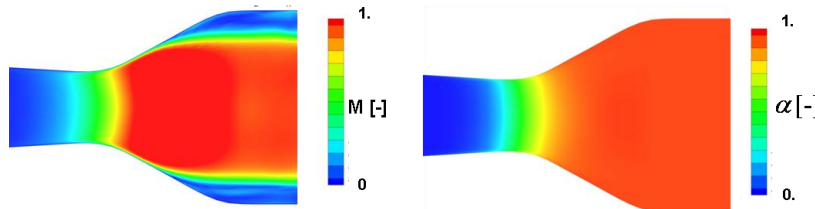


Figure 9-13: Contour plot of the Mach number (left) and void fraction (right) in the second nozzle of the double -nozzle design in case of moderately subcooled (11K) coolant in the backward direction.

Although the void fraction is almost constant over the choking cross section, the other flow properties may significantly vary. Mean values of the calculated density ρ^* , speed of sound c^* , pressure p^* and void fraction α^* at the choking cross section are given in Table 9-2.

ρ^*	148 kg/m ³
c^*	145 m/s
p^*	27.5 bar
α^*	0.84

Table 9-2: Mean values of the density ρ^* , speed of sound c^* , pressure p^* and void fraction α^* at the choking cross section of the double-nozzle design in case of moderately subcooled (11K) coolant in the backward direction.

9.1.2.2.3 Void generation and transport

The coolant is characterized by a moderate subcooling (11K). In the first nozzle, vaporization only occurs in the core of the largest turbulent eddies (Figure 9-14). In Figure 9-14, the Q-criterion of Hunt [225] is used to represent these turbulent structures.

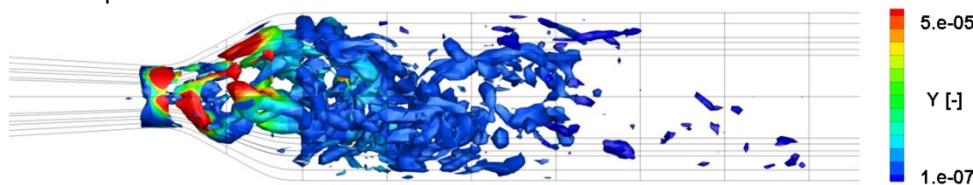


Figure 9-14: Iso-surface of $Q=5.e6s^{-2}$ colored with the vapor mass fraction in the first nozzle in case of moderately subcooled (11K) coolant in the backward direction. The solid lines represent the contour of the POR channel.

In the core of these turbulent eddies, the pressure may be below the saturation pressure due to their rotation. As an example, Figure 9-15 shows the largest eddies on the top, the pressure field in the middle and the void fraction on the bottom. The largest eddies are selected here by increasing the

values of the Q criterion. The pressure field is blue when it is below the saturation pressure. Minimum pressure regions and largest eddies exactly coincide. They are denoted by white circles in the figures at the top and in the middle. In contrast, the regions with higher vapor content coincide only with some of these eddies (denoted by white circles on the bottom figure). There, the pressure is minimal. In the other eddies (denoted by gray circles on the bottom figure), the pressure is not sufficient to induce the vaporization of the coolant. Once the vapor is generated inside the intense eddies, the vapor content seems to follow another dynamic than that of the turbulent eddies.

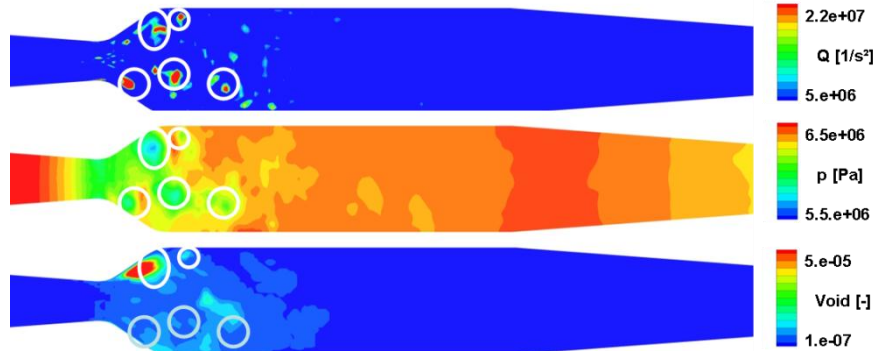


Figure 9-15: Q (top), pressure (middle) and vapor mass fraction (bottom) fields in a double-nozzle channel in case of moderately subcooled (11K) coolant in the backward direction. The regions where the pressure is below saturation pressure are colored in blue.

The turbulent eddies generate in the shear layers at the wall and at the jet boundaries. Due to the strong fluctuations (Figure 9-14 and Figure 9-16, top), the mixing of the vapor is large. The vapor is transported transversally (Figure 9-16, top) and reaches the zone with high streamwise velocities. In average (Figure 9-16, down), the vapor diffuses in the transversal direction and is advected down to the second nozzle.

The turbulent eddies dissipate at a short distance from the enlargement (Figure 9-14) and the mean pressure increases with the reattachment of the flow. The pressure is everywhere above the saturation pressure and the vapor starts to condensate.

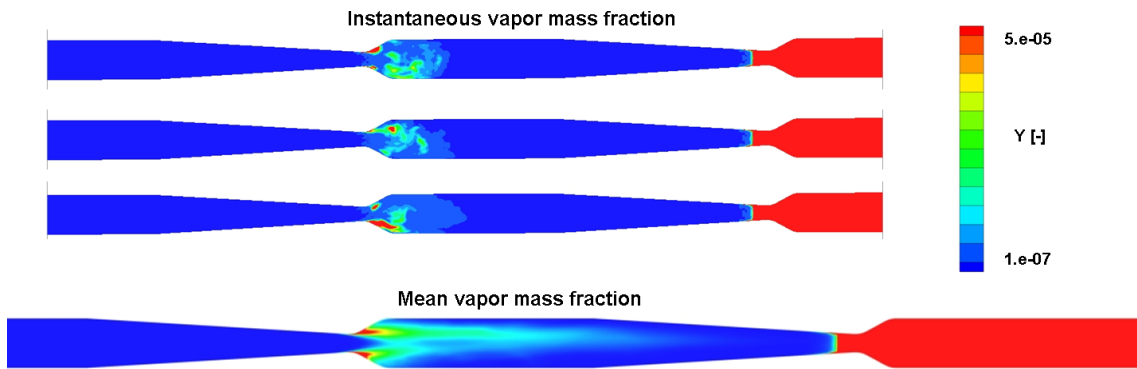


Figure 9-16: Instantaneous vapor mass fraction at three different times (top) and mean vapor mass fraction (bottom) in a double-nozzle channel in case of moderately subcooled (11K) coolant in the backward direction.

9.1.2.2.4 Bubble size spectrum

The proposed cavitation model enables to capture the bubble size spectrum in all computational cells. As an example, the bubble size spectra at the locations 1, 2 and 3 marked by a cross on Figure 9-17 are displayed on Figure 9-18.

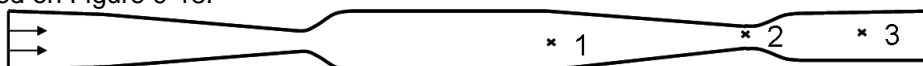


Figure 9-17: Illustration of a POR channel with the flow direction from the left to the right. Bubble size pdf are numerically sampled at the locations 1, 2 and 3.

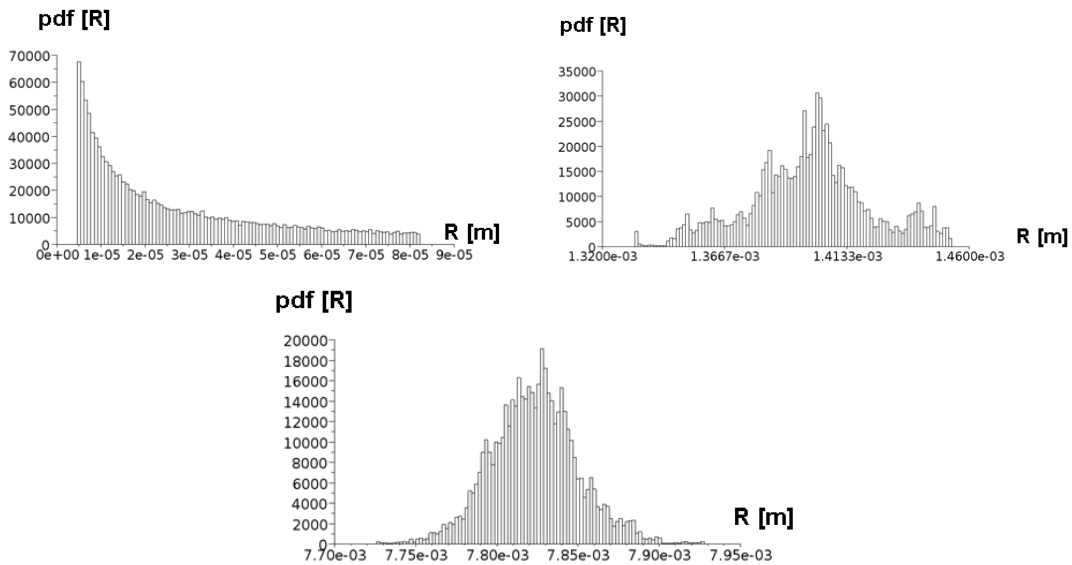


Figure 9-18: Calculated bubble size pdf in a POR channel in case of moderately subcooled (11K) coolant in the backward direction at locations 1 (top, left), 2 (top, right) and 3 (bottom) marked in Figure 9-17.

At location 1, the bubbles have condensed due to the pressure recovery. They are small. In contrast, at location 2 and 3, the coolant vaporizes. The bubbles grow and are characterized by large radius. Downstream of the second smallest cross section, the bubble size spectrum is nearly Gaussian.

These pdf are obtained from the radius-size R^k statistical probability (time history) of the 8 stochastic fields calculated at these locations. The time history of the radius-size R^k at location 2 and 3 are shown on Figure 9-19.

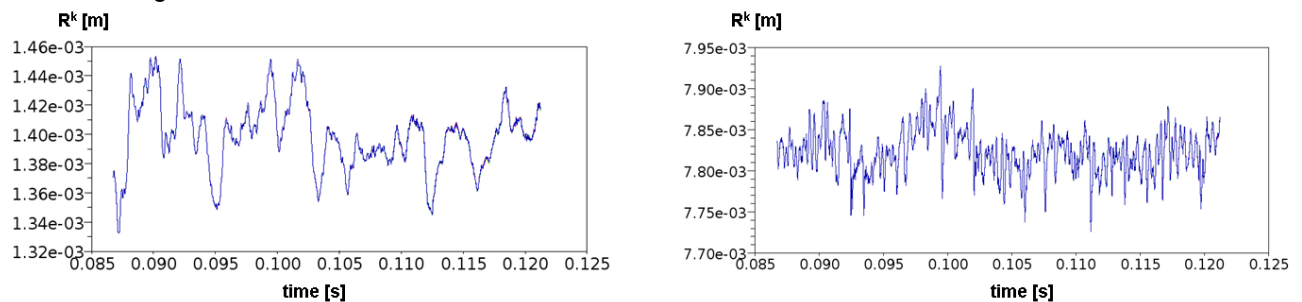


Figure 9-19: Radius-size R^k statistical probability (time history) of the 8 stochastic fields calculated at locations 2 (left) and 3 (right) marked in Figure 9-17 in case of moderately subcooled (11K) coolant in the backward direction.

In the backward direction, the local tension $p_{sat} - p$ is very large at these locations. All nuclei are activated and evolve very similarly. The fluctuation of the bubble size on the sub-grid scale is small.

9.1.2.3 Interpretation and conclusion

The double-nozzle design limits the critical two-phase mass flow rate by reducing the pressure and increasing the vapor content at the choking cross section (compare Table 9-1 and Table 9-2).

Energy dissipation is enforced in the first nozzle upstream of the choking cross section. The flow detaches, a recirculation zone develops and strong turbulent fluctuations arise. The pressure recovery is limited. The static pressure decreases faster below the saturation pressure in the converging part of the second nozzle. Thus, coolant vaporization is enhanced. The higher vapor content in the contraction yields an increased fluid acceleration, and thus a larger pressure drop. This mechanism is self-sustained since this large pressure drop, in turn, improves the vaporization of the coolant.

To illustrate the principle of the double-nozzle design, the calculated critical mass flow rate of a homogeneous water-vapor mixture is presented in Figure 9-20 at two different pressures as a function of the void fraction α^* at the critical cross section. There, it is assumed that the choking cross section

A^* is the smallest cross section of the POR channel. Under this assumption, the critical mass flow rate \dot{M}^* is given by

$$\dot{M}^* = \rho^* c^* A^* ; \quad (9.1)$$

with c^* being the speed of sound and ρ^* the density of the mixture averaged over this cross section.

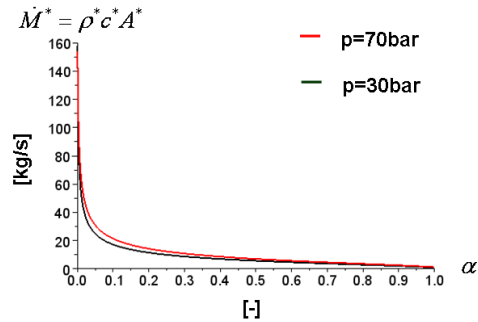


Figure 9-20: Critical mass flow rate of a homogeneous water-vapor mixture as a function of the void fraction α^* and pressure at the choking cross section. A^* is the smallest cross section of the POR channel and c^* is the speed of sound in the mixture.

The choking mass flow rate is lower at larger void fraction and lower pressure. In particular, an increase of the void fraction from 0 to 1 reduces the critical mass flow rate up to three orders of magnitude. A close up of Figure 9-20 is given in Figure 9-21. There, the effect of the first nozzle in a double-nozzle design on the flow properties at the choking cross section is materialized by a red arrow. In a single-nozzle design, the coolant chokes at the pressure p_1 and the void fraction is α_1^* . The resulting mass flow rate is \dot{M}_1^* . In contrast, in a double-nozzle design, the first nozzle enhances energy dissipation and vaporization of the coolant. The coolant chokes at the pressure $p_2 < p_1$ and the void fraction is $\alpha_2^* > \alpha_1^*$. The resulting mass flow rate \dot{M}_2^* is smaller than \dot{M}_1^* .

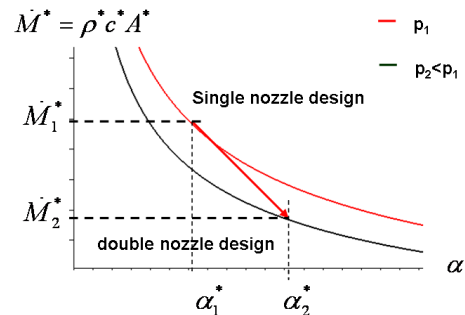


Figure 9-21: Critical mass flow rate of a homogeneous water-vapor mixture as a function of the void fraction α^* at the choking cross section. In a double-nozzle design, the properties of the mixture at the choking cross section are $\alpha_2^* > \alpha_1^*$ and $p_2 < p_1$, where α_1^* and p_1 are mixture's properties at the choking cross section of a single nozzle. The resulting mass flow rate \dot{M}_2^* is smaller in the double-nozzle design than the mass flow rate \dot{M}_1^* in a single-nozzle design.

9.1.3 Effect of coolant subcooling

The resistance coefficient of a POR channel in the backward direction is remarkably large at low subcooling and decreases with increasing subcooling (chapter *performance tests*).

To investigate this phenomenon, a simulation is performed with smaller coolant subcooling (4K). This simulation is the second validation case presented in section 9.1.1.4.

9.1.3.1 Small subcooling

9.1.3.1.1 General flow behavior

In case of coolant with small subcooling, the vaporization of the coolant in the first smallest cross section occurs over the whole cross section (Figure 9-22).

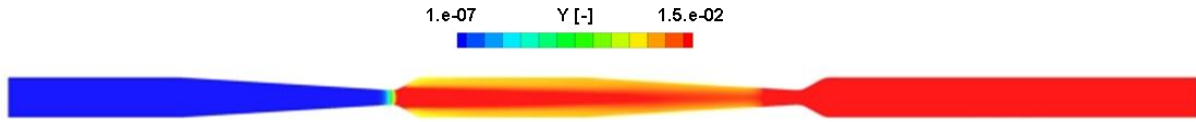


Figure 9-22: Mean vapor mass fraction in one POR channel in case of slightly subcooled (4K) coolant in the backward direction.

The pressure in the bulk is below saturation conditions [see calculated pressure (blue line) and saturation pressure (black line) in Figure 9-23] and high vapor mass fraction are obtained [see green solid line in Figure 9-23] upstream of the second nozzle.

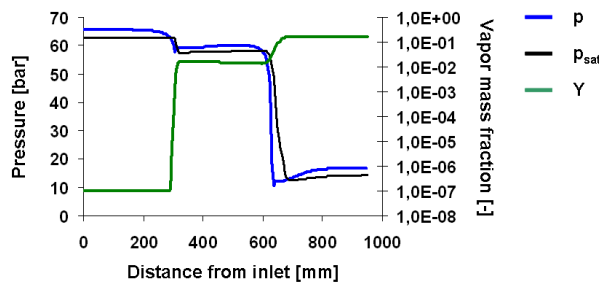


Figure 9-23: Pressure (blue solid line), saturation pressure (black solid line) and vapor mass fraction (green solid line) in the bulk along one POR channel in case of slightly subcooled (4K) coolant in the backward direction.

Then, the vapor is advected in the direction of the second smallest cross section by the jet coming from the first nozzle. This jet is very stable over a long distance. It starts to fluctuate only at a short distance from the beginning of the contraction of the second nozzle. Figure 9-24 shows the instantaneous velocity field.

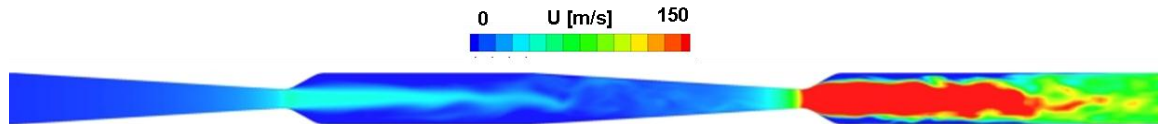


Figure 9-24: Instantaneous velocity field in one POR channel in case of slightly subcooled (4K) coolant in the backward direction.

The reattachment point (compare Figure 9-10 and Figure 9-25), and thus the maximum pressure recovery, occurs further downstream. The cavities are advected further downstream before they collapse.

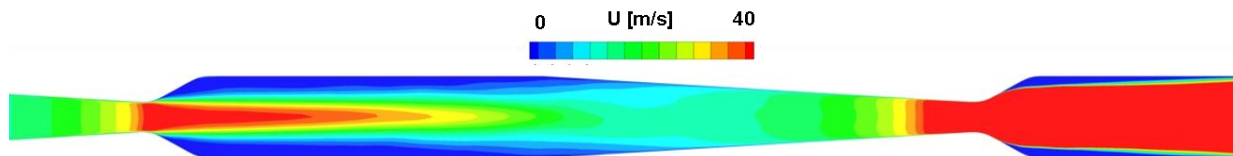


Figure 9-25: Mean velocity field in one POR channel in case of slightly subcooled (4K) coolant in the backward direction.

Furthermore, the recirculation zone is very long, the velocity is high and the flow reattaches inside the converging part of the second nozzle. These phenomena induce a very bad pressure recovery downstream of the first enlargement. Only a small fraction of the vapor phase condensates.

The turbulent structures differ in case of coolant with small subcooling. They are primarily produced in the free shear layer around the jet far downstream of the enlargement. The same Q criterion for their graphical representation is used in Figure 9-26. However, the value of the parameter Q of the iso-surface is lower in Figure 9-26 than in Figure 9-14.

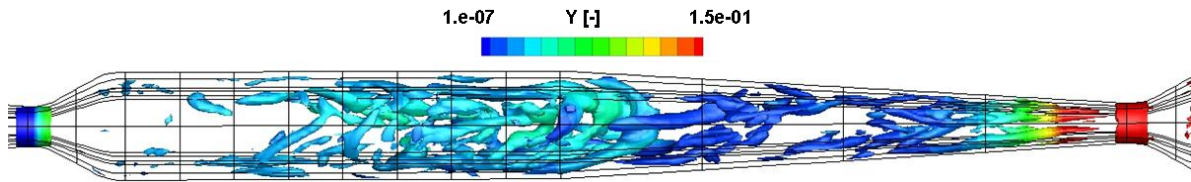


Figure 9-26 Iso-surface of $Q=5.e5 \text{ s}^{-2}$ colored with vapor mass fraction in case of slightly subcooled (4K) coolant in the backward direction. The solid lines represent the contour of the POR channel.

In the second nozzle, the phenomena are rather similar under both flow conditions. The vaporization induces a reduction of the speed of sound and an increase of the velocity (Figure 9-27).

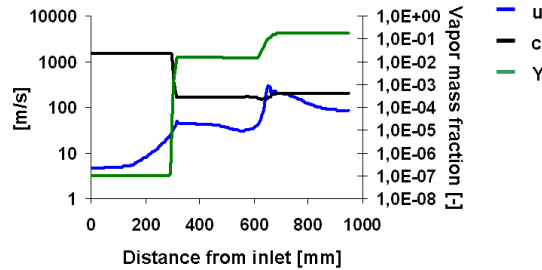


Figure 9-27: Velocity (blue solid line), sound speed (black solid line) and vapor mass fraction (green solid line) in the bulk along the POR channel in case of slightly subcooled (4K) coolant in the backward direction.

9.1.3.1.2 Choking

The flow chokes in the second smallest cross section (Figure 9-28). In this case, the choking cross section almost coincides with the smallest cross section, which is also an iso-surface of the void fraction.

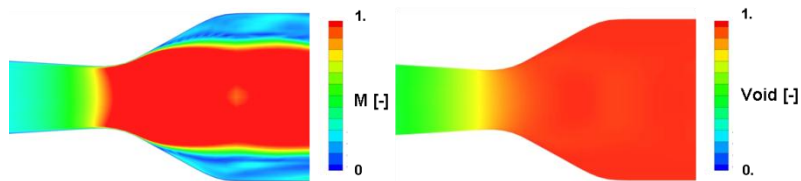


Figure 9-28: Contour plot of the Mach number (left) and void fraction (right) in the second nozzle of the double-nozzle design in case of slightly subcooled (4K) coolant in the backward direction.

Although the void fraction is almost constant over the choking cross section, the other flow properties may vary. Mean values of the calculated density ρ^* , speed of sound c^* , pressure p^* and void fraction α^* at the choking cross section are given in Table 9-3.

ρ^*	155 kg/m ³
c^*	152 m/s
p^*	31 bar
α^*	0.84

Table 9-3: Mean values of the density ρ^* , speed of sound c^* , pressure p^* and void fraction α^* at the choking cross section of the double-nozzle design in case of slightly subcooled coolant in the backward direction.

9.1.3.1.3 Bubble size spectrum

The bubble size spectra at the locations 1, 2 and 3 marked by a cross on Figure 9-17 are also calculated for the case of coolant with small subcooling. These spectra are displayed on Figure 9-29.

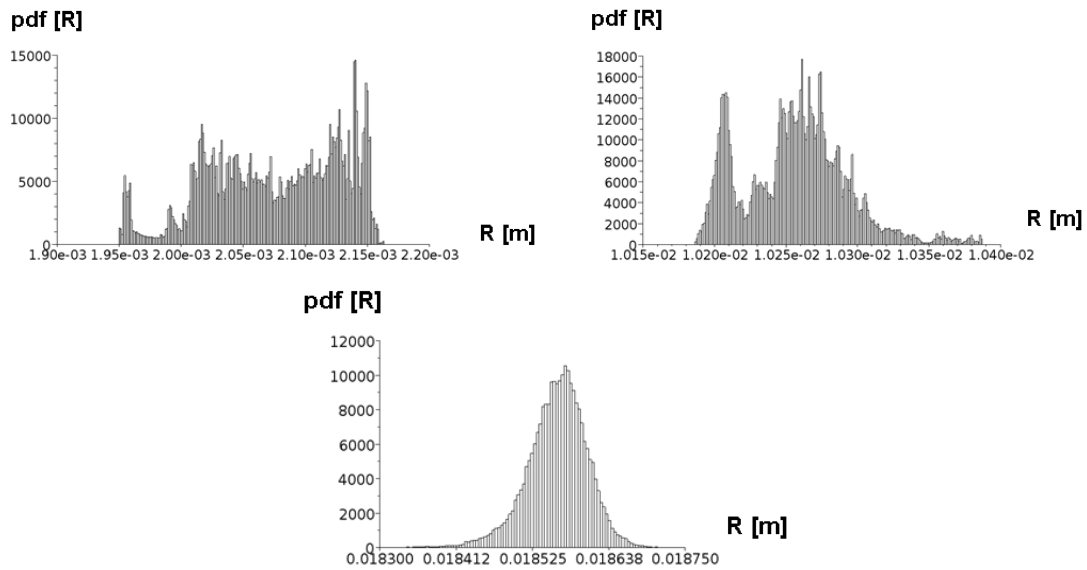


Figure 9-29: Calculated bubble size pdf in a POR channel at locations 1 (top, left), 2 (top, right) and 3 (bottom) marked in Figure 9-17 in case of slightly subcooled (4K) coolant in the backward direction.

In that case, the coolant strongly vaporizes at the first smallest cross section and a large amount of vapor is present at location 1. The bubbles have a large radius which continues to grow down to location 3. Similarly to the case of coolant with moderate subcooling, the bubble size spectrum at location 3 is near Gaussian.

The stochastic fields evolve very similarly at these positions. The sub-grid fluctuations of the bubble size are small.

9.1.3.2 Interpretation and conclusion

Again, the choking mass flow rate reduces due to enhanced energy dissipation and coolant vaporization.

The efficiency of the double-nozzle design is very large in case of coolant slightly subcooled. The static pressure decreases at low mass flow rate below the saturation pressure. The vaporization is large in the first nozzle and occurs also in the bulk. A stabilized jet develops between both nozzles. A large recirculation zone, high velocity and a reattachment point in the converging part of the second nozzle prevent from a significant pressure recovery. Therefore, vapor does not significantly condense and the pressure remains near or at saturation conditions. The vaporization is improved in the converging part of the second nozzle and the void fraction is large at the choking cross section. For the test simulated in this chapter with small subcooling (4K), experimental results indicate that the resistance coefficient is about 70 times larger in this direction than in the opposite flow direction (chapter *performance tests*).

The efficiency of the double-nozzle design is lower in case of coolant moderately subcooled than in case of coolant slightly subcooled. The vaporization occurs in the core of turbulent eddies in the shear layer near the flow separation. The growth and collapse of the bubbles at this location induce disturbances which are drastically amplified at the expansion. The jet streaming out of the first nozzle is destabilized and reattaches near the enlargement. The recirculation zone is much smaller and the pressure recovery is larger. This pressure recovery entrains the further collapse of the bubbles. Nevertheless, the vaporization, the recirculation zone and the strong fluctuations enhanced the energy dissipation upstream of the choking cross section. Even at 11K subcooling, the pressure recovery is not sufficient to ensure that all bubbles collapse. The void content is larger in the second nozzle than without a first nozzle. Furthermore, the pressure upstream and at the choking cross section is also lower than in a single nozzle (section 9.1.2). In this manner, vaporization is further enhanced in the second nozzle. For the test simulated in this chapter with moderate subcooling, experimental results indicate that the resistance coefficient is about 30 times larger than in the opposite flow direction (chapter *performance tests*).

In this particular case, the flow properties at the choking cross section do not significantly differ (compare Table 9-2 and Table 9-3). Instead, increased energy dissipation and coolant vaporization induces the migration of the choking cross section upstream in the nozzle. There, the cross section of the nozzle is smaller. For example, the choking cross section almost coincides with the smallest cross section in case of coolant with small subcooling. As a result, the area of the choking cross section, and thus the mass flow rate, reduce. To illustrate this phenomenon, the position of the choking cross section calculated in both simulations is represented on Figure 9-30.

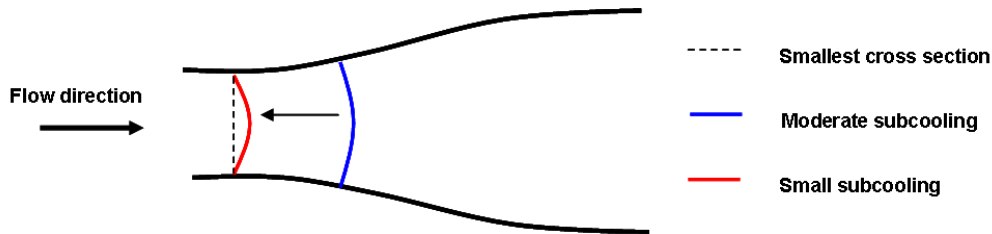


Figure 9-30: Position of the choking cross section calculated with moderately subcooled (11K, blue solid line) and slightly subcooled (4K, red solid line) coolant. This cross section migrates in direction of the smallest cross section (dashed line) with decreasing subcooling.

9.2 Forward direction

In the forward direction, two calculations are performed to analyze the effect of cavitation on the POR flow behavior. Both calculations are performed with a very low coolant subcooling. The first simulation is characterized by a coolant near saturation. The coolant is at 538K. At this temperature, the coolant is superheated by 1K at the outlet of the POR. In the second calculation, the coolant is at 536K. The coolant is subcooled by 1K at the outlet of the POR.

9.2.1 Numerical setup

One POR channel is represented by a three dimensional block-structured computational mesh consisting of about 2.8 million cells. In spite of the mesh refinement at the walls, the y^+ values are larger than those usually recommended in LES calculations [37]. For example, y^+ values up to 130 may be encountered locally. The mean y^+ value is about 60. In contrast, the mesh is sufficiently fine to resolve the largest fluctuating scales in the bulk. The maximal ratio between the sub-grid scale viscosity and the laminar viscosity is about 7 in the computational domain. Far upstream and downstream of the smallest cross sections; the cells are stretched out to increase the damping of the disturbances. In this manner, increased code stability and faster statistical convergence are obtained.

A mass flow of 1.8kg/s is imposed at the inlet of the computational domain. There, the flow direction is assumed to be normal to the boundary and the temperature of the coolant is imposed. The pressure known from the experiments is prescribed at the outlet. These boundary conditions are shown on Figure 9-31.

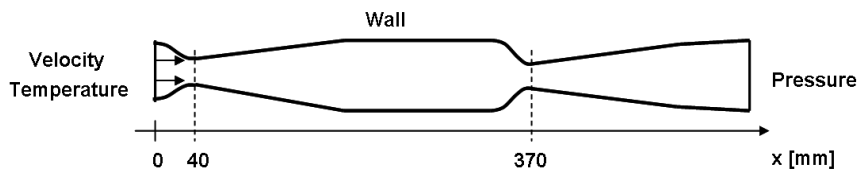


Figure 9-31: Representation of the computational domain and boundary conditions in the forward direction. $x=0$ mm is the position of geometry inlet.

The variations of the flow properties along the POR channel are presented in this section in diagrams. The abscissa of these diagrams represents the distance from the inlet of the geometry. As an example, the first smallest cross section is situated at 40mm of the inlet of the geometry and the second smallest cross section at 370mm (Figure 9-31).

In all calculations, the equilibrium vapor mass fraction is set to 10^{-7} and the number density to $n_0 = 10^7 \text{ m}^{-3}$. This numerical setup is exactly the same as for the validation case described in chapter *stochastic-field cavitation model* and for the LES calculations presented in the precedent section 9.1.

9.2.2 Validation of the code

No experimental results are available to validate precisely the simulations. However, the experimental result presented in chapter *performance tests*, and repeated on Figure 9-32 for convenience, indicates that the pressure loss under such flow conditions drastically increases. The domain of investigation is represented by red arrows on this figure.

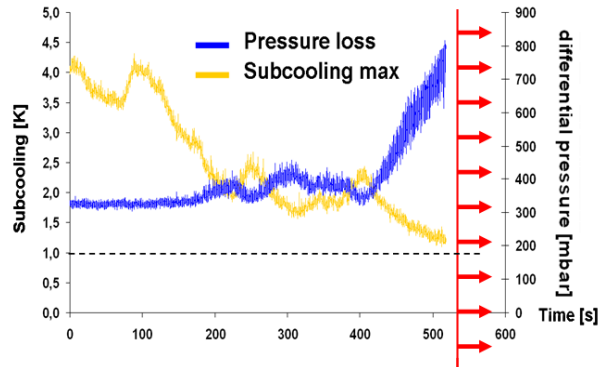


Figure 9-32: Pressure loss (blue line) measured in the POR in the forward direction; corresponding maximal subcooling (yellow); and domain of investigation in the present simulations (red arrows).

As it will be described in the following, the predicted pressure loss also is large in the simulations under such conditions.

9.2.3 Near saturation

9.2.3.1 General flow behavior

Figure 9-33 represents the calculated pressure (blue solid line), the calculated saturation pressure (black solid line) and the vapor mass fraction (green solid line) in the bulk along the POR channel in the forward direction in case of coolant near saturation.

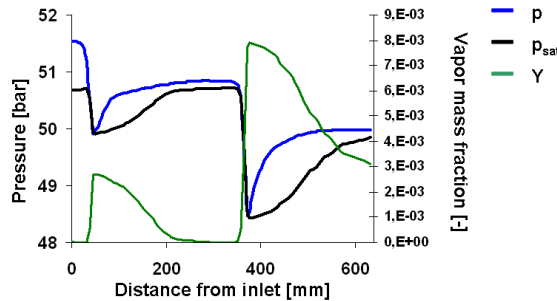


Figure 9-33: Pressure (blue solid line), saturation pressure (black solid line) and vapor mass fraction (green solid line) in the bulk along one POR channel in case of saturated coolant in the forward direction.

The static pressure strongly decreases in the smallest cross sections due to the acceleration of the fluid (see Figure 9-34).

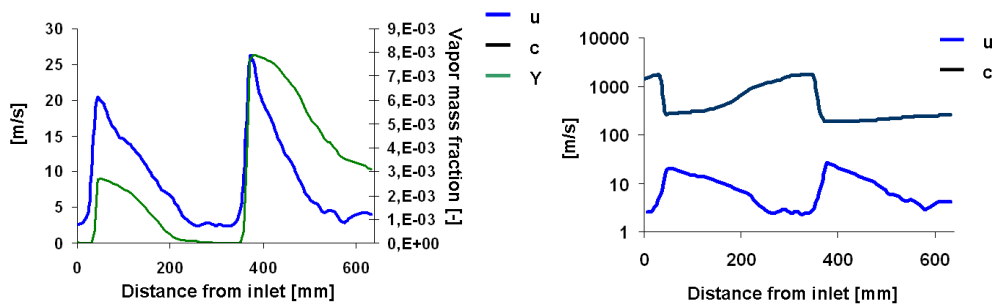


Figure 9-34: Velocity (blue line), vapor mass fraction (green line, left) and speed of sound (black line, right) in the bulk along one POR channel in case of saturated coolant in the forward direction.

When the coolant is near saturation at the inlet of the POR, the static pressure in the bulk reaches the saturation pressure at both smaller cross sections and both POR nozzles are filled with vapor (Figure 9-35).

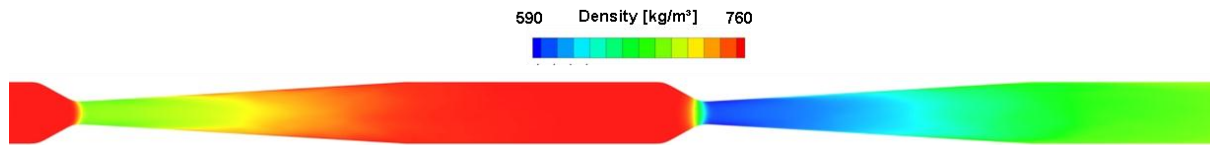


Figure 9-35: Mean density field in one POR channel in case of saturated coolant in the forward direction.

The speed of sound decreases in both nozzles (Figure 9-34, right) but, under these flow conditions, the velocity is significantly below the speed of sound in the mixture. The flow does not choke.

Acceleration and static pressure drop accentuate in the second nozzle due to intense coolant vaporization. The velocity in the second nozzle reaches 27m/s while it is only 20m/s in the first nozzle (see Figure 9-34).

Following the flow deceleration, the static pressure recovers in the diffuser and the pipes. The coolant condenses. This condensation is enhanced by the thermal effects: The temperature, and thus the saturation pressure, decreases (Figure 9-33) as a result of coolant vaporization.

9.2.3.2 Flow resistance

The two-phase mixture does not choke. However, the pressure loss significantly increases in comparison to single-phase conditions. The total pressure loss amounts 1.2bar while it is only 0.3bar when no vaporization occurs.

The total pressure distribution in the double-nozzle design is represented on Figure 9-36. Energy is principally dissipated in the vicinity of the smallest cross sections and in the diffusers while dissipation is negligible in the straight pipes and contractions.

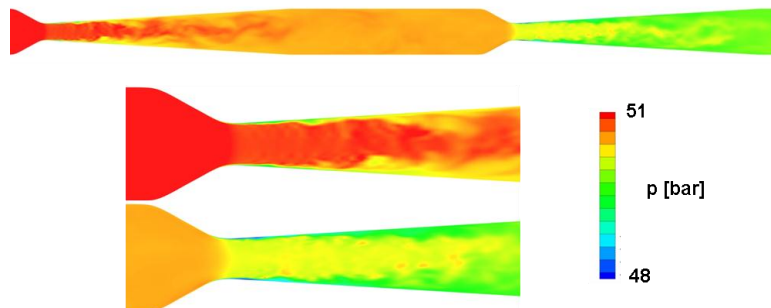


Figure 9-36: Total pressure in one POR channel (top) in case of saturated coolant in the forward direction; and zoom on the first nozzle (middle) and second nozzle (bottom).

Increased energy dissipation results from larger velocities and increased fluctuations.

Larger velocities occur in regions with higher vapor content where the density is lower. As an example, the maximal velocity in the second nozzle is 27m/s instead of 20m/s in the first nozzle. This mechanism has a direct impact on the flow resistance: the pressure loss is higher in the second nozzle (0.7bar) than in the first nozzle (0.5bar).

Larger velocities are also observed in the vicinity of the smallest cross sections. There, the growth and collapse of the vaporous region has a destabilizing effect on the incoming flow. The flow detaches, the effective cross section reduces, and a jet with higher velocities develops.

The larger fluctuations (Figure 9-37) are intimately related to this flow detachment since they occur primarily in the bounding region of the jet.

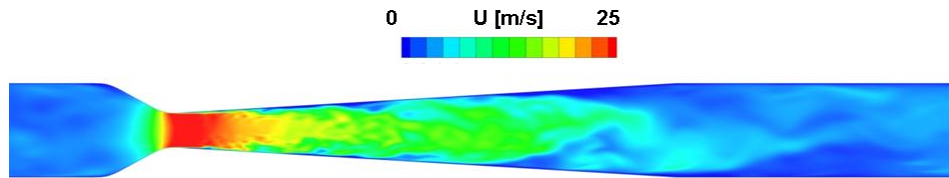


Figure 9-37: Instantaneous velocity field in the second nozzle of one POR channel in case of saturated coolant in the forward direction.

9.2.3.3 Bubble size spectrum

The radius-size statistical probability (time history) of the 8 stochastic fields at three positions in the double-nozzle design is represented in Figure 9-38.

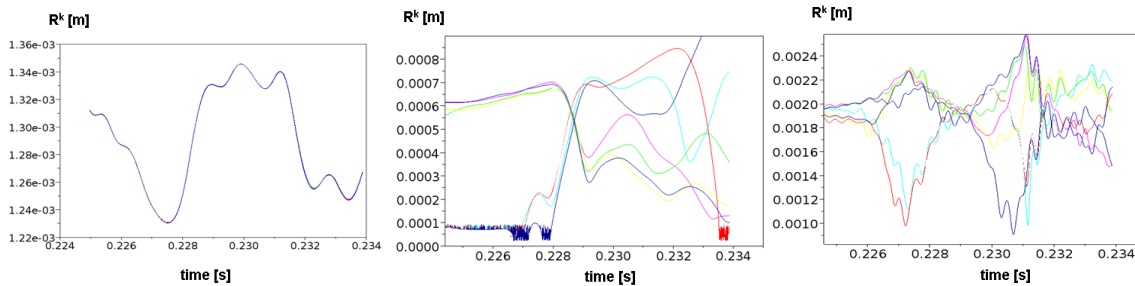


Figure 9-38: Radius-size R^k statistical probability (time history) of the 8 stochastic fields calculated at location 1 (left), 2 (middle) and 3 (right) marked in Figure 9-39 in case of saturated coolant in the forward direction.

These three locations are marked on Figure 9-39. Position 1 is situated in the cavitation sheet of the first nozzle; position 2 is at the inlet of the second nozzle and position 3 is located in the cavitation sheet of the second nozzle.



Figure 9-39: Positions in the double-nozzle design where the pdf are sampled numerically in the forward direction.

The behavior of the stochastic fields obtained in this simulation illustrates the advantage of the stochastic-field method.

In the first nozzle, the pressure decrease is large. All nuclei are activated and grow. The fluctuation of the bubble size on the sub-grid scale is small. The stochastic fields behave very similarly at location 1 (Figure 9-38, left). In contrast, in the straight pipe connecting the two nozzles, the instantaneous static pressure decreases below the saturation pressure only in the core of turbulent eddies. There, the turbulent fluctuations are low and, thus, the local tension is small. As an example, Figure 9-40 on the top shows the most intense eddies present in the straight pipe with the Q criterion at an arbitrary time. The corresponding pressure field is represented on the same Figure 9-40 on the bottom. The regions where the pressure in the pipe is below saturation pressure are colored in blue.

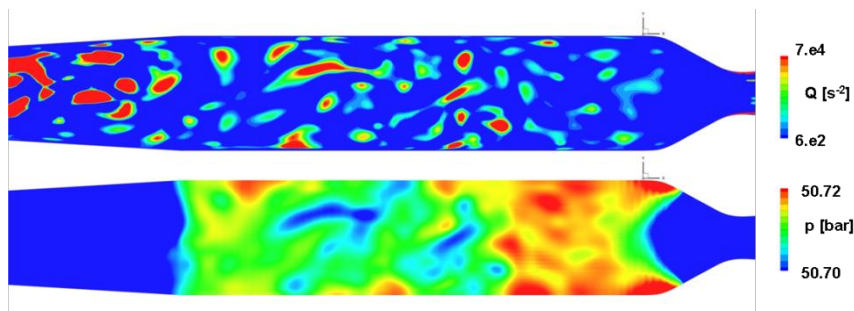


Figure 9-40: Contour plots of the Q criterion (top) and pressure (bottom) in the straight pipe connecting the two nozzles in case of saturated coolant in the forward direction. The regions where the pressure is below saturation pressure in the pipe are colored in blue.

Since the local tension is small, only the largest nuclei are activated, and then grow and collapse. The other nuclei remain inactivated. The fluctuations of the bubble size on the sub-grid scale are large. The stochastic fields evolve very differently at location 2 (Figure 9-38, middle). These fluctuations accentuate in the second nozzle (Figure 9-38, right).

The corresponding bubble size pdf are shown on Figure 9-41.

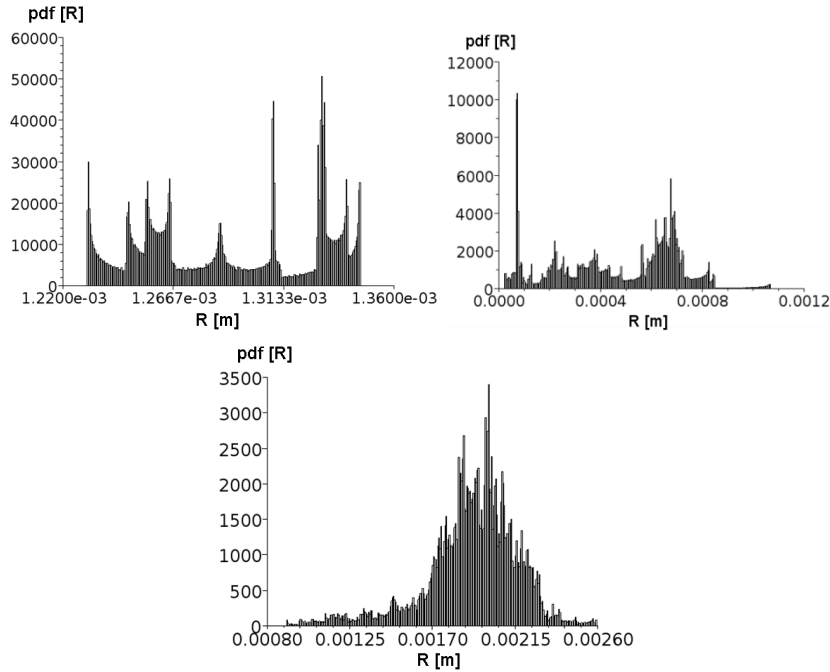


Figure 9-41: Calculated bubble size pdf in a double-nozzle design at location 1 (left), 2 (middle) and 3 (right) marked in Figure 9-39 in case of saturated coolant in the forward direction.

The contour plot of some of these stochastic fields is represented on Figure 9-42. There, the instantaneous fields are shown on the left and the ensemble-average fields on the right. Three of the eight fields are given at the top while the vapor mass fraction is at the bottom.

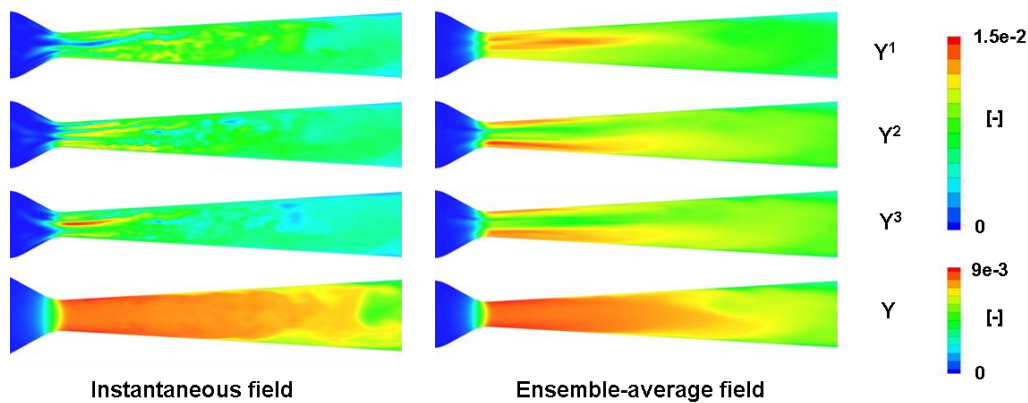


Figure 9-42: Instantaneous (left) and ensemble-average (right) contour plots of three stochastic fields (top) and of the vapor mass fraction (bottom) in the second nozzle in case of saturated coolant in the forward direction.

While the density is characterized by a low variance in the cavitation sheet (Figure 9-43, right), the stochastic fields significantly fluctuate in this region (Figure 9-43, left).

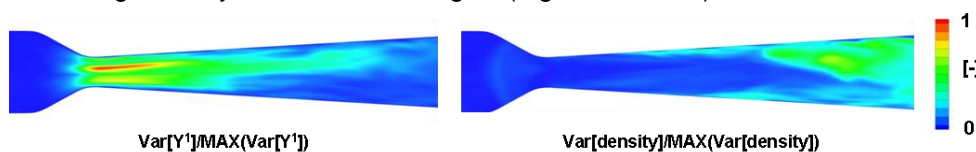


Figure 9-43: Non-dimensional variance of one of the stochastic field (left) and of the density (right) in the second nozzle in case of saturated coolant in the forward direction.

9.2.4 Small subcooling

The total pressure loss calculated with a small subcooling (1K) is 0.9bar.

In this simulation, coolant vaporization also occurs in both nozzles but the vapor mass fraction is much lower than in the preceding investigated case (Figure 9-44, green solid line). Therefore, the coolant has lower velocities at the smallest cross sections than in case of coolant near saturation (Figure 9-44, right).

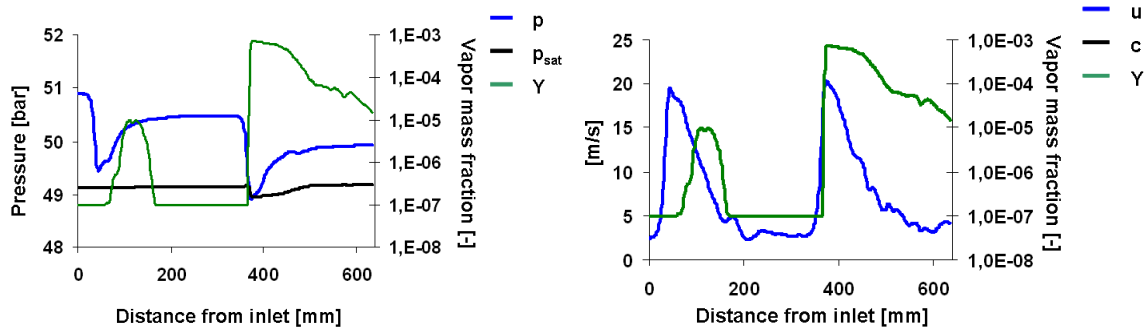


Figure 9-44: Pressure (blue solid line, left), saturation pressure (black solid line, left), vapor mass fraction (green solid line) and instantaneous velocity (blue solid line, right) in the bulk along one POR channel in case of slightly subcooled coolant in the forward direction.

The pressure in the bulk (Figure 9-44, blue solid line) at the first smallest cross section remains above the saturation pressure (Figure 9-44, black solid line).

In the first nozzle, the static pressure reaches saturation conditions only at the wall due to wall curvature. In the bulk, no vaporization is observed (Figure 9-45).

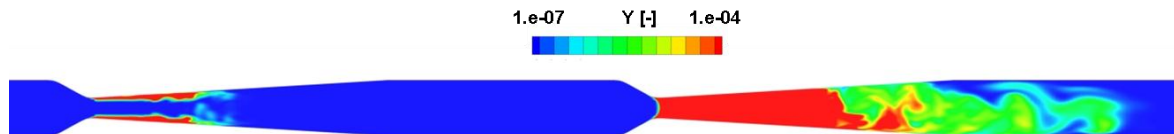


Figure 9-45: Vapor mass fraction in a double-nozzle design in case of slightly subcooled coolant in the forward direction.

Nevertheless, the flow detaches in both nozzles and energy is dissipated in the vicinity of the smallest cross sections and in the diffusers. As an example, the instantaneous vector field in the first nozzle is represented on Figure 9-46 colored with the total pressure.

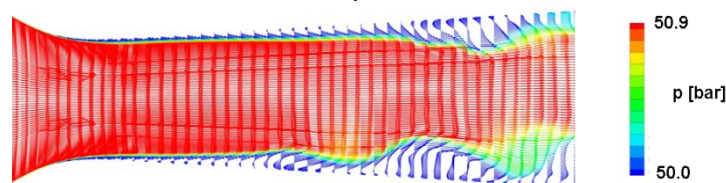


Figure 9-46: Instantaneous velocity field colored with the total pressure in the first nozzle of the double-nozzle design in case of slightly subcooled coolant in the forward direction.

9.2.5 Interpretation and conclusion

In this section, the flow behavior of one double-nozzle design in the forward direction under cavitating conditions is investigated. Two LES are performed with a coolant at differing temperatures.

In accordance with experimental results, the subcooling of the coolant has a major impact on the flow resistance. Figure 9-47 shows the resistance coefficient as a function of the subcooling. This subcooling is defined in reference to the outlet pressure. At very low subcooling (-1K), the resistance coefficient increases to 41. A temperature drop of 2K enables to reduce the resistance coefficient to 31. The last point on Figure 9-47 at 3K subcooling is calculated with available experimental results without cavitation in the double-nozzle channel (Figure 9-32). Under these flow conditions, the flow resistance is 10.7.

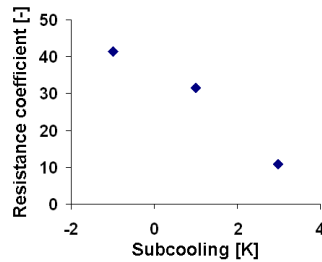


Figure 9-47: Resistance coefficient of a double-nozzle design in the forward direction as a function of the subcooling.

In this flow direction, cavitation increases energy dissipation according to two main mechanisms. First, vaporization induces a decrease of the density, and thus an increase of the velocity. This phenomenon is important at the smallest cross sections, in particular at very low subcooling. Second, growth and collapse of the vaporous regions destabilize the incoming flow at the contraction. As a result, the flow detaches and a jet develops. The effective cross section is smaller; the velocities, and thus the losses, further increase. Moreover, disturbances amplify in the bounding regions of the jet. Large amount of energy are dissipated.

According to the simulations, the cavitation patterns, and their impact on the flow resistance, evolve with the reduction of the subcooling in a double-nozzle channel as follows.

- Starting from single-phase conditions, the first manifestation of cavitation occurs at the wall in the second nozzle. There, the static pressure is low due to wall curvature, fluid acceleration and energy dissipation in the first diffuser. The flow detaches in the second nozzle and energy is dissipated downstream of the smallest cross section. The flow resistance increases in comparison to single-phase conditions.
- A further decrease of subcooling causes the coolant to vaporize further in the second nozzle. The velocity rises as a result of lower densities. Energy dissipation is enhanced.
- Then, at lower subcooling, the coolant starts to vaporize inside the first nozzle at the wall. The flow detaches and the flow resistance further increases.
- At saturation conditions, both nozzles are filled with vapor. The flow detaches and the velocity amplifies due to low densities. Energy dissipation is very large.

Choking would further increase the flow resistance. However, critical conditions do not occur with a subcooled or saturated coolant whose mass flow rate is 1.8kg/s. Thus, in the POR design with 37 parallel pipes, choking does not occur with a mass flow rate of 67kg/s.

One-dimensional critical mass flow rate calculation indicates that the void fraction at the smallest cross section should be about 0.94 for this to happen (Figure 9-48, left). In the simulation with a coolant near saturation, the void fraction only amounts 0.3.

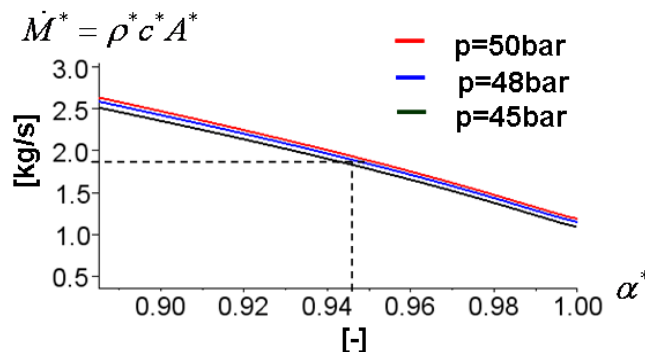


Figure 9-48: Critical mass flow rate of a homogeneous water-vapor mixture as a function of the void fraction α^* and pressure at the choking cross section. A^* is the smallest cross section of the POR channel and c^* is the speed of sound in the mixture.

9.3 Conclusion

In this chapter, the flow behavior of a double-nozzle design is investigated in both directions under cavitating conditions.

Three LES are performed to analyze the effect of the first smallest cross section and the influence of the subcooling on the critical mass flow rate in the backward direction. The calculations agree with the experimental results obtained in Karlstein (chapter *performance tests*):

- The mass flow rate is larger in a single-nozzle design than in a double-nozzle design under the same flow conditions.
 - The efficiency of the double-nozzle design is very high at small subcooling.
 - The efficiency of the double-nozzle design decreases with increasing subcooling.
- The simulations also provide further insight into the mechanisms yielding the mass flow reduction:
- Choking occurs in the second nozzle.
 - The choking cross section does not exactly coincide with the geometrical smallest cross section of the second nozzle.
 - The choking cross section displaces in direction of the smallest cross section at lower subcooling. As a result, the choking cross section, and thus the critical mass flow rate, is smaller.
 - At moderate subcooling, vaporization occurs in the first nozzle only in the core of turbulent eddies.
 - At smaller subcooling, vaporization occurs also in the bulk of the first nozzle.
 - In both cases, large amounts of energy are dissipated upstream of the choking cross section due to cavitation and large fluctuations.
 - Vaporization and pressure loss upstream of the choking cross section induce higher vapor content and lower pressure at the choking cross section. The speed of sound and the density, and thus the critical mass flow rate, significantly reduce.

Two LES are carried out to study the effect of the subcooling on the flow resistance in the forward direction. The calculations match the experimental results:

- The flow resistance drastically increases under cavitating conditions.
- The flow resistance is very sensitive to the subcooling of the coolant.

In addition, the numerical results help understanding the driving phenomena:

- Under the investigated conditions, the flow resistance is not due to choking.
- Energy primarily is dissipated in the vicinity of the smallest cross sections and in the diffusers.
- In contrast to single-phase conditions, the flow detaches in the diffusers as a result of cavitation sheet's growth and collapse.
- Flow detachment enhances energy dissipation. The effective cross section reduces and, thus, the velocity increases. Furthermore, strong fluctuations develop in the bounding regions of the jet.
- Coolant vaporization also yields larger energy dissipation because the density decreases, and thus the velocity rises.

The numerical analysis of the POR design also demonstrates the capability of the proposed modeling approach. The agreement between numerical and experimental results is very satisfactory under very differing flow conditions. The stochastic-field cavitation model accurately reproduces the behavior of the polydisperse cavities. All nuclei are activated at large local tension. These large local tensions are typically encountered in the backward direction. By contrast, only large nuclei are activated at small local tension. This phenomenon occurs for instance in the pipe between the two nozzles in the forward direction.

10 Conclusion

In the present thesis, an innovative fluidic diode for critical two-phase flows is presented. It consists of a short and compact bundle of parallel double-nozzle channels. This component is developed for the KERENA reactor. There, it limits the loss of coolant in the backward direction after the break of the EC condensate return line. In the opposite flow direction, the forward direction, the pressure loss in the component is minimized not to jeopardize emergency core cooling.

The reduction of the mass flow rate in the backward direction with this design relies on the efficient choking of the two-phase mixture in the second Venturi-nozzle. The vaporization of the coolant and energy dissipation are enforced upstream of the choking cross section with the first nozzle. Then, the two-phase mixture chokes in the second smallest cross section at a low pressure and with high vapor content. Both low pressure and high vapor content yield a drastic reduction of the choking mass flow rate. This principle is particularly advantageous when the coolant leaving the reactor pressure vessel is moderately subcooled or saturated. Experiments performed in both directions under realistic boundary conditions at the AREVA Technical Center in Karlstein with a double-nozzle channel demonstrate that ratios up to 70 can be achieved between backward and forward direction resistance coefficients.

Due to the simplicity of this innovative design, its development is possible with standard system codes in the backward direction and with standard CFD codes in the forward direction. The flow behavior of the fluidic diode is accurately described by the homogeneous equilibrium model in the backward direction; while single-phase CFD simulations are sufficient in the opposite flow direction since cavitation only occurs at very low subcooling. For the KERENA reactor, a parallel arrangement of 37 pipes yields a component with 250mm diameter and 900mm length. This design can easily be adapted to similar applications.

A CFD code able to simulate the flow behavior in the backward direction was not available. Therefore, a novel cavitation model is developed and implemented in the density-based code SPARC. This novel cavitation model uses the stochastic-field method developed by Valiño [10] to solve the vapor mass fraction pdf and capture the bubble size spectrum with stochastic Euler fields. The fluctuations of the vapor mass fraction and the bubble size on the sub-grid scale are resolved in a pure Euler formulation, and thus without excessive computational demand and complex algorithms.

The interfacial mass transfer term appearing in the transport equation of the vapor mass fraction only requires a modeling of the mass transfer mechanism but no modeling is necessary to account for the fluctuations. In this context, a mechanism for the interfacial mass transfer is proposed in this work to account for thermal, inertial and water quality effects. Furthermore, constitutive relations and equations of state valid over large pressure and temperature ranges are implemented.

In the present version of the code, the bubble size spectrum is used to improve the description of the mass transfer mechanism. Other stochastic processes and highly non-linear, radius dependent phenomena such as break-up and coalescence could be accounted for. The method is compatible with existing physical models available for Lagrange techniques, presumed pdf or binning methods. Therefore, this method is also very attractive for other multi-phase flows which in general possess similar characteristics (stochastic processes, highly non-linear interfacial exchanges, crucial dependence on interfacial area).

Some properties of the stochastic Euler fields are analyzed and the cavitation model is validated with both RANS and LES calculations. The stochastic-field method adapted to cavitation shows very encouraging results. The various shapes of the bubble spectrum at different locations are obtained and the agreement between numerical and experimental results is very satisfactory. The validation cases are characterized by very differing flow conditions. For instance, the flow behavior of the fluidic diode under cavitating conditions is analyzed in both directions.

Experiments with statistical data are required to further validate the code.

Nomenclature

List of abbreviations

BWR	Boiling water reactor
CD	Central difference scheme
CDF	Cumulative density function
CFD	Computational fluid dynamics
CFL	Courant-Friedrichs-Lewy criterion
DQMOM	Direct quadrature method of moment
EC	Emergency condenser
eos	Equation of state
FPE	Fokker-Planck equation
HEM	Homogeneous equilibrium model
HPF	High pass filter
I&C	Instrumentation and control
IEM	Interaction by exchange with the mean
LES	Large eddy simulation
LOCA	Loss of coolant accident
MILES	Monotone integrated LES
ODE	Ordinary differential equation
pdf	Probability density function
PIV	Particle image velocimetry
POR	Passive outflow reducer
RANS	Reynolds-averaged Navier-Stokes equations
RP	Rayleigh-Plesset equation
RPV	Reactor pressure vessel
scram	Emergency shutdown of a nuclear reactor
SDE	Stochastic differential equation
SIMPLE	Semi-implicit method for pressure linked equations
SF	Stochastic field
SFM	Stochastic-field method

Nomenclature

Latin symbols

a_i	Interfacial area concentration
\underline{a}	Interpolation coefficient between Euler mesh and Lagrange particle position
a_1	Model constant in $k-\omega$ SST turbulence model
\tilde{a}_1	Model constant in $k-\omega$ SST turbulence model
$\underline{\underline{a}}$	Model constant in Van der Waals equation of state
A	Surface area (cross section, bubble, interface)
A, B	Drift and diffusion term in a Fokker-Planck equation
$\underline{\underline{A}}$	Matrix defined in DQMOM
\underline{b}	Model constant in Van der Waals equation of state
B_T	Model constant in Tait equation of state
$\underline{\underline{b}}$	Vector consisting of \bar{S}_{m_k} in DQMOM
B_B	Birth rate due to breakup of larger particles
B_C	Birth rate due to coalescence of smaller particles
B	Interval of \mathbb{R}
c	Speed of sound
C or $C_{\tilde{x}}$	Auto-covariance of a stochastic process \tilde{x}
C_{v1}	Model constant in Spalart-Allmaras turbulence model
C_o	Universal constant derived by Kolmogorov

C_{cond}	Condensation coefficient
\tilde{C}	Constant in DQMOM
C_{am}	Added mass coefficient
C_{cond}	Condensation coefficient
C_d	Discharge coefficient
C_D	Drag force coefficient
C_{LF}	Lift force coefficient
C_{vap}	Vaporization coefficient
cO	Concentration of species
c_v	Specific heat capacity at constant volume
c_p	Specific heat capacity at constant pressure
C_{b1}	Model constant in Spalart-Allmaras turbulence model
C_{b2}	Model constant in Spalart-Allmaras turbulence model
C_{w1}	Model constant in Spalart-Allmaras turbulence model
C_{w2}	Model constant in Spalart-Allmaras turbulence model
C_{w3}	Model constant in Spalart-Allmaras turbulence model
C_s	Model constant in Smagorinsky-Lilly turbulence model
C_τ	Constant of proportionality between pressure and velocity fluctuations
C_ϕ, C_Y	Scaling factors between characteristic turbulent time scales
$C_{SST} = \{\tilde{\alpha}, \tilde{\beta}, \sigma_\omega, \sigma_k\}$	Model constants in $k-\omega$ SST turbulence model
$C_{k-\omega} = \{\tilde{\alpha}_1, \tilde{\beta}_1, \sigma_{\omega 1}, \sigma_{k1}\}$	Model constants in $k-\omega$ SST turbulence model
$C_{k-\varepsilon} = \{\tilde{\alpha}_2, \tilde{\beta}_2, \sigma_{\omega 2}, \sigma_{k2}\}$	Model constants in $k-\omega$ SST turbulence model
C_{TD}	Turbulent dispersion model constant
C_{WL1}, C_{WL2}	Wall lubrication model constants
C_{DQM}	Model constant in DQMOM
\tilde{c}_m	Model constant in homogeneous cavitation model in CFD
$CD_{k\omega}$	Model constant in $k-\omega$ SST turbulence model
dt	Infinitesimal time increment or observation time
\tilde{d}^q	Characteristic particle diameter in DQMOM
D	Diameter (pipe, bubble)
D	Diffusion coefficient
dp	Pressure difference
D_B	Death rate due to breakup into smaller particles
$\mathcal{D}, \underline{\mathcal{D}}$	Discretization operators
D_C	Death rate due to coalescence with other particles
D_Y	Diffusion coefficient of Y
$(D_Y)_t$	Turbulent diffusion coefficient of Y
e	Specific internal energy
e_{ij}	Component (i, j) of the deformation tensor
E	Specific total energy
EO	Eötvös number
f	Generic function or probability density function
\mathbf{f}	Force per unit volume
f_{CV}	Face of a control volume
\mathbf{f}_i	Coordinate of intersection of segment $(\mathbf{x}_N, \mathbf{x}_p)$ with cell surface
\mathbf{f}_d	Drag force per unit volume acting on the dispersed phase

f_{ds}	Ratio of distance
$f_{RT}(R,T)$	Joint- probability density function of process R and T
$f(x_1;t_1 x_0;t_0)$	Transition density function
f^ϕ	Cavities distribution function
f'	Marginal cavities distribution function
f_i	Size fraction of bin i
f_1, f_2	Joint-pdf
f^+	Fine-grained pdf
f_1	Damping function in Spalart-Allmaras turbulence model
f_{v2}	Damping function in Spalart-Allmaras turbulence model
f_w	Damping function in Spalart-Allmaras turbulence model
f_l, g_m, h_n	Basis functions of interpolation between Euler mesh and Lagrange particle position
$\mathbf{F} = (f_1, f_2, f_3)$	Total volume force
F_{RT}	Joint-cumulative density function of process R and T
F_1	Damping function in $k-\omega$ SST turbulence model
F_2	Damping function in $k-\omega$ SST turbulence model
\mathbf{F}_A	Added mass force
\mathbf{F}_B	Buoyancy force
\mathbf{F}_D	Drag force
\mathbf{F}_p	Pressure gradient force
\mathbf{F}_H	History force
F_i	Two-phase correlation of interfacial shear stress
F_{ia}, F_{is}, F_{id} and F_{id}	Coefficients for the calculation of the interfacial shear stress F_i
\mathbf{F}_r	Volume variation force
\mathbf{F}_L	Lift force
\mathbf{F}_{Ma}	Marangoni force
\mathbf{F}_d^{TD}	Turbulent dispersion force
$\mathbf{F}_{WL,bub}$	Wall lubrication force
\mathbf{F}_{WD}	Wall deformation force
\mathbf{F}_u	Convection vector in density-based solver
F	Force or generic function or cumulative density function
F'	Fluctuations of a force or generic function
\mathbf{g}, g	Gravity field
g_1, g_2, g_3 and g_4	Generic functions
g_c	Collision frequency
g_b	Break-up frequency
$g_{br,m}(\varepsilon, m)$	Break-up frequency in multi-group approach
g_{sp}	Damping function in Spalart-Allmaras turbulence model
G	Filter function
\mathbf{G}	Viscous flux vector in density-based solver
G_c	Mass flux
G_{v_i}	Production term in Spalart-Allmaras turbulence model
h	Specific enthalpy
H	Curvature
\mathbf{H}	Source term vector in density-based solver
\mathcal{H}	Discretization operator
H_G	Henry's law constant

$\mathbf{j} = (j_1, j_2, j_3)$	Flux vector of specie Y
\mathbf{J}	Molecular diffusion flux of momentum or heat
k	Turbulent kinetic energy
k_1	Model constant for drainage time
k_d	Ratio of pressure loss coefficient
k_E	Wave number of turbulent eddies
k_w, k_b	Convection heat coefficient
K	Resistance coefficient
K_σ	Cavitation number
k_{dr}	Model constant in drainage time
K_g	Model constant in breakup frequency
K_T	Model constant in Tamman equation of state
$K^{(2)}, K^{(4)}$	Model constant in artificial dissipation scheme
l	Specific latent heat
l_K	Kolmogorov length scale
L	Characteristic length
m or M	Mass
M	Mach number
\mathbf{m}	Vector $\mathbf{x}_j - \mathbf{f}_i$
\dot{M}	Mass flow rate
\dot{m}	Volume mass flow
\dot{m}_k	Mass transfer in phase k
\dot{m}_{12}	Intergroup mass transfer from group 1 to 2
\dot{m}_{cond}	Vapor condensation rate
\underline{M}	Gas molar mass
\mathcal{M}	Spatial operator
\mathbf{M}_k	Source in momentum equation of phase k
\mathbf{M}_m	Source in mixture momentum equation
\mathcal{M}	Event
M_γ	γ 'th distribution moment
n	Cavities number density or number density distribution function
$n \in \mathbb{N}$	Time step or number of pipe or number of moment
\mathcal{N}_A	Avogadro constant
n_E	Frequency of turbulent eddies
n_T	Model constant in Tait equation of state
n_γ	Polytropic exponent
\mathbf{n}	Vector normal to the surface
\underline{N}	Number of pipes
\widehat{N}	Number of characteristic particle diameters in DQMOM
\underline{N}	Number of stochastic fields
\widehat{N}	Number of class in MUSIG approach
N_b	Number of dispersed particles
Nu	Nusselt number
p	Pressure
$p \in \mathbb{N}$	Internal iteration of iterative scheme
p'	Pressure fluctuations
Pe	Peclet number
Pr	Prandtl number
Pr_t	Turbulent Prandtl number
p_{cr}	Pressure at which cavitation is observed

P	Pipe perimeter
$P(\mathcal{M})$ or $P\mathcal{M}$ or $P[\mathcal{M}]$	Probability of the event \mathcal{M}
P_k	Phase indicator of phase k , also called phase density function
\underline{P}_k	Production term in the k -equation
P_g, P_l	Pipe perimeter in contact with gas and liquid, respectively
P_i	Interfacial perimeter
P_{col}	Probability of collision
$p_{l,s}$	Model constant in barotropic equation of state
p_T	Model constant in Tamman equation of state
$\mathbf{q} = (q_1, q_2, q_3)$	Heat flux density
\mathbf{q}_k^T	Apparent turbulent heat flux in phase k
\mathbf{q}^D	Apparent turbulent heat flux in drift model
q_w	Heat transfer coefficient at the wall
q_{wg}, q_{wl}	Heat transfer coefficient of gas and liquid phase at the wall, respectively
q_{ig}, q_{il}	Heat transfer coefficient at the interface of gas and liquid phase, respectively
Q	Heat source term
Q	Second scalar invariant of the velocity gradient tensor
$\dot{R}_{\bar{\gamma}}$	Mean bubble growth rate in presumed pdf approach
R	Radius size
R or $R_{\bar{x}}$	Autocorrelation of a stochastic process \bar{x}
r	Radial coordinate in cylindrical or spherical coordinate system
\dot{R}	Bubble growth rate
\mathcal{R}	Universal gas constant
\mathcal{R}_g	Gas constant (vapor)
\mathcal{R}_G	Gas constant (dissolved gas)
Re	Reynolds number
Re_b	Reynolds number related to bubble
r_{sp}	Variable in Spalart-Allmaras turbulence model
R_F	Coefficient used in the calculation of interfacial shear stress F_i
s	Specific entropy or size step of a random walk
S_l	Velocity ratio
$S(Y)$	Source term in the transport equation of the scalar property Y
$\mathbf{S} = (e_{ij})$	Deformation tensor
S	Flow property in Spalart-Allmaras turbulence model
S_{Ω}	Flow property in Spalart-Allmaras turbulence model
\dot{S}	Source term for coalescence and breakup processes
S_i	Source term for coalescence and breakup processes of bin i
\mathbf{S}_f	Surface area vector
\dot{S}_{break}	Breakup source term
\dot{S}_{coal}	Coalescence source term
\dot{S}'_{break}	Marginal breakup source term
\dot{S}'_{coal}	Marginal coalescence source term
\dot{S}_{ph}	Nuclei activation source term
\bar{S}_{m_k}	Mean source term ($k \in \mathbb{N}$) in DQMOM

S_ϕ	Source of variable ϕ
$S_{\hat{\gamma}}$	Intensity of dispersion ($\hat{\gamma} \in \mathbb{N}$)
S_{ω_q}	Source term in the transport equation of the weights ω_q in DQMOM
S_{δ_q}	Source term in the transport equation of the weighted abscissas δ_q in DQMOM
$S_{Q,k}$	Source term in the energy equation of the phase k
$S_{Q,m}$	Source term in the energy equation of the mixture
S_{bn}	Nuclei activation in the bulk
S_{wn}	Nuclei activation at the wall
SR	Surface ratio
S_l	Velocity ratio
σ_Y	Schmidt number associated to scalar property Y
t	Time
t_K	Kolmogorov time scale
T	Temperature or time step of a Random walk
T'	Temperature fluctuations
\dot{T}	Temperature variation rate
$\mathbf{T} = (\sigma_{ij})$	Stress tensor
$\tilde{\mathbf{T}}$	Temperature explicitly represented as a stochastic process
\mathbf{T}_k^T	Apparent stress tensor in phase k
\mathbf{T}^D	Apparent stress tensor in drift-flux model
T_T	Model constant in Tamman equation of state
$\mathbf{u} = (u_1, u_2, u_3)$	Velocity vector
T_a	Characteristic time scale of the Lagrange acceleration
T_L	Characteristic time scale of the Lagrange velocity
$\mathbf{u}' = (u'_1, u'_2, u'_3)$	Velocity fluctuations vector
$\mathbf{u}_{\hat{\gamma}}$	Mean velocity in the transport equation of the intensity of dispersion ($\hat{\gamma} \in \mathbb{N}$)
u^+	Normalized velocity
U or u	Characteristic or bulk velocity
$\tilde{\mathbf{U}}$	Velocity vector explicitly represented as a stochastic process
u_s	Superficial velocity
u_i	Interfacial velocity
u_{ni}	Normal component of the interfacial velocity
U_{gj}, U_{lj}	Drift velocity of gas and liquid phase, respectively
\mathbf{U}_{kn}	Drift velocity of phase k
V	Volume
\dot{V}	Volume flow rate
V_{cr}	Volume of maximum distorted bubble
V_{sp}	Volume in phase space
$\tilde{\mathbf{w}}$	Wiener-Levy process
$w(x_i x_0; t_0)$	Transition rate
\mathbf{W}	Conserved variables vector
$\mathbf{x} = (x_1, x_2, x_3)$	Position vector
x^+, y^+, z^+	Non-dimensional sizes of the first cells at the wall in the flow direction, normal to the wall and transverse to the flow direction, respectively
x_l, y_m, z_n	Grid point coordinates
$\tilde{\mathbf{x}}$	Vector of S_{ω_q} in DQMOM
$\tilde{\mathbf{x}}$	Stochastic process

$(\mathbf{x}, \mathbf{y}, \mathbf{z})$ or $(\mathbf{x}_1, \mathbf{x}_2, \mathbf{x}_3)$	Unit coordinate axis vectors
Y	Scalar property or vapor mass fraction
\mathbf{Y}	Vector of discrete values of the scalar property Y
Y'	Fluctuation of Y
Y_{ν_i}	Dissipation term in Spalart-Allmaras turbulence model
y_w	Distance to the wall

Greek symbols

α	Gas volume fraction or contraction / diffuser angle
α_k	Volume fraction of phase k
$\underline{\alpha}$	Volume fraction of the characteristic particles in DQMOM
$\tilde{\alpha}$, $\tilde{\alpha}_1$, $\tilde{\alpha}_2$	Model constants in $k-\omega$ SST turbulence model
α_i	Volume fraction of bin i
α_t	Thermal diffusivity
$\check{\beta}$, $\check{\beta}_1$, $\check{\beta}_2$	Model constants in $k-\omega$ SST turbulence model
β	Model constant for breakup frequency
β^*	Model constant in $k-\omega$ SST turbulence model
γ	Isentropic expansion factor
$\hat{\gamma}$	Integer used in the presumed pdf approach
Γ_ρ	Density ratio
Γ_η	Viscosity ratio
Γ_{c_p}	Specific heat ratio
Γ_N	Numerical diffusion coefficient
δ_{ij}	Kronecker delta
$\delta_{\sim q}$	Weighted abscissa in DQMOM
Δ	Grid size or characteristic filter width
$\mathbf{\Delta}$	Length vector between two grid centroids
Δp	Pressure drop
ΔR	Bubble cluster radius
Δt	Time step or averaging time
ε	Turbulent kinetic energy dissipation rate
$\tilde{\varepsilon}$	Mass in multi-group approach
ε_r	Wall roughness
$\varepsilon^{(2)}$, $\varepsilon^{(4)}$	Coefficients in artificial numerical scheme
ε_{it}	Truncation error in iterative scheme
ζ	Single phase pressure loss
η	Dynamic viscosity
η_t	Turbulent eddy viscosity
η_{sgs}	Sub-grid dynamic viscosity
$\tilde{\eta}$	Expectation value
κ	Von Karman constant
λ	Mean free path
λ_{x_1} , λ_{x_2}	Spectral radii of the flux Jacobian matrices of the convective terms
$\lambda^* = -2/3\eta$	Viscosity
λ_T	Thermal conductivity
$(\lambda_T)_t$	Turbulent thermal conductivity
Λ	Scaling factor in artificial dissipation scheme
Λ	Constant in Kubota bubble growth model

μ	Chemical potential
ν	Specific volume
ν	Kinematic viscosity
ν_t	Turbulent kinematic viscosity
$\tilde{\nu}_t$	Modified form of the turbulent kinematic viscosity in Spalart-Allmaras model
$\tilde{\nu}_{i,j}$	Pressure sensor in artificial dissipation scheme
ξ_i or ξ	Outcome of an experiment \mathcal{E}
$\tilde{\xi}$	White noise
ρ	Density
ρ_I	Momentum density
ρ_m	Mixture density
ρ_H	Homogeneous mixture density
ρ'	Density fluctuations
σ	Surface tension
σ_c	Collision cross section
$\tilde{\sigma}$ or $\tilde{\sigma}_{\tilde{x}}$	Variance of the stochastic process \tilde{x}
$\sigma_{\omega}, \sigma_{\omega 1}, \sigma_{\omega 2}$	Model constants in $k - \omega$ SST turbulence model
$\sigma_k, \sigma_{k1}, \sigma_{k2}$	Model constants in $k - \omega$ SST turbulence model
$\underline{\sigma}$	Exponent in artificial dissipation scheme
σ_{ν_t}	Model constant in Spalart-Allmaras turbulence model
$\tilde{\sigma}_{vN}$	Von Neumann constant
$(\sigma_t)_Y$	Turbulent Schmidt number associated to Y
σ_{ij}	Component (i, j) of the stress tensor
σ_C	Cavitation number
Σ_R	Performance factor of a fluidic diode
τ	Mean time between two collisions
$\tau_t, \tau_{\phi}, \tau_Y$	Characteristic turbulent time scales
τ'_{ij}	Apparent turbulent stress
τ_w	Wall friction coefficient
τ_W	Wall shear stress
τ_{ij}	Component (i, j) of the deviatoric stress tensor
τ_{ig}, τ_{il}	Shear stress at the interface on gas and fluid side, respectively
$\tilde{\tau}_{ij}$	Principal component (i, j) of the deviatoric stress tensor
φ	Fluid / flow property
φ_g	Angle existing between pipe and gravity field
$\varphi_{\tilde{z}}$	Source term in governing equation of $S_{\tilde{z}}$
$\tilde{\phi}$	Composition vector explicitly treated as a stochastic process
ϕ	Geometry parameter
Φ	Coefficient in artificial dissipation scheme
ϕ_{LO}^2	Two-phase flow multiplier
Φ_{x_i}	Model constant in artificial dissipation scheme
Ψ	Volume fluid/flow property
Ψ_{sh}	Shape factor
Ω_{ij}	Component (i, j) of the rotation tensor
ω	Specific dissipation rate or scaled specific dissipation rate
$\omega_{\tilde{z}^q}$	Weight of the delta functions in DQMOM

Indices

Subscript

0	Reference or mean or stagnation conditions
1, 2, etc.	Cross sections or bubble group
<i>c</i>	Continuous phase
<i>b</i>	Vaporous cavity
<i>break</i>	Breakup
<i>cav</i>	Cavitation sheet
<i>cr</i>	Critical parameter
<i>cell</i>	Control volume
<i>cond</i>	Condensation
<i>d</i>	Dispersed phase
<i>dr</i>	Drainage
<i>D</i>	Droplet
<i>DQM</i>	DQMOM
<i>e</i>	Equilibrium condition or equivalent
<i>EE</i>	Euler explicit
<i>EI</i>	Euler implicit
<i>f</i>	Cell surface
<i>fr</i>	Friction
<i>g</i>	Gas phase
<i>G</i>	Residual gas
<i>H</i>	Halo cell
<i>H</i>	Calculated with HEM
<i>i, j, k</i>	Indices in x, y and z coordinate direction
<i>i</i>	Internal iteration <i>i</i> or bin <i>i</i>
<i>i</i> or int	Fluid / flow properties at the interface between two phases
<i>in</i>	Interaction
<i>j</i>	<i>j</i> 'th passage of the interface during the averaging time
<i>k</i>	Phase <i>k</i>
<i>l</i>	Liquid phase
<i>m</i>	Mixture
<i>m</i>	Outlet in critical mass flux calculation or middle
<i>N</i>	Neighboring cell
max	Maximum value
min	Minimum value
<i>num</i>	Numerical results
<i>pl</i>	Realistic plant conditions
<i>P</i>	Grid point <i>P</i>
<i>p</i>	Particle
<i>q</i>	Characteristic particle diameter in DQMOM
<i>R</i>	Surface of bubble of radius <i>R</i>
<i>sat</i>	Saturation condition
<i>sgs</i>	Sub-grid scale
<i>sk</i>	Skewness
<i>test</i>	Test conditions
<i>T</i>	Total
<i>UD</i>	Upwind-scheme
<i>v</i>	Viscosity
<i>vap</i>	Evaporation
x_1, x_2	Coordinate abscises x_1, x_2
σ	Surface tension
<i>w</i>	Wall values
∞	Characteristic values
2- <i>Ph</i>	Two-phase

Superscript

d	Discretized
$*$	Critical cross section or notional particle (chapter <i>stochastic</i>)
m	Modeled
(n)	Evaluated at time step n
t	Throat
T	Turbulent fluctuations

Mathematical operators

$E[]$ or $\langle \rangle$	Mean value
$\mathbf{S} \cdot ()_f$	Scalar product with the face area vector \mathbf{S}_f
∇	Nabla operator
∇_{x_i}	Forward difference operator
Δ_{x_i}	Backward difference operator
∇_s	Surface gradient operator
$\langle \rangle$	Conditional expectation
$\langle \rangle$ or $^-$	Averaging operator
$=$	Phase averaging operator
\wedge	Mass weighted averaging operator
$\langle \rangle_N$	Ensemble averaging of N realizations
$ $ or $\ \ $	Euclidean norm

Nomenclature cavitation stochastic-field model

The abbreviations and symbols used in the chapter cavitation stochastic-field model are summarized in this table for convenience.

Latin symbols

C_{am}	Added mass coefficient
C_{cond}	Model constant of the condensation source term
c_p	Specific heat capacity at constant pressure
C_ϕ, C_Y	Scaling factor between velocity and scalar property turbulent time scales
D	Molecular diffusivity
D_b	Bubble diameter
D_c	Critical bubble diameter
D'	Combined molecular and turbulent diffusivity
e	Specific internal energy
E	Total specific internal energy
$f_{\tilde{\phi}}$	Probability density function of the random variable $\tilde{\phi}$
g_c	Collision frequency
h	Specific enthalpy
\mathbf{j}	Mass flux vector of Y
k	Turbulent kinetic energy
k_1, k_{dr}	Model constants of the drainage time
$K_{v,v}, K_{v,l}, K_T$	Functions of the temperature

$K_{v,1}, K_{v,2}, K_{v,3}$	Model constants of the caloric eos
m_G	Mass of dissolved gas
n	Nuclei number density
n_0	Initial nuclei number density
\underline{N}	Number of stochastic fields
N_ϕ	Number of scalar properties
p	Pressure
P_{col}	Probability of collision
p_T, T_T, K_T	Model constants of the water eos
Pr	Prandtl number
\mathbf{q}	Mixture heat flux density
R	Vaporous cavity radius
\mathcal{R}_g	Gas constant (vapor)
S	Non-linear process or source term of the vapor mass fraction transport equation
S_+, S_-	Evaporation and condensation term, respectively
S_b, S_c	Break-up and coalescence source term, respectively
S_α	Source term of the scalar property transport equation
t	Time
T	Temperature
\mathbf{T}	Mixture stress tensor
$\mathbf{u} = (u_i), i = 1..3$	Velocity vector
U_{rel}	Bubble relative velocity
U_{turb}	Turbulent bubble relative velocity
W_i^k	Wiener process associated to the spatial component i and the stochastic field k
$\mathbf{x} = (x_i), i = 1..3$	Position vector
$x+, y+, z+$	Non-dimensional sizes of the first cells at the wall in the flow direction, normal to the wall and transverse to the flow direction, respectively
Y	Vapor mass fraction

Greek symbols

α	Void fraction
α_{max}	Maximum packing number
δ	Dirac function
Δ	Cell size
ε	Turbulent dissipation rate
ε_{stat}	Statistical error
η	Dynamic viscosity
λ_T	Thermal conductivity
μ	Chemical potential
ρ	Density
σ	Surface tension
σ_Y	Schmidt number associated to the scalar Y
τ_{nuc}	Model time constant of the cavitation stochastic-field model
$\tau_\phi, \tau_Y, \tau_t$	Characteristic turbulent time scales
$\tilde{\phi}$	Vector of stochastic composition properties $\tilde{\phi}_\alpha$
$\tilde{\phi}_\alpha$	stochastic composition property
ϕ^k	Stochastic-field vector k associated to the vector $\tilde{\phi}$
ϕ_α^k	Stochastic field k associated to the scalar property $\tilde{\phi}_\alpha$
$\Psi = (\psi_\alpha)$	Sample space of the scalar properties

ω Turbulent specific dissipation rate

Indices

Subscript

<i>cell</i>	Computational cell
<i>cr</i>	Critical parameter
<i>dr</i>	Drainage
<i>e</i>	Equilibrium
<i>g</i>	Gas phase
<i>in</i>	Interaction
<i>l</i>	Liquid phase
<i>mod</i>	Modeled
<i>sat</i>	Saturation conditions
<i>Y</i>	Vapor mass fraction
∞	Infinity
α	Scalar property $\tilde{\phi}_\alpha$
φ	Scalar property $\tilde{\phi}$

Superscript

k Stochastic field *k*

Bibliography

- [1] « KERENA™ Plant General Description ». AREVA, 2010.
- [2] J.-P. Schaefer, « P2 - System Description - Emergency Condenser (JNB System) », AREVA, NESB-G/2009/en/1021, 2009.
- [3] J. Tamminga, « Loss-of-Coolant Accidents of the SWR1000 at an Initial Thermal Output of 3370 MW », Framatome ANP GmbH, Erlangen, Internal NGPS1/2004/en/0505, 2004.
- [4] A. A. Kulkarni, V. V. Ranade, R. Rajeev, et S. B. Koganti, « Pressure drop across vortex diodes: Experiments and design guidelines », *Chemical Engineering Science*, vol. 64, n° 6, p. 1285-1292, mars 2009.
- [5] N. Syred, J. Grant, et B. S. Sidhu, « Vortex diodes », U.S. Patent F15C 116.
- [6] K. Fischer, « Design of a supercritical water-cooled reactor pressure vessel and internals », PhD, TU Karlsruhe, Karlsruhe, 2008.
- [7] J. Wilkinson, A. Motamed-Amini, et I. Owen, « Compressible and confined vortex flow », *International Journal of Heat and Fluid Flow*, vol. 9, n° 4, p. 373-380, déc. 1988.
- [8] A. Motamed-Amini et I. Owen, « The expansion of wet steam through a compressible confined vortex in a fluidic vortex diode », *International Journal of Multiphase Flow*, vol. 13, n° 6, p. 845-856, nov. 1987.
- [9] R. Hertlein, « private communication », avr-2010.
- [10] L. Valiño, « A field Monte Carlo formulation for calculating the probability density function of a single scalar in a turbulent flow », *Flow Turbulence and Combustion*, vol. 60, n° 2, p. 157-172, 1998.
- [11] R. E. A. Arndt, « Cavitation in Fluid Machinery and Hydraulic Structures », *Annual Review of Fluid Mechanics*, vol. 13, n° 1, p. 273-326, 1981.
- [12] C. Brennen, *Cavitation and Bubble Dynamics*. Mcgraw Hill Book Co, 1995.
- [13] A. M. Kamp, A. K. Chesters, C. Colin, et J. Fabre, « Bubble coalescence in turbulent flows: A mechanistic model for turbulence-induced coalescence applied to microgravity bubbly pipe flow », *International Journal of Multiphase Flow*, vol. 27, n° 8, p. 1363-1396, août 2001.
- [14] C. Dopazo et E. E. O'Brien, « An approach to the autoignition of a turbulent mixture », *Acta Astronautica*, vol. 1, n° 9-10, p. 1239-1266, sept. 1974.
- [15] S. B. Pope, « PDF methods for turbulent reactive flows », *Progress in Energy and Combustion Science*, vol. 11, n° 2, p. 119-192, 1985.
- [16] A. Garmory, E. S. Richardson, et E. Mastorakos, « Micromixing effects in a reacting plume by the Stochastic Fields method », *Atmospheric Environment*, vol. 40, n° 6, p. 1078-1091, févr. 2006.
- [17] W. P. Jones et A. Tyliczszak, « Large Eddy Simulation of Spark Ignition in a Gas Turbine Combustor », *Flow Turbulence and Combustion*, vol. 85, n° 3-4, p. 711-734, 2010.
- [18] M. Bini, W. P. Jones, et C. Lettieri, « Large Eddy Simulation of Spray Atomization with Stochastic Modelling of Breakup », *Proceedings of the European Combustion Meeting*, vol. 22, n° 11, p. 115106, 2009.
- [19] W. P. Jones, S. Navarro-Martinez, A. Boguslawski, C. Lacor, et B. Geurts, « Large Eddy Simulation and the Filtered Probability Density Function Method », 2009, p. 39-62.
- [20] F. Magagnato, B. Pritz, et M. Gabi, « A Novel Approach to Predict the Stability Limit of Combustion Chambers with LES », presented at the 9th International Symposium on Experimental and Computational Aerothermodynamics of Internal Flows, Gyeongju, South Korea, 2009.
- [21] H. Herwig, *Strömungsmechanik: Einführung in die Physik von technischen Strömungen*, 2008^e éd. Vieweg+Teubner Verlag, 2008.
- [22] G. G. Stokes, « On the theories of the internal friction of fluids in motion, and of the equilibrium and motion of elastic solids », *Trans. Cambr. Phil. Soc.*, vol. 8, p. 287-319.
- [23] G. K. Batchelor, *An Introduction to Fluid Dynamics*. Cambridge University Press, 2000.
- [24] P. W. Atkins, *Physikalische Chemie*, 2., vollst. neubearb. A. Wiley-VCH, 1996.
- [25] Y.-C. Cheng, *Macroscopic And Statistical Thermodynamics*. World Scientific, 2006.
- [26] A. Dhar, K. Saito, et B. Derrida, « Exact solution of a Levy walk model for anomalous heat transport », *arXiv:1207.1184*, juill. 2012.
- [27] A. H. Harvey et D. G. Friend, « Chapter 1 - Physical properties of water », in *Aqueous Systems at Elevated Temperatures and Pressures*, London: Academic Press, 2004, p. 1-27.
- [28] D. C. Prieve et E. Ruckenstein, « Effect of London forces upon the rate of deposition of Brownian particles », *AIChE Journal*, vol. 20, n° 6, p. 1178-1187, 1974.
- [29] G. A. Jeffrey, *An Introduction to Hydrogen Bonding*. Oxford University Press, USA, 1997.

- [30] M. Massimi, *Pauli's Exclusion Principle: The Origin and Validation of a Scientific Principle*. Cambridge University Press, 2005.
- [31] J.-P. Franc et J.-M. Michel, *Fundamentals Of Cavitation*. Springer, 2004.
- [32] C. H. Cooke et T.-J. Chen, « On shock capturing for pure water with general equation of state », *Communications in Applied Numerical Methods*, vol. 8, n° 4, p. 219-233, juin 2005.
- [33] H. Schlichting et K. Gersten, *Boundary-Layer Theory*. Springer, 2000.
- [34] P. Petitjeans et J.-E. Wesfreid, « Vortex stretching and filaments », *Applied Scientific Research*, vol. 57, n° 3, p. 279-290, 1996.
- [35] P. Gerlinger, *Numerische Verbrennungssimulation: Effiziente Numerische Simulation Turbulenter Verbrennung*. Springer DE, 2005.
- [36] N. T. Andersen, « The Central Limit Theorem for Stochastic Processes », *Ann. Probab.*, vol. 15, n° 1, p. 164-177, janv. 1987.
- [37] J. Fröhlich, *Large Eddy Simulation turbulenter Strömungen*, 2006^e éd. Vieweg+Teubner Verlag, 2006.
- [38] P. S. Klebanoff, « Characteristics of turbulence in boundary layer with zero pressure gradient », 1955.
- [39] A. N. Kolmogorov, « Die lokale Struktur der Turbulenz in einer inkompressiblen zähen Flüssigkeit bei sehr großen Reynoldsschen Zahlen », *Dokl. Akad. Wiss. USSR*, vol. Bd. 30, p. 301-305.
- [40] I. E. Idelchik, *Handbook of Hydraulic Resistance*, 3^e éd. Jaico Publishing House, 2005.
- [41] J. H. Spurk, *Strömungslehre: Einführung in die Theorie der Strömungen*, 4., neubearb. Aufl. 1996. Nachdruck. Springer Berlin Heidelberg, 1996.
- [42] E. Schmidt, K. Stephan, et F. Mayinger, *Technische Thermodynamik: Grundlagen u. Anwendungen*. Berlin: Springer.
- [43] V. P. Skripov, *Thermophysical Properties of Liquids in the Metastable (Superheated) State*, 1^{re} éd. Routledge, 1988.
- [44] Caupin et E. Herbert, « Cavitation in water: a review », *Comptes Rendus Physique*, vol. 7, n° 9-10, p. 1000-1017, 2006.
- [45] N. I. Kolev, *Multiphase Flow Dynamics 2: Mechanical Interactions*, 4th éd. Springer, 2011.
- [46] R. T. Lahey et F. J. Moody, *The thermal-hydraulics of a boiling water nuclear reactor*. American Nuclear Society, 1993.
- [47] J. M. Delhay et M. L. Riethmuller, *Thermohydraulics of two-phase systems for industrial design and nuclear engineering*. Hemisphere Pub. Corp., 1981.
- [48] M. Wörner, « A compact introduction to the numerical modeling of multiphase flows », Forschungszentrum Karlsruhe, Karlsruhe, Wissenschaftliche Berichte FZKA 6932, nov. 2003.
- [49] O. Baker, « Simultaneous flow of oil and gas », *Oil Gas J.*, vol. 53, p. 185.
- [50] J. W. PALEN, G. BREBER, et J. TABOREK, « Prediction of Flow Regimes in Horizontal Tube-Side Condensation », *Heat Transfer Engineering*, vol. 1, n° 2, p. 47-57, 1979.
- [51] T. Schulenberg, « KIT - IKET - Zweiphasenströmung - 001 », Karlsruhe, 2012.
- [52] D. Chisholm, « Pressure gradients due to friction during the flow of evaporating two-phase mixtures in smooth tubes and channels », *International Journal of Heat and Mass Transfer*, vol. 16, n° 2, p. 347-358, févr. 1973.
- [53] P. Lombardi, V. De Angelis, et S. Banerjee, « Direct numerical simulation of near interface turbulence in coupled gas liquid flow », *Physics of Fluids*, vol. 8, n° 6, p. 1643-1665, juin 1996.
- [54] M. Chrigui, « Eulerian-Lagrangian Approach for Modeling and Simulations of Turbulent Reactive Multi-Phase Flows under Gas Turbine Combustor Conditions », TU Darmstadt, Darmstadt, 2005.
- [55] S. S. Kutateladze, « Academician S. S. Kutateladze: Selected works », *Novosibirsk Izdatel Nauka*, vol. -1, 1989.
- [56] J. W. Miles, « On the generation of surface waves by shear flows Part 3. Kelvin-Helmholtz instability », *Journal of Fluid Mechanics*, vol. 6, n° 04, p. 583-598, 1959.
- [57] D. H. Sharp, « An overview of Rayleigh-Taylor instability », *Physica D: Nonlinear Phenomena*, vol. 12, n° 1-3, p. 3-18, juill. 1984.
- [58] R. I. Nigmatulin, *Dynamics Of Multiphase Media*. Hemisphere Publishing Corporation, 1990.
- [59] J. A. Boure, A. E. Bergles, et L. S. Tong, « Review of two-phase flow instability », *Nuclear Engineering and Design*, vol. 25, n° 2, p. 165-192, juill. 1973.
- [60] L. G. Neal et S. G. Bankoff, « A high resolution resistivity probe for determination of local void properties in gas-liquid flow », *AIChE Journal*, vol. 9, n° 4, p. 490-494, 1963.

- [61] H. Auracher et M. Buchholz, « Experiments on the fundamental mechanisms of boiling heat transfer », *Journal of the Brazilian Society of Mechanical Sciences and Engineering*, vol. 27, n° 1, p. 1-22, mars 2005.
- [62] H. Toral, « A study of the hot-wire anemometer for measuring void fraction in two phase flow », *Journal of Physics E: Scientific Instruments*, vol. 14, n° 7, p. 822-827, juill. 1981.
- [63] H. Shamsborhan, O. Coutier-Delgosha, G. Caignaert, et F. Abdel Nour, « Experimental determination of the speed of sound in cavitating flows », *Experiments in Fluids*, vol. 49, n° 6, p. 1359-1373, avr. 2010.
- [64] H. Städtke, *Gasdynamic Aspects of Two-Phase Flow: Hyperbolicity, Wave Propagation Phenomena, and Related Numerical Methods*. John Wiley & Sons, 2006.
- [65] S. Levy, *Two-Phase Flow In Complex Systems*, 1. Auflage. John Wiley & Sons, 1999.
- [66] A. Prosperetti, « A Brief Summary of L. van Wijngaarden's Work Up Till His Retirement », *Applied Scientific Research*, vol. 58, n° 1, p. 13-32, 1997.
- [67] A. Attou, L. Bolle, et J. M. Seynhaeve, « Experimental study of the critical flashing flow through a relief line: evidence of the double-choked flow phenomenon », *International Journal of Multiphase Flow*, vol. 26, n° 6, p. 921-947, juin 2000.
- [68] F. A. Williams, *Combustion theory*. Addison-Wesley Pub. Co., 1965.
- [69] A. Dzibur, B. Bajic, et I. Jovanovic, « On the applicability of the coulter counter to the cavitation nuclei size distribution analysis », 1993.
- [70] T. J. O'Hern, L. d' Agostino, et A. J. Acosta, « Comparison of holographic and coulter counter measurements of cavitation nuclei in the ocean », in *American Institute of Aeronautics and Astronautics*, Cincinnati, Ohio, 1988.
- [71] E. Yilmaz, F. G. Hammitt, et A. Keller, « Cavitation inception thresholds in water and nuclei spectra by light-scattering technique », *The Journal of the Acoustical Society of America*, vol. 59, n° 2, p. 329-338, 1976.
- [72] L. d' Agostino et A. J. Acosta, « A Cavitation Susceptibility Meter with Optical Cavitation Monitoring -- Part Two: Experimental Apparatus and Results », *Journal of Fluids Engineering*, juin-1991. .
- [73] Z. Liu, « Nuclei population dynamics and cavitation », Dissertation (Ph. D.), California Institute of Technology, 1995.
- [74] Z. Liu et C. E. Brennen, « Cavitation Nuclei Population and Event Rates », *Journal of Fluids Engineering*, vol. 4, n° 120, p. 728-737, déc. 1998.
- [75] E. Giannadakis, D. Papoulias, M. Gavaises, C. Arcoumanis, C. Soteriou, et W. Tang, « Evaluation of the Predictive Capability of Diesel Nozzle Cavitation Models », SAE International, Warrendale, PA, 2007-01-0245, avr. 2007.
- [76] J. W. Holl et G. F. Wislicenus, « Scale effects on cavitation », *ASME J. Basic Eng.*, vol. 83, p. 385-398, 1961.
- [77] M. S. Plesset et A. Prosperetti, « Bubble Dynamics and Cavitation », *Annual Review of Fluid Mechanics*, vol. 9, n° 1, p. 145-185, 1977.
- [78] P. S. Epstein et M. S. Plesset, « On the Stability of Gas Bubbles in Liquid-Gas Solutions », *The Journal of Chemical Physics*, vol. 18, n° 11, p. 1505, 1950.
- [79] A. I. Eller, « Effects of diffusion on gaseous cavitation bubbles », *The Journal of the Acoustical Society of America*, vol. 57, n° 6, p. 1374-1378, 1975.
- [80] L. A. Crum, « Measurements of the growth of air bubbles by rectified diffusion », *The Journal of the Acoustical Society of America*, vol. 68, n° 1, p. 203, 1980.
- [81] A. Kubota, H. Kato, et H. Yamaguchi, « A new modelling of cavitating flows: a numerical study of unsteady cavitation on a hydrofoil section », *Journal of Fluid Mechanics*, vol. 240, n° -1, p. 59-96, 1992.
- [82] C. F. Delale, G. H. Schnerr, et J. Sauer, « Quasi-one-dimensional steady-state cavitating nozzle flows », *Journal of Fluid Mechanics*, vol. 427, p. 167-204, janv. 2001.
- [83] T. Xing et S. H. Frankel, « Effect of Cavitation on Vortex Dynamics in a Submerged Laminar Jet », *AIAA Journal*, vol. 40, n° 11, p. 2266-2276, nov. 2002.
- [84] D. D. Joseph, « Cavitation and the state of stress in a flowing liquid », *Journal of Fluid Mechanics*, vol. 366, p. 367-378, juill. 1998.
- [85] K. S. Suslick et D. J. Flannigan, « Inside a Collapsing Bubble: Sonoluminescence and the Conditions During Cavitation », *Annual Review of Physical Chemistry*, vol. 59, n° 1, p. 659-683, 2008.
- [86] O. Louisnard et J. González-García, « Acoustic Cavitation », in *Ultrasound Technologies for Food and Bioprocessing*, H. Feng, G. Barbosa-Canovas, et J. Weiss, Éd. Springer New York, 2011, p. 13-64.

- [87] F. R. Gilmore, « The growth or collapse of a spherical bubble in a viscous compressible liquid », California Institute of Technology, Pasadena, CA., 01-avr-1952.
- [88] Y. Saito et K. Sato, « Bubble Collapse Propagation and Pressure Wave at Periodic Cloud Cavitation », in *ICMF*, Leipzig, Germany, 2007.
- [89] T. Hibiki et M. Ishi, « Interfacial area transport of air-water bubbly flow in vertical round tubes », presented at the 33rd Nat. Heat Transfer Conf, Albuquerque, New Mexico, 1999.
- [90] E. Giannadakis, M. Gavaises, et C. Arcoumanis, « Modelling of cavitation in diesel injector nozzles », *Journal of Fluid Mechanics*, vol. 616, p. 153, nov. 2008.
- [91] C. MARTÍNEZ-BAZÁN, J. L. Montanes, et J. C. Lasheras, « On the breakup of an air bubble injected into a fully developed turbulent flow. Part 1. Breakup frequency », *Journal of Fluid Mechanics*, vol. 401, n° 1, p. 157-182, 1999.
- [92] ANSYS, Inc., *ANSYS CFX-Solver Theory Guide*. Canonsburg, PA: .
- [93] C.-Y. Li et S. L. Ceccio, « Interaction of single travelling bubbles with the boundary layer and attached cavitation », *Journal of Fluid Mechanics*, vol. 322, p. 329-353, 1996.
- [94] C. A. Fattor, M. C. Lopardo, J. M. Casado, et R. A. Lopardo, « Cavitation by macroturbulent pressure fluctuations in hydraulic jump stilling basins », in *International Association for Hydro-Environment Engineering and Research Congress*, Beijing, China, 2001.
- [95] S. B. Martynov, D. J. Mason, et M. R. Heikal, « Numerical Simulation of Cavitation Flows Based on Their Hydrodynamic Similarity », *International Journal of Engine Research*, vol. 7, n° 3, p. 283-296, 2006.
- [96] R. S. R. Gorla et A. A. Khan, *Turbomachinery: Design and Theory*. CRC Press, 2003.
- [97] S. H. Winoto, D. A. Shah, et H. Liu, « Estimation of turbulent shear stress in free jets: application to valvular regurgitation », *Ann Biomed Eng*, vol. 24, n° 2, p. 321-327, avr. 1996.
- [98] S. Douady, Y. Couder, et M. E. Brachet, « Direct observation of the intermittency of intense vorticity filaments in turbulence », *Phys. Rev. Lett.*, vol. 67, n° 8, p. 983-986, 1991.
- [99] O. Métais et M. Lesieur, « Spectral large-eddy simulation of isotropic and stably stratified turbulence », *Journal of Fluid Mechanics*, vol. 239, p. 157-194, 1992.
- [100] K. K. Ooi, « Scale effects on cavitation inception in submerged jets », Ph. D., California Institute of Technology, 1982.
- [101] P. Ausoni, M. Farhat, X. Escaler, E. Egusquiza, et F. Avellan, « Cavitation Influence on von Kármán Vortex Shedding and Induced Hydrofoil Vibrations », *Journal of Fluids Engineering*, vol. 129, n° 8, p. 966, 2007.
- [102] M. S. Plesset et R. B. Chapman, « Collapse of an initially spherical vapour cavity in the neighbourhood of a solid boundary », *Journal of Fluid Mechanics*, vol. 47, n° 02, p. 283-290, 1971.
- [103] R. S. Kulp et J. V. Altieri, « Cavitation Damage of Mechanical Pump Impellers Operating in Liquid Metal Space Power Loops », juill. 1965.
- [104] W. Lee et J. A. Hoopes, « Prediction of Cavitation Damage for Spillways », *Journal of Hydraulic Engineering*, vol. 122, n° 9, p. 481-488, sept. 1996.
- [105] M. ČDINA, « Detection of cavitation phenomenon in a centrifugal pump using audible sound », *Mechanical Systems and Signal Processing*, vol. 17, n° 6, p. 1335-1347, nov. 2003.
- [106] R. E. A. Arndt, G. J. Balas, et M. Wosnik, « Control of Cavitating Flows: A Perspective », *JSME International Journal Series B Fluids and Thermal Engineering*, vol. 48, n° 2, p. 334-341, 2005.
- [107] W. H. Nurick, « Orifice cavitation and its effect on spray mixing », *Journal of Fluid Engineering*, vol. 98, p. 681-689, 1976.
- [108] C. Soteriou, R. Andrews, et M. Smith, « Direct Injection Diesel Sprays and the Effect of Cavitation and Hydraulic Flip on Atomization », SAE International, Warrendale, PA, 950080, févr. 1995.
- [109] D. P. Schmidt et M. L. Corradini, « The internal flow of diesel fuel injector nozzles: A review », *International Journal of Engine Research*, vol. 2, n° 1, p. 1-22, févr. 2001.
- [110] C. E. Brennen, *Hydrodynamics of Pumps*. Oxford University Press, USA, 1995.
- [111] M. Bailey, V. Khokhlova, O. Sapozhnikov, S. Kargl, et L. Crum, « Physical mechanisms of the therapeutic effect of ultrasound (a review) », *Acoustical Physics*, vol. 49, n° 4, p. 369-388, 2003.
- [112] C. Chaussy, W. Brendel, et E. Schmiedt, « Extracorporeally induced destruction of kidney stones by shock waves », *The Lancet*, vol. 316, n° 8207, p. 1265-1268, déc. 1980.
- [113] S. Amy, « An environmentally friendly tool for the textile industry », *Agricultural Research*, vol. 51, n° 2, p. 10, 2003.
- [114] A. Spillman, « An environmentally friendly tool for the textile industry. (Ultrasound). », *Agricultural Research*, janv. 2003.

- [115] A. G. Chakinala, P. R. Gogate, A. E. Burgess, et D. H. Bremner, « Treatment of industrial wastewater effluents using hydrodynamic cavitation and the advanced Fenton process », *Ultrasonics Sonochemistry*, vol. 15, n° 1, p. 49-54, janv. 2008.
- [116] N. Perrone et R. Kao, « A general finite difference method for arbitrary meshes », *Computers & Structures*, vol. 5, n° 1, p. 45-57, avr. 1975.
- [117] I. Information Systems Laboratories, « RELAP5/MOD3.3 code manual », in *RELAP5*, vol. I, Rockville, Maryland: U.S. Nuclear Regulatory Commission, 2003.
- [118] J. H. Ferziger et M. Peric, *Computational Methods for Fluid Dynamics*, 3rd ed. Springer Berlin Heidelberg, 2010.
- [119] H. Jasak, « Error analysis and estimation for the finite volume method with applications to fluid flows », PhD, University of London, London, 1996.
- [120] M. Peric, « A finite volume method for the prediction of three-dimensional fluid flow in complex ducts », PhD, University of London, London, 1985.
- [121] H. Mase, K. Oki, T. S. Hedges, et H. J. Li, « Extended energy-balance-equation wave model for multidirectional random wave transformation », *Ocean Engineering*, vol. 32, n° 8-9, p. 961-985, juin 2005.
- [122] F. Badrot-Nico, F. Brissaud, et V. Guinot, « A finite volume upwind scheme for the solution of the linear advection–diffusion equation with sharp gradients in multiple dimensions », *Advances in Water Resources*, vol. 30, n° 9, p. 2002-2025, sept. 2007.
- [123] A. Jameson, W. Schmidt, et E. Turkel, « Numerical solution of the Euler equations by finite volume methods using Runge Kutta time stepping schemes », in *AIAA, Fluid and Plasma Dynamics Conference, 14th, Palo Alto, CA, June 23-25, 1981. 15 p.*, 1981, vol. -1.
- [124] S. Patankar, *Numerical Heat Transfer and Fluid Flow*. Taylor & Francis, 1980.
- [125] A. Prosperetti et G. Tryggvason, Éd., *Computational Methods for Multiphase Flow*, 1^{re} éd. Cambridge University Press, 2007.
- [126] L. S. de B. Alves, « Review of numerical methods for the compressible flow equations at low Mach numbers », Instituto militar de engenharia, CNPq 480599/2007.
- [127] ANSYS, Inc., *ANSYS Fluent Theory Guide*. Canonsburg, PA: , 2009.
- [128] J. Franke, A. Hellsten, K. H. Schlunzen, et B. Carissimo, « The COST 732 Best Practice Guideline for CFD simulation of flows in the urban environment: a summary », *International Journal of Environment and Pollution*, vol. 44, n° 1-4, p. 419-427, 2011.
- [129] CD-adapco, *Methodology STAR-CD*. 2009.
- [130] S. P. Sutera et R. Skalak, « The History of Poiseuille's Law », *Annual Review of Fluid Mechanics*, vol. 25, n° 1, p. 1-20, janv. 1993.
- [131] O. Giustolisi, L. Berardi, et T. M. Walski, « Some explicit formulations of Colebrook–White friction factor considering accuracy vs. computational speed », *Journal of Hydroinformatics*, vol. 13, n° 3, p. 401, juill. 2011.
- [132] A. E. Lawrence, « A Note on the Prandtl-Taylor Equation », *Ind. Eng. Chem.*, vol. 24, n° 11, p. 1318-1321, 1932.
- [133] J. Zierep et K. Bühler, *Grundzüge der Strömungslehre: Grundlagen, Statik und Dynamik der Fluide*. Vieweg+Teubner Verlag, 2010.
- [134] B. Baldwin et H. Lomax, « Thin-layer approximation and algebraic model for separated turbulent flows », *American Institute of Aeronautics and Astronautics*, 1978.
- [135] D. R. Apostolis, *Cebeci-Smith Model*. DIC Press, 2012.
- [136] P. Spalart et S. Allmaras, « A one-equation turbulence model for aerodynamic flows », *AIAA-Paper 92-0439*.
- [137] W. P. Jones et B. E. Launder, « The prediction of laminarization with a two-equation model of turbulence », *International Journal of Heat and Mass Transfer*, vol. 15, n° 2, p. 301-314, févr. 1972.
- [138] D. C. Wilcox, « Reassessment of the scale-determining equation for advanced turbulence models », *AIAA Journal*, vol. 26, n° 11, p. 1299-1310, nov. 1988.
- [139] A. J. Reynolds, « The prediction of turbulent Prandtl and Schmidt numbers », *International Journal of Heat and Mass Transfer*, vol. 18, n° 9, p. 1055-1069, sept. 1975.
- [140] R. Bourguet, M. Braza, R. Perrin, et G. Harran, « Physical Analysis of an Anisotropic Eddy-Viscosity Concept for Strongly Detached Turbulent Unsteady Flows », in *IUTAM Symposium on Unsteady Separated Flows and their Control*, vol. 14, M. Braza et K. Hourigan, Éd. Springer Netherlands, 2009, p. 381-393.
- [141] K. Hanjalić et S. Jakirlić, « Contribution towards the second-moment closure modelling of separating turbulent flows », *Computers & Fluids*, vol. 27, n° 2, p. 137-156, févr. 1998.
- [142] F. Menter, « Zonal two-equation k-omega turbulence models for aerodynamic flows », *AIAA Journal*, p. 2906, 1993.

- [143] M. Ilıcak, T. M. Özgökmen, H. Peters, H. Z. Baumert, et M. Iskandarani, « Very large eddy simulation of the Red Sea overflow », *Ocean Modelling*, vol. 20, n° 2, p. 183-206, 2008.
- [144] M. Labois et D. Lakehal, « Very-Large Eddy Simulation (V-LES) of the flow across a tube bundle », *Nuclear Engineering and Design*, vol. 241, n° 6, p. 2075-2085, juin 2011.
- [145] W. P. Jones et S. Navarro-Martinez, « Numerical Study of n-Heptane Auto-ignition Using LES-PDF Methods », *Flow Turbulence and Combustion*, vol. 83, n° 3, p. 407-423, 2009.
- [146] F. F. Grinstein et C. Fureby, « On Monotonically Integrated Large Eddy Simulation of Turbulent Flows Based on FCT Algorithms », in *Flux-Corrected Transport*, D. Kuzmin, R. Löhner, et S. Turek, Éd. Springer Berlin Heidelberg, 2005, p. 79-104.
- [147] J. Smagorinsky, « General circulation experiments with the primitive equations », *Monthly Weather Review*, vol. 91, n° 3, p. 99-164, mars 1963.
- [148] T. E. Tezduyar, « Interface-tracking and interface-capturing techniques for finite element computation of moving boundaries and interfaces », *Computer Methods in Applied Mechanics and Engineering*, vol. 195, n° 23-24, p. 2983-3000, avr. 2006.
- [149] D. Fuster, A. Bagué, T. Boeck, L. Le Moyne, A. Leboissetier, S. Popinet, P. Ray, R. Scardovelli, et S. Zaleski, « Simulation of primary atomization with an octree adaptive mesh refinement and VOF method », *International Journal of Multiphase Flow*, vol. 35, n° 6, p. 550-565, juin 2009.
- [150] M. Ishii, « Thermo-fluid dynamic theory of two-phase flow », *NASA STI/Recon Technical Report A*, vol. 75, p. 29657, 1975.
- [151] A. Prosperetti, « Some considerations on the modeling of disperse multiphase flows by averaged equations », *JSME international journal. Series B, fluids and thermal engineering*, vol. 42, n° 4, p. 573-585, 1999.
- [152] W. P. Jones et V. N. Prasad, « Large Eddy Simulation of the Sandia Flame Series (D-F) using the Eulerian stochastic field method », *Combustion and Flame*, vol. 157, n° 9, p. 1621-1636, 2010.
- [153] G. B. Wallis, *One-dimensional two-phase flow*. McGraw-Hill, 1969.
- [154] D. Bestion, « The physical closure laws in the CATHARE code », *Nuclear Engineering and Design*, vol. 124, n° 3, p. 229-245, déc. 1990.
- [155] M. Wein, « Numerische Simulation von kritischen und nahkritischen Zweiphasenströmungen mit thermischen und fluiddynamischen Nichtgleichgewichtseffekten », Technische Universität Dresden, Maschinenwesen, 2002.
- [156] J. Riznic, M. Ishii, et N. Afgan, « A void distribution model-flashing flow », presented at the International seminar on transient phenomena in multiphase flow, Belgrade, Yugoslavia, 1987.
- [157] T. S. Shin et O. C. Jones, « Nucleation and flashing in nozzles—1. A distributed nucleation model », *International Journal of Multiphase Flow*, vol. 19, n° 6, p. 943-964, déc. 1993.
- [158] V. N. Blinkov, O. C. Jones, et B. I. Nigmatulin, « Nucleation and flashing in nozzles—2. Comparison with experiments using a five-equation model for vapor void development », *International Journal of Multiphase Flow*, vol. 19, n° 6, p. 965-986, déc. 1993.
- [159] R. Balasubramaniam et NASA Glenn Research Center, « Two phase flow modeling summary of flow regimes and pressure drop correlations in reduced and partial gravity », 2006.
- [160] S. Jolk et Á. Pérez-Salado, « Stationäre kritische Zweiphasen-Ausströmung von Wasser: Bewertung von Experimenten und Modellen + Datenbasis », AREVA, Offenbach, F+E Bericht PEPA-G/2010/de/0011, 2010.
- [161] I. Information Systems Laboratories, « RELAP5/MOD3.3 code manual », in *RELAP5*, vol. 4, Rockville, Maryland: U.S. Nuclear Regulatory Commission, 2003.
- [162] D. Hill, « The Computer Simulation of Dispersed Two Phase Flows », University of London, London, 1998.
- [163] L. Schneider, « A Concise Moment Method for Unsteady Polydisperse Sprays », Technical university of Darmstadt, 2009.
- [164] A. . Chesters, « Source terms for drop coalescence and break-up in the transport equation for intensity of dispersion », Brite-Euram project RII B.0085.UK I-36, juill. 1987.
- [165] R. McGraw, « Description of Aerosol Dynamics by the Quadrature Method of Moments », *Aerosol Science and Technology*, vol. 27, n° 2, p. 255-265, janv. 1997.
- [166] D. L. Marchisio et R. O. Fox, « Solution of population balance equations using the direct quadrature method of moments », *Journal of Aerosol Science*, vol. 36, n° 1, p. 43-73, janv. 2005.
- [167] D.-F. Choi, « Simulation von Mehrphasenströmungen mit einer Multi-Fluid-Methode », Ph. D., TU Darmstadt, Darmstadt, 2010.

- [168] R. Fan, D. L. Marchisio, et R. O. Fox, « Application of the direct quadrature method of moments to polydisperse gas–solid fluidized beds », *Powder Technology*, vol. 139, n° 1, p. 7-20, janv. 2004.
- [169] J. Madsen, « Computational and experimental study of sprays from the breakup of water sheets », PhD, Aalborg University Esbjerg, Denmark, 2006.
- [170] T. G. Leighton, « Derivation of the Rayleigh-Plesset equation in terms of volume », Institute of sound and vibration research, University of Southampton, Southampton, 2007.
- [171] A. Kubota, H. Kato, et H. Yamaguchi, « A new modelling of cavitating flows: a numerical study of unsteady cavitation on a hydrofoil section », *Journal of Fluid Mechanics*, vol. 240, p. 59-96, 1992.
- [172] E. Giannadakis, D. Papoulias, M. Gavaises, C. Arcoumanis, C. Soteriou, et W. Tang, « Evaluation of the Predictive Capability of Diesel Nozzle Cavitation Models », SAE International, Warrendale, PA, 2007-01-0245, avr. 2007.
- [173] K. J. Farrell, « Eulerian/Lagrangian Analysis for the Prediction of Cavitation Inception », in *Fourth international symposium on cavitation*, Pasadena, CA, 2001.
- [174] J. O. Hinze, *Turbulence*. McGraw-Hill, 1975.
- [175] M. Garcia, Y. Sommerer, T. Schönfeld, et T. Poinso, « Evaluation of Euler/Euler and Euler/Lagrange strategies for large-eddy simulations of turbulent reacting flows », presented at the ECCOMAS Thematic Conference on Computational Combustion, Lisbon, Portugal, 2005.
- [176] M. Garcia, Y. Sommerer, et T. Poinso, « Assessment of Euler-Euler and Euler-Lagrange strategies for reactive large-eddy-simulation », in *1st Workshop INCA*, 2005, p. 65-74.
- [177] D. I. Graham et R. A. Moeed, « How many particles for my Lagrangian simulations? », *Powder Technology*, vol. 125, n° 2-3, p. 179-186, juin 2002.
- [178] F. Durst, D. Milojevic, et B. Schönung, « Eulerian and Lagrangian predictions of particulate two-phase flows: a numerical study », *Applied Mathematical Modelling*, vol. 8, n° 2, p. 101-115, avr. 1984.
- [179] E. Goncalves et R. F. Patella, « Numerical simulation of cavitating flows with homogeneous models », *Computers & Fluids*, vol. 38, n° 9, p. 1682-1696, oct. 2009.
- [180] S. Hickel, M. Mihatsch, et S. Schmidt, « Implicit Large Eddy Simulation of Cavitation in Micro Channel Flows », in *WIMRC*, University of Warwick, 2011.
- [181] J. Sauer, G. Winkler, et G. H. Schnerr, « Kavitation und Kondensation – Physikalische Modellbildung und numerische Umsetzung », *Chemie Ingenieur Technik*, vol. 71, n° 12, p. 1399–1402, 1999.
- [182] A. Alajbegovic, G. Meister, D. Greif, et B. Basara, « Three phase cavitating flows in high-pressure swirl injectors », *Experimental Thermal and Fluid Science*, vol. 26, n° 6-7, p. 677-681, août 2002.
- [183] T. Xing et S. H. Frankel, « Effect of Cavitation on Vortex Dynamics in a Submerged Laminar Jet », *AIAA Journal*, vol. 40, n° 11, p. 2266-2276, nov. 2002.
- [184] R. Bannari, « Cavitation modelling based on Eulerian-Eulerian multiphase flow », PhD, Université de Sherbrooke, Canada, 2011.
- [185] A. Papoulis, *Probability, random variables, and stochastic processes*. McGraw-Hill, 1965.
- [186] J.-P. Minier et E. Peirano, « The pdf approach to turbulent polydispersed two-phase flows », *Physics Reports*, vol. 352, n° 1-3, p. 1-214, oct. 2001.
- [187] R. Mahnke, J. Kaupuzs, et I. Lubashevsky, « Probabilistic description of traffic flow », *Physics Reports*, vol. 408, n° 1-2, p. 1-130, mars 2005.
- [188] L. Arnold, *Stochastische Differentialgleichungen: Theorie u. Anwendung*. Oldenbourg, 1973.
- [189] S. B. Pope, *Turbulent Flows*. Cambridge University Press, 2000.
- [190] C. W. Gardiner, *Handbook of stochastic methods for physics, chemistry, and the natural sciences*. Springer-Verlag, 1985.
- [191] D. J. Thomson, « Criteria for the selection of stochastic models of particle trajectories in turbulent flows », *Journal of Fluid Mechanics*, vol. 180, p. 529-556, 1987.
- [192] B. L. Sawford, « Reynolds number effects in Lagrangian stochastic models of turbulent dispersion », *Physics of Fluids A: Fluid Dynamics*, vol. 3, n° 6, p. 1577-1586, juin 1991.
- [193] D. C. Haworth, « Progress in probability density function methods for turbulent reacting flows », *Progress in Energy and Combustion Science*, vol. 36, n° 2, p. 168-259, avr. 2010.
- [194] S. Lipp et U. Maas, « Simulations of Premixed Swirling Flames Using a Hybrid Finite-Volume/Transported PDF Approach », in *High Performance Computing in Science and Engineering '07*, W. E. Nagel, D. Kröner, et M. Resch, Éd. Springer Berlin Heidelberg, 2008, p. 215-227.
- [195] R. O. Fox, *Computational Models for Turbulent Reacting Flows*. Cambridge University Press, 2003.

- [196] S. B. POPE, « A Monte Carlo Method for the PDF Equations of Turbulent Reactive Flow », *Combustion Science and Technology*, vol. 25, n° 5-6, p. 159-174, 1981.
- [197] J. M. Papakonstantinou, « A historical development of the (n+1)-point secant method », M. A. Thesis, Rice University, 2007.
- [198] J. H. Bell, S. U. J. I. for A. and Acoustics, R. D. Mehta, A. R. Center, et U. S. N. A. and S. Administration, *Contraction design for small low speed wind tunnels*. National Aeronautics and Space Administration, 1988.
- [199] J. Dumond et J.-P. Schäfer, « Specification of the passive outflow reducer tests at the technical center Karlstein », AREVA, Offenbach, NESB-G/2009/en/1245, 2009.
- [200] F. Maisberger, « Test results of the KERENA Passive Outflow Reducer (POR) experiments », AREVA, Karlstein, Internal PTCTC-G/2012/en/0042, 2012.
- [201] I. Cremer et M. Lorenz, « Private communication ».
- [202] R. F. Kunz, D. A. Boger, D. R. Stinebring, T. S. Chyczewski, J. W. Lindau, H. J. Gibeling, S. Venkateswaran, et T. R. Govindan, « A preconditioned Navier–Stokes method for two-phase flows with application to cavitation prediction », *Computers & Fluids*, vol. 29, n° 8, p. 849-875, août 2000.
- [203] Yuan W., Sauer J., et Schnerr G.H., « Modeling and computation of unsteady cavitation flows in injection nozzles », *Mecanique & Industries*, vol. 2, n° 5, p. 383-394, 2001.
- [204] A. K. Singhal, M. M. Athavale, H. Li, et Y. Jiang, « Mathematical Basis and Validation of the Full Cavitation Model », *Journal of Fluids Engineering*, vol. 124, n° 3, p. 617, 2002.
- [205] W. P. Jones et V. N. Prasad, « Large Eddy Simulation of a piloted methane jet flame with high levels of extinction (Sandia Flame E) using the Eulerian stochastic field method », *Proceeding of the European Combustion Meeting*, 2009.
- [206] T. Barberon et P. Helluy, « Finite volume simulation of cavitating flows », *Computers & Fluids*, vol. 34, n° 7, p. 832-858, août 2005.
- [207] S. Clerc, « Numerical Simulation of the Homogeneous Equilibrium Model for Two-Phase Flows », *Jurnal of Computational Physics*, vol. 161, n° 1, p. 354-375, juin 2000.
- [208] O. Coutier-Delgosha, J. L. Reboud, et Y. Delannoy, « Numerical simulation of the unsteady behaviour of cavitating flows », *International Journal for Numerical Methods in Fluids*, vol. 42, n° 5, p. 527–548, 2003.
- [209] T. G. Liu, B. C. Khoo, et W. F. Xie, « Isentropic one-fluid modelling of unsteady cavitating flow », *Journal of Computational Physics*, vol. 201, n° 1, p. 80-108, nov. 2004.
- [210] Iben, F. Wrona, C. D. Munz, et M. Beck, « Cavitation in Hydraulic Tools Based on Thermodynamic Properties of Liquid and Gas », *Journal of Fluids Engineering*, vol. 124, n° December, p. 1011-1017, 2002.
- [211] J. Wu, G. Wang, et W. Shyy, « Time-dependent turbulent cavitating flow computations with interfacial transport and filter-based models », *International Journal for Numerical Methods in Fluids*, vol. 49, n° 7, p. 739-761, nov. 2005.
- [212] A. Murrone et H. Guillard, « A five equation reduced model for compressible two phase flow problems », *Journal of Computational Physics*, vol. 202, n° 2, p. 664-698, janv. 2005.
- [213] Lord Rayleigh, « On the pressure developed in a liquid during the collapse of a spherical cavity », *Phil. Mag.*, vol. 34, août 1917.
- [214] Y. Saito, R. Takami, I. Nakamori, et T. Ikhagi, « Numerical analysis of unsteady behavior of cloud cavitation around a NACA0015 foil », *Computational Mechanics*, vol. 40, n° 1, p. 85-96, 2007.
- [215] W. J. Garland et B. J. Hand, « Simple functions for the fast approximation of light water thermodynamic properties », *Nuclear Engineering and Design*, vol. 113, n° 1, p. 21-34, avr. 1989.
- [216] R. Schulz, *Entwicklung eines numerischen Verfahrens zur Simulation von Wolkenkavitation*. VDI-Verlag, 1995.
- [217] R. Friedrich, B. Geurts, et O. Métais, *Direct and Large-Eddy Simulation V*. Springer, 2004.
- [218] D. Fuster et T. Colonius, « Modelling bubble clusters in compressible liquids », *Journal of Fluid Mechanics*, vol. 688, p. 352-389, 2011.
- [219] D. Z. Zhang et A. Prosperetti, « Momentum and energy equations for disperse two-phase flows and their closure for dilute suspensions », *International Journal of Multiphase Flow*, vol. 23, n° 3, p. 425-453, juin 1997.
- [220] S. Barre, J. Rolland, G. Boitel, E. Goncalves, et R. F. Patella, « Experiments and modeling of cavitating flows in venturi: attached sheet cavitation », *European Journal of Mechanics - B/Fluids*, vol. 28, n° 3, p. 444-464, mai 2009.
- [221] B. R. Shin, S. Yamamoto, et X. Yuan, « Application of preconditioning method to gas-liquid two-phase flow computations », *Journal of Fluids Engineering*, p. 605/612, juill-2004.
- [222] Y. Delannoy et J. L. Kueny, « Two-phase flow approach in unsteady cavitation modelling », in *Cavitation and multiphase flow forum*, 1990, vol. 98, p. 153-158.

- [223] N. El Gharbi, R. Absi, et A. Benzaoui, « Numerical investigation toward improving heat-transfer predictions in a turbulent channel flow », *International Journal of Thermal Sciences*, 2011.
- [224] B. Stutz et J.-L. Reboud, « Measurements within unsteady cavitation », *Experiments in Fluids*, vol. 29, n° 6, p. 545-552, 2000.
- [225] J. C. R. Hunt, « Vorticity and vortex dynamics in complex turbulent flows », in *Canadian Society for Mechanical Engineering, Transactions (ISSN 0315-8977)*, vol. 11, no. 1, 1987, p. 21-35., 1987, vol. 11, p. 21-35.
- [226] A. Tomiyama, « Struggle with computational bubble dynamics », in *ICMF'98*, Lyon, 1998.
- [227] D. Lucas, E. Krepper, et H.-M. Prasser, « Use of models for lift, wall and turbulent dispersion forces acting on bubbles for poly-disperse flows », *Chemical Engineering Science*, vol. 62, n° 15, p. 4146-4157, août 2007.
- [228] A. Tomiyama, H. Tamai, I. Zun, et S. Hosokawa, « Transverse migration of single bubbles in simple shear flows », *Chemical Engineering Science*, vol. 57, n° 11, p. 1849-1858, juin 2002.

Appendix A: Forces acting on bubbles dispersed in a liquid phase.

- The drag force originates from viscous effects, surface tension and the difference between the velocities \mathbf{u}_l and \mathbf{u}_g of the continuous and dispersed phases, respectively:

$$\mathbf{F}_D = \frac{1}{2} C_D \rho_l \pi R^2 (\mathbf{u}_l - \mathbf{u}_g) |\mathbf{u}_l - \mathbf{u}_g|; \quad (\text{A.1})$$

where ρ_l is the density of the fluid, R is the radius of the bubble and C_D is a drag force coefficient. Several correlations exist for C_D . For example,

[226]:

$$C_D = \max \left[\frac{24}{\text{Re}_b} (1 + 0.15 \text{Re}_b^{0.687}), \frac{8}{3} \frac{Eo}{Eo + 4} \right]; \quad (\text{A.2})$$

with

$$Eo = \frac{g (\rho_l - \rho_g) D_b^2}{\sigma}; \quad (\text{A.3})$$

D_b bubble diameter and Re_b the Reynolds number expressed with bubble diameter.

[90]:

$$\text{if } 0 \leq \text{Re}_b \leq 5 \quad C_{D, \text{no void}} = \frac{16}{\text{Re}_b} (1 + 0.1 \text{Re}_b) - 0.02 \text{Re}_b \ln(\text{Re}_b); \quad (\text{A.4})$$

$$\text{if } 5 < \text{Re}_b \leq 1000 \quad C_{D, \text{no void}} = \frac{48}{\text{Re}_b} \left(1 + \frac{2.21}{\sqrt{\text{Re}_b}} - \frac{2.14}{\text{Re}_b} \right); \quad (\text{A.5})$$

else

$$C_D = C_{D, \text{no void}} \left(e^{3.64(1-\alpha_l)} + (1-\alpha_l)^{0.864} \right). \quad (\text{A.6})$$

[110]:

$$\mathbf{F}_D = 6 \nu_l \rho_l \pi R (\mathbf{u}_l - \mathbf{u}_b) \left(1 + \frac{\text{Re}_b^{2/3}}{6} \right). \quad (\text{A.7})$$

- When a bubble moves, it must also displace a mass of water which opposes a resistance to its motion. This force is the added mass force. Common expressions for the added mass force are:

[90]:

$$\mathbf{F}_A = \frac{D}{Dt} \left(C_{am} \rho_l \frac{4}{3} \pi R^3 (\mathbf{u}_l - \mathbf{u}_b) \right); \quad (\text{A.8})$$

with

$$C_{am} = \frac{1}{2} (1 + 2.78(1-\alpha_l)); \quad (\text{A.9})$$

or [173]:

$$\mathbf{F}_A = \frac{1}{2} \rho_l \frac{4}{3} \pi R^3 \frac{d\mathbf{u}_b}{dt}. \quad (\text{A.10})$$

- Buoyancy is due to the density difference existing between the phases.

[173]:

$$\mathbf{F}_B = -\rho_l \frac{4}{3} \pi R^3 \mathbf{g}; \quad (\text{A.11})$$

[227]:

$$\mathbf{F}_B = -(\rho_l - \rho_g) \frac{4}{3} \pi R^3 \mathbf{g}. \quad (\text{A.12})$$

- Pressure acts on the surface of the bubble and accelerates it in the direction of the pressure gradient:

[90]:

$$\mathbf{F}_p = -\frac{4}{3}\pi R^3 \nabla p ; \quad (\text{A.13})$$

[173]:

$$\mathbf{F}_p = -\frac{3}{2}\rho_l \frac{4}{3}\pi R^3 \nabla p . \quad (\text{A.14})$$

▪ History force

[173]:

$$\mathbf{F}_H = 6R^2 \sqrt{\pi\rho_l\eta} \int_{t_0}^t \frac{d(\mathbf{u}_l - \mathbf{u}_b)/d\tau}{\sqrt{t-\tau}} d\tau . \quad (\text{A.15})$$

▪ Volume variation

[173]:

$$\mathbf{F}_v = \rho_l 2\pi R^2 (\mathbf{u}_l - \mathbf{u}_b) \frac{dR}{dt} . \quad (\text{A.16})$$

▪ Lift

[228]:

$$\mathbf{F}_L = -C_{LF} \rho_l \frac{\pi D_b^3}{6} (\mathbf{u}_b - \mathbf{u}_l) \times \text{rot } \mathbf{u}_l ; \quad (\text{A.17})$$

and C_{LF} ranging from 0.25 to .3.

▪ Marangoni effect

[110] :

$$\mathbf{F}_{Ma} = -2\pi R^2 \frac{d\sigma}{dx_1} . \quad (\text{A.18})$$

▪ Turbulent dispersion force

[92] :

$$\mathbf{F}_d^{TD} = -C_{TD} (=1) C_D \frac{\nu_{lc}}{\sigma_{lc}} \left(\frac{\nabla \alpha_d}{\alpha_d} - \frac{\nabla \alpha_c}{\alpha_c} \right) . \quad (\text{A.19})$$

In the proximity of the wall, two supplementary forces act on the bubbles.

▪ Wall lubrication force

[92]:

$$\mathbf{F}_{WL,b} = -\frac{\alpha\rho_c}{R} (\mathbf{u}_r - (\mathbf{u}_r \cdot \mathbf{n}_w) \mathbf{n}_w)^2 \max \left(C_{WL_1} + C_{WL_2} \frac{D_b}{y_w}, 0 \right) \mathbf{n}_w ; \quad (\text{A.20})$$

y_w being distance to the wall and C_{WL_1}, C_{WL_2} model constants.

▪ Wall deformation force

[227]:

$$\mathbf{F}_{WD} = 2\sigma \frac{dA_b}{dD_H} ; \quad (\text{A.21})$$

with

$$A_b = 2\pi D_V^2 \left(1 + \left(\frac{D_H}{D_V} \right)^2 \frac{\text{arctanh}(\varepsilon)}{\varepsilon} \right) ; \quad (\text{A.22})$$

and

$$\varepsilon = \sqrt{1 - \left(\frac{D_H}{D_V} \right)^2} . \quad (\text{A.23})$$

Appendix B: Definition and properties of stochastic process

Definition and properties

The definitions and properties described in this appendix are taken from [185] to a large extent.

Random variable

Mathematically, a random variable is defined according to an experiment \mathcal{E} whose outcomes ξ are various objects belonging to the certain event \mathcal{G} . \mathcal{F} is the field of subsets of \mathcal{G} called events. One can assign the probability P to these events. To every ξ , a number $\tilde{\mathbf{x}}(\xi)$ is assigned according to some rule. Thus, the function $\tilde{\mathbf{x}}$ is defined over the domain \mathcal{G} of all outcomes and its range is a set of numbers.

This function $\tilde{\mathbf{x}}$ is called a random variable when it satisfies:

- 1- The set $\{\tilde{\mathbf{x}} \leq x\}$ is an event for any real number x and
- 2- The probability of the events $\{\tilde{\mathbf{x}} = +\infty\}$ and $\{\tilde{\mathbf{x}} = -\infty\}$ equals zero:

$$P\{\tilde{\mathbf{x}} = +\infty\} = P\{\tilde{\mathbf{x}} = -\infty\} = 0. \quad (\text{B.1})$$

In these expressions, the notation $\{\tilde{\mathbf{x}} \leq x\}$ represents a set consisting of all outcomes ξ such that:

$$\tilde{\mathbf{x}}(\xi) \leq x. \quad (\text{B.2})$$

Distribution and density function

Distribution function

Definition

The probability of the set $\{\tilde{\mathbf{x}} \leq x\}$ is also called the distribution function and denoted by:

$$F_{\tilde{\mathbf{x}}}(x) \quad (\text{B.3})$$

or simply $F(x)$ when there is no risk of confusion. By definition, the distribution function satisfies:

$$F(-\infty) = 0; \quad (\text{B.4})$$

$$F(+\infty) = 1; \quad (\text{B.5})$$

$$F(R_1) \leq F(R_2) \text{ for } R_1 < R_2; \quad (\text{B.6})$$

$$F(R^+) = F(R). \quad (\text{B.7})$$

The last expression indicates that the distribution function is continuous from the right.

Experimental determination

Practically, to estimate the distribution function, an experiment is performed \tilde{N} times. For each outcome ξ , the value of $\tilde{\mathbf{x}}(\xi)$ is calculated according to the assigned rule. The number of trials such that $\tilde{\mathbf{x}}(\xi) \leq x$ is \tilde{N}_x . Then the distribution function is estimated as:

$$F(x) = P\{\tilde{\mathbf{x}} \leq x\} \approx \frac{\tilde{N}_x}{\tilde{N}}. \quad (\text{B.8})$$

Density function

Definition

The derivative $f_{\tilde{\mathbf{x}}}$ of $F_{\tilde{\mathbf{x}}}(x)$:

$$f_{\tilde{\mathbf{x}}}(x) = \frac{dF_{\tilde{\mathbf{x}}}(x)}{dx}, \quad (\text{B.9})$$

or simply $f(x) = \frac{dF(x)}{dx}$, is called the probability density function (pdf). It possesses following characteristics:

$$\int_{-\infty}^{+\infty} f(x)dx = 1; \quad (\text{B.10})$$

$$\forall x, f(x) \geq 0. \quad (\text{B.11})$$

By definition, $f(x)dx$ represents the probability of the set consisting of all outcomes ξ such that:

$$x \leq \mathbf{x}(\xi) \leq x + dx \quad (\text{B.12})$$

for $dx \rightarrow 0$ since

$$f(x)dx = dF|_x = F(x+dx) - F(x) = P\{\mathbf{x} \leq x+dx\} - P\{\mathbf{x} \leq x\} = P\{x \leq \mathbf{x} \leq x+dx\}. \quad (\text{B.13})$$

Experimental determination

The density function is determined by the number of trials $\Delta\tilde{N}_x$ such that $x \leq \tilde{\mathbf{x}}(\xi) \leq x + \Delta x$:

$$f(x) = P\{x \leq \tilde{\mathbf{x}} \leq x + \Delta x\} \approx \frac{\Delta\tilde{N}_x}{\tilde{N}}; \quad (\text{B.14})$$

when \tilde{N} is sufficiently large and Δx is sufficiently small.

Expectation value

Definition

The expectation value $E[\tilde{\mathbf{x}}]$ (or $\langle \tilde{\mathbf{x}} \rangle$) of $\tilde{\mathbf{x}}$ (also called mean value) can be expressed with its pdf $f(x)$ as:

$$E[\tilde{\mathbf{x}}] = \int_{-\infty}^{+\infty} x f(x)dx. \quad (\text{B.15})$$

Experimental determination

Considering our experiment, the outcomes of the \tilde{N} trials is:

$$\xi_1, \xi_2, \dots, \xi_{\tilde{N}}.$$

Correspondingly, the random variable $\tilde{\mathbf{x}}$ is assigned the values:

$$\tilde{\mathbf{x}}(\xi_1), \tilde{\mathbf{x}}(\xi_2), \dots, \tilde{\mathbf{x}}(\xi_{\tilde{N}}).$$

Then, the expectation value $E[\tilde{\mathbf{x}}]$ of the random variable $\tilde{\mathbf{x}}$ generally is approximated by:

$$E[\tilde{\mathbf{x}}] \approx \frac{\tilde{\mathbf{x}}(\xi_1) + \tilde{\mathbf{x}}(\xi_2) + \dots + \tilde{\mathbf{x}}(\xi_{\tilde{N}})}{\tilde{N}}; \quad (\text{B.16})$$

although it does not correspond, at a first sight, to definition (B.15).

However, if Δx is sufficiently small, the sum of the $\Delta\tilde{N}_k$ numbers $\tilde{\mathbf{x}}(\xi_i)$ in (B.16) for which the outcome is such that $x_k \leq \tilde{\mathbf{x}}(\xi_i) \leq x_k + \Delta x$ satisfies:

$$\sum \tilde{\mathbf{x}}(\xi_i) \approx x_k \Delta\tilde{N}_k \quad (\text{B.17})$$

since $\tilde{\mathbf{x}}(\xi_i) \approx x_k$.

According to eq. (B.14), $\Delta\tilde{N}_k$ can be expressed with the density function:

$$\Delta\tilde{N}_k \approx f(x_k) \tilde{N} \Delta x. \quad (\text{B.18})$$

Thus,

$$\frac{\tilde{\mathbf{x}}(\xi_1) + \tilde{\mathbf{x}}(\xi_2) + \dots + \tilde{\mathbf{x}}(\xi_{\tilde{N}})}{\tilde{N}} \approx \sum_k x_k f(x_k) \Delta x \approx E[\tilde{\mathbf{x}}]. \quad (\text{B.19})$$

Conditional distribution and density

Definition

Considering an event \mathcal{M} such that

$$P(\mathcal{M}) \neq 0;$$

the conditional probability of an event \mathcal{A} , assuming \mathcal{M} is given by

$$P(\mathcal{A}|\mathcal{M}) = \frac{P(\mathcal{A} \cap \mathcal{M})}{P(\mathcal{M})}. \quad (\text{B.20})$$

The conditional distribution $F_{\tilde{\mathbf{x}}}(x|\mathcal{M})$ and density $f_{\tilde{\mathbf{x}}}(x|\mathcal{M})$ can be expressed as:

$$F_{\tilde{\mathbf{x}}}(x|\mathcal{M}) = \frac{P(\{\tilde{\mathbf{x}} \leq x\} \cap \mathcal{M})}{P(\mathcal{M})}; \quad (\text{B.21})$$

$$f_{\tilde{\mathbf{x}}}(x|\mathcal{M}) = \lim_{\Delta x \rightarrow 0} \frac{P(\{x \leq \tilde{\mathbf{x}} \leq x + \Delta x\} \cap \mathcal{M})}{P(\mathcal{M}) \Delta x}. \quad (\text{B.22})$$

Experimental determination

To obtain $F(x|b < x \leq a) = \frac{P(\{\tilde{\mathbf{x}} \leq x\} \cap \{b < x \leq a\})}{P(\{b < x \leq a\})}$ for an experiments with \tilde{N} trials, one rejects all outcomes ξ such that

$$\tilde{\mathbf{x}}(\xi) \leq b \text{ and } a < \tilde{\mathbf{x}}(\xi).$$

Then, $F(x|b < x \leq a)$ is approximated using the procedure described in section *distribution function* considering only the remaining outcomes.

Properties

Interestingly, the conditional distribution $F_{\tilde{\mathbf{x}}}(x|\mathcal{M})$ and density $f_{\tilde{\mathbf{x}}}(x|\mathcal{M})$ are also distribution and density function, respectively.

However, they do not contain the same amount of information as the “unconditional” distribution $F_{\tilde{\mathbf{x}}}(x)$ and density $f_{\tilde{\mathbf{x}}}(x)$. Their statistics account for fewer events than the “unconditional” statistics, either because the events are disregarded or, more commonly, because they are unknown. A simple example found in [185] is reproduced here for better understanding.

A fair-die is tossed and the random variable $\tilde{\mathbf{x}}$ is defined as:

$$\tilde{\mathbf{x}}(\xi_i) = 10i, \quad i = 1, \dots, 6; \quad (\text{B.23})$$

where ξ_i is an outcome of the experiment “one fair-die is tossed once” and i is the number of eye of the visible face for the outcome ξ_i .

The distribution function $F_{\tilde{\mathbf{x}}}(x)$ of $\tilde{\mathbf{x}}$ has a staircase form and is displayed in Figure 0-1 (left). Considering the event $\mathcal{M} = \{\xi_2, \xi_4, \xi_6\}$, $F_{\tilde{\mathbf{x}}}(x|\mathcal{M})$ has still a staircase form but is “coarser” (Figure 0-1, right). $F_{\tilde{\mathbf{x}}}(x|\mathcal{M})$ contains less information than $F_{\tilde{\mathbf{x}}}(x)$.

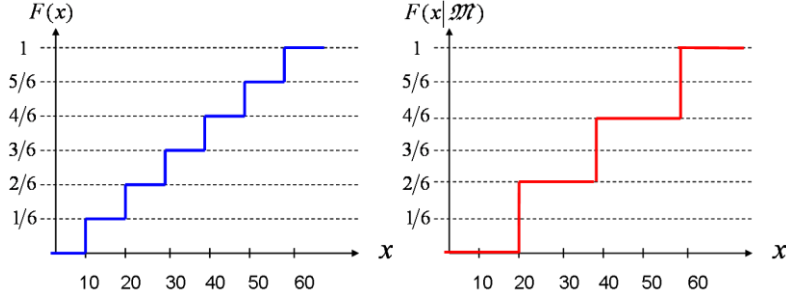


Figure 0-1: Representation of distribution function $F_{\tilde{x}}(x)$ (left) and conditional distribution function $F_{\tilde{x}}(x|M)$ (right) of the random variable \tilde{x} defined in eq. (B.23).

Function of a random variable

Definition

The function $\tilde{y} = g(\tilde{x})$, where $g(x)$ is a function of the real variable x , is also a random variable (actually $g(x)$ must be a *Baire* function). The probability of the set of outcomes ξ such that $\{\tilde{y} = g[\tilde{x}(\xi)] \leq y\}$ for a given number y is the distribution of the random variable \tilde{y} :

$$F_{\tilde{y}}(y) = P\{\tilde{y} = g[\tilde{x}(\xi)] \leq y\} = P\{g[\tilde{x}(\xi)] \leq y\}. \quad (\text{B.24})$$

Statistics

$F_{\tilde{y}}(y)$ and its derivative

$$f_{\tilde{y}}(y) = \frac{dF_{\tilde{y}}(y)}{dy} \quad (\text{B.25})$$

can be estimated with $g(x)$ and the distribution $F_{\tilde{x}}(x)$ or density $f_{\tilde{x}}(x)$ of the random variable \tilde{x} .

However, in general, the statistics of $\tilde{y} = g(\tilde{x})$ is not a simple function in terms of the statistics of \tilde{x} . Indeed, the fundamental theorem states that

$$f_{\tilde{y}}(y) = \frac{f_{\tilde{x}}(x_1)}{|g'(x_1)|} + \dots + \frac{f_{\tilde{x}}(x_n)}{|g'(x_n)|} + \dots \quad (\text{B.26})$$

where the x_i are the real roots of the equation

$$y = g(x)$$

for the given y .

Expectation value

Definition

Fortunately, it can be shown that the expectation value $E[g(\tilde{x})]$ of any function $g(\tilde{x})$, including any non-linearity, simply is given by:

$$E[g(\tilde{x})] = \int_{-\infty}^{+\infty} g(x) f(x) dx. \quad (\text{B.27})$$

Thus, knowing the statistics (pdf) of \tilde{x} is sufficient to close any non-linear terms; in particular source terms in fluid dynamic governing equations. Furthermore, eq. (B.27) implies that any moments of a random variable \tilde{x} can be calculated as soon as its pdf is known.

Experimental determination

Considering our experiment, the outcomes of the \tilde{N} trials is:

$$\xi_1, \xi_2, \dots, \xi_{\tilde{N}}.$$

Correspondingly, the random variable $\tilde{y} = g(\tilde{x})$ is assigned the values:

$$g[\tilde{x}(\xi_1)], g[\tilde{x}(\xi_2)], \dots, g[\tilde{x}(\xi_{\tilde{N}})].$$

Then, the expectation value $E[\tilde{y}] = E[g(\tilde{x})]$ of random variable $\tilde{y} = g(\tilde{x})$ generally is approximated by:

$$E[g(\tilde{x})] \approx \frac{g[\tilde{x}(\xi_1)] + g[\tilde{x}(\xi_2)] + \dots + g[\tilde{x}(\xi_{\tilde{N}})]}{\tilde{N}}, \quad (\text{B.28})$$

or, equivalently, by (see eq. (B.17) and (B.18)):

$$E[\tilde{y}] = E[g(\tilde{x})] \approx \sum_k g(x_k) f(x_k) \Delta x. \quad (\text{B.29})$$

Approximation (B.28) is intensively employed in Monte-Carlo techniques.

Conditional expectation value

Since the conditional density $f_{\tilde{x}}(x|\mathcal{M})$ assuming an event \mathcal{M} is also a density function, eq. (B.27) can directly applied to calculate $E[\tilde{x}|\mathcal{M}]$ or $E[g(\tilde{x})|\mathcal{M}]$:

$$E[\tilde{x}|\mathcal{M}] = \int_{-\infty}^{+\infty} x f(\tilde{x}|\mathcal{M}) dx; \quad (\text{B.30})$$

$$E[g(\tilde{x})|\mathcal{M}] = \int_{-\infty}^{+\infty} g(x) f(\tilde{x}|\mathcal{M}) dx. \quad (\text{B.31})$$

Variance and moments

The expectation value is one information on the statistics of the random variable \tilde{x} . It can be considered as the center of gravity of $f(x)$. A more comprehensive description of the statistics of \tilde{x} is obtained when other "moments" of \tilde{x} are known. For example, the moments \tilde{m}_k of \tilde{x} are defined as:

$$\tilde{m}_k = E[\tilde{x}^k] = \int_{-\infty}^{+\infty} x^k f(x) dx. \quad (\text{B.32})$$

By definition, $\tilde{m}_0 = 1$ and $\tilde{m}_1 = E[\tilde{x}]$.

The central moments $\tilde{\mu}_k$, and in particular $\tilde{\mu}_2$, usually are also introduced to specify \tilde{x} :

$$\tilde{\mu}_k = E\left[(\tilde{x} - E[\tilde{x}])^k\right] = \int_{-\infty}^{+\infty} (\tilde{x} - E[\tilde{x}])^k f(x) dx. \quad (\text{B.33})$$

For instance, $\tilde{\mu}_0 = 1$, $\tilde{\mu}_1 = 0$ and $\tilde{\mu}_2 = \hat{\sigma}_{\tilde{x}}^2$, where $\hat{\sigma}_{\tilde{x}}^2$ (or simply $\hat{\sigma}^2$, when there is no risk of confusion) is called the variance of the random variable \tilde{x} .

Tchebycheff inequality

The variance is an important parameter for the description of the statistics of a random variable. It gives a measure of the concentration of the values of \tilde{x} near its expectation value $E[\tilde{x}]$. The Tchebycheff inequality translates this idea in terms of probability:

$$P\{|\tilde{x} - E[\tilde{x}]| \geq k\hat{\sigma}\} \leq \frac{1}{k^2}, \quad \forall k \in \mathbb{R}_+^*. \quad (\text{B.34})$$

(B.34) is true independently of the shape of the pdf. Introducing $\tilde{\eta} \equiv E[\tilde{x}]$, the probability that \tilde{x} takes values in the interval $[\tilde{\eta} - \varepsilon, \tilde{\eta} + \varepsilon]$ centered at $\tilde{\eta}$ is close to 1 provided $\hat{\sigma} \ll \varepsilon = k\hat{\sigma}$. Figure 0-2 gives an illustration of the Tchebycheff inequality.

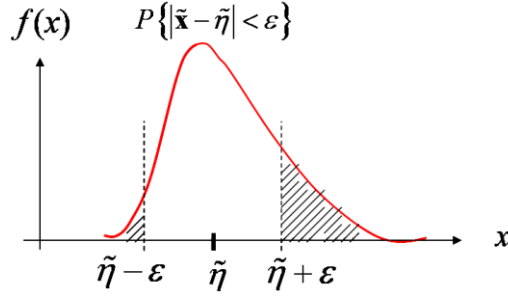


Figure 0-2: Graphical representation of the Tchebycheff inequality: probability that the random variable \tilde{x} takes values in the interval $[\tilde{\eta} - \varepsilon; \tilde{\eta} + \varepsilon]$ is not dashed.

Examples

Normal distribution

A normal distribution is defined by a Gaussian density function:

$$f(x) = \frac{1}{\hat{\sigma}\sqrt{2\pi}} e^{-(x-\tilde{\eta})/2\hat{\sigma}^2}; \quad (\text{B.35})$$

where $\hat{\sigma}$ is the variance and $\tilde{\eta}$ the expectation value of the random variable whose pdf is given by (B.35). The corresponding distribution function is

$$F(x) = \int_{-\infty}^x f(x)dx = \frac{1}{2} + \text{erf}\left(\frac{x-\tilde{\eta}}{\hat{\sigma}}\right). \quad (\text{B.36})$$

While, in general, expectation value and variance cannot completely describe the statistic of a random variable, random variables which are normally distributed are completely determined by the two parameters $\tilde{\eta}$ and $\hat{\sigma}$.

Normal distributed random variables have a central importance in the law of large number and in the theory of stochastic process.

Discrete distribution

If the total number of outcomes of the experiment \mathcal{E} is finite, then any random variable \tilde{x} define on its space is of discrete type. In that case, $F(x)$ is of a staircase form and $f(x)$ consists of a sum of impulse function $\delta(x)$, also called delta or Dirac function. The impulse function is defined by its integral property. This property reads for any x_0 and any function $\phi(x)$ continuous at x_0 :

$$\int_{-\infty}^{+\infty} \phi(x)\delta(x-x_0)dx = \phi(x_0). \quad (\text{B.37})$$

Supposing the staircase function $F(x)$ is discontinuous at the points x_i and defining by k_i the magnitude of discontinuity of $F(x)$ at x_i :

$$k_i = F(x_i^+) - F(x_i^-); \quad (\text{B.38})$$

then, $f(x)$ is given by:

$$f(x) = \sum_i k_i \delta(x-x_i). \quad (\text{B.39})$$

Discrete distributions can be used to approximate continuous distributions.

Two random variables

Joint distribution function

Definition

The joint distribution function $F_{\tilde{\mathbf{x}}\tilde{\mathbf{y}}}(x, y)$ (or more simply $F(x, y)$) of the random variable $\tilde{\mathbf{x}}$ and $\tilde{\mathbf{y}}$ represent the probability of the set $\{\tilde{\mathbf{x}} \leq x\} \cap \{\tilde{\mathbf{y}} \leq y\}$:

$$F_{\tilde{\mathbf{x}}\tilde{\mathbf{y}}}(x, y) = P\{\tilde{\mathbf{x}} \leq x, \tilde{\mathbf{y}} \leq y\}. \quad (\text{B.40})$$

Properties

The marginal distribution $F_{\tilde{\mathbf{x}}}(x)$ and $F_{\tilde{\mathbf{y}}}(y)$ of the random variable $\tilde{\mathbf{x}}$ and $\tilde{\mathbf{y}}$ can be obtained from $F_{\tilde{\mathbf{x}}\tilde{\mathbf{y}}}(x, y)$ as:

$$F_{\tilde{\mathbf{x}}}(x) = F_{\tilde{\mathbf{x}}\tilde{\mathbf{y}}}(x, \infty); \quad (\text{B.41})$$

$$F_{\tilde{\mathbf{y}}}(y) = F_{\tilde{\mathbf{x}}\tilde{\mathbf{y}}}(\infty, y). \quad (\text{B.42})$$

Joint density function

Definition

The joint density function $f(x, y)$ of random variable $\tilde{\mathbf{x}}$ and $\tilde{\mathbf{y}}$ is defined as the derivative of the joint distribution function $F(x, y)$:

$$f(x, y) = \frac{\partial^2 F(x, y)}{\partial x \partial y}. \quad (\text{B.43})$$

$f(x, y)dx dy$ represents the probability of the outcomes ξ of the experiment such that

$$x \leq \tilde{\mathbf{x}}(\xi) \leq x + dx \quad \text{and} \quad y \leq \tilde{\mathbf{y}} \leq y + dy,$$

when dx and dy tend to 0.

Properties

The marginal density functions $f_{\tilde{\mathbf{x}}}(x)$ and $f_{\tilde{\mathbf{y}}}(y)$ are obtained from the joint-pdf $f_{\tilde{\mathbf{x}}\tilde{\mathbf{y}}}(x, y)$ by differentiating eq. (B.41) and (B.42) by x and y , respectively:

$$f_{\tilde{\mathbf{x}}}(x) = \int_{-\infty}^{\infty} f_{\tilde{\mathbf{x}}\tilde{\mathbf{y}}}(x, y) dy; \quad (\text{B.44})$$

$$f_{\tilde{\mathbf{y}}}(y) = \int_{-\infty}^{\infty} f_{\tilde{\mathbf{x}}\tilde{\mathbf{y}}}(x, y) dx. \quad (\text{B.45})$$

Conditional distribution and density

Definition

The conditional distribution $f_{\tilde{\mathbf{y}}}(y|\mathcal{M})$ of the random variable $\tilde{\mathbf{y}}$ assuming an event \mathcal{M} can be defined for an event \mathcal{M} expressed in terms of the random variable $\tilde{\mathbf{x}}$. Then, conditional distribution and density can be expressed in terms of joint and marginal distribution and density functions. Typically,

$$f_{\tilde{\mathbf{y}}}(y|\tilde{\mathbf{x}} = x) = \frac{f_{\tilde{\mathbf{x}}\tilde{\mathbf{y}}}(x, y)}{f_{\tilde{\mathbf{x}}}(x)}; \quad (\text{B.46})$$

$$F_{\tilde{\mathbf{y}}}(y|x_1 < \tilde{\mathbf{x}} \leq x_2) = \frac{F_{\tilde{\mathbf{x}}\tilde{\mathbf{y}}}(x_2, y) - F_{\tilde{\mathbf{x}}\tilde{\mathbf{y}}}(x_1, y)}{F_{\tilde{\mathbf{x}}}(x_2) - F_{\tilde{\mathbf{x}}}(x_1)}. \quad (\text{B.47})$$

Conditional expected values

Whereas $E[\tilde{y}|\tilde{x} = x] = \int_{-\infty}^{\infty} y f(y|x) dy$ is a number depending on the value x , $E[\tilde{y}|\tilde{x}]$ is also a random variable defined as follows [185]: For a given experimental outcome ξ , the random variable takes the value $\tilde{x}(\xi)$ and the random variable $E[\tilde{y}|\tilde{x}]$ is $E[\tilde{y}|\tilde{x}(\xi)]$.

The expected value of $E[\tilde{y}|\tilde{x}]$ equals the expected value of the random variable \tilde{y} :

$$E[E[\tilde{y}|\tilde{x}]] = E[\tilde{y}]. \quad (\text{B.48})$$

Correlation

Two random variables \tilde{x} and \tilde{y} are called uncorrelated if

$$E[\tilde{x}\tilde{y}] = E[\tilde{x}]E[\tilde{y}]. \quad (\text{B.49})$$

Independence

Two random variables \tilde{x} and \tilde{y} are called independent if

$$f(x, y) = f_{\tilde{x}}(x)f_{\tilde{y}}(y). \quad (\text{B.50})$$

Sum of two random variables

If the random variables \tilde{x} and \tilde{y} are independent then the density of their sum $\tilde{z} = \tilde{x} + \tilde{y}$ equals the convolution of their respective densities:

$$f_{\tilde{z}}(z) = \int_{-\infty}^{\infty} f_{\tilde{x}}(z-y)f_{\tilde{y}}(y)dy = \int_{-\infty}^{\infty} f_{\tilde{x}}(x)f_{\tilde{y}}(z-x)dx. \quad (\text{B.51})$$

Sequence of random variables

Definitions and properties for one and two random variables are summarized in the last sections. Distribution and density functions can be extended to more than two random variables. In this section, interesting properties of the sequence of random variables are described.

Conditional densities

The conditional density function $f(x_1, \dots, x_k | x_{k+1}, \dots, x_n)$ of $\tilde{x}_1, \dots, \tilde{x}_k$ assuming $\tilde{x}_{k+1}, \dots, \tilde{x}_n$ is

$$f(x_1, \dots, x_k | x_{k+1}, \dots, x_n) = \frac{f(x_1, \dots, x_k, \dots, x_n)}{f(x_{k+1}, \dots, x_n)}. \quad (\text{B.52})$$

Independence

The random variables $\tilde{x}_1, \dots, \tilde{x}_n$ are independent if the events

$$\{\tilde{x}_1 \leq x_1\}, \dots, \{\tilde{x}_n \leq x_n\}$$

are independent for any x_1, \dots, x_n . In this case, the distribution and density functions satisfy:

$$F(x_1, \dots, x_n) = F(x_1) \dots F(x_n); \quad (\text{B.53})$$

$$f(x_1, \dots, x_n) = f(x_1) \dots f(x_n). \quad (\text{B.54})$$

Independent random variables are generally generated by independent experiments.

Law of large numbers

Introducing the random variable

$$\tilde{\mathbf{x}}_m = \frac{\tilde{\mathbf{x}}_1 + \dots + \tilde{\mathbf{x}}_{\tilde{N}}}{\tilde{N}} \quad (\text{B.55})$$

where the random variables $\tilde{\mathbf{x}}_i$ all have the same expectation value $\tilde{\eta} = E[\tilde{\mathbf{x}}_i]$ and the same variance $\tilde{\sigma}$; it can be shown that the expectation value of $\tilde{\mathbf{x}}_m$ is $\tilde{\eta}$ and its variance $\tilde{\sigma}_{\tilde{\mathbf{x}}_m}$ is such that

$$\tilde{\sigma}_{\tilde{\mathbf{x}}_m}^2 = \frac{\tilde{\sigma}^2}{\tilde{N}}. \quad (\text{B.56})$$

According to the Tchebycheff inequality eq. (B.34), the probability of the events ξ such that $|\tilde{\mathbf{x}}_m(\xi) - \tilde{\eta}| < \varepsilon$ is:

$$P\{|\tilde{\mathbf{x}}_m - \tilde{\eta}| < \varepsilon\} \leq 1 - \frac{\tilde{\sigma}^2}{\tilde{N}\varepsilon^2}, \quad \forall \varepsilon \in \mathbb{R}_+^*. \quad (\text{B.57})$$

Thus, for \tilde{N} sufficiently large, it is almost certain that the mean value of the random variables $\tilde{\mathbf{x}}_i$ takes a value near $\tilde{\eta}$.

Central limit theorem

Finally, the central limit theorem indicates the random variable $\tilde{\mathbf{x}}_m = \frac{\tilde{\mathbf{x}}_1 + \dots + \tilde{\mathbf{x}}_{\tilde{N}}}{\tilde{N}}$ tends to a normal curve regardless of the shape of the densities $f_i(x)$.

Stochastic process

Definition

Mathematically, a stochastic process is defined according to an experiment \mathcal{E} whose outcomes ξ are various objects belonging to the certain event \mathcal{G} . To every ξ , a time function $\tilde{\mathbf{x}}(t, \xi)$ is assigned according to some rule. Thus, the stochastic process $\tilde{\mathbf{x}}(t)$ is a family of time functions $\tilde{\mathbf{x}}(t, \xi)$.

The stochastic process $\tilde{\mathbf{x}}(t)$ has four meaning:

- 1- a family of time functions (t variable, ξ variable)
- 2- a single time function (t variable, ξ fixed)
- 3- a random variable (t fixed, ξ variable)
- 4- a number (t fixed, ξ fixed)

Statistics of a stochastic process

First order

For a specific time t , $\tilde{\mathbf{x}}(t)$ is a random variable. Thus, its distribution

$$F(x; t) = P\{\tilde{\mathbf{x}}(t) \leq x\} \quad (\text{B.58})$$

can be defined. It represents the probability of all outcomes ξ such that, at the specified time t , the function $\tilde{\mathbf{x}}(t)$ do not exceed the number x . $F(x; t)$ is called first-order distribution of the process $\tilde{\mathbf{x}}(t)$. The corresponding density is

$$f(x, t) = \frac{\partial F(x, t)}{\partial x}. \quad (\text{B.59})$$

Second-order statistic

The distribution of the joint distribution of the two random variables $\tilde{\mathbf{x}}(t_1)$ and $\tilde{\mathbf{x}}(t_2)$, whereby t_1 and t_2 are two time instances, is called second-order distribution. It is defined as:

$$F(x_1, x_2; t_1, t_2) = P\{\tilde{\mathbf{x}}(t_1) \leq x_1, \tilde{\mathbf{x}}(t_2) \leq x_2\}. \quad (\text{B.60})$$

The corresponding density is given by:

$$f(x_1, x_2; t_1, t_2) = \frac{\partial^2 F(x_1, x_2; t_1, t_2)}{\partial x_1 \partial x_2}. \quad (\text{B.61})$$

Higher order statistic

The n th order distribution function is defined as:

$$F(x_1, \dots, x_n; t_1, \dots, t_n) = P\{\tilde{\mathbf{x}}(t_1) \leq x_1, \dots, \tilde{\mathbf{x}}(t_n) \leq x_n\}. \quad (\text{B.62})$$

The corresponding density is given by:

$$f(x_1, \dots, x_n; t_1, \dots, t_n) = \frac{\partial^n F(x_1, \dots, x_n; t_1, \dots, t_n)}{\partial x_1 \dots \partial x_n}. \quad (\text{B.63})$$

A real stochastic process is statistically determined if one knows its n th order distribution function for any n and t_1, \dots, t_n .

Function of a stochastic process

Expectation value

For any given time t , the stochastic process $\tilde{\mathbf{x}}(t)$ is a random variable. As such, one can define its expectation value:

$$\tilde{\eta}(t) = E[\tilde{\mathbf{x}}(t)] = \int_{-\infty}^{\infty} x f(x; t) dx; \quad (\text{B.64})$$

which is a function of time.

Autocorrelation

The autocorrelation $R(t_1, t_2)$ of a stochastic process $\tilde{\mathbf{x}}(t)$ is the joint moment of the random variables $\tilde{\mathbf{x}}(t_1)$ and $\tilde{\mathbf{x}}(t_2)$:

$$R(t_1, t_2) = E[\tilde{\mathbf{x}}(t_1)\tilde{\mathbf{x}}(t_2)] = \int_{-\infty}^{\infty} x_1 x_2 f(x_1, x_2; t_1, t_2) dx_1 dx_2. \quad (\text{B.65})$$

$R(t_1, t_2)$ is a function of t_1 and t_2 .

If the stochastic process $\tilde{\mathbf{x}}(t)$ is stationary, it can be shown that the autocorrelation function only depends on the time difference $t_1 - t_2$:

$$R(t_1, t_2) = R(t_2 - t_1). \quad (\text{B.66})$$

The autocorrelation has a maximum at the origin:

$$|R(\tau)| \leq R(0). \quad (\text{B.67})$$

Autocovariance

The autocovariance $C(t_1, t_2)$ of $\tilde{\mathbf{x}}(t)$ is the covariance of the random variables $\tilde{\mathbf{x}}(t_1)$ and $\tilde{\mathbf{x}}(t_2)$:

$$C(t_1, t_2) = E[\{\tilde{\mathbf{x}}(t_1) - \tilde{\eta}(t_1)\}\{\tilde{\mathbf{x}}(t_2) - \tilde{\eta}(t_2)\}]. \quad (\text{B.68})$$

The variance $\tilde{\sigma}_{\tilde{\mathbf{x}}(t)}^2$ of the random variable $\tilde{\mathbf{x}}(t)$ is given by:

$$\tilde{\sigma}_{\tilde{\mathbf{x}}(t)}^2 = C(t, t) = R(t, t) - \tilde{\eta}^2(t). \quad (\text{B.69})$$

Ergodicity

Ergodicity deals with the problem of determining the statistics of a process $\tilde{\mathbf{x}}(t)$ from a single observation. $\tilde{\mathbf{x}}(t)$ is ergodic if its statistics can be determined from a single function $\tilde{\mathbf{x}}(t, \xi)$ of the process.

For example, the mean average

$$\tilde{\mathbf{n}}_T = \frac{1}{2T} \int_{-T}^T \tilde{\mathbf{x}}(t) dt \quad (\text{B.70})$$

of a given stochastic process $\tilde{\mathbf{x}}(t)$ is also a random variable. For the limit of $\tilde{\mathbf{n}}_T$ with $T \rightarrow \infty$ to be the expectation value of $\tilde{\mathbf{x}}(t)$, its variance $\widehat{\sigma}_{\tilde{\mathbf{n}}_T}$ must tend to zero with $T \rightarrow \infty$.

Only in that case, the time average of $\tilde{\mathbf{x}}(t)$ equal its ensemble average, i.e. its expectation value.

The estimation of the autocorrelation function $R(\tau)$ with a single observation is more difficult: the function

$$\tilde{\mathbf{R}}_T(\tau) = \frac{1}{2T} \int_{-T}^T \tilde{\mathbf{x}}(t+\tau)\tilde{\mathbf{x}}(t) dt \quad (\text{B.71})$$

of a given stationary stochastic process $\tilde{\mathbf{x}}(t)$ is also a random variable and knowledge of fourth-order moments is required [185] to ensure that the limit of $\tilde{\mathbf{R}}_T(\tau)$ with $T \rightarrow \infty$ actually is the autocorrelation $R(\tau)$ function of the process $\tilde{\mathbf{x}}(t)$.

Examples

Example of random variables is given in chapter *numerical modeling*: the particle number density function has been presented for both monodisperse and polydisperse flows (reproduced here in Figure 0-3).

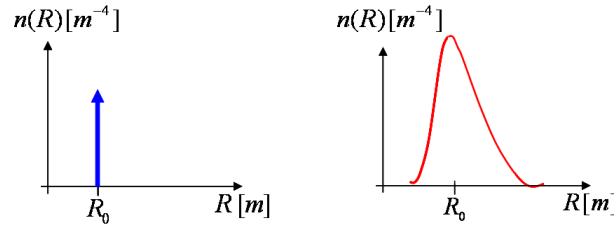


Figure 0-3: Representation of the particle number density distribution function $n(R)$ for monodisperse (left) and polydisperse (right) flows.

Scaling these functions by the total number of particles n_T , one obtains the function $f(R) \equiv n(R)/n_T$ which possesses following characteristics:

$$\int_{-\infty}^{+\infty} f(R) dR = 1; \quad (\text{B.72})$$

$$\forall R, f(R) \geq 0. \quad (\text{B.73})$$

Thus, $f(R)$ can be considered to be a pdf; and the function $F(R)$ satisfying:

$$f(R) = \frac{dF}{dR}; \quad (\text{B.74})$$

$$F(-\infty) = 0; \quad (\text{B.75})$$

$$F(+\infty) = 1; \quad (\text{B.76})$$

$$F(R_1) \leq F(R_2) \text{ for } R_1 < R_2; \quad (\text{B.77})$$

$$\text{and } F(R^+) = F(R); \quad (\text{B.78})$$

is its distribution function. For a given R_0 , $F(R_0)$ represents the probability to find in the flow particles whose radius is smaller than or equal R_0 :

$$F(R_0) = P\{R \leq R_0\}; \quad (\text{B.79})$$

while, $f(R_0)dR$ represents the probability to find in the flow particles whose radius is between R_0 and $R_0 + dR$, whereby $dR \rightarrow 0$.

The distribution is discontinuous for ideal monodisperse flows, while it generally is continuous for polydisperse flows (Figure 0-4).

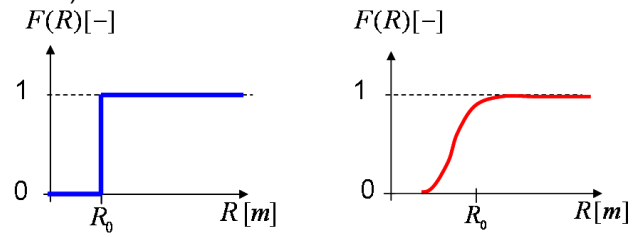


Figure 0-4: Representation of the cumulative density functions $F(R)$ for monodisperse (left) and polydisperse (right) flows.